

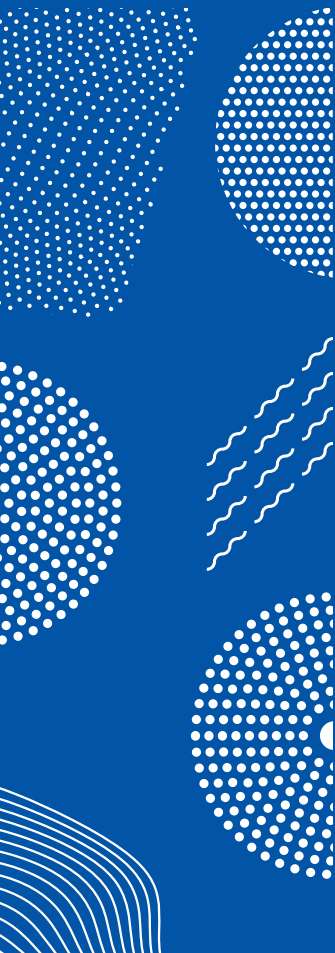


ILMATIETEEN LAITOS  
METEOROLOGISKA INSTITUTET  
FINNISH METEOROLOGICAL INSTITUTE

185  
CONTRIBUTIONS

# **AEROSOL MODELLING: IMPROVING THE UNDERSTANDING OF AEROSOL PROCESSES AND THEIR EFFECTS ON THE CLIMATE AT PROCESS AND GLOBAL-SCALE**

EEMELI HOLOPAINEN



FINNISH METEOROLOGICAL INSTITUTE  
CONTRIBUTIONS

No. 185

**AEROSOL MODELLING: IMPROVING THE  
UNDERSTANDING OF AEROSOL PROCESSES AND THEIR  
EFFECTS ON THE CLIMATE AT PROCESS AND  
GLOBAL-SCALE**

Eemeli Holopainen

Finnish Meteorological Institute  
Atmospheric Research Centre of Eastern Finland  
Kuopio, Finland

ACADEMIC DISSERTATION

To be presented by the permission of the Faculty of Science, Forestry and  
Technology of the University of Eastern Finland for public examination in the  
auditorium SN200, Yliopistonranta 1, Kuopio, on March 31, 2023, at 12 o'clock  
noon.

Kuopio 2023

ISBN: 978-952-336-168-3 (print)  
ISSN: 0782-6117 (print)  
ISBN: 978-952-336-169-0 (online)  
ISSN: 2814-5658 (online)

Edita Prima Oy  
Helsinki 2023

Author's address:	<p>Finnish Meteorological Institute          Atmospheric Research Centre of Eastern Finland          P.O.Box 1627          70211 Kuopio, Finland          email: eemeli.holopainen@fmi.fi</p>
Supervisors:	<p>Docent Thomas Kühn, Ph.D.          Finnish Meteorological Institute          Weather and Climate Change Impact Research          P.O.Box 503          00101 Helsinki, Finland          email: thomas.kuhn@fmi.fi</p> <p>Docent Harri Kokkola, Ph.D.          Finnish Meteorological Institute          Atmospheric Research Centre of Eastern Finland          P.O.Box 1627          70211 Kuopio, Finland          email: harri.kokkola@fmi.fi</p> <p>Research Professor Anton Laakso, Ph.D.          Finnish Meteorological Institute          Atmospheric Research Centre of Eastern Finland          P.O.Box 1627          70211 Kuopio, Finland          email: anton.laakso@fmi.fi</p> <p>Associate Professor Taina Yli-Juuti, Ph.D.          University of Eastern Finland          Department of Technical Physics          P.O.Box 1627          70211 Kuopio, Finland          email: taina.yli-juuti@uef.fi</p>
Reviewers:	<p>Professor Veli-Matti Kerminen, Ph.D.          University of Helsinki          Institute for Atmospheric and Earth System Research          P.O. Box 64          00014 Helsinki, Finland          email: veli-matti.kerminen@helsinki.fi</p> <p>Professor Miikka Dal Maso, Ph.D.          Tampere University          Physics Unit          P.O.Box 589          33720 Tampere, Finland          email: miikka.dalmaso@tuni.fi</p>
Opponent:	<p>Research Associate Marc Salzmann, Ph.D.          University of Leipzig          Institute for Meteorology          P.O.Box 100920          04103 Leipzig, Germany          email: marc.salzmann@uni-leipzig.de</p>





Published by

**Finnish Meteorological Institute**  
Erik Palménin aukio 1, P.O. Box 503  
FIN-00101 Helsinki, Finland

Series title, number, and report code of publication  
Finnish Meteorological Institute  
Contributions, 185, FMI-CONT-185

Date

March 2023

Author(s)

Eemeli Holopainen

ORCID iD

0000-0001-9782-3430

Title

Aerosol modelling: Improving the understanding of aerosol processes and their effects on the climate at process and global-scale

## Abstract

Atmospheric aerosol particles have the ability to affect climate through cloud interactions and direct scattering and absorption of radiation. These aerosol particles can also affect human health through respiratory system. Aerosol particles are emitted to the atmosphere through direct sources or they can be formed through chemical processes from gas phase precursors. The different atmospheric processes and climate feedbacks of aerosol particles can be studied using process-scale models as well as larger global-scale models. In recent years, it has been found out that certain aerosol species lack information on their thermodynamic properties, causing uncertainties in process-scale modelling as well as global-scale modelling. In addition, transport of aerosols to remote regions, where emissions of aerosol particles are low, is poorly modelled in global-scale models. Furthermore, sources for formed secondary organic aerosol (SOA) include uncertainties in global aerosol-climate models, which causes uncertainty to estimating the radiative forcing (RF).

In this thesis, these aspects relating to uncertainties are addressed using process and global-scale modelling. This was done first by evaluating the capability of thermodynamic equilibrium model to reproduce observed hygroscopicity in terms of dimethylamine, sulfuric acid and ammonia containing particles. Second, an in-cloud wet deposition scheme was developed (hereafter referred to as the newly-developed scheme) for global models which use sectional aerosol description. The newly-developed wet deposition scheme was tested using ECHAM-HAMMOZ global aerosol-climate model with Sectional Aerosol model for Large-Scale Applications (SALSA) in terms of aerosol vertical distributions and lifetimes. Third, the biotic stress effects to trees over boreal region and their effects to SOA formation, clouds and radiative effects were studied using ECHAM-HAMMOZ with SALSA.

The results showed that when the thermodynamic equilibrium model was used to model particles with sizes of the order of couple of tens of nanometers, it was inadequate in estimating the hygroscopic growth of dimethylamine (DMA), sulfuric acid (SA) and ammonia containing particles. Thus, more investigation is needed in terms of thermodynamics of DMA containing systems to properly evaluate its effects to climate. Global aerosol-climate models are very complex and thus making aerosol processes more physically sound can even impair the results. This was seen in the results of the newly-developed, more physical, in-cloud wet deposition scheme as it produced spurious vertical profiles and atmospheric black carbon lifetime when compared to the pre-existing scheme. Especially, the atmospheric lifetime of black carbon, in the newly-developed scheme, was 1.6 times longer than in the pre-existing scheme and over 2.6 times longer than has been suggested by experimental studies. Thus, the sensitivity of the newly-developed scheme was tested in terms of internal mixing and emission size distribution of black carbon as well as ageing of aerosol species. These results showed that mixing black carbon with soluble substances produced best results in comparison with the observations as well as atmospheric lifetimes of aerosol species when compared to AEROCOM model means. Lastly, the results studying the biotic stress effects on climate showed that increasing the extent of stress in boreal trees enhanced SOA formation as the emissions of volatile organic compounds (VOCs) were increased. The enhanced SOA formation increased cloud droplet number concentration (CDNC) at cloud top and caused stronger negative RF in both all-sky and clear-sky cases. In the future, aerosol model development should investigate further on the thermodynamic properties of aerosol species, especially with respect to DMA. The wet removal and extent of internal mixing of different aerosol species, especially black carbon, should be further investigated and revised, in global climate models, to properly evaluate the transport of aerosol particles. In addition, sources of atmospheric SOA needs further investigation to properly describe its behaviour in the atmosphere as well as the effects on the climate.

Publishing unit

Finnish Meteorological Institute, Atmospheric Research Centre of Eastern Finland

Classification (UDC)

551.58, 551.510, 551.510.412

Keywords

Process modelling, Global modelling, Aerosol, Clouds, Hygroscopicity, Wet deposition, Biotic stress, SOA

ISSN and series title

0782-6117

2814-5658

Finnish Meteorological Institute Contributions

ISBN

978-952-336-168-3 (print)

978-952-336-169-0 (online)

DOI

10.35614/isbn.9789523361690

Language

English

Pages

62



Julkaisija

**Ilmatieteiden laitos**  
Erik Palménin aukio 1  
PL 503, 00101 Helsinki

Julkaisun sarja, numero ja raporttikoodi  
Finnish Meteorological Institute  
Contributions, 185, FMI-CONT-185

Päiväys

Maaliskuu 2023

Tekijä(t)  
Eemeli Holopainen

ORCID iD  
0000-0001-9782-3430

Nimeke

Aerosolimallinnus: Aerosoliprosessien ja aerosolien ilmastovaikutusten ymmärtämisen parantaminen prosessi- ja globaalitasolla

## Tiivistelmä

Ilmakehän aerosolihiukkasilla on kyky vaikuttaa ilmastoon pilvivoorovaikutusten kautta sekä suoraan sirottamalla ja absorboimalla itseensä säteilyä. Nämä aerosolihiukkaset voivat myös vaikuttaa ihmisterveyteen hengityselimien kautta. Aerosolihiukkasia vapautuu ilmakehään suorien lähteiden kautta tai ne voivat syntyä kemiallisissa prosesseissa kaasufaasin esiasteista. Eri aerosoliprosesseja ja aerosolihiukkasten ilmastovaikutuksia voidaan tutkia käyttäen prosessi- ja globaalin mittakaavan malleja. Viime vuosina on havaittu, että tietyiltä aerosolilyhdisteilä puuttuu tietoja niiden termodynaamisista ominaisuuksista, joka aiheuttaa epävarmuutta prosessi- ja globaalitason mallinnuksessa. Lisäksi aerosolien kaukokulkeuma syrjäisille alueille, joilla aerosolihiukkasten päästöt ovat vähäisiä, on heikosti mallinnettu globaalin mittakaavan malleissa. Lisäksi sekundaarisen orgaanisen aerosolin (SOA) päästölähteet sisältävät epävarmuuksia globaalin mittakaavan malleissa, joka aiheuttaa epävarmuutta säteilypakotteen arvioinnissa.

Tässä työssä näitä näkökohtia, jotka liittyvät kyseisiin epävarmuuksiin, käsitellään käyttäen prosessi- ja globaalin mittakaavan mallinnusta. Tämä tehtiin ensiksi arvioimalla termodynaamisen tasapainomallin kykyä kuvata dimetyyliamiinia, rikkihappoa ja ammoniakkaa sisältävien hiukkasten vedenottoa verrattuna mittauksiin. Toiseksi työssä kehitettiin pilven sisäinen märkäpoistumajärjestelmä globaalitason malleille, jotka käyttävät kokoon perustuvaa aerosolikuvausta. Vasta kehitetty märkäpoistumajärjestelmää testattiin aerosolien pystyprofiilien ja elinikien suhteen käyttämällä ECHAM-HAMMOZ globaalia aerosoli-ilmastomallia, joka sisälsi ”Sectional Aerosol model for Large-Scale Applications (SALSA)” -mikrofysiikkakuvauksen. Kolmanneksi tutkittiin havumetsävyöhykkeen puihin kohdistuneen biotillisen stressin vaikutusta SOA:n muodostumiseen, pilviin ja säteilyvaikutuksiin käyttämällä ECHAM-HAMMOZ:ia SALSA:n kanssa.

Tulokset osoittivat, että kun termodynaamista tasapainomallia käytettiin mallinnettaessa hiukkasia, joiden koko oli muutaman kymmenen nanometrien luokkaa, malli oli epäpätevä arvioimaan dimetyyliamiinia (DMA), rikkihappoa ja ammoniakkaa sisältävien hiukkasten hygroskooppisuutta. Näin ollen lisätutkimuksia tarvitaan DMA:a sisältävien systeemien termodynamiikasta, jotta voidaan arvioida kunnolla sen vaikutusta ilmastoon. Globaalit aerosoli-ilmastomallit ovat erittäin monimutkaisia ja siksi aerosoliprosessien muuttaminen fysikaalisemmaksi voi jopa heikentää tuloksia. Tämä havaittiin vasta kehitetyn, fysikaalisemman, märkäpoistumajärjestelmän tuottamista tuloksista, jotka osoittivat kehitetyn menetelmän tuottavan harhaanjohtavia pystyprofiileja sekä vääristävän mustan hiilen elinikää verrattuna aiempaan järjestelmään. Erityisesti mustan hiilen elinikää, vasta kehitetyssä järjestelmässä, oli 1.6 kertaa pidempi kuin aiemmassa järjestelmässä ja yli 2.6 kertaa pidempi kuin kokeellisissa tutkimuksissa on ehdotettu. Siksi vasta kehitetyn järjestelmän herkkyyttä testattiin mustan hiilen sisäisen sekoittumisen ja päästökokojakautuman sekä aerosolilyhdisteiden ikääntymisen kannalta. Nämä tulokset osoittivat, että mustan hiilen sekoittaminen liukoisten yhdisteiden kanssa tuotti parhaat tulokset verrattuna havaintoihin sekä aerosolilyhdisteiden eliniät verrattuna AEROCOM mallien keskiarvoihin. Lopuksi tulokset, joissa tutkittiin biotillisen stressin vaikutusta ilmastoon, osoittivat, että stressin lisääminen havumetsävyöhykkeen puissa lisäsi SOA:n muodostumista, koska haihtuvien orgaanisten yhdisteiden päästöt lisääntyivät. Lisääntynyt SOA:n muodostus lisäsi myös pilvipisaroiden lukumäärää pilvien yläpinnassa sekä aiheutti voimakkaamman negatiivisen säteilypakotteen. Tulevaisuudessa aerosolimallikehityksessä tulisi tutkia tarkemmin aerosolilyhdisteiden termodynaamisia ominaisuuksia erityisesti DMA:n suhteen. Märkäpoistumaa sekä eri aerosolilyhdisteiden, erityisesti mustan hiilen, sisäisen sekoittumisen määrää tulisi tutkia ja uudistaa globaaleissa ilmastomalleissa, jotta aerosolihiukkasten kaukokulkeumaa voitaisiin arvioida kunnolla. Lisäksi ilmakehän SOA:n lähteet tarvitsevat lisätutkimusta, jotta sen käyttäytymistä ilmakehässä ja ilmastovaikutuksia voitaisiin kuvata oikein.

Julkaisijajaysikkö

Ilmatieteenlaitos, Itä-Suomen ilmatieteellinen tutkimuskeskus

Luokitus (UDK)  
551.58, 551.510, 551.510.412

Asiasanat  
Prosessimallinnus, Globaalimallinnus, Aerosoli, Pilvet, Hygroskooppisuus, Märkäpoistuma, Biotillinen stressi, SOA

ISSN ja avainnimeke  
0782-6117  
2814-5658  
Finnish Meteorological Institute Contributions

ISBN  
978-952-336-168-3 (painettu)  
978-952-336-169-0 (verkkoversio)

DOI  
10.35614/isbn.9789523361690

Kieli  
Englanti

Sivumäärä  
62

## ACKNOWLEDGEMENTS

The research presented in this thesis was done at the Atmospheric Research Centre of Eastern Finland of the Finnish Meteorological Institute as well as at the Department of Technical physics, University of Eastern Finland, Kuopio. I am grateful to Head of Atmospheric Research Centre of Eastern Finland of the Finnish Meteorological Institute Research Prof. Sami Romakkaniemi, Head of the Department of Technical physics Prof. Jari Kaipio, and Head of the Aerosol Physics group of University of Eastern Finland Prof. Annele Virtanen for giving me the opportunity and providing the facilities and support for conducting the research behind this thesis.

I express my sincere gratitude to all of my excellent supervisors: Doc. Thomas Kühn for being my principal supervisor since my M.Sc. studies and introducing me to the world of modelling and for having time to discuss about science as well as personal matters; Doc. Harri Kokkola for his inspiring discussions about model development and giving ideas and help for my research; Research Prof. Anton Laakso for fascinating scientific discussions and for encouraging and guiding me through my research; Assoc. Prof. Taina Yli-Juuti for expressing interest towards my work and supporting me through my research.

I express my gratitude to Prof. Veli-Matti Kerminen and Prof. Miikka Dal Maso for reviewing this thesis.

I would like to thank all the co-authors and people collaborating in the research articles in this thesis. I thank both groups FMI Atmospheric Research Centre of Eastern Finland as well as UEF Aerosol Physics group. Above all, I would like to thank all of my co-workers in both modelling groups: Atmospheric modelling group at FMI, Kuopio and modelling group of Aerosol Physics at UEF, Kuopio. Special thanks go to people helping me with global modelling and the model development: Dr. Tero Mielonen and Dr. Juha Tonttila. I would also like to thank Tuuli Miinalainen for being an excellent colleague and support throughout my research.

I want to thank all of my friends for keeping me balanced between work and free time. I am grateful to my family for interesting discussions relating physics and atmosphere, and for always supporting me in my decisions.

Finally, I want to thank my wife Miia for staying with me through this journey and loving, encouraging, and supporting me when it was most needed.

Kuopio, February 2023

*Eemeli Holopainen*

# TABLE OF CONTENTS

## TABLE OF CONTENTS

<b>List of publications</b>	<b>8</b>
<b>1 Introduction</b>	<b>9</b>
<b>2 Aerosol modelling from process to global-scale</b>	<b>13</b>
2.1 Process-scale modelling.....	14
2.2 Global-scale modelling.....	15
<b>3 Process-scale modelling - Hygroscopicity</b>	<b>17</b>
3.1 Hygroscopicity .....	17
3.2 E-AIM and hygroscopic growth.....	18
<b>4 Global-scale modelling - Wet removal and biogenic SOA</b>	<b>21</b>
4.1 ECHAM-HAMMOZ .....	21
4.1.1 HAM.....	22
4.2 Wet deposition.....	24
4.3 Biogenic SOA .....	27
<b>5 Overview of the key results</b>	<b>30</b>
5.1 Evaluating hygroscopicity simulated with thermodynamic equilibrium model .....	30
5.2 Developing a physics-based parametrization for wet removal of aerosol particles.....	33
5.3 Modelling the effects of plant stress to biogenic SOA formation, clouds and radiation.....	37
<b>6 Review of papers and the author's contribution</b>	<b>41</b>
<b>7 Summary and conclusions</b>	<b>43</b>
<b>BIBLIOGRAPHY</b>	<b>46</b>

# List of publications

This thesis consists of the present review of the author's work and the following selection of the author's publications:

- I O.-P. Tikkanen, O. Väisänen, L. Hao, **E. Holopainen**, H. Wang, K. E. J. Lehtinen, A. Virtanen, and T. Yli-Juuti: "Hygroscopicity of dimethylaminium-, sulfate-, and ammonium-containing nanoparticles", *Aerosol Science and Technology*, **52**, 971–983, (2018).
- II **E. Holopainen**, H. Kokkola, A. Laakso, and T. Kühn: "In-cloud scavenging scheme for sectional aerosol modules – implementation in the framework of the Sectional Aerosol module for Large Scale Applications version 2.0 (SALSA2.0) global aerosol module", *Geoscientific Model Development*, **13**, 6215–6235, (2020).
- III **E. Holopainen**, H. Kokkola, C. Faiola, A. Laakso, and T. Kühn: "Insect herbivory caused plant stress emissions increases the negative radiative forcing of aerosols", *Journal of Geophysical Research: Atmospheres*, **127**, e2022JD036733, (2022).

**Paper I** is reprinted under a license obtained from the publisher and **Papers II-III** under the Creative Commons Attribution 4.0 License. Throughout the overview, these papers will be referred to by Roman numerals.

# 1 Introduction

Aerosol consists of solid or liquid particles which are suspended in air (Hinds, 1999). These particles are called aerosol particles and they affect our health directly by depositing deep into the lungs causing, for example, respiratory diseases or oxidative stress (Shiraiwa et al., 2017). In addition, aerosol particles can travel high up in the atmosphere and affect our living conditions through atmospheric alterations. Atmospheric aerosol particles can modify the climate directly by scattering and absorbing radiation (Seinfeld and Pandis, 2016) and indirectly by altering clouds in terms of their formation, radiative properties, and lifetime (Albrecht, 1989; Twomey, 1991).

Atmospheric aerosol particles come in a variety of compositions, and their sizes vary from a few nanometers up to hundreds of micrometers. Aerosol particles in the atmosphere consist mainly of black carbon, organic carbon, mineral dust, sea salt, sulfate, nitrate, and ammonium (IPCC, 2021; Seinfeld and Pandis, 2016). The majority of the atmospheric aerosol mass is emitted from natural sources such as oceans (sea salt) and deserts (mineral dust). Aerosol species such as organic carbon, sulfate, and black carbon, can originate from both natural and anthropogenic sources (Bond et al., 2013; IPCC, 2021; Lee et al., 2013; Seinfeld and Pandis, 2016; Vergara-Temprado et al., 2018). Nitrate is mainly emitted from anthropogenic sources (IPCC, 2021). Aerosol particles can also be formed in the atmosphere through nucleation, which is a process where molecular embryos start to form through phase transformation from vapor to liquid or from vapor to solid (Kerminen et al., 2004; Kulmala et al., 2004; Zhang et al., 2012).

The majority of the mass of aerosol particles less than 1 micron in diameter is organic matter (OM) (Jimenez et al., 2009; Murphy et al., 2006). Particles smaller than 1 micron in diameter are important as they have been found to affect human health as well as the climate. Organic aerosol (OA) particles can be emitted from, e.g., biomass/fossil fuel combustion, soil, and vascular plants as primary particles and are called primary organic aerosol (POA) (De Gouw and Jimenez, 2009; Kanellopoulos et al., 2021). In addition, biogenic sources, such as trees and plants, emit significant amounts of volatile organic compounds (VOC). VOCs can go through certain physical and chemical processes to produce secondary organic aerosol (SOA) (Faiola and Taipale, 2020; Jimenez et al., 2009; Zhang et al., 2007). SOA increases the amount of particles that are in the size range which can directly affect radiation and activate to cloud droplets. Thus, changes in SOA concentrations can contribute to direct or indirect radiative effects of aerosols in the atmosphere (Sporre et al., 2020).

As stated above, atmospheric aerosol particles can have a direct effect on the radiative balance of the Earth through scattering, reflecting and absorbing the incoming short-wave and absorbing the outgoing long-wave radiation to the Earth. This effect is called aerosol-radiation interaction and it can be observed by human eye in highly polluted regions as lowered visibility (Horvath, 1995; IPCC, 2021). Radiative forcing due to aerosol-radiation interactions ( $RF_{ari}$ ) is defined as the change in how aerosol-radiation interaction effect perturbs the radiation budget of the Earth. The sign of ( $RF_{ari}$ ) depends on the composition, size, shape, or the internal structure of aerosol particles (Ghan et al., 2012). A positive radiative forcing has a warming

effect on the climate system, while a negative radiative forcing has a cooling effect. In recent studies,  $RF_{\text{ari}}$  has been approximated to be  $-0.5 \text{ W/m}^2$  with approx.  $0.5 \text{ W/m}^2$  uncertainty (IPCC, 2021). Absorbing aerosol particles, such as black carbon, affects the Earth's radiation budget by heating the atmosphere directly, and thus enhancing the  $RF_{\text{ari}}$ . BC can also accelerate the melting of snow and ice through absorbing solar radiation after depositing on the snow and ice surfaces. In addition, BC affects cloud formation and lifetime by warming the atmosphere and changing the absorption characteristics of cloud droplets (Bond et al., 2013). However, other aerosol compounds, such as sulfate and SOA, enhance cooling and thus make  $RF_{\text{ari}}$  more negative (Ghan et al., 2012).

Radiative effects due to aerosol-cloud interactions, on the other hand, refer to how radiative effects of clouds change due to aerosols. Aerosol particles in the atmosphere can act as cloud condensation nuclei (CCN) or ice nuclei (IN) and therefore increase the cloud droplet number concentration (CDNC) or ice crystal number concentration (ICNC) which in turn affect cloud properties (Kuang et al., 2009; Kulmala et al., 2014; Twomey, 1974; Yli-Juuti et al., 2021). If the liquid water amount remains the same in non-precipitating cloud, the increase in CCN leads to smaller cloud droplets as the amount of water is divided between a larger number of droplets. An increased amount of small cloud droplets increases the cloud albedo and causes negative radiative forcing ( $RF_{\text{aci}}$ ) as the clouds reflect more incoming solar radiation back to space (IPCC, 2021; Twomey, 1974). In addition, as these cloud droplets are smaller, they are less likely to be precipitated from the cloud as rain which increases the cloud lifetime (Albrecht, 1989). This thesis only focuses on instantaneous top-of-atmosphere (TOA) radiation change due to aerosol-radiation interactions. To get a comprehensive analysis on the total effects of aerosols to radiative balance one needs to include also the  $RF_{\text{aci}}$  as well as rapid adjustments and climate feedbacks (IPCC, 2021).

As water is one of the most abundant vapors in the atmosphere, one of the most important properties contributing to the CCN activity and optical properties of aerosol particles is the ability of a particle to absorb moisture (Petters and Kreidenweis, 2007; Seinfeld and Pandis, 2016). This ability is called hygroscopicity. Hygroscopicity of an aerosol particle depends on its chemical composition (Xu et al., 2020). Particles which have high hygroscopicity consist of, for example, sulfate or salt (Lohmann, 2015). Such particles can affect  $RF_{\text{ari}}$  by affecting particle optical properties, and  $RF_{\text{aci}}$  through affecting CCN concentrations (Pilinis et al., 1995; Zieger et al., 2013, 2017).

The climate effects of aerosol particles are strongly dependent on their horizontal and vertical distribution in the atmosphere. Vertical distributions, or vertical profiles, of aerosol are representations of aerosol particle concentration as a function of altitude. Vertical distributions of aerosols are affected by emissions, advection, and deposition in the atmosphere (Kipling et al., 2016; Watson-Parris et al., 2019). Emissions affect the vertical distribution directly by setting the initial amount of the emitted aerosols. Deposition processes then constrain how far the aerosol is transported. Further, hygroscopicity of aerosol particles affects the susceptibility to aerosol removal inside a cloud. Especially in remote regions, vertical profiles are strongly affected by the transport of aerosol particles as these regions lack emission sources of particles (Croft et al., 2010; Rasch et al., 2000). One of the main processes affecting transport of aerosol particles to remote regions is wet deposition, which is a process where aerosol particles are removed from the atmosphere through their association with water (Wang et al., 1978). Wet deposition can happen through nucle-

ation, impaction, and below-cloud scavenging (Chate et al., 2011; Ladino et al., 2011; Pruppacher and Klett, 1997). In-cloud nucleation scavenging refers to activation of particles, which act as CCN or ice nuclei, to cloud droplets or ice crystals, respectively, through nucleation process (Pruppacher and Klett, 1997). Further, when the cloud droplets or ice crystals grow large enough they are removed from the cloud through precipitation. In-cloud impaction scavenging is a process where aerosol particles collide with cloud droplets or ice crystals (Chate et al., 2003). Below-cloud scavenging refers to collision-coalescence of falling rain droplets or snow crystals with aerosol particles below a cloud (Chate et al., 2011).

To properly understand the properties of aerosol particles and their impacts on clouds, radiative effects and climate, the scientific community has developed different kinds of models ranging from process-scale models all the way to global-scale models, such as chemical transport models and global climate models. These models can be accurate in some aspects, for example modelling new particle formation (NPF) in process-scale (Kürten et al., 2018) and estimating the effects of volcanic eruptions in global-scale (Hansen et al., 1992). However, in process-scale modelling, the scientific community struggles to determine some thermodynamic properties of different aerosol species. In addition, even though the wet deposition processes are mostly well known, they are poorly represented in global-scale models (Eckhardt et al., 2015). This is because the full representation of wet scavenging needs realistic descriptions of microphysics of condensation, in-cloud microphysics, precipitation as well as microphysics of aerosols which are represented very differently among models (Eckhardt et al., 2015; Rasch et al., 2000). In addition, current global-scale climate models have inaccuracies in describing different aspects of SOA formation, which leads to uncertainties in radiative effects and cloud feedbacks (Sporre et al., 2020; Tsigaridis et al., 2014).

Accurate global-scale model description, for example of nucleation and growth of particles, requires the understanding of thermodynamic properties of aerosols (Bergman et al., 2015). To get the information of these properties usually requires process-scale models which can be validated against observations to evaluate the performance of the model. For example, properly validated process-scale models can be used in modelling hygroscopicity and hygroscopic growth. This information can then be used to develop more accurate descriptions of new particle formation and growth of aerosol particles in global-scale models.

Variability in simulated vertical profiles of aerosol particles can contribute to the uncertainty in the estimation of  $RF_{\text{ari}}$  in global-scale models (Samset et al., 2013). Especially, the local vertical size distribution and composition of black carbon aerosol in remote regions lead to huge differences between modelled results and observations, as has been shown by Bourgeois and Bey (2011) and Sharma et al. (2013). As stated above, wet removal is one of the main contributors to how well aerosol is transported over long-ranges and thus understanding and properly describing the wet removal processes in global climate models leads to more realistic results in terms of vertical profiles, especially in remote regions. In addition, proper wet removal is important in describing the amount of deposited black carbon over the Arctic (Bourgeois and Bey, 2011).

In addition to uncertainties in simulate aerosol vertical profiles, there are large uncertainties in the estimation of the formation of SOA, clouds, and radiative effects in global climate models. These flaws can be due to uncertain sources, sinks, and atmospheric processing of SOA. Thus, understanding and properly describing processes leading to uncertainties, regarding SOA in global climate models, can



enhance the performance of global-scale models and give more realistic results.

In this thesis, hygroscopicity, wet removal, and factors affecting SOA formation and their effects to the climate are studied using process-scale modelling as well as global-scale modelling, to address the uncertainties related to aerosol properties, transport and SOA feedbacks in the atmosphere. The main objectives in this thesis are:

1. To evaluate the performance of thermodynamic equilibrium process model in modelling the hygroscopicity of dimethylamine-containing particles (**Paper I**)
2. To develop and evaluate the parameterization of wet deposition in a global aerosol-climate model (**Paper II**)
3. To investigate how biotic stress in boreal trees affects the formed biogenic SOA, clouds and radiative effects in a global aerosol-climate model (**Paper III**)

The structure of this thesis is as follows: first aerosol modelling in process and global-scale is introduced in Chapter 2; then, in Chapter 3, a more detailed description of the hygroscopicity of aerosol particles is presented, with details of process-scale modelling of hygroscopic growth in a thermodynamic equilibrium model. In Chapter 4, the thesis will delve into introducing the global aerosol-climate model ECHAM-HAMMOZ, with which all of the global model simulations in this thesis were performed, and into the uncertainties in terms of wet removal and sources of biogenic SOA in the model. Chapter 5 presents the key results found in **Papers I-III** and the responses to the main objectives of this thesis. Finally, a review of the papers used in this thesis and the author's contribution are presented in Chapter 6 and the concluding remarks of the thesis are presented in Chapter 7.

## 2 Aerosol modelling from process to global-scale

Models have been a part of our lives since we were little, whether it is building models of aeroplanes or model railways. Even car manufacturers utilize 3D models to see how well they would perform in real life. Similarly, in different fields of science, models are used to provide a numerical representation of real life situations and to simulate them using computers. Especially in atmospheric sciences we need models to represent the atmospheric behaviour of different compounds to help us understand their dynamics, physics, and chemistry in process level and globally in the whole atmosphere (Fanourgakis et al., 2019; IPCC, 2014; Mann et al., 2012; Morales and Nenes, 2010; Pruppacher and Klett, 1997; Topping and Bane, 2022). In addition, models can help us to test different scenarios and hypotheses of what might happen if certain aspects in the atmosphere would be changed (Nebojsa Nakicenovic et al., 2000). These aspects could be for example doubling the amount of carbon dioxide emissions in the atmosphere or reducing the amount of black carbon aerosol in the Arctic.

Aerosol models simulate the dynamic behaviour of aerosol particles defined by different aerosol properties, such as chemical composition, size, and shape (Seinfeld and Pandis, 2016). To understand this behaviour in more detail, models are needed to simulate different physical processes which affect aerosol size distributions (Ceppi and Hartmann, 2015; Myhre et al., 2013). These processes can be for example coagulation, nucleation, condensational growth of a particle, evaporational shrinking of a particle, sedimentation, and deposition of particles to surfaces (Hinds, 1999; Seinfeld and Pandis, 2016). For a single component aerosol, the different processes can change the total number of aerosol particles  $N(V, t)$  in a certain volume  $V$  of gas at a certain time  $t$  and this change is called the general dynamic equation (GDE) (Friedlander, 2000; Gelbard and Seinfeld, 1979; Seinfeld and Pandis, 2016). This equation is solved by aerosol models. The GDE has many representations, but in general it is of the form

$$\frac{dN(V, t)}{dt} = \left( \frac{dN(V, t)}{dt} \right)_{nuc} + \left( \frac{dN(V, t)}{dt} \right)_{con} + \left( \frac{dN(V, t)}{dt} \right)_{coa} + S + R, \quad (2.1)$$

where  $\left( \frac{dN(V, t)}{dt} \right)_{nuc}$  is the change in the number of particles due to formation of new particles through nucleation,  $\left( \frac{dN(V, t)}{dt} \right)_{con}$  is the change in the number of certain sized particles due to growth by condensation or shrinking through evaporation,  $\left( \frac{dN(V, t)}{dt} \right)_{coa}$  is the change in particle number due to coalescing collision between particles (coagulation),  $S$  represents the emissions of aerosol particles and  $R$  represents the sedimentation and deposition of particles (Gelbard and Seinfeld, 1979; Huertas, 2016; Seinfeld and Pandis, 2016). Growth by condensation refers to a process where vapors condense onto existing aerosol particles, increasing their size, and shrinking through evaporation refers to evaporation of molecules from particles, reducing their size. Coagulation refers to a process where two randomly

moving aerosol particles collide and stick together, thereby forming one larger particle (Hinds, 1999). Emissions and removal of aerosol particles are usually called external processes as in these terms there is movement of particles across the fictive walls of the volume of interest (Friedlander, 2000). Formation through nucleation, coagulation and condensation are usually called internal processes as they happen inside the volume (Huertas, 2016).

## 2.1 PROCESS-SCALE MODELLING

Process-scale models aim to give a detailed representation of aerosol dynamics, thermodynamics, chemistry, optical properties, or composition (Ghan and Schwartz, 2007). Thus, process-scale models are usually numerical representations of certain individual processes of the GDE (Huertas, 2016). Process-scale models are usually computationally light which gives them the capability to thoroughly test the theory and calculations behind the process (Naumann, 2003; Wentzel et al., 2003).

The scientific community in atmospheric sciences uses a variety of process-scale models. For example, evaporation of molecules from liquid phase particles can be solved using models, such as the liquid-like evaporation model (LLEVAP) or the kinetic multi-layer model of gas-particle interactions in aerosols and clouds (KM-GAP) (Shiraiwa et al., 2012; Yli-Juuti et al., 2017). These models can provide insight into the evaporation dynamics of different aerosol particles under different conditions, like high and low temperature and a wide range of relative humidities (RH).

Condensational growth of aerosol particles is driven by their ability to absorb vapors. The ability of aerosol particle to absorb water vapor is called hygroscopicity. To calculate the amount of absorbed water in an aerosol particle at thermodynamic equilibrium, one needs to know the activity coefficient of water and the amounts of all of the compounds in the particle. When the number of compounds increases, the calculation becomes more difficult and thus numerical models are needed to calculate the composition of the system at thermodynamic equilibrium. These models can be for example uManSysProp, AIOMFAC or E-AIM (Clegg et al., 1998; Topping et al., 2016; Wexler and Clegg, 2002; Zuend et al., 2008, 2010). E-AIM is shortly presented in **Paper I**.

The skill of process-scale models to reproduce different aerosol processes is usually tested by evaluating and validating their results against observations in well regulated environments (laboratory experiments) (Ghan and Schwartz, 2007). Process-scale models are tested thoroughly, and properly working models can then be used to provide insight into the properties of different aerosol compounds. In **Paper I**, the capability of the Extended Aerosol Inorganics Model (E-AIM) to evaluate hygroscopicity of dimethylamine-containing particles is presented. The properly tested and defined aerosol properties can then be used in parametrizations which can further be used, for example, in regional or global-scale aerosol-climate models. In addition, most of the process models are constructed to work as an individual box model which is a simple 3-dimensional, offline tool, allowing efficient modification and evaluation of different aerosol processes (Topping and Bane, 2022). Box models for different processes can then be used to work as part of a larger, multi-dimensional program, such as global aerosol-climate model.

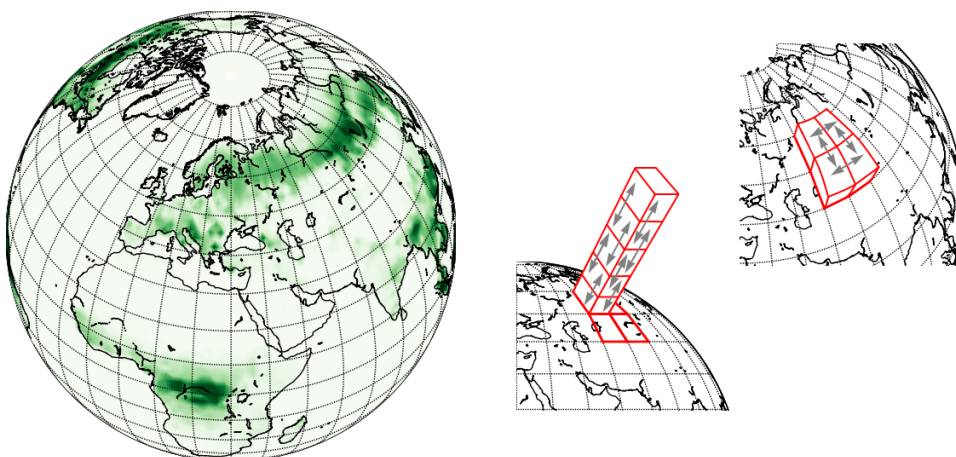


**Figure 2.1:** A schematic representation of the atmospheric grid structure and interaction between grid cells in a GCM.

## 2.2 GLOBAL-SCALE MODELLING

Once the different aerosol process models are validated and box models for aerosol processes are evaluated, they, or the information they provide, can be combined and implemented into a larger-scale model, for instance a global aerosol-climate model (Ghan and Schwartz, 2007; Kokkola et al., 2018; Lin et al., 2018). These general circulation models (GCMs) are complex representations of major climate system components, such as atmosphere, land surface, oceans and sea ice (IPCC, 2014). An atmospheric GCM simulates physical processes which transfer energy and matter, such as aerosols, through the global climate system (Lupo et al., 2013). Usually, in atmospheric GCMs the Earth's atmosphere is divided into three-dimensional grid cells according to latitude, longitude and altitude (IPCC, 2014). A schematic representation of the grid structure of the atmosphere is presented in Fig. 2.1. The physics of different system components are calculated in each grid cell and the neighboring cells interact by moving energy and matter between each other (Lupo et al., 2013; Topping and Bane, 2022). The available computational power and disk space define how fine a resolution can be used in a GCM. Usually, the amount of grid points in a GCM is large (in the order of hundreds of thousands up until several millions), which demands a large amount of computational power and thus supercomputers are needed to use them.

Atmospheric GCMs coupled with an ocean model are used to predict the future behavior of the atmosphere and climate (IPCC, 2014). Once it has been validated that a certain GCM is producing adequate results when comparing to the past and present observations of the climate and atmosphere, the GCM can also be used to test how the climate system evolves, based on how people will live in the future (Nebojsa Nakicenovic et al., 2000; von Storch, 2010).

Even though the basic physics of aerosol processes in the atmosphere are the same, aerosols and their interactions with the climate are represented quite differently in different atmospheric GCMs. The different representation of aerosols between atmospheric GCMs may originate from the fact that many of the described aerosol processes occur at subgrid scales of GCMs (i.e., scales that are much smaller

than the grid spacing of the GCM) and they have to be parametrised for the grid of the GCM in question. In addition, many GCMs have various representations of parametrizations and calculations of aerosol processes such as activation and removal. For example, cloud activation can be parametrised very differently in different GCMs (Abdul-Razzak and Ghan, 2002; Lin and Leaitch, 1997; Nenes and Seinfeld, 2003). In addition, different models can have differences in the representation of aerosol size distributions. For example, aerosol size distribution can be represented using the modal method, which presents the aerosol size distribution as a sum of log-normal distributions called modes, moment method, which treats the size distribution as a limited number of moments (particle number density, volume density, mean radius, etc.), or sectional method, which represents the size distribution as monodisperse hybrid size bins (Chen and Lamb, 1994; McGraw, 1997; Seinfeld and Pandis, 2016; Vignati et al., 2004).

There are several atmospheric GCMs used by the scientific community and every one of them is unique in its own way and all of them have their strengths and weaknesses. Examples of GCMs are, for instance, the Community Atmosphere Model (CAM) or the European Centre Hamburg Model (ECHAM6) (Neale et al., 2010; Stevens et al., 2013). The latter is shortly presented in **Paper II** and **Paper III**. The performance of a GCM is hard to measure as some of them might simulate certain aspects, such as cloud properties, of the atmosphere better than others but are inadequate on some other features. This is because many processes are heavily parameterized and many of the processes are not well constrained. Therefore, models have to be tuned choosing values for uncertain, or even non-observable parameters so that the model simulation better matches observations. Differences in how models treat these processes cause big differences between models (Oreskes et al., 1994). In addition, in some of the models, when modelling the climate, it is possible that even though the past is performing well, the future may have errors (Reifen and Toumi, 2009). Thus, one cannot say which model is the best and to get the best possible representation of the atmospheric processes, it is best to use an ensemble of several GCM results, which has been done in the recent Intergovernmental Panel on Climate Change (IPCC) reports (IPCC, 2014, 2021).

GCMs are very complex and their development requires a lot of time and work as one needs to be accurate on the descriptions and theories behind the different processes. Additionally, some of the theories may be revised in the future, which needs to be taken into account in the improvements of models (Oreskes et al., 1994). Sometimes, little modifications in some of the processes can have huge effects on certain climate feedbacks and behaviors in the whole atmosphere (Lorenz, 1963). Some of the processes in current GCMs, which cause this kind of big uncertainty, are related to emissions or transport of aerosols (Bourgeois and Bey, 2011; Sharma et al., 2013). Problems, related to transport and emissions of aerosols, are addressed in **Paper II** and **Paper III**.

### 3 Process-scale modelling - Hygroscopicity

Knowing the hygroscopicity of an aerosol compound can provide information on identifying the species of ambient aerosols (Chang et al., 2010; Huang et al., 2022; Peng et al., 2014; Zamora et al., 2019). In addition, hygroscopicity can affect the optical properties of aerosol particles and CCN activity of the compounds (Väisänen et al., 2016; Zieger et al., 2013, 2017). Further, uptake of water vapor to existing aerosol particles can alter their chemical composition through opening a path to aqueous phase processing (McNeill, 2015). The scientific community lacks information of thermodynamic and chemical properties of some of the atmospheric aerosol particles, such as amine-containing particles, which leads to uncertainties in amine induced new particle formation (NPF) and the subsequent growth of particles in the models. Especially with respect to chemical properties, partitioning, and removal processes, amine-containing particles cause uncertainties in global model simulations (Bergman et al., 2015). Thus, more investigation is needed in terms of measurements of thermodynamic properties, which can be used to develop and evaluate process-scale models. These thermodynamic process-scale models can further be used to test the understanding of physics and chemistry behind the observations. Properly validated process-scale models can be used to develop parametrizations for global-scale models.

In this chapter, calculations of hygroscopicity parameter and hygroscopic growth are presented. In addition, this chapter presents the thermodynamic equilibrium model, E-AIM, and how it is used to model hygroscopic growth of aerosol particles.

#### 3.1 HYGROSCOPICITY

Hygroscopicity and hygroscopic growth of an aerosol particle are defined by the ability of an aerosol particle to absorb water vapor and growth of the particle due to absorption. When the aerosol particles grow large enough, due to condensation of water and other compounds, they can act as CCN and further on participate in the formation of cloud droplets in the atmosphere. A schematic representation of absorption and growth of an aerosol particle is presented in Fig. 3.1

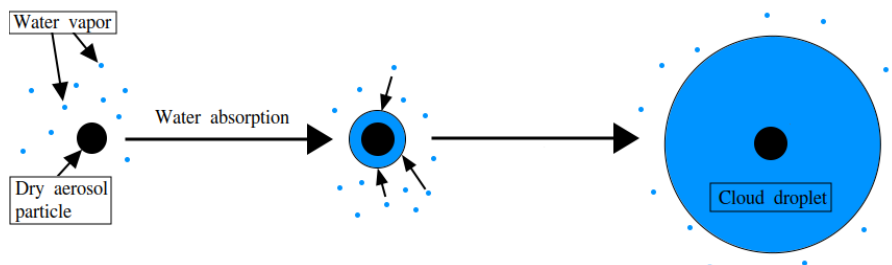


**Figure 3.1:** A schematic representation of water absorption and condensational growth of an aerosol particle.

For a solution, the water activity,  $a_w$ , is the partial pressure of water in a solution,  $p_v$ , divided by partial pressure of pure water,  $p_{v,s}$ . Thus, for an aqueous droplet in equilibrium with the gas phase,  $a_w$  can be expressed as

$$a_w = \frac{p_v}{p_{v,s}} = \left( \frac{S}{\exp\left(\frac{4\sigma M_w}{RT\rho_w D}\right)} \right), \quad (3.1)$$

where  $S$  is the ambient saturation ratio around the droplet,  $\sigma$  is the surface tension of the solution,  $M_w$  is the molecular weight of water,  $R$  is the universal gas constant,  $T$  is temperature,  $\rho_w$  is the density of water and  $D$  is the diameter of the droplet (Köhler, 1936; Petters and Kreidenweis, 2007). The term  $\exp\left(\frac{4\sigma M_w}{RT\rho_w D}\right)$  is called the Kelvin term, or curvature effect. The Kelvin effect describes the effectiveness of bonding of molecules in a solution due to curvature of a droplet. When the droplet is small, there is greater possibility of the molecules to escape from the droplet. Thus, the Kelvin effect has to be taken into account in the case of nano-sized particles (Köhler, 1936; Thomson, 1872). The water activity in an aqueous droplet can be used to determine the hygroscopicity parameter  $\kappa$ .  $\kappa$  is one of the ways of parametrizing the ability of a particle to act as CCN in the atmosphere (Petters and Kreidenweis, 2007). Petters and Kreidenweis (2007) proposed a parametrization for the hygroscopicity parameter for a droplet to be of the form

$$\kappa = \left( \text{GF}_S^3 - 1 \right) \left( \frac{\exp\left(\frac{4\sigma M_w}{RT\rho_w D_{p,S}}\right)}{S} - 1 \right), \quad (3.2)$$

where  $D_{p,S}$  is the droplet diameter in saturation ratio  $S$  and GF is the hygroscopic growth factor of the droplet and it is defined at a certain saturation ratio  $S$  as

$$\text{GF}_S = \frac{D_{p,S}}{D_{p,dry}}. \quad (3.3)$$

Here  $D_{p,dry}$  is the diameter of the dried up droplet (when there is no or a very low amount of water condensed to the particle) (Kim et al., 2016; Petters and Kreidenweis, 2007).

The calculation of the amount of absorbed water by the particle becomes complex when the number of compounds inside the particle increases. For these calculations, a thermodynamic equilibrium model was used in **Paper I** and it is presented in the next section.

### 3.2 E-AIM AND HYGROSCOPIC GROWTH

When a system is in thermodynamic equilibrium, there are no fluxes of energy or matter between the system and its surroundings (Mandl, 1988). For example, when an aerosol particle is in thermodynamic equilibrium with the surrounding water vapor, the condensation of vapor to the particle and evaporation of vapor from the particle are equal. Thermodynamic equilibrium is achieved when the thermodynamic potential, Gibbs free energy ( $G$ ), is minimum (Wexler and Clegg, 2002). The Extended Aerosols Inorganics Model (E-AIM) is a thermodynamic equilibrium model, which utilizes the minimization of Gibbs free energy. It can be used to calculate, for example, the equilibrium water content in a particle. E-AIM is a unique

modelling tool as it can handle non-ideal solutions (solutions where the interactions between molecules are not identical) and it is currently one of the few available models with accurate amine thermodynamics.

As E-AIM minimizes the Gibbs free energy, it can represent the amount of moles of water in a solution when knowing the RH and the amount and thermodynamical properties of the compounds in the solution. In addition, for calculating the thermodynamic equilibrium, E-AIM calculates the activities of the water-ion and water-organic solutions. The total water activity can be calculated as a product of the water activities of the ionic and organic solutions (Clegg et al., 2001). In **Paper I**, activity coefficients were calculated using the approach by Clegg et al. (1992, 1998), for ionic organic compounds and the UNIFAC model for neutral organic compounds (Fredenslund et al., 1975; Hansen et al., 1991).

If the dry particle diameter is known, to be able to calculate the hygroscopic growth factor, also the information of the wet particle diameter is needed. Assuming that water is the only compound which is allowed to be transferred between the gas and liquid phases, E-AIM provides the density of the particle and the molar amount of water in the particle liquid phase at a given saturation ratio. For a dry particle, the saturation ratio can be assumed to be low (in **Paper I** the saturation ratio was assumed to be 0.01). Thus, the mass of a spherical dry particle,  $m_{p,dry}$ , can be calculated using the density, provided by E-AIM, at a saturation ratio of 0.01 and the dry diameter of the particle. If the molar amounts of other compounds are known, the mass fractions in the dry particle can be calculated for each compound,  $i$ , by

$$w_{i,dry} = \frac{m_i}{\sum_j m_j} = \frac{n_i M_i}{\sum_j n_j M_j}, \quad (3.4)$$

where  $m_i$  represents the individual mass of compound  $i$  in the particle,  $n_i$  represents the amount of moles of compound  $i$  and  $M_i$  is the molar mass of compound  $i$ . Using the mass fraction of individual compounds in the dry particle, the individual masses in the particle can be calculated by

$$m_{i,dry} = w_{i,dry} m_{p,dry}. \quad (3.5)$$

For a wet particle, the mass fraction for compound  $i$ ,  $w_{i,wet}$ , can be calculated using Eq. 3.4, but including the molar amount of water at given saturation ratio  $S$  in the summation, which is provided by E-AIM. As the masses of individual compounds (excluding water),  $m_{i,dry}$ , do not change in the particle even as it is exposed to saturation ratio  $S$ ,  $m_{i,dry}$  can be expressed using the mass of the wet particle,  $m_{p,S}$ , and the mass fraction of compound  $i$  in the wet particle,  $w_{i,wet}$ . Thus, the mass of the wet particle can be calculated using Eq. 3.5. Further, the particle diameter at a given saturation ratio can be calculated by

$$D_{p,S} = \left( \frac{6m_{p,S}}{\pi\rho_{p,S}} \right)^{1/3}, \quad (3.6)$$

where  $\rho_{p,S}$  refers to the density of the particle at saturation ratio  $S$ , provided by E-AIM.

E-AIM assumes that the phase boundary between gas and liquid particle is a flat surface. However, in **Paper I**, the measurements were done using nano-sized particles. Thus, to get the best agreement of E-AIM results with the measurements, one



needs to take the Kelvin term into account for the saturation ratio. The saturation ratio then becomes

$$S = S_{\text{E-AIM}} \exp \left( \frac{4\sigma M_w}{RT\rho D_{p,S}} \right), \quad (3.7)$$

where  $S_{\text{E-AIM}}$  is the saturation ratio used in E-AIM calculations and  $\rho$  and  $\sigma$  are the liquid phase density and surface tension of the particle, respectively, calculated by E-AIM.

In **Paper I**, E-AIM was used to model hygroscopicity of particles containing dimethylamine (DMA), sulfate and ammonia. The model results were evaluated against measurements, where particles were generated using five different aqueous phase DMA and sulfuric acid containing solutions with different molar ratios. This was done to test the ability of E-AIM to model hygroscopic growth and to evaluate the skill of E-AIM in modelling interactions between aminium and other the compounds contained in the particles. Further, the evaluation of E-AIM to model hygroscopic growth of amine-containing particles can provide insight on the atmospheric behaviour of amines as well as their thermodynamic properties.

## 4 Global-scale modelling - Wet removal and biogenic SOA

Current global aerosol-climate models are able to reproduce observed properties of aerosol particles, such as aerosol and CCN concentrations, in certain regions, especially near emission sources (Stier et al., 2005; Wang et al., 2011). However, many of the models struggle to correctly reproduce the transport of aerosols to remote regions, which causes uncertainty in estimating, for example, the vertical profiles of aerosols as well as the amount of deposited black carbon over the Arctic (Bourgeois and Bey, 2011; Kristiansen et al., 2016). Especially the transport of atmospheric black carbon (BC) to the Arctic is difficult to model and the differences between modelled and observed concentrations in the Arctic can be substantial (Sharma et al., 2013). In addition, many of the models have uncertainties in representing the sources, sinks and atmospheric processes of certain aerosol species adequately. For example, the sources of SOA are uncertain, which causes variability in estimating the RF in global aerosol-climate models (Sporre et al., 2020; Tsigaridis et al., 2014).

In **Papers II-III** the ECHAM-HAMMOZ global aerosol-climate model was used to provide all of the simulations. In this chapter, the ECHAM-HAMMOZ model and its aerosol microphysics package HAM are presented. In addition, the basics of wet deposition in ECHAM-HAMMOZ and the development of a more physically accurate parametrization of wet removal are presented. Furthermore, in this chapter, the sources and processing of atmospheric biogenic SOA along with the abiotic and biotic stress factors affecting trees are presented. Abiotic and biotic stress factors modify the VOC emissions by the trees and thus affect the biogenic SOA formation and further clouds and climate.

### 4.1 ECHAM-HAMMOZ

In **Papers II-III** the latest version of the ECHAM-HAMMOZ (ECHAM6.3-HAM2.3-MOZ1.0) global aerosol-climate model was used (Schultz et al., 2018). ECHAM-HAMMOZ is a 3-dimensional aerosol-chemistry-climate model and it consists of the sixth generation atmospheric general circulation model ECHAM6.3 (Stevens et al., 2013), the Hamburg Aerosol Model (HAM2.3) (Kokkola et al., 2018; Tegen et al., 2019), and the tropospheric chemistry model Model of Ozone and Related Tracers (MOZART1.0) (Schultz et al., 2018). The atmospheric host model ECHAM6.3 has been developed by Max Planck Institute for Meteorology and it solves the prognostic equations for temperature, divergence, vorticity and surface pressure using spherical harmonics (Stier et al., 2005). The physics in the model are solved on a Gaussian grid.

ECHAM6.3 can be configured using five different resolutions with different number of truncation and vertical levels. The horizontal grid is defined by the triangular truncation of wave numbers in the spectral representation. In practice this means that, for example, in truncation 255 (T255) the horizontal grid is divided into approximately  $0.54^\circ \times 0.54^\circ$  latitude and longitude grid cells. The vertical grid

in the model uses hybrid sigma-pressure levels, meaning that the lowest vertical levels follow the topography of the Earth, while the upper vertical levels follow the atmospheric pressure. The vertical levels can be selected to be L31, L47 or L95 which state how many vertical levels there are. Each vertical representation incorporates the model top to be at 0.01 hPa which corresponds to around 80 km in altitude, with an exception of the lowest vertical resolution (L31), for which the model top is at 0.1 hPa (around 30 km in altitude). In ECHAM6.3, the lowest resolution is T31L31 and the highest is T255L95. In **Papers II-III**, the default resolution of T63L47 was used in ECHAM-HAMMOZ simulations which means that the world is divided into approximately  $1.9^\circ \times 1.9^\circ$  latitude and longitude grid cells, which corresponds to  $96 \times 192$  grid points with 47 vertical levels.

In ECHAM6.3 the meteorology can be nudged (as was done in **Paper II**) towards reanalysis data. This means that the large-scale meteorological prognostic variables can be pushed towards different operational weather reanalysis data using Newtonian relaxation. Such data can be, for example, ERA-Interim reanalysis data from the European Centre for Medium-Range Weather Forecasts (ECMWF) (Berrisford et al., 2011; Simmons et al., 1989).

#### 4.1.1 HAM

ECHAM6.3 is coupled with Hamburg Aerosol Model version 2.3 (hereafter referred to as HAM) which includes all of the aerosol processes of the GDE (Eq. 2.1) within ECHAM-HAMMOZ. HAM calculates the interactions between aerosols and the atmosphere and it predicts the evolution of composition and size distribution of aerosol populations. HAM has an extensive parametrization for both sectional and modal aerosol size distribution representations in terms of all of the aerosol processes (Kokkola et al., 2018; Stier et al., 2005; Tegen et al., 2019).

The modal aerosol module in HAM is called M7 and it uses a superposition of seven log-normal modes to represent the aerosol spectrum (Vignati et al., 2004). The different modes are called nucleation, Aitken, accumulation and coarse modes. The Aitken, accumulation and coarse mode particles are divided into two populations, soluble and insoluble, depending on how hydrophilic the particles are (Stier et al., 2005). Each mode can be a mixture of different aerosol species. In addition, insoluble particles can become soluble by condensation of soluble substances on the particles or collision with soluble particles. The different modes are defined by using log-normal modes, defined by the geometric standard deviation as well as the median radius of each mode. In M7, the geometric standard deviation is fixed for each mode and it is 2.00 for coarse mode and 1.59 for the other modes (Wilson et al., 2001). The median radius, for each mode, can then be calculated using the corresponding aerosol number concentration. The visualization of M7 aerosol spectrum as well as the chemical compounds associated in each mode are presented in Fig. 4.1. The mass and number concentrations of aerosols are transferred between modes when they grow in different processes by merging the modes (Stier et al., 2005).

The sectional method of representing the aerosol size distribution in HAM is called Sectional Aerosol module for Large Scale Applications v2.0 (SALSA) (Kokkola et al., 2018). In SALSA the aerosol size distribution is defined using a hybrid bin sectional approach in which each size bin (section) the aerosol particles are assumed to be monodisperse and the width of the bins are fixed (Chen and Lamb, 1994). As in M7, in SALSA the aerosol population is divided into soluble and insoluble populations and the soluble population is further divided into two subranges to reduce

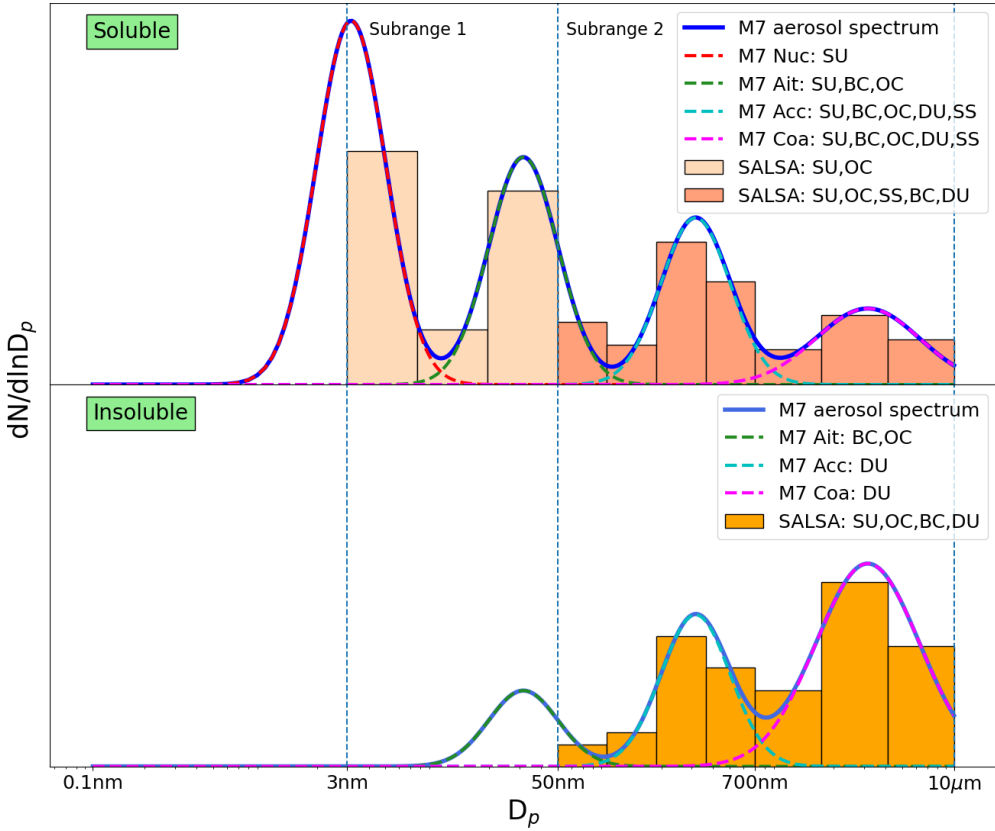


**Figure 4.1:** A schematic representation of the aerosol spectrum of M7 and SALSA and the corresponding chemical compounds associated in each mode or bin. The chemical compounds are sulfate (SU), black carbon (BC), organic carbon (OC), mineral dust (DU) and sea salt (SS).

the number of compounds in smallest size bins. Diameters of aerosol particles in the first subrange span from 3 nm to 50 nm including 3 bins and in the second subrange from 50 nm to 10 μm. The schematic visualization of SALSA aerosol spectrum as well as the chemical compounds associated in each size bin are presented in Fig. 4.1. For each size bin the microphysical processes and chemistry are calculated separately as well as the NPF for the smallest size bin. In the hybrid bin method, particles in different bins can be allowed to transfer between bins due to evaporation, growth or through chemical interactions (Chen and Lamb, 1994).

As M7 has predefined mode ranges, it is unable to describe the coagulation and condensational growth of particles with high accuracy. The inaccuracies in describing coagulation and condensational growth are due to using prescribed mode limits which force the modes to vary very little in size. This can neglect mass or number of aerosol particles in certain sizes, primarily causing underestimation in aerosol activation to cloud droplets as well as underestimation in light extinction (Korhola et al., 2014). The sectional representation in SALSA, on the other hand, allows the model to solve aerosol processes in GDE more accurately, thus describing the particle coagulation and condensational growth more properly. The more accurate solving of

GDE is due to high number of size bins, which allows more accurate description of aerosol size distribution. However, using the sectional method, and especially with high number of size bins, the simulations become computationally heavy. In **Papers II-III** ECHAM-HAMMOZ was used with SALSA aerosol size distribution representation as it has been found to be more accurate than M7 representation.

## 4.2 WET DEPOSITION

As stated above, current global aerosol-climate models struggle to correctly model aerosol size distributions and vertical profiles in remote regions which is mainly due to poor representation of transport of aerosols. One process which affects the transport of aerosols is wet deposition. In the atmosphere, wet deposition refers to a process where aerosol particles are removed from the atmosphere through scavenging by hydrometeors and precipitation (Wang et al., 1978). Wet removal is divided into two processes: in-cloud and below-cloud scavenging. In-cloud scavenging is further divided into two processes: in-cloud nucleation and in-cloud impaction scavenging. A schematic representation of in-cloud and below-cloud scavenging processes are presented in Fig. 4.2. Wet deposition affects aerosol transport by affecting the rate of removal directly at source regions. If the rate is strong, aerosol particles are not allowed to transport to higher altitudes or longer ranges in the atmosphere.

In-cloud nucleation scavenging refers to a process where aerosol particles can act as CCN or ice nuclei (IN). When water vapor reaches supersaturation, aerosol particles, acting as CCN, can activate to cloud droplets when growing large enough (Köhler, 1936; Seinfeld and Pandis, 2016). In addition, particles acting as IN can form ice crystals through collision with supercooled droplet, which initiates ice formation, or adsorption of supercooled water on the surface of IN and transformation to ice (Seinfeld and Pandis, 2016). Ice crystals can also be formed through transformation of a supercooled droplet to an ice crystal. Cloud droplets and ice crystals, containing the aerosol species, can then grow large enough to be precipitated to the surface of the Earth and thus the aerosol particles are removed from the atmosphere (Korolev et al., 2011; Wang et al., 1978). Activation of aerosol particles to cloud droplets depends on the size and composition of the aerosol particle as well as the ambient supersaturation (Köhler, 1936). Formation of ice crystals in the presence of IN, on the other hand, depends on the ice nucleation rate, which depends strongly on the ambient temperature and composition of IN (Hobbs, 1993; Tabazadeh et al., 2002). In ECHAM-HAMMOZ particles acting as IN are only considered to be mineral dust and black carbon containing particles (Lohmann et al., 2007).

In-cloud impaction scavenging refers to a process where aerosol particles collide with existing cloud droplets or ice crystals and stick to them. Thus, the aerosol particles are removed from the interstitial air of the cloud and associated with cloud droplets or ice crystals (Chate et al., 2003; Ladino et al., 2011). The rate of removal of aerosol particles, in in-cloud impaction scavenging, can be described with coagulation theory (Pruppacher and Klett, 1997).

Below-cloud scavenging is a process where precipitating rain droplets or snow crystals collide with aerosol particles below the cloud. Below-cloud scavenging is based on collision-coalescence process. Thus, the rate of removal of aerosol particles in below-cloud scavenging depends mostly on the collection efficiency (product of collision and coalescence efficiency) of rain droplets or snow crystals (Chate et al., 2011). Further, the collection efficiency depends on aerosol and falling hydrometeor

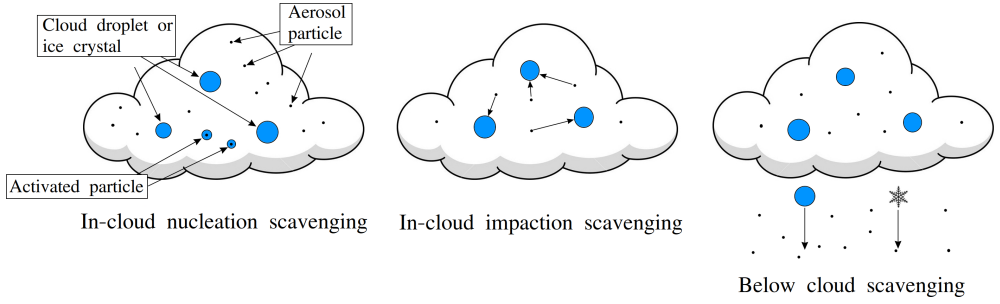


**Figure 4.2:** A schematic representation of the wet removal processes.

size distribution (Bergman et al., 2012). Below-cloud scavenging has been found to be inefficient in contributing to mass deposition budgets when compared to in-cloud scavenging (Croft et al., 2009, 2010; Flossmann and Wobrock, 2010).

In current global aerosol-climate models, scavenging coefficients for in-cloud processes are often prescribed and thus more accurate parametrizations for wet removal are needed. Originally, in ECHAM-HAMMOZ with SALSA size distribution representation, the change in certain aerosol mixing ratio (in size bin  $i$ ),  $C_i$ , in time  $t$ , due to in-cloud scavenging was calculated as

$$\frac{dC_i}{dt} = F_i C_i f^{cl} \left( \frac{Q^{liq} f^{liq}}{C_{liq}} + \frac{Q^{ice} f^{ice}}{C_{ice}} \right), \quad (4.1)$$

where  $Q^{liq}$  and  $Q^{ice}$  are the total conversion rates of water and ice to precipitation,  $f^{liq}$  and  $f^{ice}$  are the liquid water and ice fractions,  $f^{cl}$  is the cloud fraction,  $C_{liq}$  and  $C_{ice}$  refer to the cloud liquid and ice water mixing ratios and  $F_i$  is the scavenging coefficient for size bin  $i$  including both in-cloud nucleation and impaction scavenging (Croft et al., 2010). These scavenging fractions, including values for stratiform and convective clouds with different phases, were prescribed and based on the work by Stier et al. (2005) (Bergman et al., 2012; Stier et al., 2005). Even though using fixed scavenging coefficients might give reasonable results, they have limitations in taking into account the aerosol composition and updrafts leading to cloud droplet activation in wet deposition calculations and thus more physical parametrizations are needed to properly describe the transport of aerosol species to remote regions (Croft et al., 2010). In **Paper II** a more physical parametrization for sectional aerosol modules was developed in terms of in-cloud nucleation and impaction scavenging.

For in-cloud nucleation scavenging, the parametrization was based on activation of aerosol particles to cloud droplets and ice nucleation rates to calculate the scavenging fractions for different aerosol compounds. For liquid clouds, the cloud activation parametrization scheme, developed by Abdul-Razzak and Ghan (2002), was used to calculate the size segregated cloud activation of aerosol particles. The activation scheme calculates the online fractions of activated particles which were used to define the scavenging coefficients,  $F_{i,nuc,liq}$ , in liquid cloud case for each size bin  $i$ . The activated fraction for number,  $n_i$ , and mass,  $m_i$ , for each size bin  $i$  are defined by calculating the maximum supersaturation,  $S_{max}$ , of the air parcel. The maximum supersaturation is then compared to the lower,  $S_{i,l}$ , and upper,  $S_{i,u}$ , critical supersaturation bounds in each aerosol size bin. Thus, the number and mass fraction activated in each size bin are

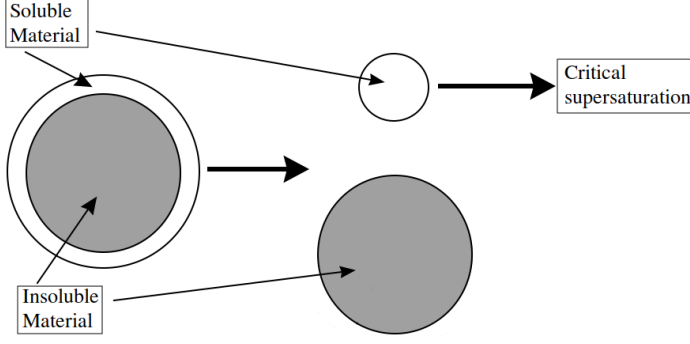


**Figure 4.3:** A schematic representation of the volume reduction of a particle when the insoluble substance is large in the original description of activation scheme.

$$\begin{aligned}
 n_i &= m_i = 0, \text{ if } S_{max} < S_{i,l} \\
 n_i &= \frac{\log(S_{max}/S_{i,l})}{\log(S_{i,u}/S_{i,l})}, \text{ if } S_{i,l} < S_{max} < S_{i,u} \\
 m_i &= \frac{r_{i,max}^3 - r_{i,l}^3}{r_{i,u}^3 - r_{i,l}^3}, \text{ if } S_{i,l} < S_{max} < S_{i,u} \\
 n_i &= m_i = 1, \text{ if } S_{i,u} < S_{max},
 \end{aligned}$$

where  $r_{i,max}$  is the dry aerosol particle radius corresponding to  $S_{max}$ , and  $r_{i,l}$  and  $r_{i,u}$  are the aerosol particle radii corresponding to  $S_{i,l}$  and  $S_{i,u}$ , respectively (Abdul-Razzak and Ghan, 2002).

The original activation scheme in ECHAM-HAMMOZ calculates the fraction of activated particles by considering only the volume of the soluble substance in the particle and thus neglecting any insoluble material volume (Abdul-Razzak and Ghan, 2002). The critical supersaturation, which is used in defining the maximum supersaturation, is dependent on the particle size. The original activation scheme assumed a new particle, defined from the soluble volume, for which the critical supersaturation was calculated. The assumption is usually good, as most particles in CCN size range contain large fraction of soluble material, but becomes problematic when the fraction of insoluble material in the particle is large. A schematic representation of the original assumption when the fraction of the insoluble material is large is presented in Fig. 4.3. Thus, in **Paper II**, the calculations for the activation were modified to account for the insoluble core of the particles according to technical report by Kokkola et al. (2008).

For ice cloud case, in **Paper II**, the nucleation rate was assumed to be a surface-based process as suggested by Tabazadeh et al. (2002). Thus, the scavenging coefficients for ice clouds were calculated by

$$F_{i,nuc,ice} = \frac{s_i}{\sum_j s_j} \frac{\Delta ICNC}{n_i}, \quad (4.2)$$

where  $\Delta ICNC$  is the ice crystal number concentration (ICNC) obtained from the host model ice cloud activation scheme,  $n_i$  is the number concentration in size bin  $i$

and  $s_i$  are the surface area concentration of size bin  $i$ .

For in-cloud impaction scavenging, the parametrization used wet aerosol size and cloud droplet radii to calculate the removal rate and the method was based on modal aerosol size distribution representation described by Croft et al. (2010). In **Paper II**, this was done by approximating each size bin using a log-normal mode in the calculations of scavenging coefficients for liquid cloud case,  $F_{i,imp,liq}$ , and ice cloud case,  $F_{i,imp,ice}$ .

When including the more physical scavenging coefficients to account for the in-cloud nucleation and impaction scavenging, Eq. 4.1 expands to the form

$$\frac{dC_i}{dt} = C_i f^{cl} \left( \frac{(F_{i,nuc,liq} + F_{i,imp,liq}) Q^{liq} f^{liq}}{C_{liq}} + \frac{(F_{i,nuc,ice} + F_{i,imp,ice}) Q^{ice} f^{ice}}{C_{ice}} \right). \quad (4.3)$$

In **Paper II** the newly-developed in-cloud wet deposition scheme was tested with ECHAM-HAMMOZ using SALSA size distribution representation by comparing to the pre-existing calculation method. In addition, the sensitivity of the simulated aerosol concentrations to aging, mixing and emission sizes was tested.

### 4.3 BIOGENIC SOA

Biogenic SOA can affect clouds by affecting the growth of particles to CCN sizes as well as radiative effects through aerosol-radiation and aerosol-cloud interactions. Thus, one major contributor to inaccuracies in estimating the RF and clouds, in global aerosol-climate models, stem from the description of sources, sinks, and atmospheric processing of biogenic SOA (Sporre et al., 2020; Tsigaridis et al., 2014). For example, when comparing different global aerosol-climate models, there can be large differences in chemical production of SOA and total organic aerosol sources (Tsigaridis et al., 2014). Large differences in production of SOA can further cause large difference in direct radiative effects between models (Sporre et al., 2020). Many of the models struggle to properly describe atmospheric processing, sources and sinks of SOA, and especially, with respect to sources of biogenic SOA, more research is needed to properly evaluate the effects of SOA to atmosphere.

Biogenic sources, such as trees and plants, emit carbon containing molecules, biogenic VOCs, to gaseous phase (Guenther et al., 2012). Plants and trees emit biogenic VOCs constantly, but the emissions usually increase when the plants and trees are attacked by insects (Kigathi et al., 2019). Thus, VOCs are also important for the plants defense and communication mechanisms (Materić et al., 2015; Sharkey and Yeh, 2001). Terrestrial vegetation emits VOCs as a mean to protect them from high temperatures and herbivores, to attract pollinators, and to even communicate with each other (Materić et al., 2015; Proffit et al., 2020; Runyon et al., 2006). In the atmosphere, some of the VOCs are oxidized by OH radical, ozone, and NO<sub>3</sub> almost immediately after emission to form less volatile compounds. The less volatile compounds can form biogenic SOA particles through gas-to-particle partitioning of the oxidation products (Faiola and Taipale, 2020; Hallquist et al., 2009; Jimenez et al., 2009). The whole chemical transformation of these primary biogenic VOC emissions to biogenic SOA particles is a complicated process including gas-phase oxidation and multiphase ageing reactions (Hallquist et al., 2009). Thus, implementing the whole chemical process to global aerosol-climate models becomes fairly complex.



Biogenic VOC emissions in ECHAM-HAMMOZ are calculated using information from the Model of Emissions of Gases and Aerosols from Nature (MEGAN) version 2.1. In ECHAM-HAMMOZ, the whole land area of the Earth is divided into 16 different terrestrial types which are defined as plant functional types (PFTs), and they include bare soil, different tree types, shrubs, grass types, and crop. For different biogenic VOCs, MEGAN provides average emission factors (EFs), which can be used with PFTs to calculate the total emission of each VOC in ECHAM-HAMMOZ (Guenther et al., 2012; Henrot et al., 2017). In the model, the volatility basis set (VBS) approach is used to treat the different organic compounds involved in SOA formation (Koo et al., 2014). After the treatment, the gas-to-aerosol partitioning of both SOA and POA is calculated in the model.

ECHAM-HAMMOZ, with the SALSA aerosol size distribution representation, uses a simple VBS approach to calculate the biogenic SOA formation from biogenic monoterpene and isoprene (the main VOCs emitted by trees) emissions (Donahue et al., 2006; Sporre et al., 2020). In the VBS approach, the individual organic compounds in gas phase are categorized according to their volatilities, which are represented with the saturation concentration coefficient,  $C^*$ . The value for the saturation concentration coefficient for each volatility bin is prescribed for a reference temperature of 298.15 K and the temperature dependence is calculated, when the gas phase SOA precursor physical properties and concentrations are known, using the Clausius-Clapeyron equation. The temperature-dependent saturation concentration coefficient is further used for the precursor gas partitioning to each size bin in SALSA (Stadtler et al., 2018).

When trees experience stress, their optimal living conditions are altered and thus the spectrum and rate of biogenic VOC emissions are altered (Faiola and Taipale, 2020; Holopainen and Gershenson, 2010). Different stress factors can be abiotic or biotic. Abiotic stress factors are caused by non-living stressors and they include light and heat, drought, soil salinity, and cold (He et al., 2018). Biotic stress factors, on the other hand, are caused by living stressors such as pathogens and insect herbivory (Faiola and Taipale, 2020; Zhao et al., 2017). Especially, biotic stress factors, such as insect herbivory, can enhance the VOC emissions of the trees and thus induce increased SOA formation (Faiola and Taipale, 2020; Taipale et al., 2021). A schematic representation of how biotic stress increases VOC emissions which in turn enhances the SOA formation and thus affects clouds and direct radiative effects is presented in Fig 4.4.

Biotic stressors can have a huge effect on the amount and size of formed SOA from biogenic VOC emissions (Joutsensaari et al., 2015; Taipale et al., 2021). However, the biotic stress factors, especially insect herbivory, have not been studied extensively in global aerosol-climate models (Faiola and Taipale, 2020). Thus, to achieve more knowledge about how biotic stress affects SOA, clouds, and radiative effects, in **Paper III**, ECHAM-HAMMOZ with SALSA was used to simulate the effects of insect herbivore infestation in boreal trees.

In **Paper III**, the description of needleleaf evergreen boreal and broadleaf deciduous boreal trees, represented as PFTs, including their monoterpene EFs, was modified to account for different biotic stress percentages caused by insect herbivory. This was done by increasing the percentage of the stressed trees and using EFs, obtained from several observation based studies, in calculating the VOC emissions. Only monoterpene EFs were studied as they were readily available from other studies and since they are a major contributor to biogenic SOA especially in boreal region (Faiola and Taipale, 2020; Hakola et al., 2006; Rinne et al., 2009). The modified

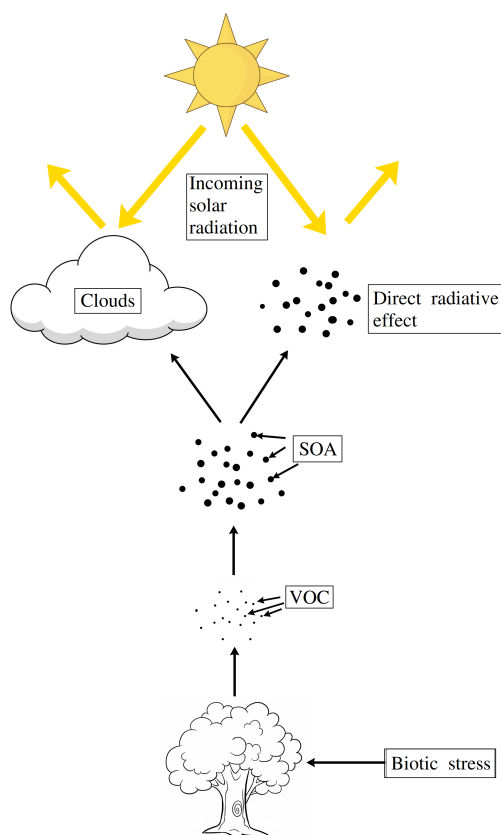


**Figure 4.4:** A schematic representation of how biotic stress affects VOC emissions from trees and thus formed biogenic SOA, clouds and direct radiative effects.

PFTs and EFs were used in ECHAM-HAMMOZ simulations to study the effects of biotic stress affected VOCs to atmosphere in terms of SOA burden, CDNC and top-of-atmosphere (TOA) clear-sky (without including clouds) and all-sky (including clouds)  $RF_{ari}$ .

## 5 Overview of the key results

In this chapter, the main findings of this work are presented. First, the capability of E-AIM to capture the measured hygroscopic growth of dimethylamine, sulfuric acid and ammonia containing particles in process-scale will be discussed. Next, the differences between pre-existing and newly-developed wet removal schemes, in ECHAM-HAMMOZ global aerosol-climate model, as well as the sensitivity of the newly-developed scheme to changes in BC emissions and particle aging will be discussed in global-scale. Finally, the atmospheric effects of increased biogenic SOA formation due to biotic stress to boreal trees will be discussed in terms of SOA formation, clouds and radiative effects in global-scale.

### 5.1 EVALUATING HYGROSCOPICITY SIMULATED WITH THERMODYNAMIC EQUILIBRIUM MODEL

Amines are derivatives of ammonia and they are present in the atmosphere in gaseous and particulate phase. Dimethylamine (DMA) is one of the most abundant atmospheric amines and it has been found that DMA can be present during NPF event and during subsequent particle growth (Mäkelä et al., 2001). Especially, DMA can be an important stabilizing base for sulfuric acid and even a slight amount of gaseous DMA can enhance nucleation rates massively compared to pure ammonia (Almeida et al., 2013; Kürten et al., 2014). Thus, it is evident that proper thermodynamic models are needed to validate DMA thermodynamic properties to further include them in for example global-scale models (Bergman et al., 2015). In **Paper I**, E-AIM was used to compare the modelled hygroscopic growth of DMA containing particles to measured values, to test the applicability of E-AIM in terms of amine thermodynamic properties.

The measurements were conducted in laboratory environment using nano hygroscopicity tandem differential mobility analyzer (HTDMA) and aerosol mass spectrometer (AMS). In the measurements, aerosol particles were atomized from five different DMA, sulphuric acid (SA) and water containing solutions. Solutions were prepared by mixing different molar amounts of DMA and SA with deionized water to reduce impurities. The molar ratios of these five DMA-SA solutions were 1:3, 1:2, 1:1, 3:2 and 2:1 and they were referred to as nominal molar ratios. From the aqueous solutions, aerosol particles were atomized using a conventional aerosol nebulizer to generate polydisperse aerosol population. The population was guided to the HTDMA which selected nearly monodisperse aerosol population from the polydisperse population. The monodisperse dry aerosol particles were exposed to certain RH and the particle size for the exposed population was determined. The analysis, in **Paper I**, focused on evaluating the modelled hygroscopic growth as a function of RH and hygroscopicity parameter as a function of particle diameter against those of measured values. The hygroscopic growth for the aerosol population was calculated using Eq. 3.3 with mean diameter of the humidified aerosol particles as  $D_{p,S}$  and the dry diameter of the selected dry aerosol particles as  $D_{p,dry}$ . Using the hygroscopic growth factor, the hygroscopicity parameter in a given satu-

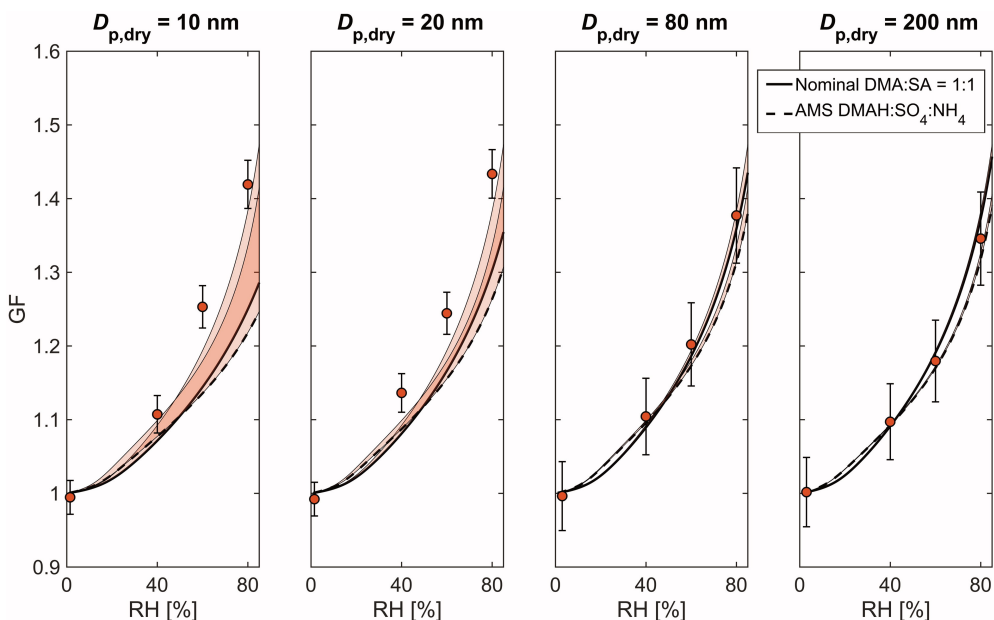


**Figure 5.1:** Modelled (E-AIM) and measured (HTDMA) growth factors as a function of RH for dry particle sizes 10, 20, 80 and 200 nm for DMA and SA molar ratio of 1:1. The solid line represents the E-AIM simulated growth factors in nominal molar ratio and the dashed line represents those modelled with the composition measured with AMS. The shaded areas represent the models sensitivity to Kelvin effect (upper bound determined by neglecting the Kelvin effect). The round markers represents the HTDMA measured values with the maximum uncertainty of the instrument (whiskers). Figure from **Paper I**.

ration ratio was calculated using Eq. 3.2. In addition to nominal molar ratios, AMS was used to determine the chemical composition of the submicrometer aerosol particles. Along with dimethylammonium (DMAH) and sulfate ( $\text{SO}_4$ ), AMS detected a considerable amount of ammonium, which had to be included in the modelling. The contribution of ammonium was most likely due to contamination.

In Fig. 5.1, an example of results from **Paper I** is presented. Fig. 5.1 presents the comparison between the modelled (with E-AIM) and measured (with HTDMA) growth factors as a function of RH for dry particle sizes 10, 20, 80 and 200 nm. E-AIM calculated growth factors are presented for DMA and SA nominal molar ratio of 1:1 (solid line) and AMS measured composition including ammonium (dashed line). For this DMA and SA composition, nominal and AMS measured, the E-AIM underestimated the measured growth factors for the smaller dry particle diameters (10 and 20 nm), but produced more adequate results when going to larger diameters (80 and 200 nm).

Another example from **Paper I** is presented in Fig. 5.2. In Fig. 5.2, modelled (E-AIM) and measured (HTDMA) hygroscopicity parameters,  $\kappa$ , are presented as a function of particle diameter in RH of 80 % for each DMA and SA solutions. The measured values for hygroscopicity parameter showed a large (approximately decrease by half) decrease when the particle size increased from 10 nm to 200 nm in all of the compositions. However, this behavior was not noticeable in hygroscopicity

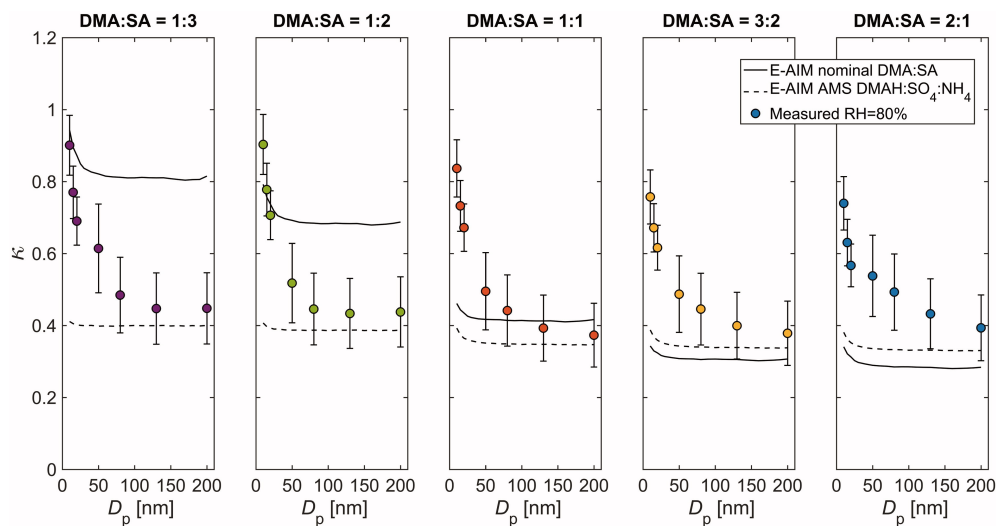


**Figure 5.2:** Modelled (E-AIM) and measured (HTDMA) hygroscopicity parameter as a function of particle diameter in 80 % RH for each DMA and SA molar ratios. The solid line represents the  $\kappa$  parameter from E-AIM model assuming nominal molar ratio and dashed line that modelled with the composition measured with AMS. The markers with whiskers represent the HTDMA measured values with the maximum uncertainty of the instrument. Figure from **Paper I**.

parameters modelled with the E-AIM which highlighted the uncertainty related to the composition of the smallest particles in the measurements. The uncertainty in the composition of the smallest particles could be due to evaporation of the bases in the sampling lines of the measurement device.

To address the evaporation in the sampling lines and thus the changing of chemical composition, in **Paper I**, the Model for Acid-Base chemistry in NANoparticle Growth (MABNAG) was used (Yli-Juuti et al., 2013). MABNAG, which uses E-AIM for thermodynamics, can be used to calculate the gas-particle partitioning of the DMA and ammonia dynamically. The results showed that even for the smallest particle size (10 nm), for which the maximum evaporation would be most favorable, the nanoparticles should have been significantly more acidic than what could be obtained with MABNAG. Thus, E-AIM coupled with MABNAG could not produce compositions which could match the hygroscopicity of the measurements.

The conclusion of **Paper I** was that there are still uncertainties in thermodynamics of E-AIM in terms of DMA, SA, ammonia and water systems which causes E-AIM to inadequately model hygroscopic growth of the aerosol particles containing DMAH,  $\text{SO}_4$  and ammonium. Thus, more investigation is needed in terms of chemical characterization of the analyzed compounds, in order to fill the gaps of the thermodynamics of DMA, SA, ammonia, and water system.

## 5.2 DEVELOPING A PHYSICS-BASED PARAMETRIZATION FOR WET REMOVAL OF AEROSOL PARTICLES

In **Paper II**, the new, more physical parametrization, of wet deposition was developed and evaluated against results from the pre-existing method, which used prescribed scavenging coefficients. The simulations were done using ECHAM-HAMMOZ global aerosol-climate model with SALSA aerosol particle size distribution representation. Without any adjustments, the simulation using the newly-developed wet deposition scheme produced spurious BC vertical profiles (as seen later on in Fig. 5.5) and atmospheric lifetimes compared to the simulation done with the pre-existing scheme. The atmospheric lifetime of BC was found to be 9.23 days for the pre-existing and 14.62 days for the newly-developed scheme. However, experimental studies have found that BC lifetime should be in the range of 5.5 days (Lund et al., 2018). Thus, in addition to default simulations done with the pre-existing and newly-developed schemes, the simulations included 4 sensitivity simulations to test the sensitivity of the newly-developed wet deposition scheme to changes in internal mixing and emission size distribution of BC as well as ageing of aerosol particles. The sensitivity studies were based on findings from Kipling et al. (2016) who found that strongest effect on aerosol vertical profiles, in global aerosol-climate model, are emission distribution, microphysical processes, deposition, and hygroscopicity.

To study the sensitivity to BC emission size distribution, two tests were conducted where BC emissions were directed to a small insoluble size bin, "BC\_small", and where BC emissions were directed to a large insoluble size bin, "BC\_large". When BC particles are directed to soluble size bins during emission time, it increases their ability to absorb water and thus they become more hygroscopic, by becoming internally mixed with soluble substances. Therefore, the sensitivity to BC hygroscopicity was tested by directing all of the BC emissions to soluble size bins, using the same size distribution as in default configuration, "BC\_soluble".

Aerosol particles age in the atmosphere when their physicochemical properties have changed enough. In global models, this is modelled by transferring particles from insoluble to soluble size bins after a certain time. Thus, the sensitivity to ageing of aerosol particles was tested by directing insoluble particles to soluble region after their activation, "insol2sol". A schematic representation of how the aerosol size distribution is represented in different simulation setups is presented in Fig. 5.3.

The analysis, in **Paper II**, was done in terms of vertical profiles of BC, organic carbon (OC), organic aerosol (OA), and  $\text{SO}_4$  as well as total number concentration (sum of all the particles in aerosol size distribution),  $N_{tot}$ , and number concentration of particles larger than 100 nm,  $N_{100}$ . In addition, wet deposition flux size distributions, which are the wet deposition fluxes for certain size bins, from all simulations, were analyzed in terms of OC,  $\text{SO}_4$ , sea salt (SS), BC, and mineral dust (DU). The vertical profiles from all of the simulations were also compared against those obtained from Atmospheric Tomography mission (ATom) aircraft measurements performed by NASA (Wofsy et al., 2018). The data was collocated to the same times and locations of the mean aircraft measurements from all of the missions (1-4) using Community Intercomparison Suite (CIS) tool (Watson-Parris et al., 2016). Lastly, OC,  $\text{SO}_4$ , SS, BC, and DU lifetimes of each simulation were compared against the several models from Aerosol Comparisons between Observations and Models (AEROCOM) (Gliß et al., 2020). The vertical profile analysis, in **Paper II**, focused on different latitude bands, which were 0-30 ° (tropics), 30-60 ° (midlatitudes), and 60-90 ° (the

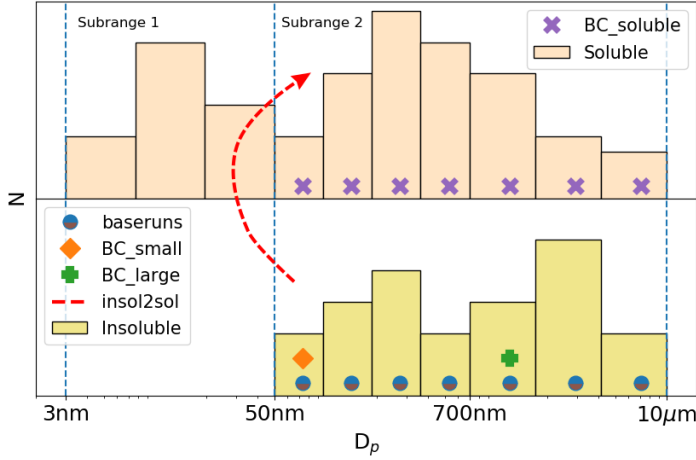


**Figure 5.3:** A schematic visualization of the aerosol number size distribution for SALSA. The different colors represent the different simulation setups. Figure from **Paper II**.

Arctic). This was to see how the different schemes and sensitivity studies affect the aerosol transport. For the wet deposition flux size distributions, the analysis focused on annual and global average values.

An example from the results from **Paper II** is presented in Fig. 5.4. In Fig. 5.4, the vertical profiles modelled with ECHAM-HAMMOZ using SALSA for  $N_{100}$  and  $N_{tot}$  are presented. The vertical profiles from the pre-existing wet deposition scheme are presented in brown and the vertical profiles from the newly-developed wet deposition scheme in blue. For the different latitude bands the  $N_{100}$  vertical profiles showed an increase when switching from the pre-existing wet deposition scheme to the newly-developed scheme. The increase in  $N_{100}$  vertical profiles showed evidence that the transport of large particles to remote regions was enhanced in the newly-developed scheme, and it was mainly due to changes in nucleation scavenging, which reduced the wet removal of large particles, allowing them to be transported further. However, for  $N_{tot}$ , the vertical profiles showed a decrease in all latitude bands, which was due to increase in the amount of large particles which act as a condensation sink to gas-phase sulfuric acid and thus reduce the NPF which further decreases the concentration of small particles.

Another example from the results from **Paper II** is presented in Fig. 5.5. In Fig. 5.5, the ECHAM-HAMMOZ with SALSA modelled vertical profiles, with all 6 configurations, are evaluated against ATom aircraft measurements. The modelled simulations are presented in different colors and the ATom aircraft measurements are presented as solid black line. Over all latitude bands, the best representation, compared to measurements, were given by the default pre-existing scheme, directing BC to large size bin, enabling ageing of aerosol particles, and directing BC to soluble size bins, configurations in terms of BC vertical profiles, but were overestimated by the default newly-developed scheme and directing BC to small size bin configurations which indicates, that using the default configuration with the newly-developed wet deposition scheme overestimated the transport of BC. However, for OA the default newly-developed wet removal scheme produced profiles which were

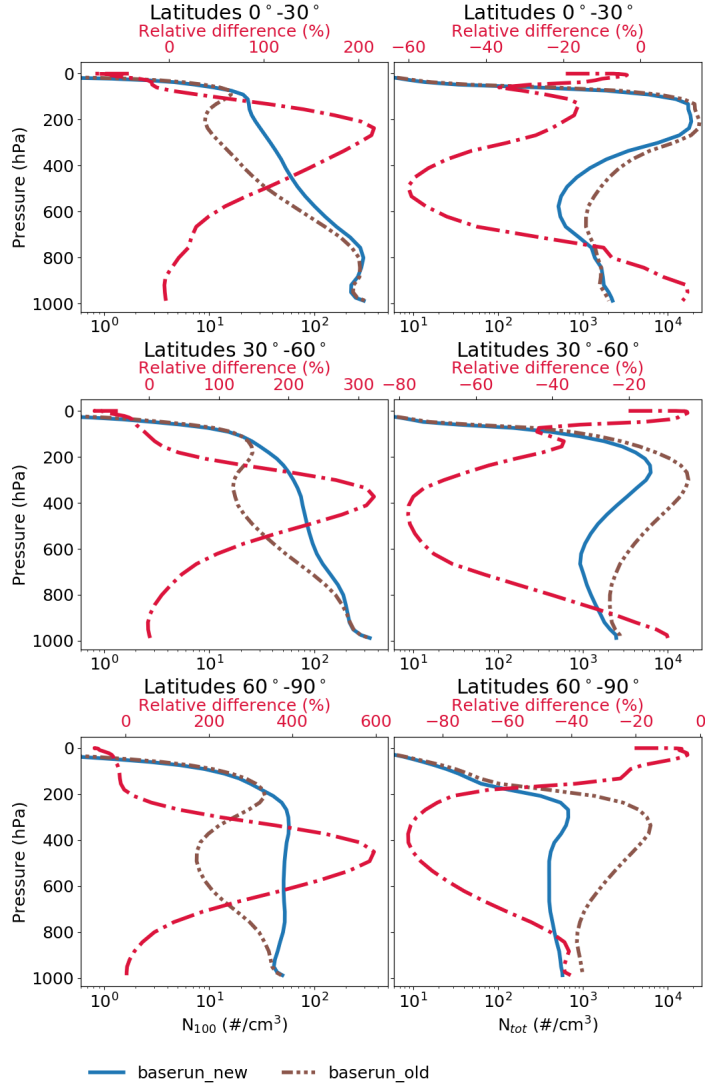


**Figure 5.4:** Vertical profiles for  $N_{100}$  and  $N_{tot}$  for different latitude bands modelled with the pre-existing and the newly-developed wet deposition schemes. The brown dashed line represents the values obtained from the simulation using the pre-existing wet deposition scheme and the blue solid line represents the values from the newly-developed wet deposition scheme. The red dashed line represents the relative difference between the newly-developed and the pre-existing scheme values. Figure from **Paper II**.



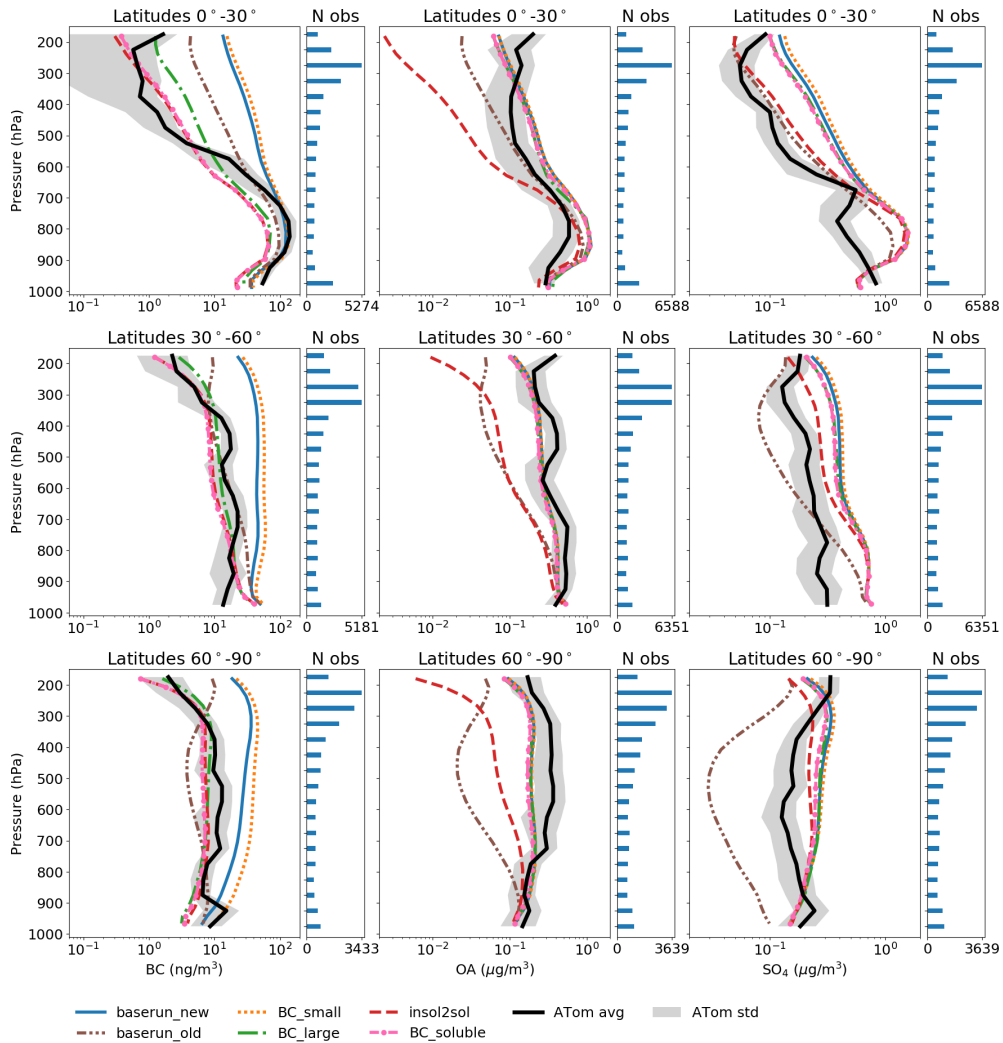


**Figure 5.5:** Vertical profiles for BC, OA and SO<sub>4</sub> for different latitude bands modelled with the pre-existing and the newly-developed wet deposition schemes and the sensitivity configurations in the newly-developed scheme compared against mean vertical profiles obtained from ATom aircraft measurements. The different colors represent the modelled results and the solid black line represent the ATom aircraft measurements with the gray shaded area representing the standard deviation in the measurements. On the right side of each panel is the number of observations at each vertical level. Figure from **Paper II**.

closer to measured values. Thus, for OA, the wet removal in the pre-existing scheme was too fast which reduced the OA transportation to higher altitudes. For  $\text{SO}_4$ , the vertical profiles in all configurations were similar, with an exception of the pre-existing wet deposition scheme, which underestimated the  $\text{SO}_4$  concentrations over the Arctic. The underestimation in the  $\text{SO}_4$  concentrations was also due to faster wet removal of  $\text{SO}_4$  particles in the pre-existing scheme.

To delve more deeply in the effects of the newly-developed wet deposition scheme and the sensitivity, in **Paper II**, the mass and size distribution of wet deposition flux were analyzed in terms of different compounds. When comparing the pre-existing and the newly-developed removal schemes, wet deposition flux of small sulfate particles was decreased which confirmed the results shown in vertical profiles. The decrease in small sulfate particle wet deposition flux was due to increase in medium and large particle concentrations which act as condensation sink for sulfate gas. Similarly, the wet deposition fluxes simulated with different sensitivity configurations showed confirmation to the vertical profiles. The mass wet deposition flux of large DU-containing particles was increased in configurations where BC was emitted to large size bin and BC was directed to soluble size bins which was due to more efficient removal of BC particles allowing more  $\text{SO}_4$  to condense on large DU particles, enhancing their activation.

In **Paper II**, the model skill, in different simulation configurations, was tested by comparing yearly and global mean atmospheric lifetimes of OC,  $\text{SO}_4$ , SS, BC, and DU to lifetimes achieved from AEROCOM models. The results showed that the most closest lifetimes were achieved with the newly-developed removal scheme when BC was internally mixed with soluble substances.

The conclusion of **Paper II** was that, without adjustments, the newly-developed, more physical, parametrization of in-cloud wet deposition scheme was inadequate in reproducing the global aerosol fields and lifetimes of aerosol species. However, when BC is mixed with soluble substances during emissions, the vertical profiles and atmospheric lifetimes were closest to the measurements and other model results. Thus, global aerosol-climate model development should investigate further the issue of how much of BC should be mixed with soluble substances, to increase their hygroscopicity, at emission time.

### 5.3 MODELLING THE EFFECTS OF PLANT STRESS TO BIOGENIC SOA FORMATION, CLOUDS AND RADIATION

The increased VOC emissions due to plant stress can enhance the SOA formation causing strong impacts on radiative transfer and cloud formation (Kerminen and Kulmala, 2002; Taipale et al., 2021). However, these plant stress induced VOC emissions are usually not included in global aerosol-climate models. Thus, it is evident that more investigation is needed in terms of biotic stress factors in global models to adequately evaluate the atmospheric effects of SOA.

In **Paper III**, the ECHAM-HAMMOZ with SALSA was used to simulate the effects of insect herbivory caused biotic stress on boreal trees and to study the atmospheric effects of the biotic stress induced VOCs. The study was done by altering the stress percentage of the boreal trees. The different fractions of the stressed and healthy trees were used to weigh the monoterpene EFs of the studied trees. The monoterpene EFs, for both healthy and stressed trees, were obtained by using average values from several measurement-based articles, which had investigated biotic

stress. The measured EFs were scaled to match the EFs from MEGAN, as the measured values were much higher than the original MEGAN values. For healthy trees the original MEGAN EFs were used. For stressed trees the factor between the measured healthy EFs and MEGAN EFs was used to scale the EFs for stressed trees. Different percentages of the stressed trees represented different scenarios caused by insect outbreaks. Simulation where 0 % of trees were stressed represented the base case, 10 % represented the background aerosol (emissions from stressed trees travelling from remote areas far from the studied regions), 25 % represented the current day high outbreak scenario, 50 % represented the future scenario when the climate is warming and the insect outbreaks are increased, 75 % was used to see the linearity of the stress increase, and 100 % represented the maximum effect of the biotic stress. The analysis, in **Paper III**, was done in terms of SOA formation, represented with SOA burden, clouds, represented with cloud top CDNC, and radiative effects, represented with shortwave  $RF_{\text{ari}}$  (radiative forcing due to aerosol-radiation interactions for the direct shortwave radiation emitted by the sun) in clear and all-sky cases. The analysis focused only on land areas from 40 ° latitude northward as radiative forcing is usually strongest close to the areas where aerosol particles are emitted. In addition, it was found that the most statistically significant difference ( $p$ -value below 0.5 in Wilcoxon signed-rank test) in SOA burden, between the base scenario and maximum effect of biotic stress, was from 40 ° latitude northward. Furthermore, the analysis focused only on summer period (June-August) as it had the highest monoterpene emissions compared to other seasons.

An example from the results from **Paper III** is presented in Fig. 5.6. Fig. 5.6 presents the absolute mean value of SOA burden from the base scenario with absolute differences in SOA burden between the different stress scenarios and base scenario as mean from summer periods over 10-year simulation. The absolute difference in SOA burden showed almost a linear increase when the stress percentage of boreal trees were increased. In addition, the increase was dependent on the areas where the boreal trees were located. The maximum increase in SOA burden was approximately 120 %, achieved with the maximum extent of stress, when compared to the base scenario, which showed evidence that increasing monoterpene emissions, due to biotic stress, enhanced the SOA formation through oxidation of monoterpene VOC.

In addition to SOA burden, in **Paper III**, CDNC at cloud top and TOA  $RF_{\text{ari}}$  for both clear-sky and all-sky cases were analyzed throughout the area from 40 ° latitude northward. In the results, CDNC at cloud top showed an increase when the stress percentage was increased which was due to enhanced SOA formation which increases the number of particles acting as CCN. However, the highest increase was not observed over the areas where SOA burden was increased most. In addition, in 75 % and 100 % stressed simulations, the increase in CDNC was similar to that of 50 % stressed simulation. The discrepancies between areas of the most intense increase in SOA burden and CDNC, as well as the small differences in CDNC in the largest stress percentages, were due to susceptibility of CDNC to CCN as it decreases when the CCN concentrations are increased. Both all-sky and clear-sky  $RF_{\text{ari}}$  were more negative when stress percentage was increased, compared to base scenario. Especially, in the clear-sky case the strongest decrease was over the same areas where the strongest SOA burden was observed. All-sky case, however, showed less pronounced effect, which was due to clouds which reflect incoming solar radiation, leaving less radiation for the aerosols to reflect.

Another example from the results from **Paper III** is presented in Fig. 5.7. In Fig.

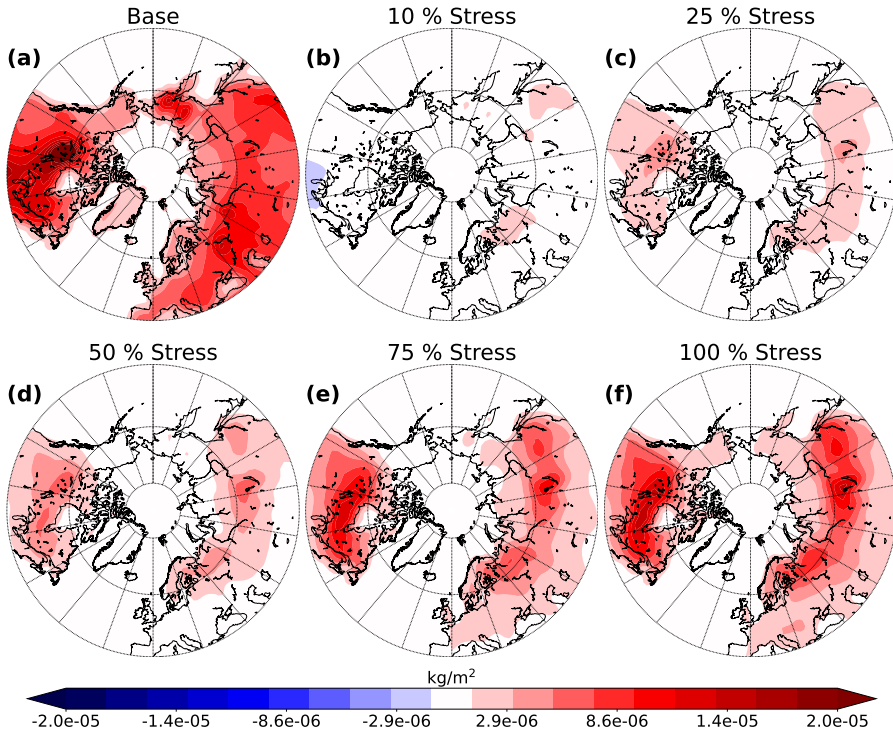


**Figure 5.6:** SOA burden modelled with the base configuration as well as absolute difference between different biotic stress percentage scenarios and the base scenario. The data is presented as mean value throughout the summer periods from 10-year simulation for all the scenarios. Figure from **Paper III**.

5.7, the SOA burden, CDNC at cloud top, and clear-sky and all-sky  $\text{RF}_{\text{ari}}$  are presented as a function of biotic stress percentage as a box plot graph. The Pearson correlation showed a moderate correlation in SOA burden and stress percentage. Thus, the increase was quite linear. Similarly, CDNC at cloud top increased linearly with an exception of the largest stress percentages which made the correlation weaker. Both clear and all-sky  $\text{RF}_{\text{ari}}$  showed negative correlations with biotic stress percentage with a weaker negative correlation in all-sky case which confirm the results found in area figures. When the stress percentage was increased it enhanced the SOA formation adding more particles to act as CCN in the atmosphere. Enhanced SOA formation further caused more negative  $\text{RF}_{\text{ari}}$  as there were more particles in the atmosphere reflecting the incoming solar radiation.

The conclusion of **Paper III** was that increasing plant stress, caused by biotic stressors, for needleleaf evergreen boreal and broadleaf deciduous boreal trees, enhanced SOA formation, through oxidation, due to increase in monoterpene emissions. The enhanced SOA burden further increased CDNC at cloud top and caused stronger negative shortwave  $\text{RF}_{\text{ari}}$  in both clear-sky and all-sky cases. Thus, in future global aerosol-climate model simulations the effect of biotic stress in trees should be addressed as it has substantial effect on clouds and radiative effects.

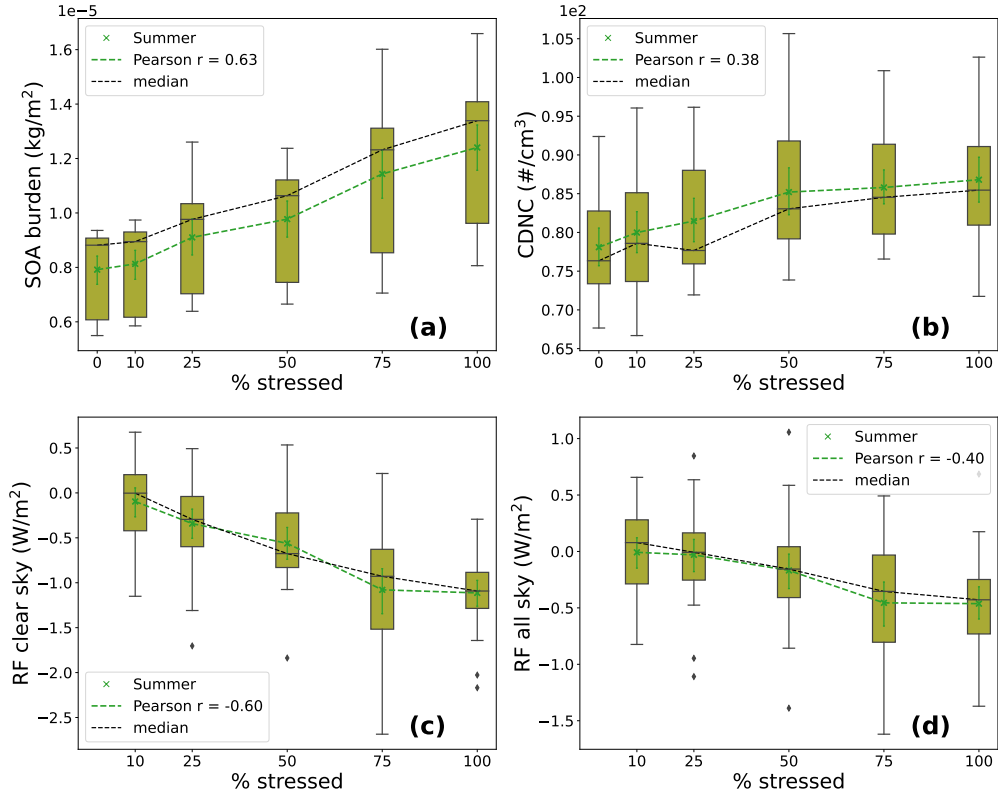


**Figure 5.7:** Mean SOA burden over land area, CDNC at cloud top, and TOA clear-sky and all-sky  $RF_{\text{ari}}$  as a function of biotic stress percentage. The data is presented as a mean from summer period over 10-year simulation from  $40^\circ$  latitude northward. The black dashed line represents the median values and the green dashed lines represent the mean values. The boxes show the interquartile range (IQR) and the black whiskers represent the minimum and maximum values without the outliers. The black diamond shapes show the outlier data. Figure from **Paper III**.

## 6 Review of papers and the author's contribution

The author alone is responsible for writing this introductory part of the thesis.

**Paper I** O.-P. Tikkanen, O. Väisänen, L. Hao, E. Holopainen, H. Wang, K. E. J. Lehtinen, A. Virtanen, and T. Yli-Juuti: "Hygroscopicity of dimethylammonium-, sulfate-, and ammonium-containing nanoparticles", *Aerosol Science and Technology*, **52**, 971–983, (2018).

**Overview:** The ability of process-scale model E-AIM in predicting hygroscopicity of dimethylamine, sulfuric acid, ammonia and water containing particles was tested. The modelled hygroscopic growth and hygroscopicity parameter of the particles were compared against measurements by switching the dry particle sizes and varying RH. E-AIM was found to produce inadequate hygroscopic growth of dimethylamine-containing particles and thus more investigation is needed in terms of thermodynamics of these particles.

**Author contribution:** The author participated in the model calculations and data analysis. In addition, the author participated in the interpretation of the results.

**Paper II** E. Holopainen, H. Kokkola, A. Laakso, and T. Kühn: "In-cloud scavenging scheme for sectional aerosol modules – implementation in the framework of the Sectional Aerosol module for Large Scale Applications version 2.0 (SALSA2.0) global aerosol module", *Geoscientific Model Development*, **13**, 6215–6235, (2020).

**Overview:** The in-cloud wet deposition scheme was introduced for global aerosol-climate models with size-segregated aerosol description. The scheme was implemented in ECHAM-HAMMOZ with SALSA aerosol size distribution representation. The modelled vertical profiles were compared against those from the pre-existing wet deposition scheme as well as ATom aircraft measurements and atmospheric lifetimes of aerosol species against AERO-COM models. With default configuration, the newly-developed wet deposition scheme produced spurious vertical profiles and lifetimes of black carbon containing particles. Thus, the sensitivity of the scheme was tested in terms of black carbon emission size distribution, internal mixing and ageing. The best response in terms of vertical profiles and lifetimes was found with the newly-developed scheme when black carbon was mixed with soluble substances during emission.

**Author contribution:** The author was responsible for the coding and implementation of the wet deposition scheme to ECHAM-HAMMOZ. The author designed and performed all of the model simulations and did all of the data analysis. In addition, the author wrote most of the paper.

**Paper III** E. Holopainen, H. Kokkola, C. Faiola, A. Laakso, and T. Kühn: "Insect herbivory caused plant stress emissions increases the negative radiative forcing

of aerosols", *Journal of Geophysical Research: Atmospheres*, **127**, e2022JD036733, (2022).

**Overview:** ECHAM-HAMMOZ with SALSA aerosol size distribution representation was used to simulate the effect of biotic stress caused by insect herbivory in boreal trees. The analysis included the effects of increased stress percentage on secondary organic aerosol (SOA) formation, cloud droplet number concentration (CDNC) and radiative forcing due to aerosol-radiation interactions ( $RF_{\text{ari}}$ ). Increasing the stress percentage, enhanced the SOA formation and thus CDNC at cloud top. Further, enhanced SOA caused stronger negative shortwave  $RF_{\text{ari}}$  in clear-sky and all-sky cases. Thus, global aerosol-climate model simulations should include the effects of biotic stress on trees.

**Author contribution:** The author was responsible for the modification of the ECHAM-HAMMOZ model code to include the effects of biotic stress in monoterpene emissions. The author designed and performed all of the model simulations and did all of the data analysis. In addition, the author wrote most of the paper.

## 7 Summary and conclusions

This thesis aimed to address the understanding of thermodynamic properties and hygroscopicity of aerosol particles, in process-scale modelling, as well as wet deposition and sources of SOA, in global-scale modelling. The thermodynamic equilibrium process-scale model was evaluated against measured hygroscopic growth of DMA, sulfuric acid and ammonia containing organic aerosol particles (**Paper I**). The study was conducted to get insight on the atmospheric behaviour of amines as well as to address the understanding of thermodynamic properties of amines by testing the ability of thermodynamic equilibrium model to represent measured hygroscopic growth of amine-containing particles. A new in-cloud wet deposition scheme for global aerosol-climate models using size-segregated aerosol descriptions was developed and evaluated. For the evaluation, the global aerosol-climate model ECHAM-HAMMOZ with the SALSA aerosol microphysics module was used, and evaluation was done against the pre-existing description as well as aircraft measurements and various other climate models (**Paper II**). The study was conducted to improve the description of transport and wet deposition of atmospheric aerosols in global aerosol-climate models as well as to provide knowledge on the processes affecting the sensitivity of wet deposition in models. In addition, biotic stress in boreal trees was studied in ECHAM-HAMMOZ, with SALSA, in terms of SOA formation, clouds and radiative effects (**Paper III**). The study was conducted to provide insight of the significance of SOA sources to clouds and radiative effects in global aerosol-climate models.

In this thesis, the first objective was to evaluate the performance of thermodynamic equilibrium model in modelling the hygroscopic growth of dimethylamine-containing particles. **Paper I** showed that the thermodynamic equilibrium model, E-AIM, was able to reproduce the measured hygroscopic growth factors for DMA, sulfuric acid and ammonia containing aerosol particles when the particle size was large (above 80 nm in diameter), but was inadequate for the smaller particles (smaller than 20 nm in diameter). The results stated that there are uncertainties in thermodynamic properties of DMA, SA, ammonia and water systems in the E-AIM model. Amines, and especially dimethylamine, are important contributors to atmospheric aerosol particles. Thus, it is evident that further investigation is needed in terms of thermodynamic properties of DMA-containing particles as even state-of-the-art thermodynamic equilibrium model was inadequate in modelling hygroscopicity of these particles when the particle sizes were in orders of tens of nanometers. Using improper thermodynamic properties in models leads to uncertainties in several aspects of aerosols, such as, NPF, activation to cloud droplets and growth. To improve the understanding of thermodynamics of DMA-containing particles, further laboratory measurements are needed including measurements for careful particle phase composition characterization.

The second objective of this thesis was to develop and evaluate a parametrization of wet removal of aerosols in a global aerosol-climate model. In **Paper II**, the newly-developed, wet deposition scheme, although being more physically sound, produced spurious vertical profiles and lifetimes when compared to the pre-existing



scheme. Thus, it was evident that the sensitivity of the newly-developed scheme needed to be tested in terms of BC emission size distribution and internal mixing of the BC particles as well as ageing of aerosol particles. Results in **Paper II** showed that mixing BC with soluble substances during emissions produced more accurate vertical profiles, when compared to the aircraft measurements, as well as more reasonable atmospheric lifetimes of aerosol species, when compared to those from other global climate models. The results indicate that the level of internal mixing of BC with soluble substances (hygroscopicity) is in dire need for further investigation as even more physical representation of wet deposition is not enough to describe the observed aerosol concentrations. As transport of aerosol species to remote regions, such as the Arctic, is strongly dependent on deposition processes and especially wet deposition, more physical parametrizations for aerosol wet removal should be incorporated to several global aerosol-climate models. Especially, the modelled black carbon concentrations in the Arctic are usually underestimated when compared to the observations. Underestimation of modelled black carbon concentrations in the Arctic can lead to underestimation in the absorbed solar radiation around the Arctic region, which further leads to underestimation in temperature. To further improve the understanding of the wet deposition and transport of BC to the Arctic, additional field measurements are needed as well as measurements near the source regions to evaluate the incorporation of BC in more soluble substances.

The third objective of this thesis was to study the effects of biotic stress in boreal trees in terms of formed biogenic SOA, clouds and radiative effects in a global aerosol-climate model. Results, in **Paper III**, showed that increasing the biotic stress, due to herbivore infestation, by increasing monoterpene emission factors, enhanced SOA formation through oxidation of monoterpene VOC. The increase in SOA concentrations were almost linear with increasing stress percentage. The enhanced SOA concentrations resulted in an increase in CDNC at cloud top through increasing number of particles acting as CCN. In addition, the elevated SOA concentrations caused stronger negative RF due to aerosol-radiation interactions. In **Paper III**, the global aerosol-climate model simulations assumed the insect herbivory on boreal trees simultaneously, which is not the case in reality, but rather some parts of the areas can have more intense herbivory than others. As SOA is an important contributor to the atmospheric aerosol particles and SOA has been found to be enhancing cooling of the atmosphere, more accurate SOA parametrizations, especially in terms of contributors to sources of SOA, should be incorporated in global aerosol-climate models. Improperly incorporating SOA sources, especially biotic stress enhanced SOA formation, in models, can lead to uncertainties in modelled radiative forcings as well as cloud formation. There are still many uncertainties related to biotic stress in global aerosol-climate models: for example, whether the effect of biotic stress to VOC emissions is known well enough, or whether the occurrence of biotic stress factors is known well enough to be incorporated in global models. Thus, to improve the understanding of biotic stress, additional field measurements are needed in terms of insect herbivory to address their intensity and infected areas during outbreaks.

The process- and global-scale models applied in this thesis showed reasonable skill in reproducing hygroscopicity and wet deposition of aerosol particles. However, certain modelled aerosol species are still poorly described, especially with respect to thermodynamic properties and internal mixing. In addition, the sources, sinks, and atmospheric processing of SOA contributes significantly to clouds and radiative effects and thus more investigation is needed, especially in terms of sources of atmospheric SOA to properly describe its climatic effects. Furthermore, addi-

tional laboratory and field measurements and satellite observations are needed to properly evaluate process-scale models as well as global aerosol-climate models.

# BIBLIOGRAPHY

- Abdul-Razzak, H. and Ghan, S.: A parameterization of aerosol activation. Part 3: Sectional representation, *Journal of Geophysical Research*, 107, 1–6, <https://doi.org/10.1029/2001JD000483>, 2002.
- Albrecht, B. A.: Aerosols, Cloud Microphysics, and Fractional Cloudiness, *Science*, 245, 1227–1230, <https://doi.org/10.1126/science.245.4923.1227>, 1989.
- Almeida, J., Schobesberger, S., Kürten, A., Ortega, I. K., Kupiainen-Määttä, O., Praplan, A. P., Adamov, A., Amorim, A., Bianchi, F., Breitenlechner, M., David, A., Dommen, J., Donahue, N. M., Downard, A., Dunne, E., Duplissy, J., Ehrhart, S., Flagan, R. C., Franchin, A., Guida, R., Hakala, J., Hansel, A., Heinritzi, M., Henschel, H., Jokinen, T., Junninen, H., Kajos, M., Kangasluoma, J., Keskinen, H., Kupc, A., Kurtén, T., Kvashin, A. N., Laaksonen, A., Lehtipalo, K., Leiminger, M., Leppä, J., Loukonen, V., Makhmutov, V., Mathot, S., McGrath, M. J., Nieminen, T., Olenius, T., Onnela, A., Petäjä, T., Riccobono, F., Riipinen, I., Rissanen, M., Rondo, L., Ruuskanen, T., Santos, F. D., Sarnela, N., Schallhart, S., Schnitzhofer, R., Seinfeld, J. H., Simon, M., Sipilä, M., Stozhkov, Y., Stratmann, F., Tomé, A., Tröstl, J., Tsagkogeorgas, G., Vaattovaara, P., Viisanen, Y., Virtanen, A., Vrtala, A., Wagner, P. E., Weingartner, E., Wex, H., Williamson, C., Wimmer, D., Ye, P., Yli-Juuti, T., Carslaw, K. S., Kulmala, M., Curtius, J., Baltensperger, U., Worsnop, D. R., Vehkamäki, H., and Kirkby, J.: Molecular understanding of sulphuric acid–amine particle nucleation in the atmosphere, *Nature*, 502, 359–363, <https://doi.org/10.1038/nature12663>, URL <https://doi.org/10.1038/nature12663>, 2013.
- Bergman, T., Kerminen, V.-M., Korhonen, H., Lehtinen, K. J., Makkonen, R., Arola, A., Mielonen, T., Romakkaniemi, S., Kulmala, M., and Kokkola, H.: Evaluation of the sectional aerosol microphysics module SALSA implementation in ECHAM5-HAM aerosol-climate model, *Geoscientific model development*, 5, 845–868, <https://doi.org/10.5194/gmd-5-845-2012>, 2012.
- Bergman, T., Laaksonen, A., Korhonen, H., Malila, J., Dunne, E. M., Mielonen, T., Lehtinen, K. E. J., Kühn, T., Arola, A., and Kokkola, H.: Geographical and diurnal features of amine-enhanced boundary layer nucleation, *Journal of Geophysical Research: Atmospheres*, 120, 9606–9624, <https://doi.org/10.1002/2015JD023181>, URL <https://agupubs.onlinelibrary.wiley.com/doi/abs/10.1002/2015JD023181>, 2015.
- Berrisford, P., Dee, D., Poli, P., Brugge, R., Fielding, K., Fuentes, M., Kållberg, P., Kobayashi, S., Uppala, S., and Simmons, A.: The ERA-Interim archive Version 2.0, Shinfield Park, Reading, 2011.
- Bond, T. C., Doherty, S. J., Fahey, D. W., Forster, P. M., Berntsen, T., DeAngelo, B. J., Flanner, M. G., Ghan, S., Kärcher, B., Koch, D., Kinne, S., Kondo, Y., Quinn, P. K., Sarofim, M. C., Schultz, M. G., Schulz, M., Venkataraman, C., Zhang, H., Zhang, S., Bellouin, N., Guttikunda, S. K., Hopke, P. K., Jacobson, M. Z., Kaiser, J. W., Klimont, Z., Lohmann, U., Schwarz, J. P., Shindell, D., Storelvmo, T., Warren,

- S. G., and Zender, C. S.: Bounding the role of black carbon in the climate system: A scientific assessment, *Journal of Geophysical Research: Atmospheres*, 118, 5380–5552, <https://doi.org/10.1002/jgrd.50171>, 2013.
- Bourgeois, Q. and Bey, I.: Pollution transport efficiency toward the Arctic: Sensitivity to aerosol scavenging and source regions, *Journal of Geophysical Research*, 116, D08 213, <https://doi.org/10.1029/2010JD015096>, 2011.
- Ceppi, P. and Hartmann, D. L.: Connections Between Clouds, Radiation, and Midlatitude Dynamics: a Review, *Current Climate Change Reports*, 1, 94–102, <https://doi.org/10.1007/s40641-015-0010-x>, URL <https://doi.org/10.1007/s40641-015-0010-x>, 2015.
- Chang, R. Y.-W., Slowik, J. G., Shantz, N. C., Vlasenko, A., Liggio, J., Sjostedt, S. J., Leaitch, W. R., and Abbatt, J. P. D.: The hygroscopicity parameter ( $\kappa$ ) of ambient organic aerosol at a field site subject to biogenic and anthropogenic influences: relationship to degree of aerosol oxidation, *Atmospheric Chemistry and Physics*, 10, 5047–5064, <https://doi.org/10.5194/acp-10-5047-2010>, URL <https://acp.copernicus.org/articles/10/5047/2010/>, 2010.
- Chate, D., Rao, P., Naik, M., Momin, G., Safai, P., and Ali, K.: Scavenging of aerosols and their chemical species by rain, *Atmospheric Environment*, 37, 2477 – 2484, [https://doi.org/https://doi.org/10.1016/S1352-2310\(03\)00162-6](https://doi.org/https://doi.org/10.1016/S1352-2310(03)00162-6), 2003.
- Chate, D., Murugavel, P., Ali, K., Tiwari, S., and Beig, G.: Below-cloud rain scavenging of atmospheric aerosols for aerosol deposition models, *Atmospheric Research*, 99, 528 – 536, <https://doi.org/https://doi.org/10.1016/j.atmosres.2010.12.010>, 2011.
- Chen, J.-P. and Lamb, D.: Simulation of Cloud Microphysical and Chemical Processes Using a Multicomponent Framework. Part I: Description of the Microphysical Model, *Journal of Atmospheric Sciences*, 51, 2613–2630, [https://doi.org/10.1175/1520-0469\(1994\)051<2613:SOCMAC>2.0.CO;2](https://doi.org/10.1175/1520-0469(1994)051<2613:SOCMAC>2.0.CO;2), 1994.
- Clegg, S. L., Pitzer, K. S., and Brimblecombe, P.: Thermodynamics of multicomponent, miscible, ionic solutions. Mixtures including unsymmetrical electrolytes, *Journal of Physical Chemistry*, 96, 9470–9479, <https://doi.org/10.1021/j100202a074>, URL <https://doi.org/10.1021/j100202a074>, 1992.
- Clegg, S. L., Brimblecombe, P., and Wexler, A. S.: Thermodynamic Model of the System  $\text{H}^+ - \text{NH}_4^+ - \text{SO}_4^{2-} - \text{NO}_3^- - \text{H}_2\text{O}$  at Tropospheric Temperatures, *The Journal of Physical Chemistry A*, 102, 2137–2154, <https://doi.org/10.1021/jp973042r>, URL <https://doi.org/10.1021/jp973042r>, 1998.
- Clegg, S. L., Seinfeld, J. H., and Brimblecombe, P.: Thermodynamic modelling of aqueous aerosols containing electrolytes and dissolved organic compounds, *Journal of Aerosol Science*, 32, 713–738, [https://doi.org/https://doi.org/10.1016/S0021-8502\(00\)00105-1](https://doi.org/https://doi.org/10.1016/S0021-8502(00)00105-1), URL <https://www.sciencedirect.com/science/article/pii/S0021850200001051>, 2001.
- Croft, B., Lohmann, U., Martin, R. V., Stier, P., Wurzler, S., Feichter, J., Posselt, R., and Ferrachat, S.: Aerosol size-dependent below-cloud scavenging by rain and snow in the ECHAM5-HAM, *Atmospheric Chemistry and Physics*, 9, 4653–4675, <https://doi.org/10.5194/acp-9-4653-2009>, 2009.

- Croft, B., Lohmann, U., Martin, R. V., Stier, P., Wurzler, S., Feichter, J., Hoose, C., Heikkilä, U., van Donkelaar, A., and Ferrachat, S.: Influences of in-cloud aerosol scavenging parameterizations on aerosol concentrations and wet deposition in ECHAM5-HAM, *Atmospheric Chemistry and Physics*, 10, 1511–1543, <https://doi.org/10.5194/acp-10-1511-2010>, 2010.
- De Gouw, J. and Jimenez, J. L.: Organic Aerosols in the Earth’s Atmosphere, *Environmental Science and Technology*, 43, 7614–7618, <https://doi.org/doi:10.1021/es9006004>, URL <https://doi.org/10.1021/es9006004>, 2009.
- Donahue, N. M., Robinson, A. L., Stanier, C. O., and Pandis, S. N.: Coupled Partitioning, Dilution, and Chemical Aging of Semivolatile Organics, *Environmental Science & Technology*, 40, 2635–2643, <https://doi.org/doi:10.1021/es052297c>, URL <https://doi.org/10.1021/es052297c>, 2006.
- Eckhardt, S., Quennehen, B., Olivie, D. J. L., Berntsen, T. K., Cherian, R., Christensen, J. H., Collins, W., Crepinsek, S., Daskalakis, N., Flanner, M., Herber, A., Heyes, C., Hodnebrog, Ø., Huang, L., Kanakidou, M., Klimont, Z., Langner, J., Law, K. S., Lund, M. T., Mahmood, R., Massling, A., Myriokefalitakis, S., Nielsen, I. E., Nøjgaard, J. K., Quaas, J., Quinn, P. K., Raut, J.-C., Rumbold, S. T., Schulz, M., Sharma, S., Skeie, R. B., Skov, H., Uttal, T., von Salzen, K., and Stohl, A.: Current model capabilities for simulating black carbon and sulfate concentrations in the Arctic atmosphere: a multi-model evaluation using a comprehensive measurement data set, *Atmospheric Chemistry and Physics*, 15, 9413–9433, <https://doi.org/10.5194/acp-15-9413-2015>, 2015.
- Faiola, C. L. and Taipale, D.: Impact of insect herbivory on plant stress volatile emissions from trees: A synthesis of quantitative measurements and recommendations for future research, *Atmospheric Environment: X*, 5, 100060, <https://doi.org/https://doi.org/10.1016/j.aeaoa.2019.100060>, URL <https://www.sciencedirect.com/science/article/pii/S2590162119300632>, 2020.
- Fanourgakis, G. S., Kanakidou, M., Nenes, A., Bauer, S. E., Bergman, T., Carslaw, K. S., Grini, A., Hamilton, D. S., Johnson, J. S., Karydis, V. A., Kirkevåg, A., Kodros, J. K., Lohmann, U., Luo, G., Makkonen, R., Matsui, H., Neubauer, D., Pierce, J. R., Schmale, J., Stier, P., Tsigaridis, K., van Noije, T., Wang, H., Watson-Parris, D., Westervelt, D. M., Yang, Y., Yoshioka, M., Daskalakis, N., Decesari, S., Gysel-Beer, M., Kalivitis, N., Liu, X., Mahowald, N. M., Myriokefalitakis, S., Schrödner, R., Sfakianaki, M., Tsimpidi, A. P., Wu, M., and Yu, F.: Evaluation of global simulations of aerosol particle and cloud condensation nuclei number, with implications for cloud droplet formation, *Atmospheric Chemistry and Physics*, 19, 8591–8617, <https://doi.org/10.5194/acp-19-8591-2019>, URL <https://acp.copernicus.org/articles/19/8591/2019/>, 2019.
- Flossmann, A. I. and Wobrock, W.: A review of our understanding of the aerosol–cloud interaction from the perspective of a bin resolved cloud scale modelling, *Atmospheric Research*, 97, 478 – 497, <https://doi.org/https://doi.org/10.1016/j.atmosres.2010.05.008>, 2010.
- Fredenslund, A., Jones, R. L., and Prausnitz, J. M.: Group-contribution estimation of activity coefficients in nonideal liquid mixtures, *AIChE Journal*, 21,

- 1086–1099, <https://doi.org/https://doi.org/10.1002/aic.690210607>, URL <https://aiche.onlinelibrary.wiley.com/doi/abs/10.1002/aic.690210607>, 1975.
- Friedlander, S. K.: Smoke, dust and haze fundamentals of aerosol dynamics, 2nd edition, Oxford University Press, New York, 2000.
- Gelbard, F. and Seinfeld, J. H.: The general dynamic equation for aerosols. Theory and application to aerosol formation and growth, *Journal of Colloid and Interface Science*, 68, 363–382, [https://doi.org/https://doi.org/10.1016/0021-9797\(79\)90289-3](https://doi.org/https://doi.org/10.1016/0021-9797(79)90289-3), URL <https://www.sciencedirect.com/science/article/pii/0021979779902893>, 1979.
- Ghan, S. J. and Schwartz, S. E.: Aerosol Properties and Processes: A Path from Field and Laboratory Measurements to Global Climate Models, *Bulletin of the American Meteorological Society*, 88, 1059 – 1084, <https://doi.org/10.1175/BAMS-88-7-1059>, URL <https://journals.ametsoc.org/view/journals/bams/88/7/bams-88-7-1059.xml>, 2007.
- Ghan, S. J., Liu, X., Easter, R. C., Zaveri, R., Rasch, P. J., Yoon, J.-H., and Eaton, B.: Toward a Minimal Representation of Aerosols in Climate Models: Comparative Decomposition of Aerosol Direct, Semidirect, and Indirect Radiative Forcing, *Journal of Climate*, 25, 6461 – 6476, <https://doi.org/10.1175/JCLI-D-11-00650.1>, URL <https://journals.ametsoc.org/view/journals/clim/25/19/jcli-d-11-00650.1.xml>, 2012.
- Gliß, J., Mortier, A., Schulz, M., Andrews, E., Balkanski, Y., Bauer, S. E., Benedictow, A. M. K., Bian, H., Checa-Garcia, R., Chin, M., Ginoux, P., Griesfeller, J. J., Heckel, A., Kipling, Z., Kirkevåg, A., Kokkola, H., Laj, P., Le Sager, P., Lund, M. T., Lund Myhre, C., Matsui, H., Myhre, G., Neubauer, D., van Noije, T., North, P., Olivié, D. J. L., Sogacheva, L., Takemura, T., Tsigaridis, K., and Tsyro, S. G.: Multi-model evaluation of aerosol optical properties in the AeroCom phase III Control experiment, using ground and space based columnar observations from AERONET, MODIS, AATSR and a merged satellite product as well as surface in-situ observations from GAW sites, *Atmospheric Chemistry and Physics Discussions*, 2020, 1–62, <https://doi.org/10.5194/acp-2019-1214>, 2020.
- Guenther, A. B., Jiang, X., Heald, C. L., Sakulyanontvittaya, T., Duhl, T., Emons, L. K., and Wang, X.: The Model of Emissions of Gases and Aerosols from Nature version 2.1 (MEGAN2.1): an extended and updated framework for modeling biogenic emissions, *Geoscientific Model Development*, 5, 1471–1492, <https://doi.org/10.5194/gmd-5-1471-2012>, 2012.
- Hakola, H., Tarvainen, V., Bäck, J., Ranta, H., Bonn, B., Rinne, J., and Kulmala, M.: Seasonal variation of mono- and sesquiterpene emission rates of Scots pine, *Biogeosciences*, 3, 93–101, <https://doi.org/10.5194/bg-3-93-2006>, URL <https://bg.copernicus.org/articles/3/93/2006/>, 2006.
- Hallquist, M., Wenger, J. C., Baltensperger, U., Rudich, Y., Simpson, D., Claeys, M., Dommen, J., Donahue, N. M., George, C., Goldstein, A. H., Hamilton, J. F., Herrmann, H., Hoffmann, T., Iinuma, Y., Jang, M., Jenkin, M. E., Jimenez, J. L., Kiendler-Scharr, A., Maenhaut, W., McFiggans, G., Mentel, T. F., Monod, A., Prévôt, A. S. H., Seinfeld, J. H., Surratt, J. D., Szmigielski, R., and Wildt,

- J.: The formation, properties and impact of secondary organic aerosol: current and emerging issues, *Atmospheric Chemistry and Physics*, 9, 5155–5236, <https://doi.org/10.5194/acp-9-5155-2009>, URL <https://acp.copernicus.org/articles/9/5155/2009/>, 2009.
- Hansen, H. K., Rasmussen, P., Fredenslund, A., Schiller, M., and Gmehling, J.: Vapor-liquid equilibria by UNIFAC group contribution. 5. Revision and extension, *Industrial & Engineering Chemistry Research*, 30, 2352–2355, <https://doi.org/10.1021/ie00058a017>, URL <https://doi.org/10.1021/ie00058a017>, 1991.
- Hansen, J., Lacis, A., Ruedy, R., and Sato, M.: Potential climate impact of Mount Pinatubo eruption, *Geophysical Research Letters*, 19, 215–218, <https://doi.org/https://doi.org/10.1029/91GL02788>, URL <https://agupubs.onlinelibrary.wiley.com/doi/abs/10.1029/91GL02788>, 1992.
- He, M., He, C.-Q., and Ding, N.-Z.: Abiotic Stresses: General Defenses of Land Plants and Chances for Engineering Multistress Tolerance, *Frontiers in Plant Science*, 9, 1771, <https://doi.org/10.3389/fpls.2018.01771>, URL <https://www.frontiersin.org/article/10.3389/fpls.2018.01771>, 2018.
- Henrot, A.-J., Stanelle, T., Schröder, S., Siegenthaler, C., Taraborrelli, D., and Schultz, M. G.: Implementation of the MEGAN (v2.1) biogenic emission model in the ECHAM6-HAMMOZ chemistry climate model, *Geoscientific Model Development*, 10, 903–926, <https://doi.org/10.5194/gmd-10-903-2017>, URL <https://gmd.copernicus.org/articles/10/903/2017/>, 2017.
- Hinds, W. C.: *Aerosol Technology: Properties, Behavior, and Measurement of Airborne Particles*, 2nd Edition, Wiley & Sons, 1999.
- Hobbs, P.: *Aerosol-cloud-climate interactions*, vol. 54, Academic Press, San Diego, 1993.
- Holopainen, J. K. and Gershenzon, J.: Multiple stress factors and the emission of plant VOCs, *Trends in Plant Science*, 15, 176–184, <https://doi.org/https://doi.org/10.1016/j.tplants.2010.01.006>, 2010.
- Horvath, H.: Estimation of the average visibility in central Europe, *Atmospheric Environment*, 29, 241–246, [https://doi.org/https://doi.org/10.1016/1352-2310\(94\)00236-E](https://doi.org/https://doi.org/10.1016/1352-2310(94)00236-E), URL <https://www.sciencedirect.com/science/article/pii/135223109400236E>, 1995.
- Huang, S., Wu, Z., Wang, Y., Poulain, L., Höpner, F., Merkel, M., Herrmann, H., and Wiedensohler, A.: Aerosol Hygroscopicity and its Link to Chemical Composition in a Remote Marine Environment Based on Three Transatlantic Measurements, *Environmental Science & Technology*, 56, 9613–9622, <https://doi.org/10.1021/acs.est.2c00785>, URL <https://doi.org/10.1021/acs.est.2c00785>, 2022.
- Huertas, J. I.: Modeling Aerosol Processes, in: *Montecarlo Simulation of Two Component Aerosol Processes*, edited by Huertas, J. I., chap. 3, IntechOpen, Rijeka, <https://doi.org/10.5772/62022>, URL <https://doi.org/10.5772/62022>, 2016.
- IPCC: *Climate Change 2013 – The Physical Science Basis: Working Group I Contribution to the Fifth Assessment Report of the Intergovernmental Panel on Climate Change*, p. 659–740, Cambridge University Press, <https://doi.org/10.1017/CBO9781107415324.018>, 2014.

IPCC: Climate Change 2021: The Physical Science Basis. Contribution of Working Group I to the Sixth Assessment Report of the Intergovernmental Panel on Climate Change, pp. 6–1 – 7–204, Cambridge University Press, URL <https://www.ipcc.ch/report/ar6/wg1/#FullReport>, 2021.

Jimenez, J. L., Canagaratna, M. R., Donahue, N. M., Prevot, A. S. H., Zhang, Q., Kroll, J. H., DeCarlo, P. F., Allan, J. D., Coe, H., Ng, N. L., Aiken, A. C., Docherty, K. S., Ulbrich, I. M., Grieshop, A. P., Robinson, A. L., Duplissy, J., Smith, J. D., Wilson, K. R., Lanz, V. A., Hueglin, C., Sun, Y. L., Tian, J., Laaksonen, A., Raatikainen, T., Rautiainen, J., Vaattovaara, P., Ehn, M., Kulmala, M., Tomlinson, J. M., Collins, D. R., Cubison, M. J., Dunlea, J., Huffman, J. A., Onasch, T. B., Alfarra, M. R., Williams, P. I., Bower, K., Kondo, Y., Schneider, J., Drewnick, F., Borrmann, S., Weimer, S., Demerjian, K., Salcedo, D., Cottrell, L., Griffin, R., Takami, A., Miyoshi, T., Hatakeyama, S., Shimono, A., Sun, J. Y., Zhang, Y. M., Dzepina, K., Kimmel, J. R., Sueper, D., Jayne, J. T., Herndon, S. C., Trimborn, A. M., Williams, L. R., Wood, E. C., Middlebrook, A. M., Kolb, C. E., Baltensperger, U., and Worsnop, D. R.: Evolution of Organic Aerosols in the Atmosphere, *Science*, 326, 1525–1529, <https://doi.org/10.1126/science.1180353>, 2009.

Joutsensaari, J., Yli-Pirilä, P., Korhonen, H., Arola, A., Blande, J. D., Heijari, J., Kivimäenpää, M., Mikkonen, S., Hao, L., Miettinen, P., Lyytikäinen-Saarenmaa, P., Faiola, C. L., Laaksonen, A., and Holopainen, J. K.: Biotic stress accelerates formation of climate-relevant aerosols in boreal forests, *Atmospheric Chemistry and Physics*, 15, 12 139–12 157, <https://doi.org/10.5194/acp-15-12139-2015>, 2015.

Kanellopoulos, P. G., Verouti, E., Chrysochou, E., Koukoulakis, K., and Bakeas, E.: Primary and secondary organic aerosol in an urban/industrial site: Sources, health implications and the role of plastic enriched waste burning, *Journal of Environmental Sciences*, 99, 222–238, <https://doi.org/https://doi.org/10.1016/j.jes.2020.06.012>, URL <https://www.sciencedirect.com/science/article/pii/S1001074220302679>, 2021.

Kerminen, V.-M. and Kulmala, M.: Analytical formulae connecting the “real” and the “apparent” nucleation rate and the nuclei number concentration for atmospheric nucleation events, *Journal of Aerosol Science*, 33, 609–622, [https://doi.org/https://doi.org/10.1016/S0021-8502\(01\)00194-X](https://doi.org/https://doi.org/10.1016/S0021-8502(01)00194-X), 2002.

Kerminen, V.-M., Lehtinen, K. E. J., Anttila, T., and Kulmala, M.: Dynamics of atmospheric nucleation mode particles: a timescale analysis, *Tellus B*, 56, 135–146, <https://doi.org/https://doi.org/10.1111/j.1600-0889.2004.00095.x>, URL <https://onlinelibrary.wiley.com/doi/abs/10.1111/j.1600-0889.2004.00095.x>, 2004.

Kigathi, R. N., Weisser, W. W., Reichelt, M., Gershenson, J., and Unsicker, S. B.: Plant volatile emission depends on the species composition of the neighboring plant community, *BMC Plant Biology*, 19, 58, <https://doi.org/10.1186/s12870-018-1541-9>, URL <https://doi.org/10.1186/s12870-018-1541-9>, 2019.

Kim, J., Ahlm, L., Yli-Juuti, T., Lawler, M., Keskinen, H., Tröstl, J., Schobesberger, S., Duplissy, J., Amorim, A., Bianchi, F., Donahue, N. M., Flagan, R. C., Hakala, J., Heinritzi, M., Jokinen, T., Kürten, A., Laaksonen, A., Lehtipalo, K., Miettinen, P., Petäjä, T., Rissanen, M. P., Rondo, L., Sengupta, K., Simon,



- M., Tomé, A., Williamson, C., Wimmer, D., Winkler, P. M., Ehrhart, S., Ye, P., Kirkby, J., Curtius, J., Baltensperger, U., Kulmala, M., Lehtinen, K. E. J., Smith, J. N., Riipinen, I., and Virtanen, A.: Hygroscopicity of nanoparticles produced from homogeneous nucleation in the CLOUD experiments, *Atmospheric Chemistry and Physics*, 16, 293–304, <https://doi.org/10.5194/acp-16-293-2016>, URL <https://acp.copernicus.org/articles/16/293/2016/>, 2016.
- Kipling, Z., Stier, P., Johnson, C. E., Mann, G. W., Bellouin, N., Bauer, S. E., Bergman, T., Chin, M., Diehl, T., Ghan, S. J., Iversen, T., Kirkevåg, A., Kokkola, H., Liu, X., Luo, G., van Noije, T., Pringle, K. J., von Salzen, K., Schulz, M., Seland, Ø., Skeie, R. B., Takemura, T., Tsigaridis, K., and Zhang, K.: What controls the vertical distribution of aerosol? Relationships between process sensitivity in HadGEM3–UKCA and inter-model variation from AeroCom Phase II, *Atmospheric Chemistry and Physics*, 16, 2221–2241, <https://doi.org/10.5194/acp-16-2221-2016>, 2016.
- Köhler, H.: The nucleus in and the growth of hygroscopic droplets, *Trans. Faraday Soc.*, 32, 1152–1161, <https://doi.org/10.1039/TF9363201152>, 1936.
- Kokkola, H., Vesterinen, M., Anttila, T., Laaksonen, A., and Lehtinen, K. E. J.: Technical note: Analytical formulae for the critical supersaturations and droplet diameters of CCN containing insoluble material, *Atmospheric Chemistry and Physics*, 8, 1985–1988, <https://doi.org/10.5194/acp-8-1985-2008>, 2008.
- Kokkola, H., Kuhn, T., Laakso, A., Bergman, T., Lehtinen, K. E. J., Mielonen, T., Arola, A., Stadtler, S., Korhonen, H., Ferrachat, S., Lohmann, U., Neubauer, D., Tegen, I., Siegenthaler-Le Drian, C., Schultz, M. G., Bey, I., Stier, P., Daskalakis, N., Heald, C. L., and Romakkaniemi, S.: SALSA2.0: The sectional aerosol module of the aerosol-chemistry-climate model ECHAM6.3.0-HAM2.3-MOZ1.0, *Geoscientific Model Development*, 11, 3833–3863, <https://doi.org/10.5194/gmd-11-3833-2018>, 2018.
- Koo, B., Knipping, E., and Yarwood, G.: 1.5-Dimensional volatility basis set approach for modeling organic aerosol in CAMx and CMAQ, *Atmospheric Environment*, 95, 158–164, <https://doi.org/10.1016/j.atmosenv.2014.06.031>, URL <https://www.sciencedirect.com/science/article/pii/S1352231014004774>, 2014.
- Korhola, T., Kokkola, H., Korhonen, H., Partanen, A.-I., Laaksonen, A., Lehtinen, K. E. J., and Romakkaniemi, S.: Reallocation in modal aerosol models: impacts on predicting aerosol radiative effects, *Geoscientific Model Development*, 7, 161–174, <https://doi.org/10.5194/gmd-7-161-2014>, URL <https://gmd.copernicus.org/articles/7/161/2014/>, 2014.
- Korolev, A., Emery, E., Strapp, J., Cober, S., Isaac, G., Wasey, M., and Marcotte, D.: Small Ice Particles in Tropospheric Clouds: Fact or Artifact? Airborne Icing Instrumentation Evaluation Experiment, *Bulletin of the American Meteorological Society*, 92, 967–973, <https://doi.org/10.1175/2010BAMS3141.1>, 2011.
- Kristiansen, N. I., Stohl, A., Olivié, D. J. L., Croft, B., Søvde, O. A., Klein, H., Christoudias, T., Kunkel, D., Leadbetter, S. J., Lee, Y. H., Zhang, K., Tsigaridis, K., Bergman, T., Evangeliou, N., Wang, H., Ma, P.-L., Easter, R. C., Rasch, P. J., Liu, X., Pitari, G., Di Genova, G., Zhao, S. Y., Balkanski, Y., Bauer, S. E., Faluvegi, G. S., Kokkola, H., Martin, R. V., Pierce, J. R., Schulz, M., Shindell, D.,

- Tost, H., and Zhang, H.: Evaluation of observed and modelled aerosol lifetimes using radioactive tracers of opportunity and an ensemble of 19 global models, *Atmospheric Chemistry and Physics*, 16, 3525–3561, <https://doi.org/10.5194/acp-16-3525-2016>, 2016.
- Kuang, C., McMurry, P. H., and McCormick, A. V.: Determination of cloud condensation nuclei production from measured new particle formation events, *Geophysical Research Letters*, 36, L09 822, <https://doi.org/10.1029/2009GL037584>, URL <https://agupubs.onlinelibrary.wiley.com/doi/abs/10.1029/2009GL037584>, 2009.
- Kulmala, M., Vehkamäki, H., Petäjä, T., Dal Maso, M., Lauri, A., Kerminen, V.-M., Birmili, W., and McMurry, P.: Formation and growth rates of ultrafine atmospheric particles: a review of observations, *Journal of Aerosol Science*, 35, 143–176, <https://doi.org/10.1016/j.jaerosci.2003.10.003>, URL <https://www.sciencedirect.com/science/article/pii/S0021850203004373>, 2004.
- Kulmala, M., Nieminen, T., Nikandrova, A., Lehtipalo, K., Manninen, H. E., Kajos, M. K., Kolari, P., Lauri, A., Petäjä, T., Krejci, R., et al.: CO<sub>2</sub>-induced terrestrial climate feedback mechanism: From carbon sink to aerosol source and back, *Boreal Environment Research*, 19, 122–131, URL <http://hdl.handle.net/10138/228728>, 2014.
- Kürten, A., Jokinen, T., Simon, M., Sipilä, M., Sarnela, N., Junninen, H., Adamov, A., Almeida, J., Amorim, A., Bianchi, F., Breitenlechner, M., Dommen, J., Donahue, N. M., Duplissy, J., Ehrhart, S., Flagan, R. C., Franchin, A., Hakala, J., Hansel, A., Heinritzi, M., Hutterli, M., Kangasluoma, J., Kirkby, J., Laaksonen, A., Lehtipalo, K., Leiminger, M., Makhmutov, V., Mathot, S., Onnela, A., Petäjä, T., Praplan, A. P., Riccobono, F., Rissanen, M. P., Rondo, L., Schobesberger, S., Seinfeld, J. H., Steiner, G., Tome, A., Trostl, J., Winkler, P. M., Williamson, C., Wimmer, D., Ye, P. L., Baltensperger, U., Carslaw, K. S., Kulmala, M., Worsnop, D. R., and Curtius, J.: Neutral Molecular Cluster Formation of Sulfuric Acid-Dimethylamine Observed in Real Time under Atmospheric Conditions., *Proceedings of the National Academy of Science*, 111, 15 019–15 024, <https://doi.org/10.1073/pnas.1404853111>, URL <https://doi.org/10.1073/pnas.1404853111>, 2014.
- Kürten, A., Li, C., Bianchi, F., Curtius, J., Dias, A., Donahue, N. M., Duplissy, J., Flagan, R. C., Hakala, J., Jokinen, T., Kirkby, J., Kulmala, M., Laaksonen, A., Lehtipalo, K., Makhmutov, V., Onnela, A., Rissanen, M. P., Simon, M., Sipilä, M., Stozhkov, Y., Tröstl, J., Ye, P., and McMurry, P. H.: New particle formation in the sulfuric acid–dimethylamine–water system: reevaluation of CLOUD chamber measurements and comparison to an aerosol nucleation and growth model, *Atmospheric Chemistry and Physics*, 18, 845–863, <https://doi.org/10.5194/acp-18-845-2018>, URL <https://acp.copernicus.org/articles/18/845/2018/>, 2018.
- Ladino, L., Stetzer, O., Hattendorf, B., Günther, D., Croft, B., and Lohmann, U.: Experimental Study of Collection Efficiencies between Submicron Aerosols and Cloud Droplets, *Journal of the Atmospheric Sciences*, 68, 1853–1864, <https://doi.org/10.1175/JAS-D-11-012.1>, 2011.
- Lee, Y. H., Lamarque, J.-F., Flanner, M. G., Jiao, C., Shindell, D. T., Berntsen, T., Bisiaux, M. M., Cao, J., Collins, W. J., Curran, M., Edwards, R., Faluvegi, G.,

- Ghan, S., Horowitz, L. W., McConnell, J. R., Ming, J., Myhre, G., Nagashima, T., Naik, V., Rumbold, S. T., Skeie, R. B., Sudo, K., Takemura, T., Thevenon, F., Xu, B., and Yoon, J.-H.: Evaluation of preindustrial to present-day black carbon and its albedo forcing from Atmospheric Chemistry and Climate Model Intercomparison Project (ACCMIP), *Atmospheric Chemistry and Physics*, 13, 2607–2634, <https://doi.org/10.5194/acp-13-2607-2013>, URL <https://acp.copernicus.org/articles/13/2607/2013/>, 2013.
- Lin, G., Ghan, S. J., Wang, M., Ma, P.-L., Easter, R. C., Ovchinnikov, M., Fan, J., Zhang, K., Wang, H., Chand, D., and Qian, Y.: Development and Evaluation of an Explicit Treatment of Aerosol Processes at Cloud Scale Within a Multi-Scale Modeling Framework (MMF), *Journal of Advances in Modeling Earth Systems*, 10, 1663–1679, <https://doi.org/10.1029/2018MS001287>, URL <https://agupubs.onlinelibrary.wiley.com/doi/abs/10.1029/2018MS001287>, 2018.
- Lin, H. and Leaitch, W.: *Proceedings of the Wmo Workshop on Measurement of Cloud Properties for Forecasts of Weather, Air Quality and Climate*, 1997.
- Lohmann, U.: AEROSOLS | Aerosol–Cloud Interactions and Their Radiative Forcing, in: *Encyclopedia of Atmospheric Sciences (Second Edition)*, edited by North, G. R., Pyle, J., and Zhang, F., pp. 17–22, Academic Press, Oxford, second edition edn., <https://doi.org/10.1016/B978-0-12-382225-3.00052-9>, URL <https://www.sciencedirect.com/science/article/pii/B9780123822253000529>, 2015.
- Lohmann, U., Stier, P., Hoose, C., Ferrachat, S., Kloster, S., Roeckner, E., and Zhang, J.: Cloud microphysics and aerosol indirect effects in the global climate model ECHAM5-HAM, *Atmospheric Chemistry and Physics*, 7, 3425–3446, <https://doi.org/10.5194/acp-7-3425-2007>, 2007.
- Lorenz, E. N.: Deterministic Nonperiodic Flow, *Journal of Atmospheric Sciences*, 20, 130 – 141, [https://doi.org/10.1175/1520-0469\(1963\)020<0130:DNF>2.0.CO;2](https://doi.org/10.1175/1520-0469(1963)020<0130:DNF>2.0.CO;2), URL [https://journals.ametsoc.org/view/journals/atsc/20/2/1520-0469\\_1963\\_020\\_0130\\_dnf\\_2\\_0\\_co\\_2.xml](https://journals.ametsoc.org/view/journals/atsc/20/2/1520-0469_1963_020_0130_dnf_2_0_co_2.xml), 1963.
- Lund, M. T., Samset, B. H., Skeie, R. B., Watson-Parris, D., Katich, J. M., Schwarz, J. P., and Weinzierl, B.: Short Black Carbon lifetime inferred from a global set of aircraft observations, *npj Climate and Atmospheric Science*, 1, 2397–3722, <https://doi.org/10.1038/s41612-018-0040-x>, 2018.
- Lupo, A., Kininmonth, W., Armstrong, J., and Green, K.: Global climate models and their limitations., *Climate change reconsidered II: Physical science*, 9, 148, 2013.
- Mandl, F.: *Statistical Physics*, 2nd edition, John Wiley & Sons, Hoboken, New Jersey, 1988.
- Mann, G. W., Carslaw, K. S., Ridley, D. A., Spracklen, D. V., Pringle, K. J., Merikanto, J., Korhonen, H., Schwarz, J. P., Lee, L. A., Manktelow, P. T., Woodhouse, M. T., Schmidt, A., Breider, T. J., Emmerson, K. M., Reddington, C. L., Chipperfield, M. P., and Pickering, S. J.: Intercomparison of modal and sectional aerosol microphysics representations within the same 3-D global chemical transport model, *Atmospheric Chemistry and Physics*, 12, 4449–4476,

- <https://doi.org/10.5194/acp-12-4449-2012>, URL <https://acp.copernicus.org/articles/12/4449/2012/>, 2012.
- Materić, D., Bruhn, D., Turner, C., Morgan, G., Mason, N., and Gauci, V.: Methods in plant foliar volatile organic compounds research, *Applications in Plant Sciences*, 3, 1500 044, <https://doi.org/https://doi.org/10.3732/apps.1500044>, URL <https://bsapubs.onlinelibrary.wiley.com/doi/abs/10.3732/apps.1500044>, 2015.
- McGraw, R.: Description of Aerosol Dynamics by the Quadrature Method of Moments, *Aerosol Science and Technology*, 27, 255–265, <https://doi.org/10.1080/02786829708965471>, 1997.
- McNeill, V. F.: Aqueous Organic Chemistry in the Atmosphere: Sources and Chemical Processing of Organic Aerosols, *Environmental Science & Technology*, 49, 1237–1244, <https://doi.org/doi:10.1021/es504370>, URL <https://doi.org/10.1021/es5043707>, 2015.
- Morales, R. and Nenes, A.: Characteristic updrafts for computing distribution-averaged cloud droplet number and stratocumulus cloud properties, *Journal of Geophysical Research: Atmospheres*, 115, <https://doi.org/https://doi.org/10.1029/2009JD013233>, URL <https://agupubs.onlinelibrary.wiley.com/doi/abs/10.1029/2009JD013233>, 2010.
- Murphy, D. M., Cziczo, D. J., Froyd, K. D., Hudson, P. K., Matthew, B. M., Middlebrook, A. M., Peltier, R. E., Sullivan, A., Thomson, D. S., and Weber, R. J.: Single-particle mass spectrometry of tropospheric aerosol particles, *Journal of Geophysical Research: Atmospheres*, 111, <https://doi.org/https://doi.org/10.1029/2006JD007340>, URL <https://agupubs.onlinelibrary.wiley.com/doi/abs/10.1029/2006JD007340>, 2006.
- Myhre, G., Shindell, D., Bréon, F., Collins, W., Fuglestad, J., Huang, J., Koch, D., Lamarque, J., Lee, D., Mendoza, B., and Nakajima, T.: Anthropogenic and natural radiative forcing, climate change 2013: the Physical science basis. Contribution of Working Group I to the Fifth Assessment Report of the Intergovernmental Panel on Climate Change, *Current Climate Change Reports*, pp. 659–740, 2013.
- Mäkelä, J. M., Yli-Koivisto, S., Hiltunen, V., Seidl, W., Swietlicki, E., Teinilä, K., Sillanpää, M., Koponen, I. K., Paatero, J., Rosman, K., and Hämeri, K.: Chemical composition of aerosol during particle formation events in boreal forest, *Tellus B: Chemical and Physical Meteorology*, 53, 380–393, <https://doi.org/10.3402/tellusb.v53i4.16610>, URL <https://doi.org/10.3402/tellusb.v53i4.16610>, 2001.
- Naumann, K.-H.: COSIMA—a computer program simulating the dynamics of fractal aerosols, *Journal of Aerosol Science*, 34, 1371–1397, [https://doi.org/https://doi.org/10.1016/S0021-8502\(03\)00367-7](https://doi.org/https://doi.org/10.1016/S0021-8502(03)00367-7), URL <https://www.sciencedirect.com/science/article/pii/S0021850203003677>, intercomparison of Soot Measurement Techniques, 2003.
- Neale, R. B., Gettelman, A., Park, S., Conley, A. J., Kinnison, D., Marsh, D., Smith, A. K., Vitt, F., Morrison, H., Cameron-smith, P., Collins, W. D., Iacono, M. J., Easter, R. C., Liu, X., Taylor, M. A., chieh Chen, C., Lauritzen, P. H., Williamson, D. L., Garcia, R., francois Lamarque, J., Mills, M., Tilmes, S., Ghan, S. J., Rasch,

- P. J., and Meteorology, M.: Description of the NCAR Community Atmosphere Model (CAM 5.0), Tech. Note NCAR/TN-486+STR, Natl. Cent. for Atmos, in: 6of7 ZHAO ET AL.: AEROSOL FIE SIMULATED BY CAMS L08806, pp. 2009–038 451, 2010.
- Nebojsa Nakicenovic, J. A., Davis, G., de Vries, B., Fenhann, J., Gaffin, S., Gregory, K., Griebler, A., Jung, T. Y., Kram, T., Rovere, E. L. L., Michaelis, L., Mori, S., Morita, T., Pepper, W., Pitcher, H., Price, L., Riahi, K., Roehrl, A., Rogner, H.-H., Sankovski, A., Schlesinger, M., Shukla, P., Smith, S., Swart, R., van Rooijen, S., Victor, N., and Dadi, Z.: Special report on emissions scenarios, Cambridge University Press, Cambridge, 2000.
- Nenes, A. and Seinfeld, J. H.: Parameterization of cloud droplet formation in global climate models, *Journal of Geophysical Research: Atmospheres*, 108, <https://doi.org/https://doi.org/10.1029/2002JD002911>, URL <https://agupubs.onlinelibrary.wiley.com/doi/abs/10.1029/2002JD002911>, 2003.
- Oreskes, N., Shrader-Frechette, K., and Belitz, K.: Verification, Validation, and Confirmation of Numerical Models in the Earth Sciences, *Science*, 263, 641–646, <https://doi.org/10.1126/science.263.5147.641>, URL <https://www.science.org/doi/abs/10.1126/science.263.5147.641>, 1994.
- Peng, J. F., Hu, M., Wang, Z. B., Huang, X. F., Kumar, P., Wu, Z. J., Guo, S., Yue, D. L., Shang, D. J., Zheng, Z., and He, L. Y.: Submicron aerosols at thirteen diversified sites in China: size distribution, new particle formation and corresponding contribution to cloud condensation nuclei production, *Atmospheric Chemistry and Physics*, 14, 10249–10265, <https://doi.org/10.5194/acp-14-10249-2014>, URL <https://acp.copernicus.org/articles/14/10249/2014/>, 2014.
- Petters, M. D. and Kreidenweis, S. M.: A single parameter representation of hygroscopic growth and cloud condensation nucleus activity, *Atmospheric Chemistry and Physics*, 7, 1961–1971, <https://doi.org/10.5194/acp-7-1961-2007>, URL <https://acp.copernicus.org/articles/7/1961/2007/>, 2007.
- Pilinis, C., Pandis, S. N., and Seinfeld, J. H.: Sensitivity of direct climate forcing by atmospheric aerosols to aerosol size and composition, *Journal of Geophysical Research: Atmospheres*, 100, 18739–18754, <https://doi.org/https://doi.org/10.1029/95JD02119>, URL <https://agupubs.onlinelibrary.wiley.com/doi/abs/10.1029/95JD02119>, 1995.
- Proffit, M., Lapeyre, B., Buatois, B., Deng, X., Arnal, P., Gouzerh, F., Carrasco, D., and Hossaert-McKey, M.: Chemical signal is in the blend: bases of plant-pollinator encounter in a highly specialized interaction, *Scientific Reports*, 10, 10071, <https://doi.org/10.1038/s41598-020-66655-w>, URL <https://doi.org/10.1038/s41598-020-66655-w>, 2020.
- Pruppacher, H. R. and Klett, J. D.: *Microphysics of clouds and precipitation*, Kluwer Academic Publishers, Dordrecht, Boston, London, 1997.
- Rasch, P. J., Feitcher, J., Law, J., and et al.: A comparison of scavenging and deposition processes in global models: results from the WCRP Cambridge Workshop of 1995, vol. 52, *Tellus B*, <https://doi.org/10.1034/j.1600-0889.2000.00980.x>, 2000.

- Reifen, C. and Toumi, R.: Climate projections: Past performance no guarantee of future skill?, *Geophysical Research Letters*, 36, <https://doi.org/https://doi.org/10.1029/2009GL038082>, URL <https://agupubs.onlinelibrary.wiley.com/doi/abs/10.1029/2009GL038082>, 2009.
- Rinne, J., Bäck, J., and Hakola, H.: Biogenic volatile organic compound emissions from the Eurasian taiga: Current knowledge and future directions, *BOREAL ENVIRONMENT RESEARCH*, 14, 807–826, 2009.
- Runyon, J. B., Mescher, M. C., and Moraes, C. M. D.: Volatile Chemical Cues Guide Host Location and Host Selection by Parasitic Plants, *Science*, 313, 1964–1967, <https://doi.org/10.1126/science.1131371>, URL <https://www.science.org/doi/abs/10.1126/science.1131371>, 2006.
- Samset, B. H., Myhre, G., Schulz, M., Balkanski, Y., Bauer, S., Berntsen, T. K., Bian, H., Bellouin, N., Diehl, T., Easter, R. C., Ghan, S. J., Iversen, T., Kinne, S., Kirkevåg, A., Lamarque, J.-F., Lin, G., Liu, X., Penner, J. E., Seland, Ø., Skeie, R. B., Stier, P., Takemura, T., Tsigaridis, K., and Zhang, K.: Black carbon vertical profiles strongly affect its radiative forcing uncertainty, *Atmospheric Chemistry and Physics*, 13, 2423–2434, <https://doi.org/10.5194/acp-13-2423-2013>, 2013.
- Schultz, M. G., Stadtler, S., Schröder, S., Taraborrelli, D., Franco, B., Krefting, J., Henrot, A., Ferrachat, S., Lohmann, U., Neubauer, D., Siegenthaler-Le Drian, C., Wahl, S., Kokkola, H., Kühn, T., Rast, S., Schmidt, H., Stier, P., Kinnison, D., Tyndall, G. S., Orlando, J. J., and Wespes, C.: The chemistry–climate model ECHAM6.3-HAM2.3-MOZ1.0, *Geoscientific Model Development*, 11, 1695–1723, <https://doi.org/10.5194/gmd-11-1695-2018>, 2018.
- Seinfeld, J. H. and Pandis, S. N.: *Atmospheric Chemistry and Physics: From air pollution to climate change*, 3rd edition, John Wiley & Sons, Hoboken, New Jersey, 2016.
- Sharkey, T. D. and Yeh, S.: ISOPRENE EMISSION FROM PLANTS, *Annual Review of Plant Physiology and Plant Molecular Biology*, 52, 407–436, <https://doi.org/10.1146/annurev.arplant.52.1.407>, URL <https://doi.org/10.1146/annurev.arplant.52.1.407>, PMID: 11337404, 2001.
- Sharma, S., Ishizawa, M., Chan, D., Lavoué, D., Andrews, E., Eleftheriadis, K., and Maksyutov, S.: 16-year simulation of Arctic black carbon: Transport, source contribution, and sensitivity analysis on deposition, *Journal of Geophysical Research: Atmospheres*, 118, 943–964, <https://doi.org/10.1029/2012JD017774>, 2013.
- Shiraiwa, M., Pfrang, C., Koop, T., and Pöschl, U.: Kinetic multi-layer model of gas-particle interactions in aerosols and clouds (KM-GAP): linking condensation, evaporation and chemical reactions of organics, oxidants and water, *Atmospheric Chemistry and Physics*, 12, 2777–2794, <https://doi.org/10.5194/acp-12-2777-2012>, URL <https://acp.copernicus.org/articles/12/2777/2012/>, 2012.
- Shiraiwa, M., Ueda, K., Pozzer, A., Lammel, G., Kampf, C. J., Fushimi, A., Enami, S., Arangio, A. M., Fröhlich-Nowoisky, J., Fujitani, Y., Furuyama, A., Lakey, P. S. J., Lelieveld, J., Lucas, K., Morino, Y., Pöschl, U., Takahama, S., Takami, A.,

- Tong, H., Weber, B., Yoshino, A., and Sato, K.: Aerosol Health Effects from Molecular to Global Scales, *Environmental Science and Technology*, 51, 13 545–13 567, <https://doi.org/10.1021/acs.est.7b04417>, URL <https://doi.org/10.1021/acs.est.7b04417>, 2017.
- Simmons, A. J., Burridge, D. M., Jarraud, M., Girard, C., and Wergen, W.: The ECMWF medium-range prediction models development of the numerical formulations and the impact of increased resolution, *Meteorology and Atmospheric Physics*, 40, 28–60, <https://doi.org/10.1007/BF01027467>, 1989.
- Sporre, M. K., Blichner, S. M., Schrödner, R., Karset, I. H. H., Berntsen, T. K., van Noije, T., Bergman, T., O'Donnell, D., and Makkonen, R.: Large difference in aerosol radiative effects from BVOC-SOA treatment in three Earth system models, *Atmospheric Chemistry and Physics*, 20, 8953–8973, <https://doi.org/10.5194/acp-20-8953-2020>, URL <https://acp.copernicus.org/articles/20/8953/2020/>, 2020.
- Stadtler, S., Kühn, T., Schröder, S., Taraborrelli, D., Schultz, M. G., and Kokkola, H.: Isoprene-derived secondary organic aerosol in the global aerosol–chemistry–climate model ECHAM6.3.0–HAM2.3–MOZ1.0, *Geoscientific Model Development*, 11, 3235–3260, <https://doi.org/10.5194/gmd-11-3235-2018>, URL <https://gmd.copernicus.org/articles/11/3235/2018/>, 2018.
- Stevens, B., Giorgetta, M., Esch, M., Mauritsen, T., Crueger, T., Rast, S., Salzmann, M., Schmidt, H., Bader, J., Block, K., Brokopf, R., Fast, I., Kinne, S., Kornblueh, L., Lohmann, U., Pincus, R., Reichler, T., and Roeckner, E.: Atmospheric component of the MPI-M Earth System Model: ECHAM6, *Journal of Advances in Modeling Earth Systems*, 5, 146–172, <https://doi.org/10.1002/jame.20015>, 2013.
- Stier, P., Feichter, J., Kinne, S., Vignati, E., Wilson, J., Ganzeveld, L., Tegen, I., Werner, M., Balkanski, Y., Schulz, M., Boucher, O., Minikin, A., and Petzold, A.: The aerosol-climate model ECHAM5-HAM, *Atmospheric Chemistry and Physics*, 5, 1125–1156, <https://doi.org/10.5194/acp-5-1125-2005>, 2005.
- Tabazadeh, A., Djikaev, Y. S., and Reiss, H.: Surface crystallization of supercooled water in clouds, *National Academy of Sciences*, 99, 15 873–15 878, <https://doi.org/10.1073/pnas.252640699>, 2002.
- Taipale, D., Kerminen, V.-M., Ehn, M., Kulmala, M., and Niinemets, U.: Modelling the influence of biotic plant stress on atmospheric aerosol particle processes throughout a growing season, *Atmospheric Chemistry and Physics*, 21, 17 389–17 431, <https://doi.org/10.5194/acp-21-17389-2021>, URL <https://acp.copernicus.org/articles/21/17389/2021/>, 2021.
- Tegen, I., Neubauer, D., Ferrachat, S., Siegenthaler-Le Drian, C., Bey, I., Schutgens, N., Stier, P., Watson-Parris, D., Stanelle, T., Schmidt, H., Rast, S., Kokkola, H., Schultz, M., Schroeder, S., Daskalakis, N., Barthel, S., Heinold, B., and Lohmann, U.: The global aerosol–climate model ECHAM6.3–HAM2.3 – Part 1: Aerosol evaluation, *Geoscientific Model Development*, 12, 1643–1677, <https://doi.org/10.5194/gmd-12-1643-2019>, 2019.
- Thomson, W.: 4. On the Equilibrium of Vapour at a Curved Surface of Liquid, *Proceedings of the Royal Society of Edinburgh*, 7, 63–68, <https://doi.org/10.1017/S0370164600041729>, 1872.

- Topping, D., Barley, M., Bane, M. K., Higham, N., Aumont, B., Dingle, N., and McFiggans, G.: UManSysProp v1.0: an online and open-source facility for molecular property prediction and atmospheric aerosol calculations, *Geoscientific Model Development*, 9, 899–914, <https://doi.org/10.5194/gmd-9-899-2016>, URL <https://gmd.copernicus.org/articles/9/899/2016/>, 2016.
- Topping, D. L. and Bane, M.: *Introduction to Aerosol Modelling: From Theory to Code*, John Wiley & Sons, Hoboken, United States, 2022.
- Tsigaridis, K., Daskalakis, N., Kanakidou, M., Adams, P. J., Artaxo, P., Bahadur, R., Balkanski, Y., Bauer, S. E., Bellouin, N., Benedetti, A., Bergman, T., Berntsen, T. K., Beukes, J. P., Bian, H., Carslaw, K. S., Chin, M., Curci, G., Diehl, T., Easter, R. C., Ghan, S. J., Gong, S. L., Hodzic, A., Hoyle, C. R., Iversen, T., Jathar, S., Jimenez, J. L., Kaiser, J. W., Kirkevåg, A., Koch, D., Kokkola, H., Lee, Y. H., Lin, G., Liu, X., Luo, G., Ma, X., Mann, G. W., Mihalopoulos, N., Morcrette, J.-J., Müller, J.-F., Myhre, G., Myriokefalitakis, S., Ng, N. L., O'Donnell, D., Penner, J. E., Pozzoli, L., Pringle, K. J., Russell, L. M., Schulz, M., Sciare, J., Seland, Ø., Shindell, D. T., Sillman, S., Skeie, R. B., Spracklen, D., Stavrakou, T., Steenrod, S. D., Takemura, T., Tiitta, P., Tilmes, S., Tost, H., van Noije, T., van Zyl, P. G., von Salzen, K., Yu, F., Wang, Z., Wang, Z., Zaveri, R. A., Zhang, H., Zhang, K., Zhang, Q., and Zhang, X.: The AeroCom evaluation and intercomparison of organic aerosol in global models, *Atmospheric Chemistry and Physics*, 14, 10 845–10 895, <https://doi.org/10.5194/acp-14-10845-2014>, 2014.
- Twomey, S.: Pollution and the planetary albedo, *Atmospheric Environment* (1967), 8, 1251–1256, [https://doi.org/https://doi.org/10.1016/0004-6981\(74\)90004-3](https://doi.org/https://doi.org/10.1016/0004-6981(74)90004-3), URL <https://www.sciencedirect.com/science/article/pii/0004698174900043>, 1974.
- Twomey, S.: *Aerosol, clouds, and radiation.*, vol. 25A, *Atmospheric Environment*, The University of Arizona, Tucson, AZ 85721, U.S.A., 1991.
- Väisänen, O., Ruuskanen, A., Ylisirniö, A., Miettinen, P., Portin, H., Hao, L., Leskinen, A., Komppula, M., Romakkaniemi, S., Lehtinen, K. E. J., and Virtanen, A.: In-cloud measurements highlight the role of aerosol hygroscopicity in cloud droplet formation, *Atmospheric Chemistry and Physics*, 16, 10 385–10 398, <https://doi.org/10.5194/acp-16-10385-2016>, URL <https://acp.copernicus.org/articles/16/10385/2016/>, 2016.
- Vergara-Temprado, J., Holden, M. A., Orton, T. R., O'Sullivan, D., Umo, N. S., Browse, J., Reddington, C., Baeza-Romero, M. T., Jones, J. M., Lea-Langton, A., Williams, A., Carslaw, K. S., and Murray, B. J.: Is Black Carbon an Unimportant Ice-Nucleating Particle in Mixed-Phase Clouds?, *Journal of Geophysical Research: Atmospheres*, 123, 4273–4283, <https://doi.org/https://doi.org/10.1002/2017JD027831>, URL <https://agupubs.onlinelibrary.wiley.com/doi/abs/10.1002/2017JD027831>, 2018.
- Vignati, E., Wilson, J., and Stier, P.: M7: An efficient size-resolved aerosol microphysics module for large-scale aerosol transport models, *Journal of Geophysical Research: Atmospheres*, 109, <https://doi.org/https://doi.org/10.1029/2003JD004485>, URL <https://agupubs.onlinelibrary.wiley.com/doi/abs/10.1029/2003JD004485>, 2004.



- von Storch, H.: Climate models and modeling: an editorial essay, *WIREs Climate Change*, 1, 305–310, <https://doi.org/https://doi.org/10.1002/wcc.12>, URL <https://wires.onlinelibrary.wiley.com/doi/abs/10.1002/wcc.12>, 2010.
- Wang, M., Ghan, S., Easter, R., Ovchinnikov, M., Liu, X., Kassianov, E., Qian, Y., Gustafson Jr., W. I., Larson, V. E., Schanen, D. P., Khairoutdinov, M., and Morrison, H.: The multi-scale aerosol-climate model PNNL-MMF: model description and evaluation, *Geoscientific Model Development*, 4, 137–168, <https://doi.org/10.5194/gmd-4-137-2011>, URL <https://gmd.copernicus.org/articles/4/137/2011/>, 2011.
- Wang, P., Grover, S., and Pruppacher, H.: On the Effect of Electric Charges on the Scavenging of Aerosol Particles by Clouds and Small Raindrops, *Journal of Atmospheric Sciences*, 35, 1735–1743, [https://doi.org/10.1175/1520-0469\(1978\)035<1735:OTEOEC>2.0.CO;2](https://doi.org/10.1175/1520-0469(1978)035<1735:OTEOEC>2.0.CO;2), 1978.
- Watson-Parris, D., Schutgens, N., Cook, N., Kipling, Z., Kershaw, P., Gryspeerd, E., Lawrence, B., and Stier, P.: Community Intercomparison Suite (CIS) v1.4.0: a tool for intercomparing models and observations, *Geoscientific Model Development*, 9, 3093–3110, <https://doi.org/10.5194/gmd-9-3093-2016>, 2016.
- Watson-Parris, D., Schutgens, N., Reddington, C., Pringle, K. J., Liu, D., Allan, J. D., Coe, H., Carslaw, K. S., and Stier, P.: In situ constraints on the vertical distribution of global aerosol, *Atmospheric Chemistry and Physics*, 19, 11 765–11 790, <https://doi.org/10.5194/acp-19-11765-2019>, 2019.
- Wentzel, M., Gorzawski, H., Naumann, K.-H., Saathoff, H., and Weinbruch, S.: Transmission electron microscopical and aerosol dynamical characterization of soot aerosols, *Journal of Aerosol Science*, 34, 1347–1370, [https://doi.org/https://doi.org/10.1016/S0021-8502\(03\)00360-4](https://doi.org/https://doi.org/10.1016/S0021-8502(03)00360-4), URL <https://www.sciencedirect.com/science/article/pii/S0021850203003604>, intercomparison of Soot Measurement Techniques, 2003.
- Wexler, A. S. and Clegg, S. L.: Atmospheric aerosol models for systems including the ions H<sup>+</sup>, NH<sub>4</sub><sup>+</sup>, Na<sup>+</sup>, SO<sub>4</sub><sup>2-</sup>, NO<sub>3</sub><sup>-</sup>, Cl<sup>-</sup>, Br<sup>-</sup>, and H<sub>2</sub>O, *Journal of Geophysical Research: Atmospheres*, 107, ACH 14–1–ACH 14–14, <https://doi.org/https://doi.org/10.1029/2001JD000451>, URL <https://agupubs.onlinelibrary.wiley.com/doi/abs/10.1029/2001JD000451>, 2002.
- Wilson, J., Cuvelier, C., and Raes, F.: A modelling study of global mixed aerosol fields, *Journal of Geophysical Research*, 106, 34 081–34 108, <https://doi.org/10.1029/2000JD000198>, 2001.
- Wofsy, S., Afshar, S., Allen, H., Apel, E., Asher, E., Barletta, B., Bent, J., Bian, H., Biggs, B., Blake, D., Blake, N., Bourgeois, I., Brock, C., Brune, W., Budney, J., Bui, T., Butler, A., Campuzano-Jost, P., Chang, C., Chin, M., Commane, R., Correa, G., Crounse, J., Cullis, P., Daube, B., Day, D., Dean-Day, J., Dibb, J., Digangi, J., Diskin, G., Dollner, M., Elkins, J., Erdesz, F., Fiore, A., Flynn, C., Froyd, K., Gesler, D., Hall, S., Hanisco, T., Hannun, R., Hills, A., Hints, E., Hoffman, A., Hornbrook, R., Huey, L., Hughes, S., Jimenez, J., Johnson, B., Katich, J., Keeling, R., Kim, M., Kupc, A., Lait, L., Lamarque, J.-F., Liu, J., McKain, K., McLaughling, R., Meinardi, S., Miller, D., Montzka, S., Moore, F., Morgan, E., Murphy, D., Murray, L., Nault, B., Neuman, J., Newman, P., Nicely, J., Pan, X.,

- Paplawsky, W., Peischl, J., Prather, M., Price, D., Ray, E., Reeves, J., Richardson, M., Rollins, A., Rosenlof, K., Ryerson, T., Scheuer, E., Schill, G., Schroder, J., Schwarz, J., St.Clair, J., Steenrod, S., Stephens, B., Strode, S., Sweeney, C., Tanner, D., Teng, A., Thames, A., Thompson, C., Ullmann, K., Veres, P., Vizenor, N., Wagner, N., Watt, A., Weber, R., Weinzierl, B., Wennberg, P., Williamson, C., Wilson, J., Wolfe, G., Woods, C., and Zeng, L.: ATom: Merged Atmospheric Chemistry, Trace Gases, and Aerosols, <https://doi.org/10.3334/ORNLDAAAC/1581>, URL [https://daac.ornl.gov/cgi-bin/dsviewer.pl?ds\\_id=1581](https://daac.ornl.gov/cgi-bin/dsviewer.pl?ds_id=1581), 2018.
- Xu, W., Ovadnevaite, J., Fossun, K. N., Lin, C., Huang, R.-J., O'Dowd, C., and Ceburnis, D.: Aerosol hygroscopicity and its link to chemical composition in the coastal atmosphere of Mace Head: marine and continental air masses, *Atmospheric Chemistry and Physics*, 20, 3777–3791, <https://doi.org/10.5194/acp-20-3777-2020>, URL <https://acp.copernicus.org/articles/20/3777/2020/>, 2020.
- Yli-Juuti, T., Barsanti, K., Hildebrandt Ruiz, L., Kieloaho, A.-J., Makkonen, U., Petäjä, T., Ruuskanen, T., Kulmala, M., and Riipinen, I.: Model for acid-base chemistry in nanoparticle growth (MABNAG), *Atmospheric Chemistry and Physics*, 13, 12 507–12 524, <https://doi.org/10.5194/acp-13-12507-2013>, URL <https://acp.copernicus.org/articles/13/12507/2013/>, 2013.
- Yli-Juuti, T., Pajunoja, A., Tikkanen, O.-P., Buchholz, A., Faiola, C., Väisänen, O., Hao, L., Kari, E., Peräkylä, O., Garmash, O., Shiraiwa, M., Ehn, M., Lehtinen, K., and Virtanen, A.: Factors controlling the evaporation of secondary organic aerosol from  $\alpha$ -pinene ozonolysis, *Geophysical Research Letters*, 44, 2562–2570, <https://doi.org/https://doi.org/10.1002/2016GL072364>, URL <https://agupubs.onlinelibrary.wiley.com/doi/abs/10.1002/2016GL072364>, 2017.
- Yli-Juuti, T., Mielonen, T., Heikkinen, L., Arola, A., Ehn, M., Isokääntä, S., Keskinen, H.-M., Kulmala, M., Laakso, A., Lipponen, A., Luoma, K., Mikkonen, S., Nieminen, T., Paasonen, P., Petäjä, T., Romakkaniemi, S., Tonttila, J., Kokkola, H., and Virtanen, A.: Significance of the organic aerosol driven climate feedback in the boreal area, *Nature Communications*, 12, 5637, <https://doi.org/10.1038/s41467-021-25850-7>, URL <https://doi.org/10.1038/s41467-021-25850-7>, 2021.
- Zamora, M. L., Peng, J., Hu, M., Guo, S., Marrero-Ortiz, W., Shang, D., Zheng, J., Du, Z., Wu, Z., and Zhang, R.: Wintertime aerosol properties in Beijing, *Atmospheric Chemistry and Physics*, 19, 14 329–14 338, <https://doi.org/10.5194/acp-19-14329-2019>, URL <https://acp.copernicus.org/articles/19/14329/2019/>, 2019.
- Zhang, Q., Jimenez, J. L., Canagaratna, M. R., Allan, J. D., Coe, H., Ulbrich, I., Alfarra, M. R., Takami, A., Middlebrook, A. M., Sun, Y. L., Dzepina, K., Dunlea, E., Docherty, K., DeCarlo, P. F., Salcedo, D., Onasch, T., Jayne, J. T., Miyoshi, T., Shimonono, A., Hatakeyama, S., Takegawa, N., Kondo, Y., Schneider, J., Drewnick, F., Borrmann, S., Weimer, S., Demerjian, K., Williams, P., Bower, K., Bahreini, R., Cottrell, L., Griffin, R. J., Rautiainen, J., Sun, J. Y., Zhang, Y. M., and Worsnop, D. R.: Ubiquity and dominance of oxygenated species in organic aerosols in anthropogenically-influenced Northern Hemisphere midlatitudes, *Geophysical Research Letters*, 34, <https://doi.org/https://doi.org/>

10.1029/2007GL029979, URL <https://agupubs.onlinelibrary.wiley.com/doi/abs/10.1029/2007GL029979>, 2007.

Zhang, R., Khalizov, A., Wang, L., Hu, M., and Xu, W.: Nucleation and Growth of Nanoparticles in the Atmosphere, *Chemical Reviews*, 112, 1957–2011, <https://doi.org/10.1021/cr2001756>, URL <https://doi.org/10.1021/cr2001756>, 2012.

Zhao, D., Buchholz, A., Tillmann, R., Kleist, E., Wu, C., Rubach, F., Kiendler-Scharr, A., Rudich, Y., Wildt, J., and Mentel, T.: Environmental conditions regulate the impact of plants on cloud formation, *Nature Communications*, 8, 14 067, <https://doi.org/10.1038/ncomms14067>, 2017.

Zieger, P., Fierz-Schmidhauser, R., Weingartner, E., and Baltensperger, U.: Effects of relative humidity on aerosol light scattering: results from different European sites, *Atmospheric Chemistry and Physics*, 13, 10 609–10 631, <https://doi.org/10.5194/acp-13-10609-2013>, URL <https://acp.copernicus.org/articles/13/10609/2013/>, 2013.

Zieger, P., Väisänen, O., Corbin, J. C., Partridge, D. G., Bastelberger, S., Mousavi-Fard, M., Rosati, B., Gysel, M., Krieger, U. K., Leck, C., Nenes, A., Riipinen, I., Virtanen, A., and Salter, M. E.: Revising the hygroscopicity of inorganic sea salt particles, *Nature Communications*, 8, 2041–1723, <https://doi.org/10.1038/ncomms15883>, URL <https://doi.org/10.1038/ncomms15883>, 2017.

Zuend, A., Marcolli, C., Luo, B. P., and Peter, T.: A thermodynamic model of mixed organic-inorganic aerosols to predict activity coefficients, *Atmospheric Chemistry and Physics*, 8, 4559–4593, <https://doi.org/10.5194/acp-8-4559-2008>, URL <https://acp.copernicus.org/articles/8/4559/2008/>, 2008.

Zuend, A., Marcolli, C., Peter, T., and Seinfeld, J. H.: Computation of liquid-liquid equilibria and phase stabilities: implications for RH-dependent gas/particle partitioning of organic-inorganic aerosols, *Atmospheric Chemistry and Physics*, 10, 7795–7820, <https://doi.org/10.5194/acp-10-7795-2010>, URL <https://acp.copernicus.org/articles/10/7795/2010/>, 2010.

## Paper I

O.-P. Tikkanen, O. Väisänen, L. Hao, E. Holopainen, H. Wang, K. E. J. Lehtinen, A. Virtanen and T. Yli-Juuti  
“Hygroscopicity of dimethylaminium-, sulfate-, and ammonium-containing nanoparticles”  
*Aerosol Science and Technology* **52**,  
pp. 971–983, 2018.

Reproduced under a license obtained from the publisher.






## Hygroscopicity of dimethylaminium-, sulfate-, and ammonium-containing nanoparticles

Olli-Pekka Tikkanen, Olli Väisänen, Liqing Hao, Eemeli Holopainen, Hao Wang, Kari E. J. Lehtinen, Annele Virtanen & Taina Yli-Juuti

To cite this article: Olli-Pekka Tikkanen, Olli Väisänen, Liqing Hao, Eemeli Holopainen, Hao Wang, Kari E. J. Lehtinen, Annele Virtanen & Taina Yli-Juuti (2018) Hygroscopicity of dimethylaminium-, sulfate-, and ammonium-containing nanoparticles, *Aerosol Science and Technology*, 52:9, 971-983, DOI: [10.1080/02786826.2018.1484071](https://doi.org/10.1080/02786826.2018.1484071)

To link to this article: <https://doi.org/10.1080/02786826.2018.1484071>




View supplementary material 



Published online: 17 Aug 2018.



Submit your article to this journal 



Article views: 628



View related articles 



View Crossmark data 



Citing articles: 3 View citing articles 



## Hygroscopicity of dimethylaminium-, sulfate-, and ammonium-containing nanoparticles

Olli-Pekka Tikkanen<sup>a,\*</sup> , Olli Väisänen<sup>a,\*</sup> , Liqing Hao<sup>a</sup>, Eemeli Holopainen<sup>a</sup>, Hao Wang<sup>a,b,c</sup>, Kari E. J. Lehtinen<sup>a,d</sup>, Annele Virtanen<sup>a</sup>, and Taina Yli-Juuti<sup>a</sup>

<sup>a</sup>Department of Applied Physics, University of Eastern Finland, Kuopio, Finland; <sup>b</sup>Institute for Environmental and Climate Research, Jinan University, Guangzhou, China; <sup>c</sup>JNU-QUT Joint Laboratory for Air Quality Science and Management, Jinan University, Guangzhou, China; <sup>d</sup>Atmospheric Research Centre of Eastern Finland, Finnish Meteorological Institute, Kuopio, Finland

### ABSTRACT

Dimethylamine (DMA) and sulfuric acid (SA) are the important constituents of atmospheric aerosols. To accurately predict the behavior of DMA-containing aerosol systems, exact thermodynamic models are needed. The applicability of these models needs to be tested carefully in different experimental settings to continuously validate and improve their performance. In this work, the Extended Aerosol Inorganics Model (E-AIM) was used to simulate the hygroscopicity of aerosol particles generated from five different aqueous DMA-SA solutions. The applicability of the model was tested in the 10–200 nm size range and from DMA-SA molar ratios ranging from 1:3 to 2:1. The aerosol hygroscopic growth at 0–80% RH was determined with two tandem differential mobility analyzers, and the composition of the generated particles was measured with the Aerosol Mass Spectrometer (AMS), which revealed that the particles contained also ammonium. The model accurately captured the hygroscopicity for particles larger than 80 nm. With particles smaller than 80 nm, the model underestimated the hygroscopicity in all the studied experimental conditions. An increase in hygroscopicity parameter  $\kappa$  with decreasing particle size implied a plausible base evaporation in the experimental setup, which in turn may have affected the modeled hygroscopicity as the composition of the smallest particles may have differed from the AMS measurements. Coupling E-AIM to a dynamic evaporation model, however, could not produce compositions whose modeled hygroscopic behavior would match the measured hygroscopic growth at smaller sizes. Our results, therefore, suggest that DMA thermodynamics are not modeled correctly in E-AIM or there exists uncertainty in the physicochemical parameters.

### ARTICLE HISTORY

Received 6 March 2018  
Accepted 16 May 2018

### EDITOR

Kihong Park

## 1. Introduction

Amines are organic derivatives of ammonia, in which one or more alkyl groups are bonded to nitrogen. Being present in the atmosphere, both in gaseous phase as well as in particulate matter, they comprise a vast range of different species originating from various anthropogenic and natural sources (VandenBoer et al. 2011; Ge et al. 2011a; Youn et al. 2015). The most abundant atmospheric amines are relatively low-weight aliphatic amines such as methylamine (MMA), dimethylamine (DMA), and trimethylamine (TMA). These compounds have relatively high equilibrium vapor pressures, and thus, they are highly volatile by nature. However, because they are also strong bases, they can undergo

prompt neutralization reactions to form organic salts in the presence of organic or inorganic acids.

There exist a few experimental studies on amines in the atmospheric aerosol particles. In the early 2000s, Mäkelä et al. (2001) reported an enrichment of particulate DMA during new particle formation (NPF) events and subsequent particle growth. Later, Smith et al. (2010) measured the composition of freshly nucleated particles at urban and rural sites and detected a significant presence of aminium ions. In addition to experimental atmospheric studies, several theoretical findings have highlighted amines and especially DMA as an important stabilizing base for sulfuric acid ( $\text{H}_2\text{SO}_4$ ; SA) and sulfuric acid water clusters

**CONTACT** Olli-Pekka Tikkanen [op.tikkanen@uef.fi](mailto:op.tikkanen@uef.fi); Olli Väisänen [olli.vaisanen@uef.fi](mailto:olli.vaisanen@uef.fi) Department of Applied Physics, University of Eastern Finland, P.O. Box 1627, Kuopio 70211, Finland.

\*O.-P. Tikkanen and O. Väisänen contributed equally to this work and should be considered as co-first authors.

Color versions of one or more of the figures in the article can be found online at [www.tandfonline.com/uast](http://www.tandfonline.com/uast).

Supplemental data for this article can be accessed on the publisher's website.

© 2018 American Association for Aerosol Research

(Kurtén et al. 2008; Loukonen et al. 2010; Erupe et al. 2011). These theoretical results are backed by the experimental chamber and laboratory measurements (Almeida et al. 2013; Jen et al. 2014; Kürten et al. 2014). For example, Almeida et al. (2013) observed that only a few pptv of gaseous DMA could enhance the nucleation rates by several orders of magnitudes compared to the presence of pure ammonia ( $\text{NH}_3$ ).

Overall, these results suggest that amines may contribute significantly to nanoparticle formation and growth, and therefore, should be taken into account in models to better understand the subsequent impact on climate. A proper model description of amines, however, requires information about their thermodynamic properties (Bergman et al. 2015). Furthermore, to mimic the atmospheric behavior of amines, the computational models need to be carefully validated against laboratory measurements where the physicochemical parameters can be monitored. To our knowledge, the only thermodynamic model that includes the amines, their dissolution, and subsequent protonation, is the Extended Aerosol Inorganics Model (E-AIM; Clegg et al. 1998; Wexler and Clegg 2002). E-AIM is a thermodynamic phase equilibrium model, which allows the water activity calculations for real solutions. However, in E-AIM, interactions between ammonium ions and other possible compounds are modeled similar to ammonium ( $\text{NH}_4$ ) and the validity of this approach is not fully confirmed. Earlier results (Clegg et al. 2013; Chu et al. 2015; Sauerwein et al. 2015) have shown conflicting results for E-AIM's ability to model the amine-SA- $\text{H}_2\text{O}$  system. Further, the existing model-measurement comparisons are performed against bulk solutions or particles whose Kelvin effect can be neglected leaving uncertainty in the applicability of the model to particles with high surface-to-volume ratio.

One way to assess the model performance is to compare its ability to predict the hygroscopicity against laboratory measurements. Hygroscopicity is an important parameter describing the particles ability to absorb or adsorb moisture from the surrounding air. Thus, hygroscopicity essentially effects the particle optical properties (Zieger et al. 2013, 2017), as well as their ability to act as cloud condensation nuclei (CCN) under certain atmospheric conditions (Väisänen et al. 2016). On the other hand, condensation of water onto pre-existing particles also creates a pathway for aqueous phase processes that can further alter their chemical composition (McNeill 2015

and references therein). Last, knowing the hygroscopicity of various individual aerosol constituents, allows the possibility to estimate the aerosol chemical composition indirectly through measurements of CCN activity or hygroscopic growth.

In this work, we have atomized particles from DMA-SA- $\text{H}_2\text{O}$  solutions and determined their detailed composition in the size range greater than or equal to 70 nm by means of aerosol mass spectrometry. The measured composition of the produced dimethylammonium (DMAH), sulfate ( $\text{SO}_4$ ), and ammonium ( $\text{NH}_4$ ) containing particles is combined with measured and modeled hygroscopic growth in the 10–200 nm size range. This allows us to evaluate the performance of the studied model (E-AIM) directly with larger particles, but also, enables the possibility to inspect the applicability of the model to smaller particles whose curvature has an effect on the water partitioning.

## 2. Methods

### 2.1. Solution preparation and particle generation

Five different DMA-SA- $\text{H}_2\text{O}$  solutions were prepared by mixing stoichiometric amounts of aqueous DMA (40 wt. %, Sigma Aldrich, 426458) and sulfuric acid (Sigma Aldrich, 258105) with deionized water (MilliQ,  $\sim 18.2 \text{ M}\Omega\text{cm}$ ). The prepared solutions had an approximate molar DMA-SA ratio (nominal DMA:SA) of 1:3, 1:2, 1:1, 3:2, and 2:1, and a total salt concentration of  $\sim 3 \text{ wt. \%}$ . A polydisperse aerosol population was generated by atomizing the aqueous DMA-SA solutions with a conventional aerosol nebulizer (nebulizing section of Topas ATM 226, operated with clean pressurized air). The outgoing aerosol flow was diluted with clean air to reach a total flow of 18 lpm and relative humidity (RH) around 14%. Furthermore, the sample line leading to aerosol instrumentation was equipped with a custom-made silica gel diffusion drier to decrease the inlet RH down to  $\sim 3\%$ .

### 2.2. HTDMA measurements

The hygroscopicity of 10–200 nm particles was measured with two separate hygroscopic tandem differential mobility analyzers (HTDMA). Briefly, HTDMA is a measurement device that consists of two differential mobility analyzers, a humidifier, and a condensation particle counter (CPC). The first differential mobility analyzer (DMA1) is operated to select a nearly monodisperse particle population from the polydisperse sample flow. The monodisperse dry aerosol is then exposed to certain RH, and the resulting changes in



particle size are determined with another differential mobility analyzer (DMA2) followed by a CPC. Consequently, HTDMA allows the determination of the hygroscopic growth factor

$$GF(RH) = \frac{D_p(RH)}{D_{p,dry}}, \quad (1)$$

where  $D_p$  is the mean diameter of the humidified aerosol and  $D_{p,dry}$  is the selected dry particle size. Furthermore, the measured GF can be translated into a hygroscopicity parameter  $\kappa$  according to

$$\kappa(RH, D_{p,dry}) = \frac{(GF^3 - 1) \exp\left(\frac{4M_w\sigma_w}{RT\rho_w D_{p,dry} GF}\right)}{RH} - GF^3 + 1 \quad (2)$$

where  $M_w$ ,  $\sigma_w$ , and  $\rho_w$  are the molar mass, surface tension, and density of water,  $T$  the ambient temperature and  $R$  the universal gas constant (Petters and Kreidenweis 2007).

The hygroscopic growth of 10, 15, 20, and 25 nm particles was measured with a nano-HTDMA (Keskinen et al. 2011; Kim et al. 2016). In this setup, two nano-differential mobility analyzers (TSI Inc., model 3085) are operated in an open-loop configuration (sample flow 1 lpm, sheath/excess flow 10 lpm). Besides humidifying the monodisperse aerosol, the sheath air inside the DMA2 was pre-humidified to the desired RH in order to secure stable conditions through particle sizing. The RH of the aerosol flow and the sheath air were monitored with two capacitive RH sensors (Vaisala HMP110), and the RH of the humid excess flow was measured with a dew point meter (EdgeTech, model DewMaster). After passing the DMA2, the particles were counted with a water-based condensation particle counter (TSI Inc., model 3785).

The hygroscopic growth of 50, 80, 130, and 200 nm particles was measured with an HTDMA previously described by Väisänen et al. (2016). This instrument is built around two 28 cm long Vienna-type differential mobility analyzers operated in a closed-loop arrangement (sample flow 1 lpm, sheath/excess flow 6 lpm). In other words, the sheath air slowly reaches the equilibrium with the passing sample flow in terms of RH and temperature. The RH of the humid sample flow was monitored continuously with one Vaisala HMP110 sensor and the excess flow RH downstream of DMA2 was measured with an EdgeTech dew point meter. The particles were counted with a TSI model 3010 CPC.

The HTDMA data were calibrated against dry GF offsets by determining the dry particle diameter  $D_{p,dry}$  from ammonium sulfate measurements. These dry

size scans were performed at low RH ( $RH < 10\%$ ) before each experiment. In addition, the measured GFs were corrected to target RHs of 40, 60, and 80% by assuming a constant hygroscopicity parameter  $\kappa$  within a narrow humidity range ( $\pm 1.5\%$ ) around the target value. Taking into account all the components affecting the particle sizing, the maximum instrumental uncertainties associated with the measured GFs were  $\pm 2.3\%$  ( $D_{p,dry} \leq 25$  nm) and  $\pm 4.7\%$  ( $D_{p,dry} \geq 50$  nm), as estimated through error propagation.

### 2.3. Particle composition

The chemical composition of the generated particles was measured with an Aerodyne High-Resolution Time-of-Flight Aerosol Mass Spectrometer (hereafter referred to as AMS). In summary, AMS is capable of measuring the non-refractory composition of sub-micrometer aerosol particles by applying thermal vaporization and electron impact (EI) ionization. General principles of AMS measurements, calibrations, modes of operation, and data processing have been described comprehensively in previous literature (Jayne et al. 2000; DeCarlo et al. 2006; Canagaratna et al. 2007).

In this study, the AMS was sampling through an additional differential mobility analyzer (sheath flow 7 lpm) that was set to generate almost monodisperse particle size distributions with a mean mobility diameter around 70 or 150 nm. The decision to size-select 70 nm particles over smaller sizes was made to guarantee high enough mass concentrations, and thus, sufficient ion signals for reliable composition calculations. Although the particle number size distribution passing the differential mobility analyzer was dominated by singly charged particles, it is also worth noting that the contribution of multiply charged particles was somewhat stronger in terms of particle mass (approximately 50%), shifting the mean vacuum aerodynamic diameter observed by mass-based AMS towards larger sizes.

The collected AMS data were analyzed using standard ToF-AMS data analysis toolkits (SQUIRREL v1.57I and PIKA V1.16I). The V-mode mass spectra were processed in PIKA to determine the ion mass concentrations. The majority of the produced salts in the mixed DMA-SA solutions are dimethylammonium sulfate ( $(C_2H_8N)_2SO_4$ ) or dimethylammonium bisulfate ( $C_2H_8NHSO_4$ ) depending on the molar ratios of DMA to SA. The rest should be the unreacted precursors such as either pure DMA or SA. All these salts undergo severe fragmentations in AMS. Hence, in the

data analysis, the family ions  $C_xH_yN$  and  $C_xH_y$ , where  $x \leq 2$  and  $y \leq 8$ , were integrated to quantitate the mass concentrations of dimethylammonium ions. For the ion  $CH_2N$  ( $m/z$  28), the ion peak coincides with an intensive  $N_2$  signal in the mass spectrum, making its accurate quantification difficult from the high-resolution ion fitting. Thus, its concentration was approximated as 30% of  $C_2H_6N$  ( $m/z$  44) based on the known DMA mass spectrum in the NIST database (NIST, 2018). The mass concentrations of sulfate ions were determined by the AMS default “fragmentation table” method (Allan et al. 2004). Besides, the ammonia ( $NH_3$ ) either from the water or from the ambient air could lead to the formation of ammonium sulfate and ammonium bisulfate in the mixed solutions (Section 3.1). Therefore, the concentrations of ammonium were also determined. For mass concentration calculations, the default relative ionization efficiency (RIE; Canagaratna et al. 2007) values 1.2 and 3.75 were applied for sulfate and ammonium, respectively. For dimethylammonium, we determined a RIE value of 1.84 assuming that the most basic measured composition had a molar total base-to-sulfate ratio of two.

## 2.4. Thermodynamic modelling

The Extended Aerosols Inorganics Model (E-AIM) is a thermodynamic equilibrium model for non-ideal solutions, which calculates the equilibrium partitioning of bulk chemical system by minimizing the Gibbs free energy of the system (Clegg et al. 1998; Wexler and Clegg 2002). E-AIM takes into account the particulate phase acid-base chemistry and is currently to our knowledge the only available model, which has an accurate description of amine thermodynamics relevant for atmospheric aerosols included from the work of Ge et al. (2011b).

In this work, the system consists of DMA, ammonia, and sulfuric acid in the liquid phase and water, which is the only compound allowed to equilibrate between the gas and the liquid phase. In systems where the condensed phase contains ionic and neutral organic compounds, the water activity is calculated as a product of the activities of the water-ion solution and water-organic solution (Clegg et al. 2001). This approximation allows the activity coefficients of neutral organics and ions to be calculated using different methods. We used UNIFAC (UNIQUAC Functional-group Activity Coefficients; Fredenslund et al. 1975; Hansen et al. 1991) to calculate the activity coefficient of neutral dimethylamine.

The modeled GF was calculated according to the Equation (1). The wet particle diameter  $D_{p,wet}$  was calculated by

$$D_{p,wet} = \left( \frac{6m_{p,wet}}{\pi\rho_{p,wet}} \right)^{1/3} \quad (3)$$

where  $m_{p,wet}$  is the mass of the particle, which is in equilibrium with respect to gaseous water and  $\rho_{p,wet}$  is the density of the same particle. The mass of the wet particle is calculated from the known dry diameter  $D_{p,dry}$  and the molar amounts of DMAH and  $NH_4$  in the dry and wet particles. The GF calculation requires also the densities of the dry and wet particles for which we used the values obtained from the E-AIM (Clegg and Wexler 2011a,b; Clegg et al. 2013) at RH = 1% and at the investigated RH, respectively.

The modeled system in the E-AIM is a bulk chemical system with a flat surface separating the phases. Since the size of the nanoparticles studied is of the order of tens of nanometers, the curvature of the particles must also be taken into account. The equilibrium vapor pressure of water over a curved surface of a particle can be calculated from the Kelvin equation

$$p_{eq,w} = p_{eq} \exp \left( \frac{4\sigma M_w}{RT\rho D_p} \right) \quad (4)$$

where  $p_{eq,w}$  and  $p_{eq}$  are the equilibrium vapor pressures of water over the curved and flat surfaces, respectively,  $\sigma$  is the surface tension,  $M_w$  is the molar mass of water ( $M_w = 18.02 \text{ g mol}^{-1}$ ),  $\rho$  is the liquid phase density, and  $D_p$  is the diameter of the particle. The exponential term is also known as the Kelvin term.

In practice, this means that the relative humidity in which the E-AIM simulations are performed must be multiplied by the Kelvin term in order for the model results to be comparable with the measurements, i.e.,

$$RH = RH_{E-AIM} \exp \left( \frac{4\sigma M_w}{RT\rho D_p} \right), \quad (5)$$

where RH is the relative humidity, which corresponds to the values set in the humidifier during nanoparticle hygroscopicity measurements, and  $RH_{E-AIM}$  is the relative humidity in which the E-AIM calculations are performed. For the liquid phase density  $\rho$  and surface tension  $\sigma$ , values obtained from the E-AIM output were used.

## 3. Results

### 3.1. Composition of generated particles

Table 1 shows the measured particle composition corresponding to each DMA-SA solution and the two

**Table 1.** The measured particle composition for each DMA-SA solution and for the two AMS sizes. The error intervals are calculated taking into account the AMS measured mass concentrations and their standard deviations during each measurement.

Nominal DMA:SA	AMS	
	DMAH:SO <sub>4</sub> :NH <sub>4</sub>	
	70 nm	150 nm
2:1	(1.20 ± 0.17):1:(0.74 ± 0.09)	(1.40 ± 0.17):1:(0.60 ± 0.03)
3:2	(1.09 ± 0.12):1:(0.77 ± 0.05)	(1.24 ± 0.15):1:(0.65 ± 0.05)
1:1	(0.96 ± 0.27):1:(0.79 ± 0.11)	(1.08 ± 0.24):1:(0.62 ± 0.06)
1:2	(0.57 ± 0.08):1:(0.91 ± 0.09)	(0.59 ± 0.09):1:(0.77 ± 0.10)
1:3	(0.57 ± 0.06):1:(0.74 ± 0.08)	(0.55 ± 0.06):1:(0.57 ± 0.03)

pre-selected sizes for AMS. In addition, the tabulated values are associated with error estimates calculated assuming that the uncertainty of the measured mass concentrations is equal to  $\pm 1$  standard deviation over each measurement. The most important remark concerns the fact that along with DMAH and SO<sub>4</sub> ions, AMS also detected substantial amounts of NH<sub>4</sub> (43–160% by moles of DMAH). Furthermore, the increasing contribution of NH<sub>4</sub> as a function of solution acidity implies that the observed ammonium most likely originates from a contamination. One possible explanation could be that the MilliQ water used as a solvent contained small amounts of dissolved NH<sub>3</sub>, which then had protonated and partitioned into acidic particles as NH<sub>4</sub>. On the other hand, the particles were exposed to air of unknown composition during particle generation and size-selection prior to AMS, which also may have served as an external contaminant. Hereafter, the presence of NH<sub>4</sub> has been taken into account in all model results and analyses.

Overall, we observe differences between the two AMS sizes with 150 nm particles showing generally higher DMAH molar fractions than 70 nm particles. By contrast, NH<sub>4</sub> always shows higher molar ratios at 70 nm size, and therefore, suppresses the size-dependent differences in overall acidity. Moreover, the AMS measured DMAH:SO<sub>4</sub> ratios differ from those expected based on the stoichiometric DMA-SA mixing ratios. The solutions with nominal DMA:SA of 1:1 and 1:2 produced particles with comparable DMAH:SO<sub>4</sub> molar ratios. However, for solutions with nominal DMA:SA of 2:1 and 3:2, the AMS measured compositions were pronounced towards higher sulfate content, whereas the particles with nominal DMA:SA = 1:3 contained more DMAH than expected.

### 3.2. Hygroscopicity of DMAH-SO<sub>4</sub>-NH<sub>4</sub> particles

Figures 1, 2, and 3 show the measured hygroscopic growth factors of 10, 20, 80, and 200 nm particles

corresponding to the three different compositions (nominal DMA:SA = 2:1, 1:1, and 1:2) as a function of RH. The result for 15, 25, 80, and 130 nm particle sizes and the two remaining DMA-SA solutions follow the same patterns and are presented in the online [supplementary information](#). In addition to measurements, each figure plots the results from two sets of model runs. The solid black curve shows the E-AIM derived GFs for the case where the nominal DMA-SA ratio has been used as an input composition. Meanwhile, the dashed black curve shows the model results corresponding to the AMS composition (70 nm AMS composition for  $D_{p,dry} \leq 80$  nm and 150 nm AMS composition for  $D_{p,dry} \geq 130$  nm) and therefore, includes the effect of ammonium. Hereafter, these two model runs are referred to as E-AIM<sub>nominal</sub> and E-AIM<sub>AMS</sub>, respectively. In addition, both of these curves are combined with shaded areas whose upper bounds are determined by neglecting the Kelvin effect in model calculations.

Both the modelled and measured GFs show a clear monotonous increase as a function of RH at every particle size and given composition. The model results with nominal DMA-SA composition also show a clear composition dependence with elevated GFs being associated with increased acidity. Nonetheless, when using the AMS composition, the modeled GFs become generally smaller and the variation between different compositions is considerably suppressed. This observation is not surprising keeping in mind that the measured particle composition experienced relatively less variation compared to nominal solutions.

Overall, the measured GFs at  $D_{p,dry} \geq 80$  nm tend to agree relatively well with those derived from E-AIM<sub>AMS</sub>. An especially good agreement is achieved at nominal DMA:SA of 1:3, 1:2, 1:1, and 3:2, whereas in the most basic case (nominal DMA:SA = 2:1), both E-AIM<sub>nominal</sub> and E-AIM<sub>AMS</sub> slightly underestimate the hygroscopic growth. The measured GFs start to differ considerably from the model results when particle size decreases to sub-80 nm size range. Specifically, the E-AIM<sub>AMS</sub> falls clearly below the measured GFs at every composition, and with the three most basic solutions, the same goes for E-AIM<sub>nominal</sub>. This holds even if the Kelvin term is neglected in model calculations, indicating that the discrepancy cannot be solely explained by the uncertainty related to adopted values of liquid phase density and surface tension. Furthermore, as the contribution of Kelvin effect becomes progressively important with increasing particle curvature, the modelled GFs show a clear decreasing trend with decreasing particle size.

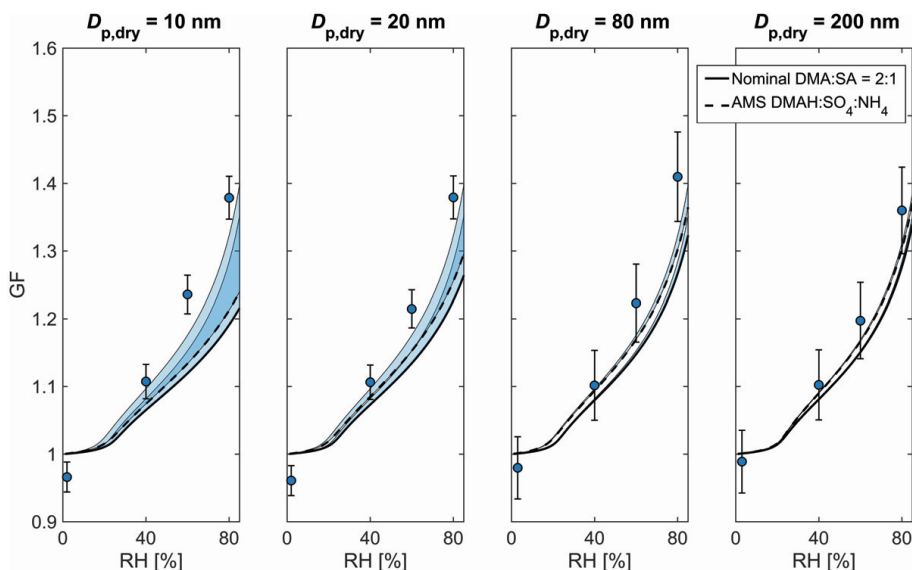


**Figure 1.** A comparison between the measured and modelled hygroscopic growth factors (GF) at different relative humidities (RH) for nominal DMA:SA = 2:1. Shown are the results for 10, 20, 80, and 200 nm particle sizes. The measurement data are plotted as markers, and the solid and dashed lines correspond to E-AIM simulations with nominal and AMS measured compositions, respectively. The shaded areas above the model curves illustrate the sensitivity to the Kelvin term and the whiskers show the maximum instrumental uncertainty.

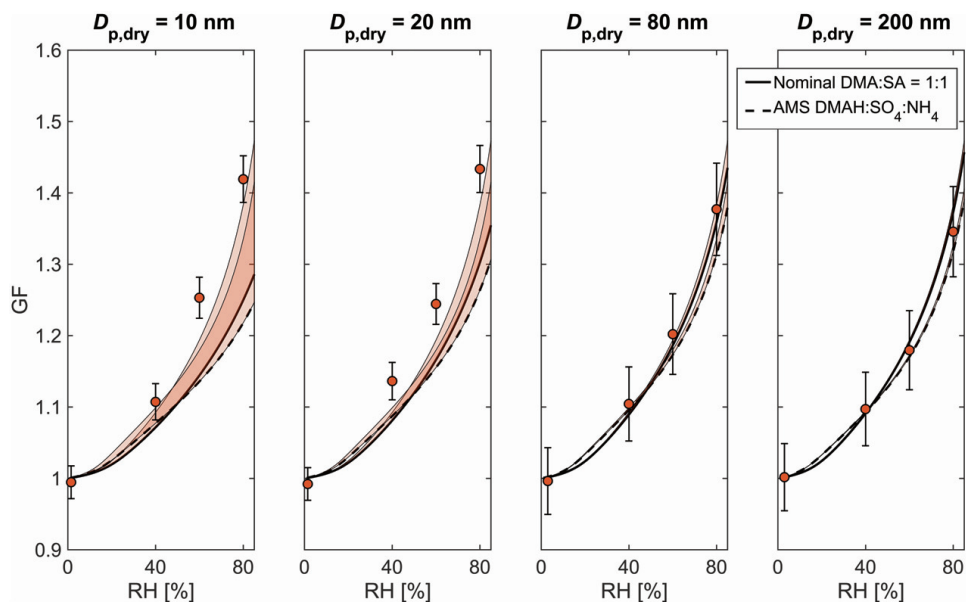


**Figure 2.** A comparison between the measured and modelled hygroscopic growth factors (GF) at different relative humidities (RH) for nominal DMA:SA = 1:1. Shown are the results for 10, 20, 80, and 200 nm particle sizes. The measurement data are plotted as markers, and the solid and dashed lines correspond to E-AIM simulations with nominal and AMS measured compositions, respectively. The shaded areas above the model curves illustrate the sensitivity to the Kelvin term and the whiskers show the maximum instrumental uncertainty.

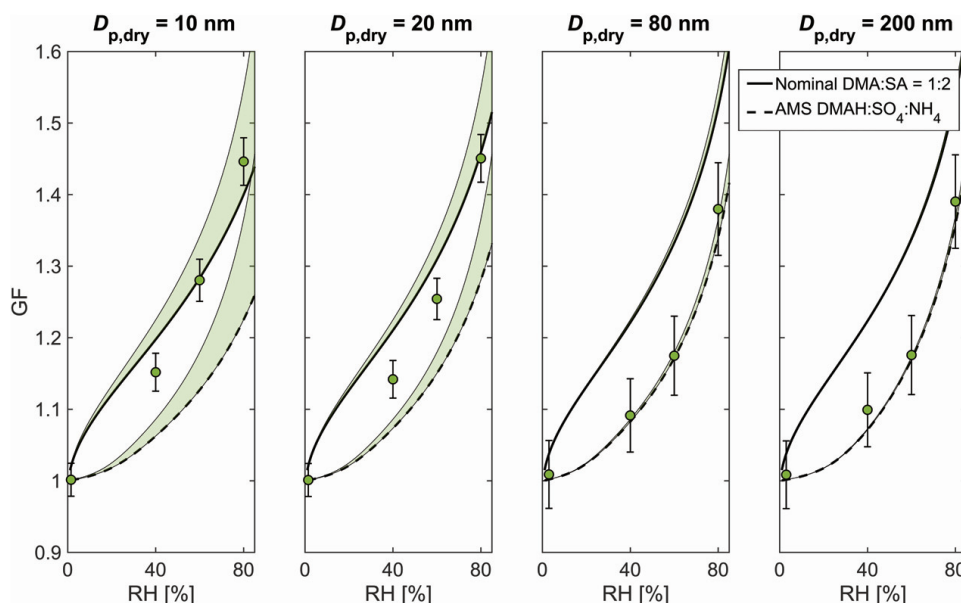


**Figure 3.** A comparison between the measured and modelled hygroscopic growth factors (GF) at different relative humidities (RH) for nominal DMA:SA = 1:2. Shown are the results for 10, 20, 80, and 200 nm particle sizes. The measurement data are plotted as markers, and the solid and dashed lines correspond to E-AIM simulations with nominal and AMS measured compositions, respectively. The shaded areas above the model curves illustrate the sensitivity to the Kelvin term and the whiskers show the maximum instrumental uncertainty.

Such behavior, however, is not apparent in the measurement data. Instead, in some cases, the GFs measured at 10–25 nm are even larger than those measured at 50–200 nm. The inverse size-trend is also illustrated in Figure 4 showing the size-dependence of hygroscopicity parameter  $\kappa$  (calculated at RH = 80%) for each of the five solutions. Interestingly, the  $\kappa$  values can increase up to 100% when particle size decreases from 200 nm down to 10 nm, highlighting the uncertainty that is related to predicting the chemical composition of the smallest atomized particles.

### 3.3. Evaporation of the bases in the sampling lines

The above results leave open the possibility that the basic compounds could have evaporated from the smallest particles after their generation, producing particles whose modeled hygroscopic growth factors would match well against the measured values. In order to assess how the chemical composition of the smallest atomized particles could change during particle sampling, a set of simulations describing the gas-particle partitioning of DMA, SA, and  $\text{NH}_3$ , was performed.

The simulations were performed with the MABNAG model (Yli-Juuti et al. 2013; Ahlm et al. 2016) modified to solve the gas-particle partitioning of DMA and  $\text{NH}_3$  dynamically. The initial composition of the particles was determined according to the 70 nm AMS measurements, and the gas phase was assumed to be infinitely diluted with respect to DMA, SA and  $\text{NH}_3$ . The simulations were performed for 10 nm particle size, meaning that the simulated conditions were favorable for the maximum possible evaporation. Hence, the evaporation time was set to 10 s, which was an upper-limit estimate for the maximum time that the particles spend in sampling lines before entering the aerosol instruments. The evaporation was also modeled in both high (RH = 80%) and low relative humidity (RH = 4%) to account for any non-ideal behavior of the compounds. The low RH case yielded higher evaporation, and thus, the compositions from these model runs were selected for further analysis. It is to be noted, however, that the MABNAG model uses E-AIM to calculate the activity of each compound. This means that any uncertainties in the amine thermodynamics are also included in the MABNAG simulations, and thus, the resulting MABNAG composition is a qualitative estimate.

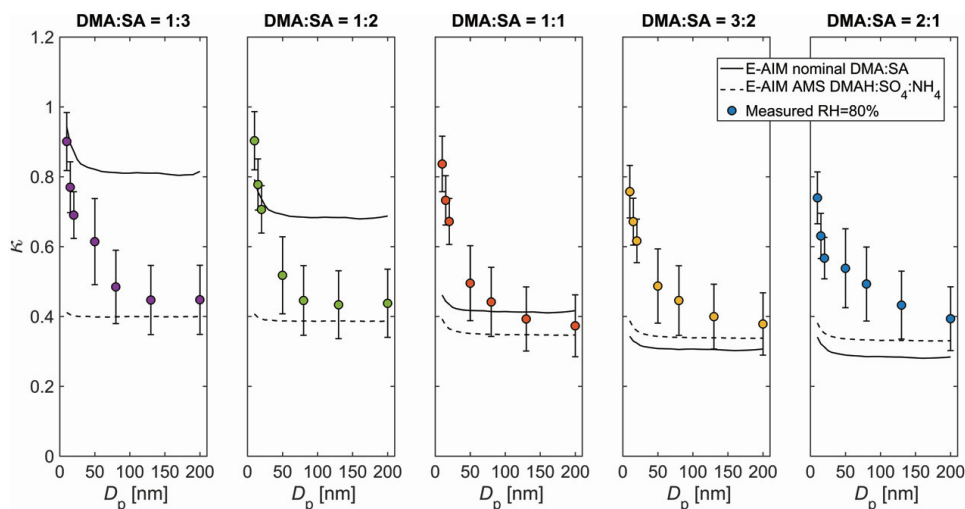


**Figure 4.** Measured and modelled hygroscopicity parameter  $\kappa$  versus particle size at RH = 80%. The measurement data are plotted as markers, and the solid and dashed lines correspond to E-AIM simulations with nominal and AMS measured compositions, respectively. The whiskers illustrate the maximum instrumental uncertainty.

The molar DMAH:SO<sub>4</sub>:NH<sub>4</sub> ratios after 10 s evaporation can be found in Table 2. The MABNAG simulations yielded DMAH evaporation between 0 and 7% and NH<sub>4</sub> evaporation between 8 and 77%, both increasing with initial basicity. To illustrate the possible impacts on hygroscopic growth, Figure 5 plots the measured GFs ( $D_{p,dry} = 10$  nm) together with two simulated hygroscopicity curves. The dashed line corresponds to the composition determined with MABNAG, and the solid line corresponds to the composition that best fits the measured GFs assuming the AMS measured DMAH-NH<sub>4</sub> ratio. Overall, the relative difference between the two simulated curves remains between 10 and 12% at RH = 80%, and the hygroscopicity calculated with the MABNAG composition produces clearly smaller water uptake than what is measured in all the studied cases. In order for the E-AIM to capture the measured hygroscopicity, the nanoparticles should be significantly more acidic than what can be obtained through the MABNAG simulations. In fact, even increasing the equilibrium vapor pressure of every compound by two orders of magnitude does not yield fast enough evaporation for the final MABNAG composition to describe the measured hygroscopic growth (Figure S8).

#### 4. Discussion

The aim of our study was to quantify the hygroscopicity of dimethylamine and sulfuric acid containing

**Table 2.** Results from E-AIM and MABNAG simulations. The second column lists the compositions resulting in the best agreement between the measured and modelled hygroscopic growth factors. The third and fourth columns show the final compositions of 10 nm particles as obtained through MABNAG simulations.

Nominal DMA:SA	E-AIM best fit DMAH:SO <sub>4</sub> :NH <sub>4</sub> 10 nm	MABNAG DMAH:SO <sub>4</sub> :NH <sub>4</sub> 10 nm; RH = 4%	MABNAG DMAH:SO <sub>4</sub> :NH <sub>4</sub> 10 nm; RH = 4%; $100 \times p_{eq}$
2:1	0.45:1:0.17	1.12:1:0.17	1.07:1:0.07
3:2	0.41:1:0.29	1.03:1:0.25	1.00:1:0.13
1:1	0.37:1:0.30	0.92:1:0.35	0.90:1:0.22
1:2	0.23:1:0.37	0.56:1:0.69	0.56:1:0.54
1:3	0.26:1:0.34	0.57:1:0.68	0.56:1:0.54

particles in the sub-200 nm size range. According to AMS measurements, the composition of the generated particles differed from the composition of the prepared DMA-SA solutions. More precisely, we observed differences in relative contribution of dimethylammonium and sulfate, but also substantial fractions of ammonium originating most likely from an external contamination. First of all, particles with nominal DMA:SA of 2:1 and 3:2 contained less DMAH than expected and the difference increased with decreasing particle size. This could be explained by DMA evaporation that can occur both during the preparation of DMA-SA solutions as well as during particle sampling and drying (Chu et al. 2015; Sauerwein et al. 2015). For example, Chu et al. (2015) observed that in the case of dimethylammonium sulfate (DMAS) particles with initial ammonium-to-sulfate ratio



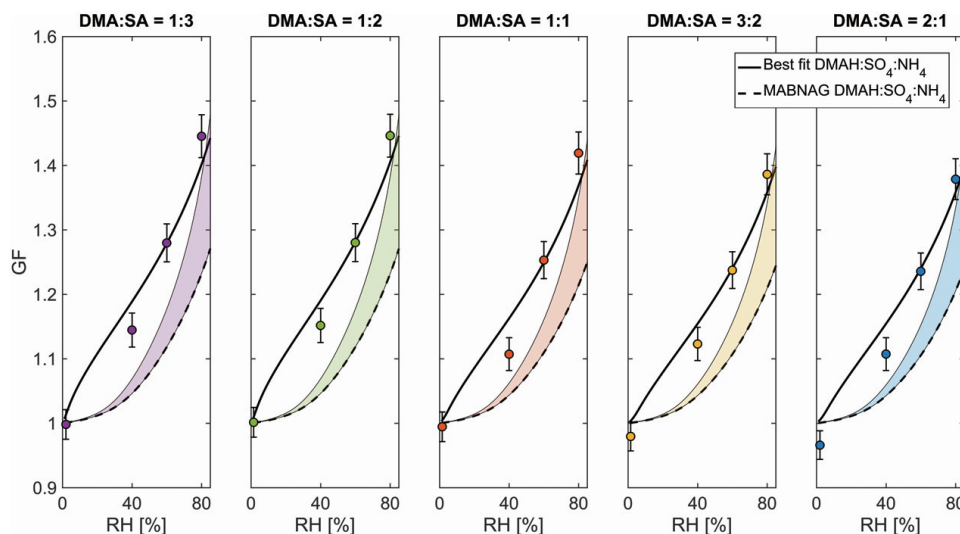


**Figure 5.** Modelled hygroscopic growth factors (GF) after 10 s evaporation and comparison to measurements at  $D_{p,dry} = 10$  nm. The measurement data are plotted as markers, the dashed lines show the E-AIM results corresponding to the compositions obtained through MABNAG simulations, and the solid lines correspond to the E-AIM simulations with compositions that best fit the measurement data. The shaded areas illustrate the model sensitivity to the Kelvin term and the whiskers show the maximum instrumental uncertainty. The composition that best fits the measurement data is determined assuming that the molar DMAH: $\text{NH}_4$  ratio is equal to that of 70 nm AMS measurements.

of 1.9 were not stable, but instead, equilibrated towards 1.5 during dehumidification. These trends are comparable to our observations at nominal DMA:SA of 2:1 and 3:2.

For nominal DMA:SA = 1:3, we observe an excess amount of DMAH. Part of this excess DMAH could be attributed to impurities in bulk SA that was used in preparation of DMA-SA solutions. While the solutions were prepared assuming 100 wt. % SA, for example Sauerwein et al. (2015) found an SA concentration of approximately 95.5 wt. %, which is close to the lower range of nominal purity (95–98 wt. %). However, such a difference in bulk SA concentration would not be sufficient to explain the observed shift towards higher DMAH content. Although Ouyang et al. (2015) suggested that SA could dissociate from DMA-SA nano-clusters, it is highly unlikely, that this could happen in the particles that are larger by almost two orders of magnitude. Nevertheless, we cannot rule out a possibility that DMA that conceivably evaporates from the smallest particles could re-condense onto larger ones and thus, serve as an internal source of DMAH.

In addition, we detected ammonium in the generated particles in all studied cases. This highlights the importance of careful chemical characterization of the measured particles. To our knowledge, this is the first

study where the composition of laboratory generated DMA-SA particles has been determined with an AMS. For example, Sauerwein et al. (2015) and Chu et al. (2015) determined the ammonium-to-sulfate ratios of the studied droplets with an ion chromatograph (IC), whereas Chan and Chan (2013) inferred the ammonium-sulfate composition indirectly from the mass change in EDB (Electrodynamic Balance). In contrast, Qiu and Zhang (2012) and Rovelli et al. (2017) did not present any direct nor indirect measurements on particle composition, but rather relied on accurate and validated solution preparation method. In addition, it is yet unclear, whether Sauerwein et al. (2015) and Chu et al. (2015) considered the possible presence of ammonium in their IC analysis, or if it simply was not observed. According to our results, this can be a crucial factor, since ammonium can strongly affect the hygroscopic properties of the studied mixtures, especially with high particulate sulfuric acid content.

Due to the presence of ammonium, direct comparison between our hygroscopicity measurements and previously reported values can be rather challenging. However, in many studies, the measured values are combined with modeled hygroscopicity curves calculated with E-AIM enabling a possibility for indirect comparison. Both Clegg et al. (2013) and Rovelli et al.

(2017) found a good agreement between the modeled and measured GFs of DMAS. In their studies, the particle sizes were large enough that the curvature effect could be disregarded. On the contrary, Chu et al. (2015) found that for 3:2 aminium-to-sulfate molar ratio, the water-to-solute molar ratios were lower than what was calculated with E-AIM. In addition, Sauerwein et al. (2015) observed higher hygroscopicity of DMAS particles than what was measured with HTDMA by Qiu and Zhang (2012) and modeled by Clegg et al. (2013). Similarly, we found that for nominal DMA:SA = 2:1, the model slightly underestimates the measured water uptake, especially at elevated RH.

Chu et al. (2015) speculated that the difference between the HTDMA results by Qiu and Zhang (2012) and other methods such as Raman spectrometry and water activity measurements (Chu et al. 2015; Sauerwein et al. 2015), could be partially attributed to the fact that Qiu and Zhang (2012) assumed GFs equal to unity at 12% RH. As Chu et al. (2015) further pointed out, aminium sulfate particles can be hydrous at 10% RH and even lower. This can eventually lead to underestimation of hygroscopic growth at elevated RH. In our measurements, as described in Section 2.2, the initial dry size selection was always performed at RH < 3%, in which the water content of the particles was assumedly imperceptible.

Sauerwein et al. (2015) also showed that the water uptake increases when the molar dimethylaminium-to-sulfate ratio increases from bisulfate towards sulfate composition. A similar behavior was also observed by Chu et al. (2015) when they compared the hygroscopicities of equilibrated and non-equilibrated DMAS particles. In our case, the GFs measured at 80% RH and  $D_{p,dry} \geq 50$  nm tend to slightly increase when the nominal DMA:SA shifts from 1:1 towards 2:1. Nevertheless, this observation contradicts with the composition-dependence predicted by E-AIM, but also, with measurements conducted at smaller particle sizes.

Along with the reversed composition-dependence, the measured GFs deviate significantly from the modeled values when the particle size decreases. According to the size-dependence of hygroscopicity parameter  $\kappa$ , it is also evident that the generated particles have a size-dependent composition. We would like to highlight that the smallest and largest particles were always generated from the same solution with constant atomizer settings, and thus, the only possible explanation for the size-dependent composition is the evaporation of compounds during the generation and subsequent dilution. Another factor that could potentially result in size-dependent composition would be the presence of

surface-active organic impurities, whose relative concentrations tend to increase with decreasing particle size. Nonetheless, as the hygroscopicity of organic compounds is generally clearly lower than that of SA, the increasing concentration of surface-active organic impurities with decreasing particle size cannot explain the simultaneous increase in GFs.

More precisely, it is likely that due to the increased particle surface-to-volume ratio, DMA and  $\text{NH}_3$  evaporate from the smallest particles resulting in higher acidity than what is measured with the AMS. This makes the direct comparison of the measured and modeled values indeed more challenging. A significant DMA and  $\text{NH}_3$  evaporation would be required for the E-AIM to be able to predict the measured GFs (Table 2). Such a base evaporation, in the timescales of a measurement, could not be produced when the E-AIM was coupled with a dynamic evaporation model (MABNAG). In fact, such evaporation was not possible even if the equilibrium vapor pressures of the compounds were 100-fold to the simulations presented in Figure 5 (see also Figure S8). In general, these results are in line with observations by Ahlm et al. (2016) who studied the evolution of a nucleating SA-DMA- $\text{H}_2\text{O}$  system in the CLOUD (Cosmics Leaving Outdoor Droplets) chamber. The authors used the MABNAG model to simulate the composition of the freshly formed particles and observed that the modeled base-to-SA ratios were generally much higher than what was directly measured with TDCIMS (Lawler et al. 2016) and indirectly inferred from nano-HTDMA data (Kim et al. 2016) using the E-AIM. In addition, they found a size-dependent disagreement between the two latter methods with E-AIM derived compositions showing much stronger increase in aerosol basicity with increasing particle size. All things considered, given that the evaporation of the bases in our simulations was not fast enough to produce DMAH: $\text{SO}_4$ : $\text{NH}_4$  ratios whose hygroscopic behavior would be similar to the measured values, it is likely that E-AIM inaccurately describes the amine thermodynamics in the DMA-SA- $\text{NH}_3$ - $\text{H}_2\text{O}$  systems.

One interesting remark concerns the fact that we observed significant changes in particle size when running the HTDMAs in low-humidity conditions. At smaller sizes, the most acidic particles lie approximately around GF = 1, whereas the measurements with nominal DMA:SA of 3:2 and 2:1 fall below unity by up to 4%. At larger sizes, the most DMA-containing particles have GF < 1, whereas the most acidic particles, which also contain comparably less evaporable amines, already start to take up water at  $\sim 3\%$



RH. Because both of the instruments were calibrated for dry size offsets before each measurement, it is very unlikely that the observed variation would occur due to changes in instrumental performance. In some studies (Zardini et al. 2008), GFs smaller than one have been associated with structural rearrangements due to condensation of water onto non-spherical or branch-shaped particles. Again, this explanation would be unlikely as the “dry” RH in our measurements always remained below  $\sim 3\%$ , and thus, the particles may have experienced only small humidity gradients between the dry size selection and DMA2. Moreover, Qiu and Zhang (2012) used an aerosol particle mass analyzer (APM) to assess the morphology of aminium sulfate particles. They observed that the particles were uniform and compact, and close to spherical in shape. However, one cannot rule out the possibility that some of the volatile material evaporates from the particle phase after the initial dry size selection. This could be the case, especially within the nano-HTDMA, where the sample flow is diluted with clean pressurized air inside the differential mobility analyzers. Nevertheless, it is yet unclear whether the possible evaporation occurs regardless of RH or if it only concerns the measurements at low humidity.

## 5. Summary and conclusions

In this study, the hygroscopic growth factors of 10–200 nm DMAH-SO<sub>4</sub>-NH<sub>4</sub> particles were measured with five different molar compositions. These values were then compared to those predicted with a state-of-the-art thermodynamic equilibrium model (E-AIM). The model was able to predict the hygroscopic growth well for the largest particles with diameters of 80 nm or above. Nevertheless, the agreement between the measurements and the model became poorer with decreasing particle size, and the model tended to underestimate the hygroscopic growth, especially when the particles were towards more basic composition.

The analysis on hygroscopicity parameter  $\kappa$  indicated that the small sub-50 nm particles were more acidic than the 70 and 150 nm particles measured with an AMS, even if they were generated from the same solution. Moreover, in order for the E-AIM to capture their measured hygroscopic growth, the particulate base-to-sulfate ratios should have been around 0.6–0.7:1, suggesting a possible base evaporation in the sampling lines. However, even with conditions favorable for maximum base evaporation, E-AIM coupled with a dynamic evaporation model (MABNAG) was not able to produce compositions that would be even

close to those required. This suggests that E-AIM may not be able to describe the amine thermodynamics accurately in DMA-SA-NH<sub>3</sub>-H<sub>2</sub>O system.

One possible reason for this discrepancy is that in E-AIM dimethylammonium is assumed to interact with water similar to ammonium. In this case, it would mean that the dimethylammonium-water interaction deviates more from the ideal solution behavior than the ammonium-water interaction. The results show that there are still knowledge gaps regarding the thermodynamics of DMA-SA-NH<sub>3</sub>-H<sub>2</sub>O system. Furthermore, the results highlight that the future studies must be accompanied by careful and thorough chemical characterization in order to diminish the uncertainties caused by instability of the studied compounds as well as temporal and size-dependent evolution of chemical composition.

## Funding

This work was supported by the Academy of Finland [grant nos. 307331, 299544] and the University of Eastern Finland Doctoral Program in Environmental Physics, Health and Biology.

## ORCID

Olli-Pekka Tikkanen  <http://orcid.org/0000-0003-1729-6349>

Olli Väisänen  <http://orcid.org/0000-0001-5674-7013>

## References

- Ahlm, L., Yli-Juuti, T., Schobesberger, S., Praplan, A. P., Kim, J., Tikkanen, O. P., Lawler, M. J., Smith, J. N., Tröstl, J., Navarro, J. C. A., Baltensperger, U., Bianchi, F., Donahue, N. M., Duplissy, J., Franchin, A., Jokinen, T., Keskinen, H., Kirkby, J., Kürten, A., Laaksonen, A., Lehtipalo, K., Petäjä, T., Riccobono, F., Rissanen, M. P., Rondo, L., Schallhart, S., Simon, M., Winkler, P. M., Worsnop, D. R., Virtanen, A., and Riipinen, I. (2016). Modeling the Thermodynamics and Kinetics of Sulfuric Acid-Dimethylamine-Water Nanoparticle Growth in the CLOUD Chamber. *Aerosol. Sci. Tech.*, 50:1017–1032.
- Allan, J. D., Delia, A. E., Coe, H., Bower, K. N., Alfarra, M. R., Jimenez, J. L., Middlebrook, A. M., Drewnick, F., Onasch, T. B., Canagaratna, M. R., Jayne, J. T., and Worsnop, D. R. (2004). A Generalised Method for the Extraction of Chemically Resolved Mass Spectra from Aerodyne Aerosol Mass Spectrometer Data. *J. Aerosol. Sci.*, 35:909–922.
- Almeida, J., Schobesberger, S., Kürten, A., Ortega, I. K., Kupiainen-Määttä, O., Praplan, A. P., Adamov, A., Amorim, A., Bianchi, F., Breitenlechner, M., David, A., Dommen, J., Donahue, N. M., Downard, A., Dunne, E., Duplissy, J., Ehrhart, S., Flagan, R. C., Franchin, A., Guida, R., Hakala, J., Hansel, A., Heinritzi, M., Henschel,

- H., Jokinen, T., Junninen, H., Kajos, M., Kangasluoma, J., Keskinen, H., Kupc, A., Kurtén, T., Kvashin, A. N., Laaksonen, A., Lehtipalo, K., Leiminger, M., Leppä, J., Loukonen, V., Makhmutov, V., Mathot, S., McGrath, M. J., Nieminen, T., Olenius, T., Onnela, A., Petäjä, T., Riccobono, F., Riipinen, I., Rissanen, M., Rondo, L., Ruuskanen, T., Santos, F. D., Sarnela, N., Schallhart, S., Schnitzhofer, R., Seinfeld, J. H., Simon, M., Sipilä, M., Stozhkov, Y., Stratmann, F., Tome, A., Tröstl, J., Tsagkogeorgas, G., Vaattovaara, P., Viisanen, Y., Virtanen, A., Vrtala, A., Wagner, P. E., Weingartner, E., Wex, H., Williamson, C., Wimmer, D., Ye, P. L., Yli-Juuti, T., Carslaw, K. S., Kulmala, M., Curtius, J., Baltensperger, U., Worsnop, D. R., Vehkamäki, H., and Kirkby, J. (2013). Molecular Understanding of Sulphuric Acid-Amine Particle Nucleation in the Atmosphere. *Nature*, 502:359.
- Bergman, T., Laaksonen, A., Korhonen, H., Malila, J., Dunne, E. M., Mielonen, T., Lehtinen, K. E. J., Kühn, T., Arola, A., and Kokkola, H. (2015). Geographical and Diurnal Features of Amine-Enhanced Boundary Layer Nucleation. *J. Geophys. Res. Atmos.*, 120:9606–9624.
- Canagaratna, M. R., Jayne, J. T., Jimenez, J. L., Allan, J. D., Alfarra, M. R., Zhang, Q., Onasch, T. B., Drewnick, F., Coe, H., Middlebrook, A., Delia, A., Williams, L. R., Trimborn, A. M., Northway, M. J., DeCarlo, P. F., Kolb, C. E., Davidovits, P., and Worsnop, D. R. (2007). Chemical and Microphysical Characterization of Ambient Aerosols with the Aerodyne Aerosol Mass Spectrometer. *Mass Spectrom. Rev.*, 26:185–222.
- Chan, L. P., and Chan, C. K. (2013). Role of the Aerosol Phase State in Ammonia/Amines Exchange Reactions. *Environ. Sci. Technol.*, 47:5755–5762.
- Chu, Y. X., Sauerwein, M., and Chan, C. K. (2015). Hygroscopic and Phase Transition Properties of Alkyl Ammonium Sulfates at Low Relative Humidities. *Phys. Chem. Chem. Phys.*, 17:19789–19796.
- Clegg, S. L., and Wexler, A. S. (2011a). Densities and Apparent Molar Volumes of Atmospherically Important Electrolyte Solutions. 1. The Solutes  $\text{H}_2\text{SO}_4$ ,  $\text{HNO}_3$ ,  $\text{HCl}$ ,  $\text{Na}_2\text{SO}_4$ ,  $\text{NaNO}_3$ ,  $\text{NaCl}$ ,  $(\text{NH}_4)_2\text{SO}_4$ ,  $\text{NH}_4\text{NO}_3$ , and  $\text{NH}_4\text{Cl}$  from 0 to 50 °C, Including Extrapolations to Very Low Temperature and to the Pure Liquid State, and  $\text{NaHSO}_4$ ,  $\text{NaOH}$ , and  $\text{NH}_3$  at 25 °C. *J. Phys. Chem. A*, 115:3393–3460.
- Clegg, S. L., and Wexler, A. S. (2011b). Densities and Apparent Molar Volumes of Atmospherically Important Electrolyte Solutions. 2. The Systems  $\text{H}^+ - \text{HSO}_4^- - \text{SO}_4^{2-} - \text{H}_2\text{O}$  from 0 to 3 Mol  $\text{Kg}^{-1}$  as a Function of Temperature and  $\text{H}^+ - \text{NH}_4^+ - \text{HSO}_4^- - \text{SO}_4^{2-} - \text{H}_2\text{O}$  from 0 to 6 Mol  $\text{Kg}^{-1}$  at 25 °C Using a Pitzer Ion Interaction Model, and  $\text{NH}_4\text{HSO}_4 - \text{H}_2\text{O}$  and  $(\text{NH}_4)_3\text{H}(\text{SO}_4)_2 - \text{H}_2\text{O}$  over the Entire Concentration Range. *J. Phys. Chem. A*, 115:3461–3474.
- Clegg, S. L., Brimblecombe, P., and Wexler, A. S. (1998). Thermodynamic Model of the System  $\text{H}^+ - \text{NH}_4^+ - \text{SO}_4^{2-} - \text{NO}_3^- - \text{H}_2\text{O}$  at Tropospheric Temperatures. *J. Phys. Chem. A*, 102:2155–2154.
- Clegg, S. L., Qiu, C., and Zhang, R. Y. (2013). The Deliquescence Behaviour, Solubilities, and Densities of Aqueous Solutions of Five Methyl- and Ethyl-Aminium Sulphate Salts. *Atmos. Environ.*, 73:145–158.
- Clegg, S. L., Seinfeld, J. H., and Brimblecombe, P. (2001). Thermodynamic Modelling of Aqueous Aerosols Containing Electrolytes and Dissolved Organic Compounds. *J. Aerosol Sci.*, 32:713–738.
- DeCarlo, P. F., Kimmel, J. R., Trimborn, A., Northway, M. J., Jayne, J. T., Aiken, A. C., Gonin, M., Fuhrer, K., Horvath, T., Docherty, K. S., Worsnop, D. R., and Jimenez, J. L. (2006). Field-Deployable, High-Resolution, Time-of-Flight Aerosol Mass Spectrometer. *Anal. Chem.*, 78:8281–8289.
- Erupe, M. E., Viggiano, A. A., and Lee, S. H. (2011). The Effect of Trimethylamine on Atmospheric Nucleation Involving  $\text{H}_2\text{SO}_4$ . *Atmos. Chem. Phys.*, 11:4767–4775.
- Fredenslund, A., Jones, R. L., and Prausnitz, J. M. (1975). Group-Contribution Estimation of Activity-Coefficients in Nonideal Liquid-Mixtures. *Aiche J.*, 21:1086–1099.
- Ge, X. L., Wexler, A. S., and Clegg, S. L. (2011a). Atmospheric Amines - Part I. A Review. *Atmos. Environ.*, 45:524–546.
- Ge, X. L., Wexler, A. S., and Clegg, S. L. (2011b). Atmospheric Amines - Part II. Thermodynamic Properties and Gas/Particle Partitioning. *Atmos. Environ.*, 45:561–577.
- Hansen, H. K., Rasmussen, P., Fredenslund, A., Schiller, M., and Gmehling, J. (1991). Vapor-Liquid-Equilibria by Unifac Group Contribution.5. Revision and Extension. *Ind. Eng. Chem. Res.*, 30:2352–2355.
- Jayne, J. T., Leard, D. C., Zhang, X. F., Davidovits, P., Smith, K. A., Kolb, C. E., and Worsnop, D. R. (2000). Development of an Aerosol Mass Spectrometer for Size and Composition Analysis of Submicron Particles. *Aerosol. Sci. Tech.*, 33:49–70.
- Jen, C. N., McMurtry, P. H., and Hanson, D. R. (2014). Stabilization of Sulfuric Acid Dimers by Ammonia, Methylamine, Dimethylamine, and Trimethylamine. *J. Geophys. Res. Atmos.*, 119:7502–7514.
- Keskinen, H., Romakkaniemi, S., Jaatinen, A., Miettinen, P., Saukko, E., Joutsensaari, J., Mäkelä, J. M., Virtanen, A., Smith, J. N., and Laaksonen, A. (2011). On-Line Characterization of Morphology and Water Adsorption on Fumed Silica Nanoparticles. *Aerosol. Sci. Tech.*, 45:1441–1447.
- Kim, J., Ahlm, L., Yli-Juuti, T., Lawler, M., Keskinen, H., Tröstl, J., Schobesberger, S., Duplissy, J., Amorim, A., Bianchi, F., Donahue, N. M., Flagan, R. C., Hakala, J., Heinritzi, M., Jokinen, T., Kürten, A., Laaksonen, A., Lehtipalo, K., Miettinen, P., Petäjä, T., Rissanen, M. P., Rondo, L., Sengupta, K., Simon, M., Tome, A., Williamson, C., Wimmer, D., Winkler, P. M., Ehrhart, S., Ye, P., Kirkby, J., Curtius, J., Baltensperger, U., Kulmala, M., Lehtinen, K. E. J., Smith, J. N., Riipinen, I., and Virtanen, A. (2016). Hygroscopicity of Nanoparticles Produced from Homogeneous Nucleation in the CLOUD Experiments. *Atmos. Chem. Phys.*, 16:293–304.
- Kürten, A., Jokinen, T., Simon, M., Sipilä, M., Sarnela, N., Junninen, H., Adamov, A., Almeida, J., Amorim, A., Bianchi, F., Breitenlechner, M., Dommen, J., Donahue, N. M., Duplissy, J., Ehrhart, S., Flagan, R. C., Franchin, A., Hakala, J., Hansel, A., Heinritzi, M., Hutterli, M., Kangasluoma, J., Kirkby, J., Laaksonen, A., Lehtipalo, K., Leiminger, M., Makhmutov, V., Mathot, S., Onnela, A., Petäjä, T., Praplan, A. P., Riccobono, F., Rissanen, M. P.,

- Rondo, L., Schobesberger, S., Seinfeld, J. H., Steiner, G., Tome, A., Tröstl, J., Winkler, P. M., Williamson, C., Wimmer, D., Ye, P. L., Baltensperger, U., Carslaw, K. S., Kulmala, M., Worsnop, D. R., and Curtius, J. (2014). Neutral Molecular Cluster Formation of Sulfuric Acid-Dimethylamine Observed in Real Time under Atmospheric Conditions. *Proc. Natl. Acad. Sci. USA*, 111:15019–15024.
- Kurtén, T., Loukonen, V., Vehkamäki, H., and Kulmala, M. (2008). Amines are Likely to Enhance Neutral and Ion-Induced Sulfuric Acid-Water Nucleation in the Atmosphere More Effectively than Ammonia. *Atmos. Chem. Phys.*, 8:4095–4103.
- Lawler, M. J., Winkler, P. M., Kim, J., Ahlm, L., Tröstl, J., Praplan, A. P., Schobesberger, S., Kürten, A., Kirkby, J., Bianchi, F., Duplissy, J., Hansel, A., Jokinen, T., Keskinen, H., Lehtipalo, K., Leiminger, M., Petäjä, T., Rissanen, M., Rondo, L., Simon, M., Sipilä, M., Williamson, C., Wimmer, D., Riipinen, I., Virtanen, A., and Smith, J. N. (2016). Unexpectedly Acidic Nanoparticles Formed in Dimethylamine-Ammonia-Sulfuric-Acid Nucleation Experiments at CLOUD. *Atmos. Chem. Phys.*, 16:13601–13618.
- Loukonen, V., Kurtén, T., Ortega, I. K., Vehkamäki, H., Padua, A. A. H., Sellegri, K., and Kulmala, M. (2010). Enhancing Effect of Dimethylamine in Sulfuric Acid Nucleation in the Presence of Water - a Computational Study. *Atmos. Chem. Phys.*, 10:4961–4974.
- Mäkelä, J. M., Yli-Koivisto, S., Hiltunen, V., Seidl, W., Swietlicki, E., Teinilä, K., Sillanpää, M., Koponen, I. K., Paatero, J., Rosman, K., and Hämeri, K. (2001). Chemical Composition of Aerosol during Particle Formation Events in Boreal Forest. *Tellus B*, 53:380–393.
- McNeill, V. F. (2015). Aqueous Organic Chemistry in the Atmosphere: Sources and Chemical Processing of Organic Aerosols. *Environ. Sci. Technol.*, 49:1237–1244.
- Ouyang, H., He, S. Q., Larriba-Andaluz, C., and Hogan, C. J. (2015). IMS-MS and IMS-IMS Investigation of the Structure and Stability of Dimethylamine-Sulfuric Acid Nanoclusters. *J. Phys. Chem. A*, 119:2026–2036.
- Petters, M. D., and Kreidenweis, S. M. (2007). A Single Parameter Representation of Hygroscopic Growth and Cloud Condensation Nucleus Activity. *Atmos. Chem. Phys.*, 7:1961–1971.
- Qiu, C., and Zhang, R. Y. (2012). Physiochemical Properties of Alkylammonium Sulfates: Hygroscopicity, Thermostability, and Density. *Environ. Sci. Technol.*, 46:4474–4480.
- Rovelli, G., Miles, R. E. H., Reid, J. P., and Clegg, S. L. (2017). Hygroscopic Properties of Ammonium Sulfate Aerosols. *Atmos. Chem. Phys.*, 17:4369–4385.
- Sauerwein, M., Clegg, S. L., and Chan, C. K. (2015). Water Activities and Osmotic Coefficients of Aqueous Solutions of Five Alkylammonium Sulfates and Their Mixtures with H<sub>2</sub>SO<sub>4</sub> at 25°C. *Aerosol. Sci. Tech.*, 49:566–579.
- Smith, J. N., Barsanti, K. C., Friedli, H. R., Ehn, M., Kulmala, M., Collins, D. R., Scheckman, J. H., Williams, B. J., and McMurry, P. H. (2010). Observations of Ammonium Salts in Atmospheric Nanoparticles and Possible Climatic Implications. *P. Natl. Acad. Sci. USA*, 107:6634–6639.
- Stein, S. E., director NIST Mass Spec Data Center. (2018). "Mass Spectra" in *NIST Chemistry WebBook, NIST Standard Reference Database Number 69*, P. J. Linstrom and W. G. Mallard, eds., National Institute of Standards and Technology, Gaithersburg MD, retrieved February 26, 2018.
- Väisänen, O., Ruuskanen, A., Ylisirniö, A., Miettinen, P., Portin, H., Hao, L. Q., Leskinen, A., Komppula, M., Romakkaniemi, S., Lehtinen, K. E. J., and Virtanen, A. (2016). In-Cloud Measurements Highlight the Role of Aerosol Hygroscopicity in Cloud Droplet Formation. *Atmos. Chem. Phys.*, 16:10385–10398.
- VandenBoer, T. C., Petroff, A., Markovic, M. Z., and Murphy, J. G. (2011). Size Distribution of Alkyl Amines in Continental Particulate Matter and Their Online Detection in the Gas and Particle Phase. *Atmos. Chem. Phys.*, 11:4319–4332.
- Wexler, A. S., and Clegg, S. L. (2002). Atmospheric Aerosol Models for Systems Including the Ions H<sup>+</sup>, NH<sub>4</sub><sup>+</sup>, Na<sup>+</sup>, SO<sub>4</sub><sup>2-</sup>, NO<sub>3</sub><sup>-</sup>, Cl<sup>-</sup>, Br<sup>-</sup>, and H<sub>2</sub>O. *J. Geophys. Res.*, 107(D14): ACH 14-1–ACH 14-14.
- Yli-Juuti, T., Barsanti, K., Hildebrandt Ruiz, L., Kieloaho, A. J., Makkonen, U., Petäjä, T., Ruuskanen, T., Kulmala, M., and Riipinen, I. (2013). Model for Acid-Base Chemistry in Nanoparticle Growth (MABNAG). *Atmos. Chem. Phys.*, 13:12507–12524.
- Youn, J. S., Crosbie, E., Maudlin, L. C., Wang, Z., and Sorooshian, A. (2015). Dimethylamine as a Major Alkyl Amine Species in Particles and Cloud Water: Observations in Semi-Arid and Coastal Regions. *Atmos. Environ.*, 122:250–258.
- Zardini, A. A., Sjogren, S., Marcolli, C., Krieger, U. K., Gysel, M., Weingartner, E., Baltensperger, U., and Peter, T. (2008). A Combined Particle Trap/HTDMA Hygroscopicity Study of Mixed Inorganic/Organic Aerosol Particles. *Atmos. Chem. Phys.*, 8:5589–5601.
- Zieger, P., Fierz-Schmidhauser, R., Weingartner, E., and Baltensperger, U. (2013). Effects of Relative Humidity on Aerosol Light Scattering: results from Different European Sites. *Atmos. Chem. Phys.*, 13:10609–10631.
- Zieger, P., Väisänen, O., Corbin, J. C., Partridge, D. G., Bastelberger, S., Mousavi-Fard, M., Rosati, B., Gysel, M., Krieger, U. K., Leck, C., Nenes, A., Riipinen, I., Virtanen, A., and Salter, M. E. (2017). Revising the Hygroscopicity of Inorganic Sea Salt Particles. *Nat. Commun.*, 8:15883.

## Supplemental information

### Hygroscopicity of dimethylaminium-, sulfate- and ammonium-containing nanoparticles

Olli-Pekka Tikkanen<sup>1</sup>, Olli Väisänen<sup>1</sup>, Liqing Hao<sup>1</sup>, Eemeli Holopainen<sup>1</sup>, Hao Wang<sup>1,2,3</sup>, Kari E. J. Lehtinen<sup>1,4</sup>, Annele Virtanen<sup>1</sup>, Taina Yli-Juuti<sup>1</sup>

<sup>1</sup>University of Eastern Finland, Department of Applied Physics, Kuopio, Finland.

<sup>2</sup>Jinan University, Institute for Environmental and Climate Research, Guangzhou, China.

<sup>3</sup>Jinan University, JNU-QUT Joint Laboratory for Air Quality Science and Management, Guangzhou, China.

<sup>4</sup>Finnish Meteorological Institute, Atmospheric Research Centre of Eastern Finland, Kuopio, Finland.

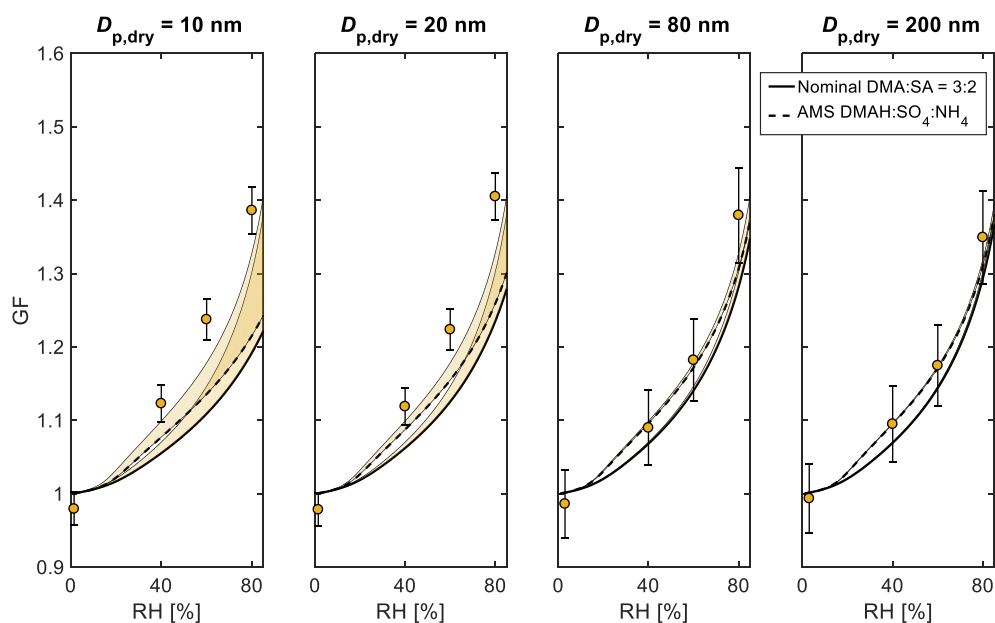


**Figure S1.** A comparison between the measured and modelled hygroscopic growth factors (GF) at different relative humidities (RH) for nominal DMA:SA = 3:2. Shown are the results for 10, 20, 80, and 200 nm particle sizes. The measurement data are plotted as markers, and the solid and dashed lines correspond to E-AIM simulations with nominal and AMS measured compositions, respectively. The shaded areas above the model curves illustrate the sensitivity to the Kelvin term and the whiskers show the maximum instrumental uncertainty.

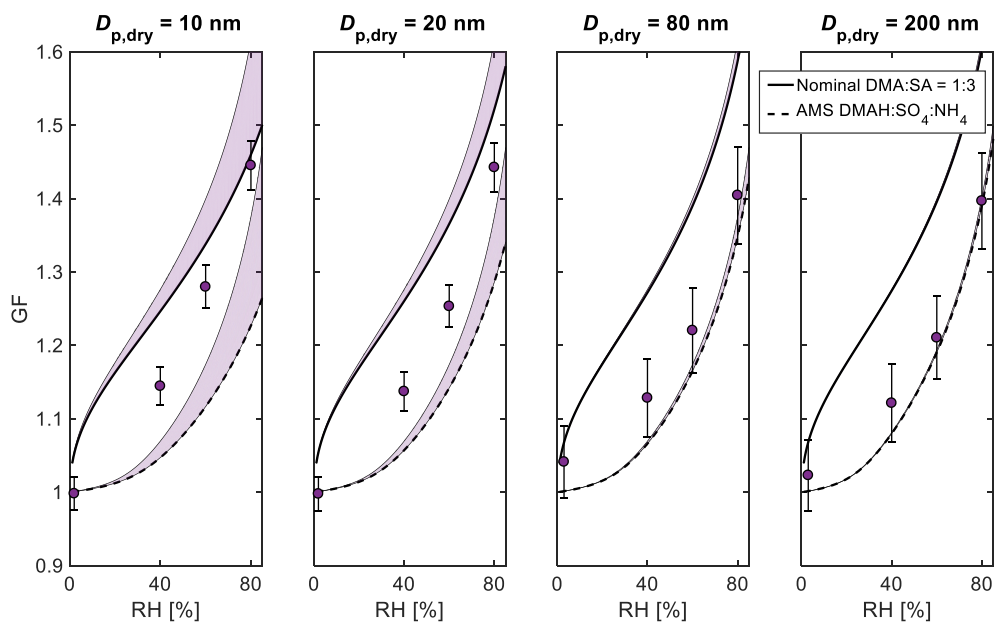


**Figure S2.** A comparison between the measured and modelled hygroscopic growth factors (GF) at different relative humidities (RH) for nominal DMA:SA = 1:3. Shown are the results for 10, 20, 80, and 200 nm particle sizes. The measurement data are plotted as markers, and the solid and dashed lines correspond to E-AIM simulations with nominal and AMS measured compositions, respectively. The shaded areas above the model curves illustrate the sensitivity to the Kelvin term and the whiskers show the maximum instrumental uncertainty.

**Figure S3-S7.** A comparison between the measured and modelled hygroscopic growth factors (GF) at different relative humidities (RH). Shown are the results for 15, 25, 50, and 130 nm particle sizes. The measurement data are plotted as markers, and the solid and dashed lines correspond to E-AIM simulations with nominal and AMS measured compositions, respectively. The shaded areas above the model curves illustrate the sensitivity to Kelvin term and the whiskers show the maximum instrumental uncertainty.

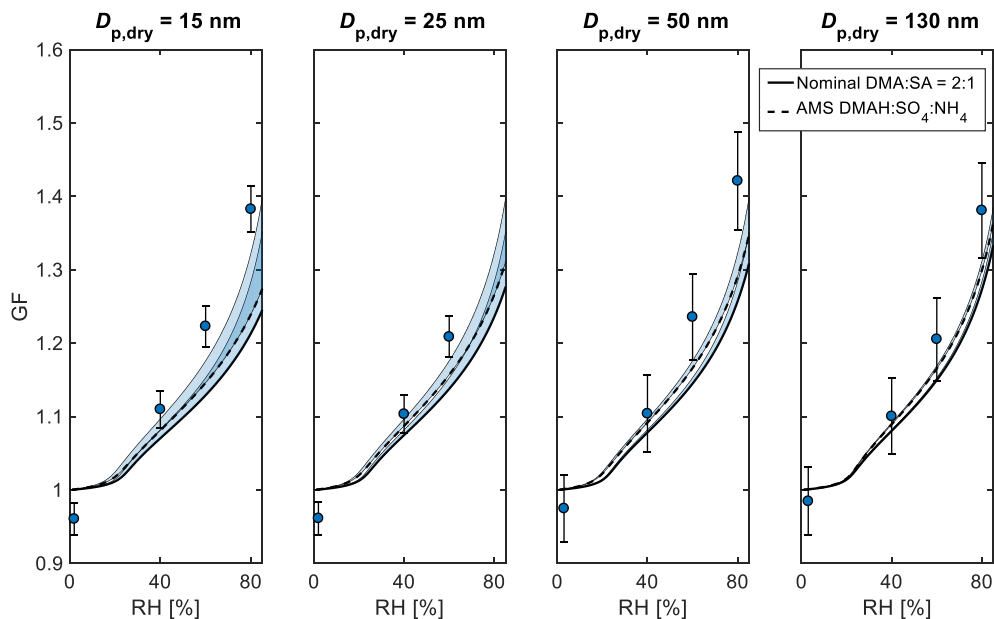


**Figure S3.** Nominal DMA:SA = 2:1

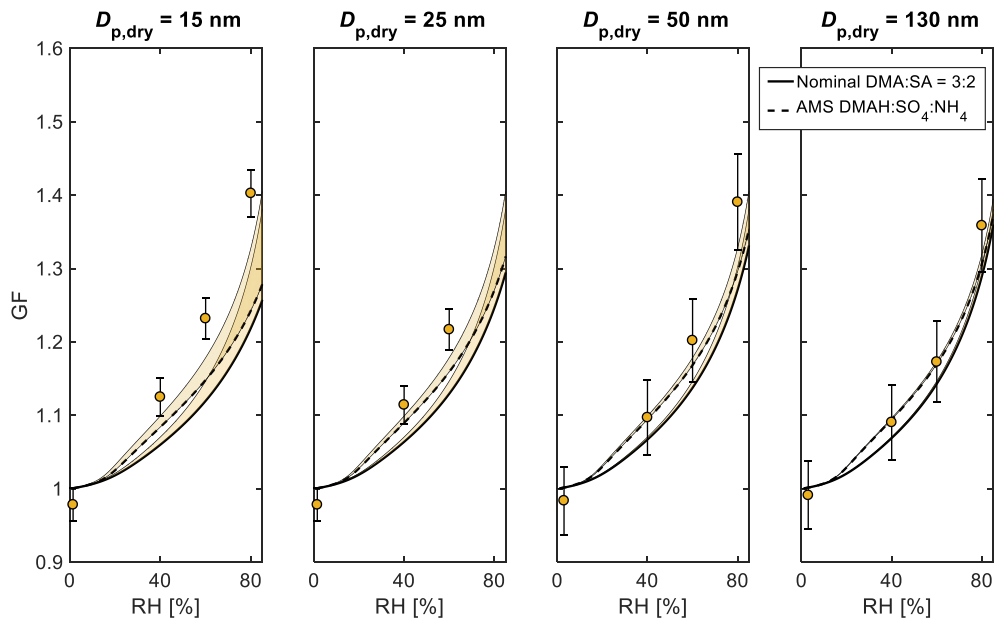


**Figure S4.** Nominal DMA:SA = 3:2

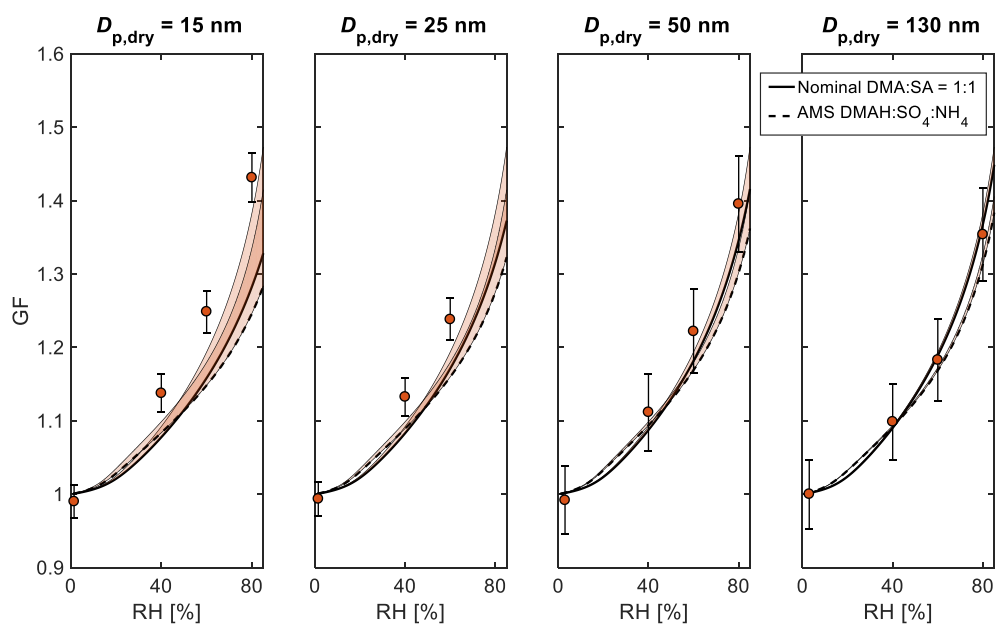


**Figure S5.** Nominal DMA:SA = 1:1

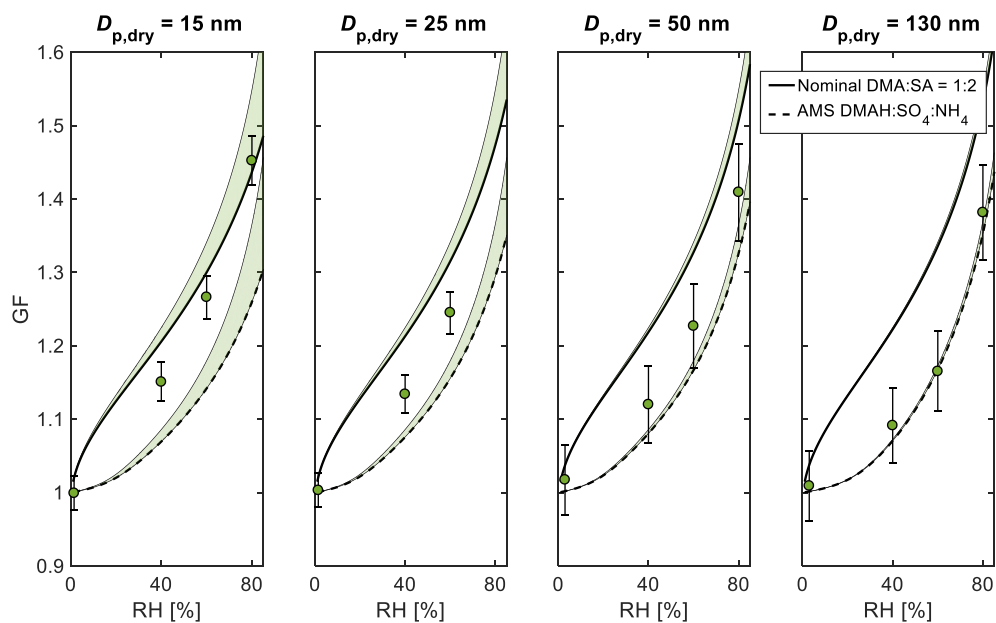


**Figure S6.** Nominal DMA:SA = 1:2

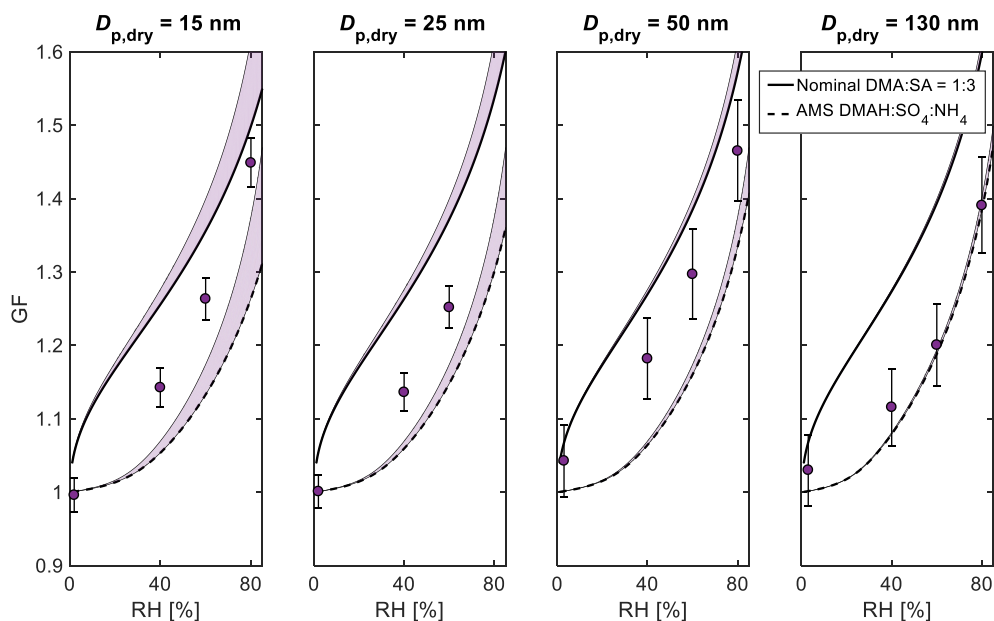


**Figure S7.** Nominal DMA:SA = 1:3

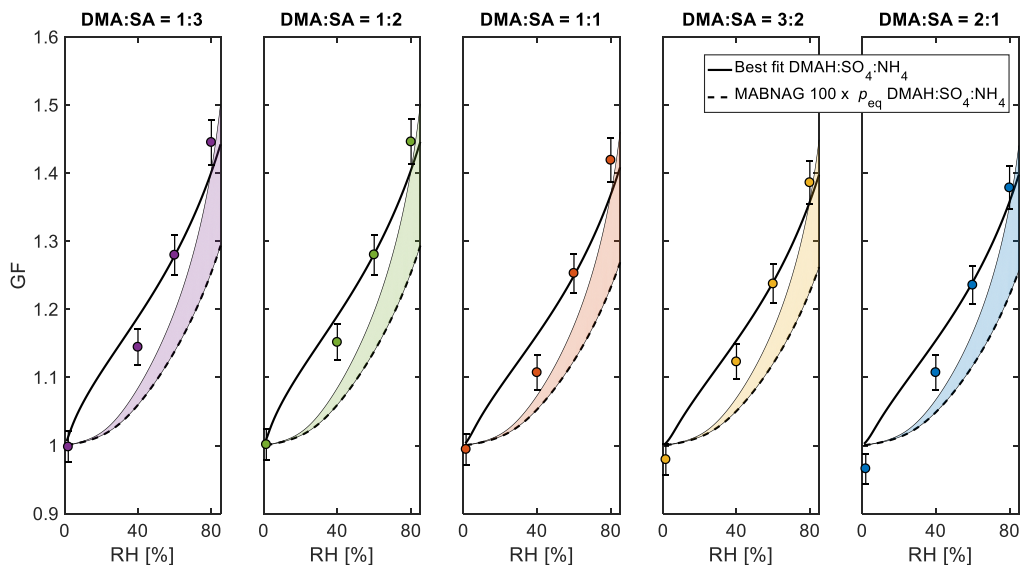


**Figure S8.** Modelled hygroscopic growth factors (GF) after 10 s evaporation (with 100-fold equilibrium vapor pressures) and comparison to measurements at  $D_{p,dry} = 10$  nm. The measurement data are plotted as markers, the dashed lines show the E-AIM results corresponding to the compositions obtained through MABNAG simulations, and the solid lines correspond to the E-AIM simulations with compositions that best fit the measurement data. The shaded areas illustrate the model sensitivity to Kelvin term and the whiskers show the maximum instrumental uncertainty. The composition that best fits the measurement data is determined assuming that the molar DMAH:NH<sub>4</sub> ratio is equal to that of 70 nm AMS measurements.





## Paper II

E. Holopainen, H. Kokkola, A. Laakso and T. Kühn  
“In-cloud scavenging scheme for sectional aerosol  
modules - implementation in the framework of the  
Sectional Aerosol module for Large Scale Applications  
version 2.0 (SALSA2.0) global aerosol module”  
*Geoscientific Model Development* **13**,  
pp. 6215–6235, 2020.

Reproduced under the Creative Commons Attribution 4.0 License  
(CC BY 4.0).





# In-cloud scavenging scheme for sectional aerosol modules – implementation in the framework of the Sectional Aerosol module for Large Scale Applications version 2.0 (SALSA2.0) global aerosol module

Eemeli Holopainen<sup>1</sup>, Harri Kokkola<sup>1</sup>, Anton Laakso<sup>1</sup>, and Thomas Kühn<sup>1,2</sup>

<sup>1</sup>Atmospheric Research Centre of Eastern Finland, Finnish Meteorological Institute, P.O. Box 1627, 70211 Kuopio, Finland

<sup>2</sup>Aerosol Physics Research Group, University of Eastern Finland, P.O. Box 1627, 70211 Kuopio, Finland

**Correspondence:** Eemeli Holopainen (eemeli.holopainen@fmi.fi)

Received: 2 July 2020 – Discussion started: 17 July 2020

Revised: 8 October 2020 – Accepted: 24 October 2020 – Published: 7 December 2020

**Abstract.** In this study we introduce an in-cloud wet deposition scheme for liquid and ice phase clouds for global aerosol–climate models which use a size-segregated aerosol description. For in-cloud nucleation scavenging, the scheme uses cloud droplet activation and ice nucleation rates obtained from the host model. For in-cloud impaction scavenging, we used a method where the removal rate depends on the wet aerosol size and cloud droplet radii. We used the latest release version of ECHAM-HAMMOZ (ECHAM6.3-HAM2.3-MOZ1.0) with the Sectional Aerosol module for Large Scale Applications version 2.0 (SALSA) microphysics package to test and compare our scheme. The scheme was compared to a scheme that uses fixed scavenging coefficients. The comparison included vertical profiles and mass and number distributions of wet deposition fluxes of different aerosol compounds and for different latitude bands. Using the scheme presented here, mass concentrations for black carbon, organic carbon, sulfate, and the number concentration of particles with diameters larger than 100 nm are higher than using fixed scavenging coefficients, with the largest differences in the vertical profiles in the Arctic. On the other hand, the number concentrations of particles smaller than 100 nm in diameter show a decrease, especially in the Arctic region. These results could indicate that, compared to fixed scavenging coefficients, nucleation scavenging is less efficient, resulting in an increase in the number concentration of particles larger than 100 nm. In addition, changes in rates of impaction scavenging and new particle formation (NPF) can be the main cause of reduction in the number concen-

trations of particles smaller than 100 nm. Without further adjustments in the host model, our wet deposition scheme produced unrealistically high aerosol concentrations, especially at high altitudes. This also leads to a spuriously long lifetime of black carbon aerosol. To find a better setup for simulating aerosol vertical profiles and transport, sensitivity simulations were conducted where aerosol emission distribution and hygroscopicity were altered. Vertical profiles of aerosol species simulated with the scheme which uses fixed scavenging rates and the abovementioned sensitivity simulations were evaluated against vertical profiles from aircraft observations. The lifetimes of different aerosol compounds were also evaluated against the ensemble mean of models involved in the Aerosol Comparisons between Observations and Models (AEROCOM) project. The best comparison between the observations and the model was achieved with our wet deposition scheme when black carbon was emitted internally mixed with soluble compounds instead of keeping it externally mixed. This also produced atmospheric lifetimes for the other species which were comparable to the AEROCOM model means.

## 1 Introduction

The estimated radiation budget of the Earth has large uncertainties, and a majority of these uncertainties are related to the uncertainties in the direct and indirect effects of atmospheric aerosol (IPCC, 2014). Aerosol particles can affect

the climate directly by scattering and absorbing radiation and indirectly through aerosol–cloud interactions (Haywood and Shine, 1997; Twomey, 1991; Albrecht, 1989). Thus, in order to estimate the radiation budget of the Earth correctly, aerosols and their physical properties affecting radiation and cloud formation have to be modeled realistically.

Black carbon (BC) is one of the aerosol compounds which has an effect on the Earth's radiation budget via absorbing solar radiation, accelerating the melting of snow and ice, and influencing cloud formation and life cycle (Bond et al., 2013). A large fraction of BC is emitted through incomplete combustion, which is due to anthropogenic activities (Bond et al., 2013). Due to its ability to darken snow and ice covers, BC has been found to be a major warming agent at high latitudes (AMAP, 2015). In addition, it has been proposed that the mitigation of BC is one of the possible means to slow Arctic warming (Stone et al., 2014).

Transport of aerosol particles to remote regions with only small amounts of emitted particles affects the local aerosol size distribution and composition (Rasch et al., 2000; Croft et al., 2010). In these areas, e.g., the Arctic, simulated aerosol and especially BC concentrations differ from those observed, as the transport to these regions is modeled poorly (Bourgeois and Bey, 2011; Sharma et al., 2013; Kristiansen et al., 2016). In addition, BC vertical profiles affect the uncertainty of its forcing emphasizing the need to improve BC vertical profiles in global aerosol–climate models (Samset et al., 2013). The vertical distribution of aerosol compounds is found to be affected by emissions, hygroscopicity, deposition, and microphysical processes, of which wet removal can be the cause of one of the major biases in the models (Kipling et al., 2016; Watson-Parris et al., 2019). Thus, one possible cause for problems in modeling long-range and vertical transport of BC is how wet removal of aerosol compounds is modeled (Bourgeois and Bey, 2011; Croft et al., 2016). Wet deposition processes are modeled very differently among global aerosol–climate models and, therefore, more research is needed to better parameterize and constrain wet deposition in models (Croft et al., 2009; Croft et al., 2010; Croft et al., 2016; Textor et al., 2006; Kipling et al., 2016).

Wet removal of aerosol particles from the atmosphere is a process where these particles are scavenged by hydrometeors and then carried to the surface by precipitation (Wang et al., 1978). There are two kinds of wet deposition processes: in-cloud and below-cloud scavenging (Slinn and Hales, 1971; Rasch et al., 2000; Zikova and Zdimal, 2016). In the process of in-cloud scavenging, aerosol species can enter the cloud droplets or ice crystals through a nucleation process, when they act as cloud condensation nuclei (CCN) or ice nuclei (IN). This process is called in-cloud nucleation scavenging (Pruppacher and Klett, 1997). In the process called in-cloud impaction scavenging, aerosol particles can be scavenged through collision with ice crystals or cloud droplets (Chate et al., 2003; Ladino et al., 2011). Aerosol compounds are then removed from the atmosphere when these cloud droplets

or ice crystals grow to precipitation sizes (Pruppacher and Klett, 1997; Croft et al., 2010). Below-cloud scavenging is a process where rain droplets or snow crystals, which precipitate from the cloud, sweep aerosol particles below the cloud through collision (Chate et al., 2011). Observational studies have shown that below-cloud scavenging is strongly dependent on the rain droplet or snow crystal size distribution (Andronache, 2003; Andronache et al., 2006).

In recent years it has become evident that more detailed descriptions of wet deposition in global climate models are important (Korhonen et al., 2008; Garrett et al., 2010; Browse et al., 2012). In addition to transport, wet removal can affect the Arctic aerosol size distribution and its seasonal cycle (Korhonen et al., 2008; Croft et al., 2016). Even though the processes involved in wet removal are well known, it is still difficult to represent them well in global climate models (Eckhardt et al., 2015). In order to realistically describe the wet removal processes, a thorough knowledge of the microphysics of condensation and precipitation, as well as aerosol microphysics, is needed (Rasch et al., 2000).

Here, we describe our scheme for wet deposition using physical parameterizations for nucleation and impaction scavenging in liquid and ice clouds for sectional aerosol modules. The new aspects of this scheme, compared to the modal aerosol scheme already implemented in ECHAM-HAMMOZ, are that it calculates the in-cloud nucleation scavenging rates using the activated fraction in each size class in the liquid cloud case and the surface area of particles in the ice cloud case. Similar approaches for liquid cloud cases exist in other global models which use modal aerosol modules, e.g., MIRAGE and CAM5 (Easter et al., 2004; Wang et al., 2013). We further tested the sensitivity of our scheme to assumptions in aerosol emission distribution and hygroscopicity. The structure of the paper is as follows. In Sect. 2 we present details on in-cloud nucleation and impaction scavenging in general and introduce our in-cloud nucleation scavenging scheme for liquid and ice clouds. In addition, we present details on the aerosol module SALSA (Sectional Aerosol module for Large Scale Applications) and its components, which we used to test and evaluate our scheme and its sensitivity. In Sect. 2 we present the modifications performed for SALSA to include in-cloud impaction scavenging and the treatment of below-cloud scavenging. In the same section, we also present the ECHAM-HAMMOZ aerosol–chemistry–climate model and its setup, which is used for testing the scheme on a global scale. In Sect. 3 we present the evaluation of our scheme against a fixed scavenging coefficient scheme in terms of vertical profiles and wet deposition fluxes of different aerosol compounds. In addition, in the same section, we evaluate the vertical profiles of different aerosol compounds from the simulations against those from the Atmospheric Tomography (ATom) aircraft campaigns (Wofsy et al., 2018). We also compare the wet deposition fluxes, of different aerosol compounds, from different sensitivity simulations to each other.

Finally, we compare the lifetimes from all of the simulations to the mean from several models in the Aerosol Comparisons between Observations and Models (AEROCOM) project.

## 2 In-cloud wet deposition scheme

In this section we will describe the in-cloud nucleation and impaction scavenging, for both liquid and ice phase clouds. For both of these cloud phases, the removal of aerosol particles is expressed in terms of a scavenging coefficient. The rate of change in the concentration of compound  $l$  in size class  $i$ ,  $C_i^l$  due to in-cloud nucleation and impaction scavenging, for both liquid and ice clouds, is of the form

$$\frac{\Delta C_i^l}{\Delta t} = C_i^l f_{cl} \left( \frac{(F_{i,nuc,liq} + F_{i,imp,liq}) f_{liq} Q_{liq}}{C_{liq}} + \frac{(F_{i,nuc,ice} + F_{i,imp,ice}) f_{ice} Q_{ice}}{C_{ice}} \right), \quad (1)$$

where  $F_{i,nuc,liq}$  and  $F_{i,nuc,ice}$  are the fractions of activated particles due to nucleation scavenging in liquid and ice clouds, respectively, and  $F_{i,imp,liq}$  and  $F_{i,imp,ice}$  are the scavenging coefficients due to impaction scavenging in liquid and ice clouds, respectively (Croft et al., 2010). Furthermore,  $f_{cl}$  is the cloud fraction,  $f_{liq}$  is the liquid fraction of the total cloud water,  $Q_{liq}$  is the sum of conversion rate of cloud liquid water to precipitation by autoconversion, accretion, and aggregation processes,  $C_{liq}$  is the cloud liquid water content, and  $f_{ice}$ ,  $Q_{ice}$ , and  $C_{ice}$  are the equivalent variables for ice (Croft et al., 2010). The values in Eq. (1) are in-cloud values (Croft et al., 2010).

### 2.1 In-cloud scavenging scheme for liquid clouds

The in-cloud process of nucleation scavenging refers to activation and growth of aerosol particles into cloud droplets (Köhler, 1936). When water vapor reaches supersaturation, a fraction of the aerosol population is activated to cloud droplets. After these cloud droplets have grown to precipitation size, the particles can be removed from the cloud through precipitation (Wang et al., 1978). The ability of an aerosol particle to activate to a cloud droplet depends on its size, chemical composition, and the ambient supersaturation (Köhler, 1936).

In aerosol modules of global climate models, the aerosol size distribution can be approximated by, for example, a modal or sectional discretization, which effectively separates the size distribution into different size classes (Stier et al., 2005; Kokkola et al., 2018a). In each size class the fraction of activated particles can be calculated as the portion of particles that exceed the critical diameter of activation in that size class (Köhler, 1936; Croft et al., 2010). However, many models describe the nucleation scavenging by assuming a con-

stant scavenging coefficient for different aerosol size classes (Stier et al., 2005; Seland et al., 2008; de Bruine et al., 2018).

The current in-cloud nucleation scavenging scheme for liquid clouds introduced here calculates the scavenging coefficients of aerosol based on the fraction of activated particles in each size class, i.e.,  $F_{i,nuc,liq}$  in Eq. (1). Thus, using the scheme requires that the atmospheric model incorporates a cloud activation parameterization that calculates size segregated cloud activation. Such parameterizations are, e.g., Abdul-Razzak and Ghan (2002) and Barahona and Nenes (2007).

In-cloud impaction scavenging, for liquid clouds, is a process where aerosol particles collide with existing cloud droplets and are thereby removed from the interstitial air of the cloud (Chate et al., 2003). This aerosol scavenging by cloud droplets is based on coagulation theory, which quantifies the rate of removal. This is further used to define the scavenging coefficients by impaction (Seinfeld and Pandis, 2006). Commonly, these scavenging coefficients, for the full aerosol particle distribution, can be calculated as

$$F_{i,imp,liq}(d_p, t) = \int_0^\infty K(d_p, D_{liq}) n(D_{liq}, t) dD_{liq}, \quad (2)$$

where  $d_p$  is the wet diameter of the aerosol particle,  $D_{liq}$  is the cloud droplet diameter,  $K(d_p, D_{liq})$  is the collection efficiency between aerosol particles and cloud droplets, and  $n(D_{liq}, t)$  is the cloud droplet number distribution (Seinfeld and Pandis, 2006).

### 2.2 In-cloud scavenging scheme for ice clouds

In-cloud nucleation scavenging in ice clouds refers to the formation and growth of ice particles (Seinfeld and Pandis, 2006). When ice particles are formed, they can quickly grow into precipitation sizes and be removed from the cloud (Korolev et al., 2011). The formation of ice particles in the atmosphere usually requires an ice nucleus (IN), but they can also be formed without IN if the temperature is very low (Hobbs, 1993). Aerosol particles which can act as IN are usually insoluble (Marcolli et al., 2007). In addition, large particles are more efficient in acting as IN than small particles (Archuleta et al., 2005).

The nucleation rate,  $J_T$ , which is the total number of ice crystals formed in a unit volume of air per unit time, can be expressed as the sum of the nucleation rate in a unit volume of liquid solution,  $J_V$ , multiplied by the total collective volume of aerosol particles in a unit volume of air,  $V_t$ , and the nucleation rate on a unit surface area of liquid solution,  $J_S$ , multiplied by the total collective surface area of aerosol particles in a unit volume of air,  $S_t$  (Tabazadeh et al., 2002). However, experimental studies and thermodynamic calculations for the ice–water–air system suggest that the total number of ice crystals formed is dominated by surface-based processes, so that  $J_S S_t \gg J_V V_t$  (Tabazadeh et al., 2002). With this as-

sumption the total nucleation rate can be simplified to

$$J_T = \frac{\Delta \text{ICNC}}{\Delta t} = J_V V_t + J_S S_t \approx J_S S_t. \quad (3)$$

Global models usually give the total in-cloud ice nucleation rate, which is here segregated into size-resolved nucleation rates. Since we assume that the number of nucleated ice particles depends only on the aerosol surface area, the scavenging coefficient in ice-containing clouds in size class  $i$  is proportional to the ratio between nucleation rate in the size class and the total nucleation rate. Thus, for the scavenging coefficient, for the ice-containing clouds, we get the following in each size class:

$$F_{i,\text{nuc,ice}} = \frac{S_i}{\sum_j S_j} \frac{\Delta \text{ICNC}}{n_i}, \quad (4)$$

where  $S_i$  is the surface area concentration of size class  $i$ ,  $\Delta \text{ICNC}$  is the ice crystal number concentration obtained from the ice cloud activation scheme, and  $n_i$  is the number concentration in size class  $i$ . The total surface area in each size class is derived using the associated number or mass median wet aerosol radius.

## 2.3 SALSA

To test how the in-cloud wet deposition scheme affects simulated global aerosol concentrations, we used it with the SALSA2.0 in our ECHAM-HAMMOZ global model simulations. In addition, we tested how sensitive the simulated aerosol concentrations are to emission sizes, mixing, and aging when this scheme is used. SALSA is the sectional aerosol module of ECHAM-HAMMOZ global climate model. Details for calculations of aerosol emissions and chemistry in SALSA are presented in Kokkola et al. (2018a). SALSA is a very versatile aerosol microphysics module, which has been implemented in several models of very different spatial resolution (Kokkola et al., 2018a; Tonttila et al., 2017; Andersson et al., 2015; Kurppa et al., 2019). To describe the aerosol population, SALSA uses a hybrid bin sectional approach for calculating the evolution of the size distribution (Chen and Lamb, 1994; Kokkola et al., 2018a). In SALSA the aerosol population is divided into two subregions depending on their size. The first subregion is from 3 nm to 50 nm and the second is from 50 to 10  $\mu\text{m}$ . These subregions are further divided into size sections defining the minimum and maximum diameter of the particles. In each size section the aerosol particles are assumed to be monodisperse, and chemistry and different microphysical processes are calculated for each size section separately. In addition, the second subregion is divided into externally mixed soluble and insoluble populations. A more detailed description of the newest SALSA version, SALSA2.0, is presented in Kokkola et al. (2018a).

Originally, SALSA used fixed scavenging coefficients,  $F_i$ , for different size classes  $i$ , in its wet deposition calculations.

These coefficients include all the processes for in-cloud and below-cloud scavenging (Bergman et al., 2012). The fixed coefficients, for stratiform and convective clouds with different phases (liquid, mixed, and ice) and solubilities, are adapted for SALSA from the calculations presented by Stier et al. (2005), and they are presented in detail in Bergman et al. (2012). Here we refine the entire scavenging scheme by calculating the scavenging coefficients online.

We used the Abdul-Razzak and Ghan (2002) cloud activation scheme to derive the fraction of activated particles in each size class for our in-cloud nucleation scavenging calculations. However, the original activation scheme considers only the soluble material in particles and therefore neglects any possible insoluble material (Abdul-Razzak and Ghan, 2002). For computing the amount of cloud droplets formed, this is a good assumption, as usually most CCN-sized particles contain a large fraction of soluble material. However, when the insoluble fraction is large ( $> 0.99$ ), the assumption may lead to an underestimation of scavenged particles. This is because for insoluble particles larger than 1  $\mu\text{m}$  with thin soluble coating (for instance mineral dust), the insoluble fraction is ignored in the cloud activation calculation, and for those particles the activation is calculated as it would be calculated for particles with an equivalent dry size derived from the soluble part of the particles, thus making them less prone to activation. Therefore, we modified the Abdul-Razzak and Ghan (2002) activation calculations to account for the insoluble core in particles. The calculations are otherwise the same, but the critical supersaturation for each size class is calculated using Eq. (17.38) in Seinfeld and Pandis (2006). The supersaturation calculations, used in the Abdul-Razzak and Ghan (2002) cloud activation, for particles containing an insoluble core are presented in Appendix A. As an input for the in-cloud nucleation scavenging coefficients in ice clouds, we used the ice crystal nucleation scheme described in Lohmann (2002). In our model, only particles which include mineral dust and black carbon are considered as ice nuclei (Lohmann et al., 2007).

As the in-cloud nucleation scavenging was changed into a more functional method, we also needed to alter the calculation of the in-cloud impaction scavenging. We calculate the in-cloud impaction scavenging in SALSA, for liquid clouds, using the same method as described in Croft et al. (2010). This method computes in-cloud impaction as a function of wet aerosol particle size ( $r_p$ ), wet median aerosol particle radius ( $r_{pg}$ ), and cloud droplet radii ( $R_{liq}$ ). Using this same information from our monodisperse size classes for aerosol particles, we can assume that each size class is a log-normal mode, and the in-cloud impaction scavenging coefficients, for liquid clouds, are then obtained as

$$F_{i,\text{imp,liq}} = \Lambda_m(r_{pg}) \Delta t, \quad (5)$$

where  $\Lambda_m(r_{pg})$  is the mean mass scavenging coefficient, and it is defined as

$$\Lambda_m(r_{pg}) = \frac{\int_0^\infty \Lambda(r_{pg}) r_p^3 n(r_p) dr_p}{\int_0^\infty r_p^3 n(r_p) dr_p}, \quad (6)$$

and

$$\Lambda(r_{pg}) = \int_0^\infty \pi R_{liq}^2 U_t(R_{liq}) E(R_{liq}, r_{pg}) n(R_{liq}) dR_{liq}, \quad (7)$$

which is called the scavenging coefficient in inverse time (Croft et al., 2010). In Eqs. (6) and (7)  $n(r_p)$  is the aerosol number,  $R_{liq}$  is the cloud droplet radius,  $U_t(R_{liq})$  is the terminal velocity of cloud droplets,  $E(R_{liq}, r_{pg})$  is the collision efficiency between the aerosol particles and cloud droplets, and  $n(R_{liq})$  is the cloud droplet number (Croft et al., 2010).

The in-cloud impaction scavenging, for ice clouds, is calculated following Croft et al. (2010), but as our model assumes that the ice crystals are monodisperse, there is no need to integrate over ice crystal number distribution (Croft et al., 2010). Thus, the in-cloud impaction scavenging coefficients are

$$F_{i, \text{imp, ice}} = \pi R_{ice}^2 U_t(R_{ice}) E(R_{ice}, r_{pg}) \text{ICNC} \Delta t, \quad (8)$$

where  $R_{ice}$  is the radius of the ice crystal in its maximum extent,  $U_t(R_{ice})$  is the terminal velocity of the ice crystals, and  $E(R_{ice}, r_{pg})$  is the collection efficiency of the collisions between aerosol particles and ice crystals (Croft et al., 2010).

For below-cloud scavenging, we used the Croft et al. (2009) method, in which we approximated each size class as a log-normal mode. The size-dependent collection efficiency for rain and snow uses an aerosol and collector drop size parameterization described in detail in Croft et al. (2009). Several studies have found that below-cloud scavenging of aerosols does not contribute to the mass deposition budgets as much as in-cloud scavenging does (Croft et al., 2009; Croft et al., 2010; Flossmann and Wobrock, 2010). Thus, we did not analyze below-cloud scavenging separately in our simulations.

## 2.4 ECHAM-HAMMOZ

For testing the effect of the current wet-scavenging scheme on global aerosol properties, we used the latest stable version of ECHAM-HAMMOZ (ECHAM6.3-HAM2.3-MOZ1.0), a three-dimensional aerosol–chemistry–climate model. ECHAM6.3 is a general circulation model (GCM) and it solves the equations for divergence, temperature, surface pressure, and vorticity (Stier et al., 2005). These large-scale meteorological prognostic variables can be nudged towards data from operational weather forecast models (Stier et al., 2005; Kokkola et al., 2018a).

ECHAM6.3 is coupled with the Hamburg Aerosol Model (HAM), which calculates all of the aerosol properties within ECHAM-HAMMOZ. These properties include emissions,

deposition, radiation, and microphysics (Stier et al., 2005; Tegen et al., 2019). HAM has a comprehensive parameterization for both modal and sectional microphysics representations of aerosol populations. In addition to BC, the aerosol compounds included in this study are organic carbon (OC), organic aerosol (OA) (here assumed to be 1.4 times the modeled OC mass), sulfate ( $\text{SO}_4$ ), mineral dust (DU), and sea salt (SS). ECHAM6.3 is further coupled to the chemistry model MOZ (not used here), which contains a detailed stratospheric and tropospheric reactive chemistry representation for 63 chemical species, including nitrogen oxides, tropospheric ozone, and hydrocarbons (Schultz et al., 2018; Horowitz et al., 2003). The model does not include secondary organic aerosols. In addition, the model assumes the same aerosol emission size distribution per compound and emission sector throughout the whole world. The SALSA global aerosol module is coupled in the ECHAM-HAMMOZ global climate model for all of the simulations presented in this study.

## 2.5 Simulations

We used a total of six different simulations to investigate the performance of the current wet deposition scheme. The first two simulations were done with the default wet deposition scheme of SALSA (hereafter referred to as “old”) and the wet deposition scheme introduced in this study (hereafter referred to as “current”). The treatment of aerosol aging is identical in baserun\_old and baserun\_new; i.e., there is no artificial transfer of insoluble particles to soluble size classes. However, aerosol mass can be transferred from the soluble to the insoluble population through coagulation. As will be shown later, in the default model configuration the current scheme resulted in spurious BC vertical profiles. To investigate the reasons for this, we carried out four additional sensitivity simulations where we changed the assumptions of emission size distribution, as well as internal mixing and aging of BC. A schematic of the aerosol emission number size distribution, ( $N$ ), as a function of diameter  $D_p$ , for the different simulations is presented in Fig. 1. In addition, an overview over the different simulations and their illustrative colors and line styles in the upcoming figures are presented in Table 1.

In the model simulations, the runs “baserun\_new” and “baserun\_old” are used to compare the current and old in-cloud scavenging schemes. The simulations “BC\_small”, “BC\_large”, “BC\_soluble”, and “insol2sol” were conducted to evaluate the sensitivity of the current in-cloud scavenging scheme. These sensitivity studies were chosen based on the findings of Kipling et al. (2016), who studied how model processes affect the simulated aerosol vertical profiles. Their study indicated that the processes which have the strongest effect on aerosol vertical profiles in the HadGEM model are emission distribution, hygroscopicity, deposition, and microphysical processes (Kipling et al., 2016).



**Table 1.** Overview of the simulations used in this study.

Setup	Description	Illustration
baserun_old	Old ECHAM-SALSA in-cloud scavenging scheme with fixed scavenging coefficients.	----
baserun_new	Current in-cloud nucleation scavenging using Abdul-Razzak and Ghan (2002) for liquid clouds and Lohmann (2002) for ice clouds. In-cloud impaction for liquid and ice clouds according to Croft et al. (2010)	—
BC_small	All BC emissions directed to small insoluble size class.	.....
BC_large	All BC emissions directed to large insoluble size class.	.....
BC_soluble	All BC emissions directed to soluble population with the same mass distribution as for baseruns.	----
insol2sol	Simulating aging of insoluble particles by moving them to soluble aerosol population after they activate at 0.5 % supersaturation.	----

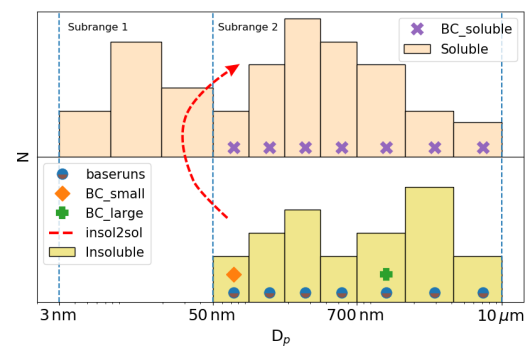


**Figure 1.** Schematic representation of the number size distribution, ( $N$ ), of aerosols in different simulations as a function of diameter  $D_p$ .

In the first two sensitivity runs, we altered the BC emission distribution for SALSA. This was done so that all of the BC emissions were directed to either size class of small or large insoluble particles, respectively. In the default configuration the BC emission size distributions are log-normal mass fraction distributions following AEROCOM emission recommendations (Stier et al., 2005; Dentener et al., 2006), which are remapped to the SALSA size classes. The mode radii ( $r_m$ ) and standard deviations  $\sigma$  for the original BC emission size distributions are  $r_m = 0.015\ \mu\text{m}$  and  $\sigma = 1.8$ , for fossil fuel emissions and  $r_m = 0.04\ \mu\text{m}$  and  $\sigma = 1.8$ , for wild-fire emissions (Dentener et al., 2006). In the BC\_small simulation, we directed all BC emissions to an insoluble size class where particle diameter spans from 50 to 96.7 nm. In the BC\_large simulation, we directed all BC emissions to an insoluble size class where particle diameter spans from 0.7 to 1.7  $\mu\text{m}$ .

To study the sensitivity of the wet deposition scheme to BC hygroscopicity, we conducted a simulation where all BC emissions were directed to soluble size classes. The size distribution for the emissions was the same as for the baserun simulations when they are directed to the insoluble classes. This simulation is referred to as BC\_soluble in the model simulations. In the fourth sensitivity study, called insol2sol, insoluble particles are transferred to parallel size classes of soluble particles. This allows for the separation of fresh and aged particles and is a method to simulate aerosol aging used also in other global aerosol models (e.g., Stier et al., 2005). The criterion for transfer is that particles activate at a supersaturation of 0.5 %.

2.6 Experimental setup

The simulations were performed with ECHAM-HAMMOZ for the year 2010, with the SALSA aerosol module, using 3-hourly data output, after a 6-month spin-up. The emissions were obtained from the ACCMIP (Emissions for Atmospheric Chemistry and Climate Model Intercomparison Project) emission inventories, which are interpolated, for the period 2000–2100 by using Representative Concentration Pathway 4.5 (RCP4.5) (Lamarque et al., 2010; van Vuuren et al., 2011). The model vorticity, divergence, and surface pressure were nudged towards ERA-Interim reanalysis data provided by ECMWF (European Centre for Medium-Range Weather Forecasts) (Simmons et al., 1989; Berrisford et al., 2011), and the sea surface temperature (SST) and sea ice cover (SIC) were also prescribed. SST and SIC were obtained from monthly mean climatologies from AMIP (Atmospheric Model Intercomparison Project). The analysis is made between the old and the current wet deposition scheme using the ECHAM-HAMMOZ global aerosol–climate model with the SALSA aerosol module. In addition, the sensitivity of the current scheme to emission sizes, aging, and hygro-

scopcity of BC-containing aerosol is tested using ECHAM-HAMMOZ with SALSA.

## 2.7 AToM aircraft measurements

To see how the current scheme and the sensitivity studies reproduce the vertical properties of different aerosol compounds, we compared the model simulations against aircraft measurements. The aircraft data were obtained from all NASA's AToM missions (1, 2, 3, and 4), and the dataset was merged data from all instruments which measure atmospheric chemistry, trace gases, and aerosols (Wofsy et al., 2018).

To get the best representative comparison between the AToM aircraft measurements and model data, the model data were sampled to the same time and locations of the aircraft measurements. For the collocation of model vertical profiles with observations, we used the Community Intercomparison Suite (CIS) tool (Watson-Parris et al., 2016).

BC concentrations were measured with a single-particle soot photometer (NOAA) (SP2) and OA and SO<sub>4</sub> concentrations with a CU aircraft high-resolution time-of-flight aerosol mass spectrometer (HR-AMS) (Wofsy et al., 2018). The number concentration of particles with a diameter larger than 100 nm,  $N_{100}$ , and total number concentration,  $N_{\text{tot}}$  were combined from the data measured with a nucleation-mode aerosol size spectrometer (NMASS), an ultra-high-sensitivity aerosol size spectrometer (UHSAS), and a laser aerosol spectrometer (LAS) (Brock et al., 2019; Wofsy et al., 2018).

## 3 Results

### 3.1 Differences between simulated values of old and current wet deposition schemes

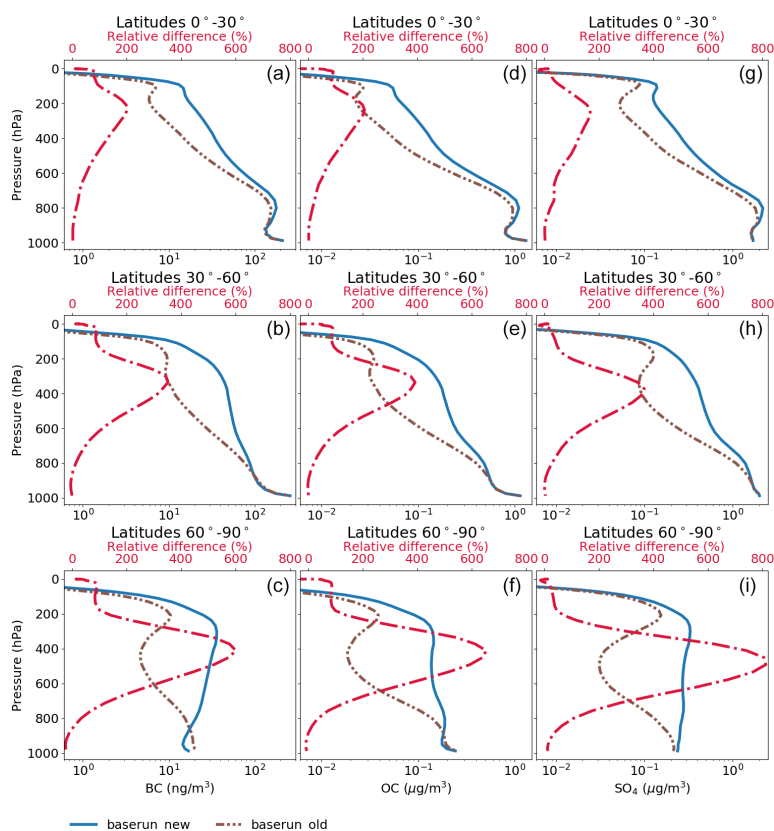
First, we compared how aerosol properties differ when using the old and the current wet deposition schemes. In order to assess how the two schemes affect aerosol transport and vertical profiles, we compared the modeled aerosol vertical profiles over the tropics (0–30° N), the midlatitudes (30–60° N), and the Arctic (60–90° N). Here we focused on SO<sub>4</sub>, OC (or OA), and BC as they are readily available from the AToM aircraft campaign measurements.

Figure 2 shows the vertical profile of BC, OC, and SO<sub>4</sub> mass concentration simulated with the old and the current in-cloud wet deposition schemes. The different rows show different latitude bands, as horizontally averaged annual means. The figure illustrates that all three of the compounds show similar differences in the vertical profiles in all three latitude bands, between the two runs. The concentrations for each compound are higher for the current scheme compared to the old scheme for almost the entire vertical domain. The differences between the different wet deposition schemes are greatest at higher altitudes starting from approximately

900 hPa upwards. In the tropics, these differences in the profiles are smaller, compared to the other latitude bands, with a maximum relative difference of approximately 200 % for BC and OC and slightly exceeding 150 % for SO<sub>4</sub>. These maxima occur at approximately 200 hPa altitude. In the midlatitudes, the differences are slightly higher than in the tropics and the maximum differences in the values are at ~300 hPa altitude. The current method shows ~350 % higher concentrations at maximum for BC and SO<sub>4</sub> and ~400 % for OC. The Arctic shows the largest differences in the compound profiles in comparison to the other latitude bands. The difference is largest at ~500 hPa altitude where the concentrations in the current scheme outweigh the concentrations in the old scheme by ~600 % for BC, 650 % for OC, and 800 % for SO<sub>4</sub>. As emissions of these aerosol particles in the Arctic are low, most aerosol is transported into the Arctic from emission regions outside the Arctic. It is thus evident that the wet removal of these aerosol particles is reduced in the current scheme, which allows for the particles to be transported to higher altitudes and longer distances. In addition, we found that the model accumulates BC at the higher altitudes in simulations spanning several years (not shown), which can be considered spurious behavior.

Figure 3 shows the vertical profile of the number concentration of particles with diameters larger than 100 nm,  $N_{100}$ , and the total number concentration,  $N_{\text{tot}}$ . The  $N_{100}$  profiles show similar differences between the old and the current scheme as for the concentration profiles of different compounds in Fig. 2. In addition, the relative increase in the concentrations in the current wet deposition scheme is similar. This can be explained by changes in nucleation scavenging in the current scheme, which reduces the wet removal of large particles and thus increases the number concentration of large particles. Particles larger than 100 nm act as a condensation sink for H<sub>2</sub>SO<sub>4</sub> and thus an increase in  $N_{100}$  leads to reduced new particle formation (NPF) and thus to decreased number concentrations of small particles. This can be seen in the  $N_{\text{tot}}$  profiles, which show a decrease in the current scheme. This difference is most pronounced in the Arctic, where the relative difference between the current and old schemes in the  $N_{\text{tot}}$  concentration reaches its maximum of ~90 % at ~400 hPa. In addition, the changes in rates of NPF and impaction scavenging in our current scheme result in an increased removal of small aerosol particles and thus reduce concentrations even more. These effects become evident when looking at size-resolved wet deposition fluxes.

The annual and global average size distributions of the wet deposition flux of the old and current in-cloud scavenging schemes are presented in Fig. 4. The wet deposition size distributions confirm what has been observed in the vertical aerosol profiles. There are only modest changes in the mass fluxes between the old and the current schemes. In the soluble population the largest difference is in the size class, which spans diameters between 190–360 nm, where the current scheme exceeds the value of the old



**Figure 2.** Vertical profiles of BC (a–c), OC (d–f), and  $\text{SO}_4$  (g–i), simulated with old and current in-cloud wet deposition schemes at different latitude bands. Note the different units for the different compounds.

scheme by  $0.003 \mu\text{g} (\text{m}^2 \text{s})^{-1}$ . On the other hand, in the size class 1.7–4.1  $\mu\text{m}$ , the old scheme has a higher value by  $0.002 \mu\text{g} (\text{m}^2 \text{s})^{-1}$ . In the insoluble population the current scheme exceeds the value of the old scheme by approximately  $0.002 \mu\text{g} (\text{m}^2 \text{s})^{-1}$  in the size class 190–360 nm, but in the largest size class the value of the old scheme is higher by  $0.005 \mu\text{g} (\text{m}^2 \text{s})^{-1}$ . As in steady state the total emissions of a compound must match its total removal, these differences mostly stem from changes in the interplay between dry- and wet deposition processes. However, the number flux in smaller than 50 nm size classes of the soluble population is halved, affecting mainly the removal of  $\text{SO}_4$  in the smallest size classes. In addition, there is a small increase of approximately  $10^6 (\text{m}^2 \text{s})^{-1}$  in the current scheme in the size class between 190 and 360 nm. For larger than 360 nm size classes the changes are insignificant. These results can be explained by increased concentrations of medium-sized and large particles in the current scheme, which act as a condensation sink for  $\text{SO}_4$ . This leads to fewer small particles as they are mainly

formed through NPF from gaseous  $\text{H}_2\text{SO}_4$ . This effect can also be seen in Fig. 4 as a slight increase in removed sulfate mass in the accumulation-sized particles of both the soluble and insoluble aerosol populations. As a consequence of the atmospheric concentration of small particles, the wet deposition flux for the smallest size classes is reduced in the current scheme compared to the old.

The lifetime of different aerosol compounds was calculated by dividing the annual mean global mass burden of each compound by the annual mean emissions of the same compound (Lund et al., 2018). The lifetimes for different compounds can be found in Table 2. The global mean lifetime for BC was 9.23 d for the old scheme and 14.62 d for the current scheme. However, experimental studies from different aircraft campaigns indicate that the BC lifetime should be less than 5.5 d (Lund et al., 2018). This is a very interesting result: the more physical wet deposition scheme produces more spurious atmospheric lifetimes for BC. Consequently, the ability of the ECHAM-HAMMOZ global climate model,

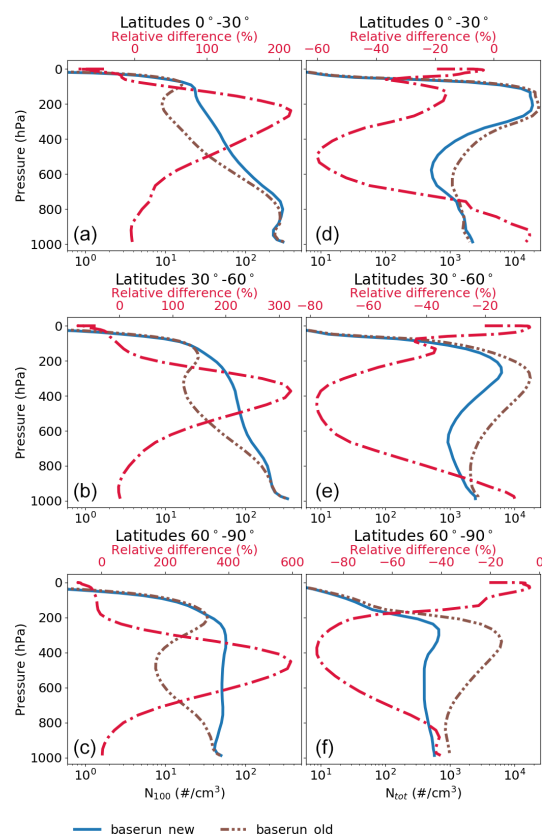


**Figure 3.** Vertical profiles of the  $N_{100}$  (a–c) and  $N_{tot}$  (d–f) concentrations, simulated with old and current in-cloud wet deposition schemes in different latitude regions.

with the SALSA aerosol module, to reliably simulate aerosol vertical profiles and long-range transport of aerosol is also decreased when using the more physical scheme with the default model setup. This may be due to the fact that a more physical treatment of the wet deposition processes makes the model more sensitive to influences outside of the parameterization. We therefore performed further sensitivity simulations and compared their results to observational data.

### 3.2 Sensitivity simulations

As reported in the previous section, ECHAM-HAMMOZ, using the SALSA aerosol module, with the current, more physical scheme, in its default setup, produced spuriously long lifetimes of all aerosol compounds, especially BC. With the sensitivity simulations we aimed to explore different possibilities to improve the BC vertical profiles and long-range transport in the model. In order to increase nucleation scavenging of BC, we considered three different possibilities

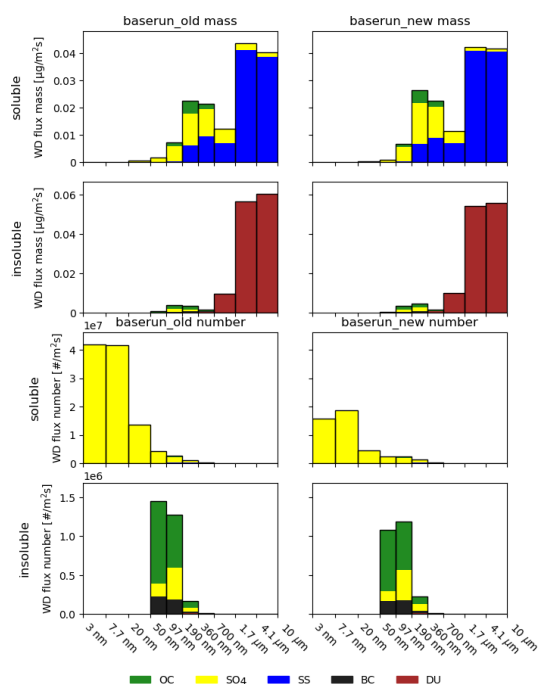


**Figure 4.** Wet deposition flux size distributions of different aerosol compounds simulated with old (left column) and current (right column) in-cloud wet deposition schemes. The top four panels show the wet deposition flux for the mass distribution and the lower four for the number distribution. Different rows show values for the different solubility types.

to make BC-containing particles more susceptible to cloud droplet activation. One way to achieve this is to emit BC into larger particles, which require less aging to be activated at a given supersaturation. This was tested in simulation BC\_large. Another way is to mix BC with soluble compounds in order to enhance hygroscopicity of BC-containing particles and thus their cloud activation susceptibility. This can be done in two ways: either by emitting BC directly to soluble size classes (simulation BC\_soluble) or by emitting BC to insoluble size classes and transferring particles to soluble classes after aging (simulation insol2sol). A third way is to emit BC into smaller size classes in order to facilitate the transfer of BC into larger, more easily activated particles by coagulation (simulation BC\_small).

Figure 5 shows vertical profiles of BC, OA, and  $\text{SO}_4$  simulated with the current wet deposition scheme for the different sensitivity simulations and with the old scavenging scheme, together with the average values from ATom aircraft measurements. The gray shaded area shows the standard deviation for the aircraft measurements. For BC, the simulations baserun\_old, BC\_large, BC\_soluble, and insol2sol show a

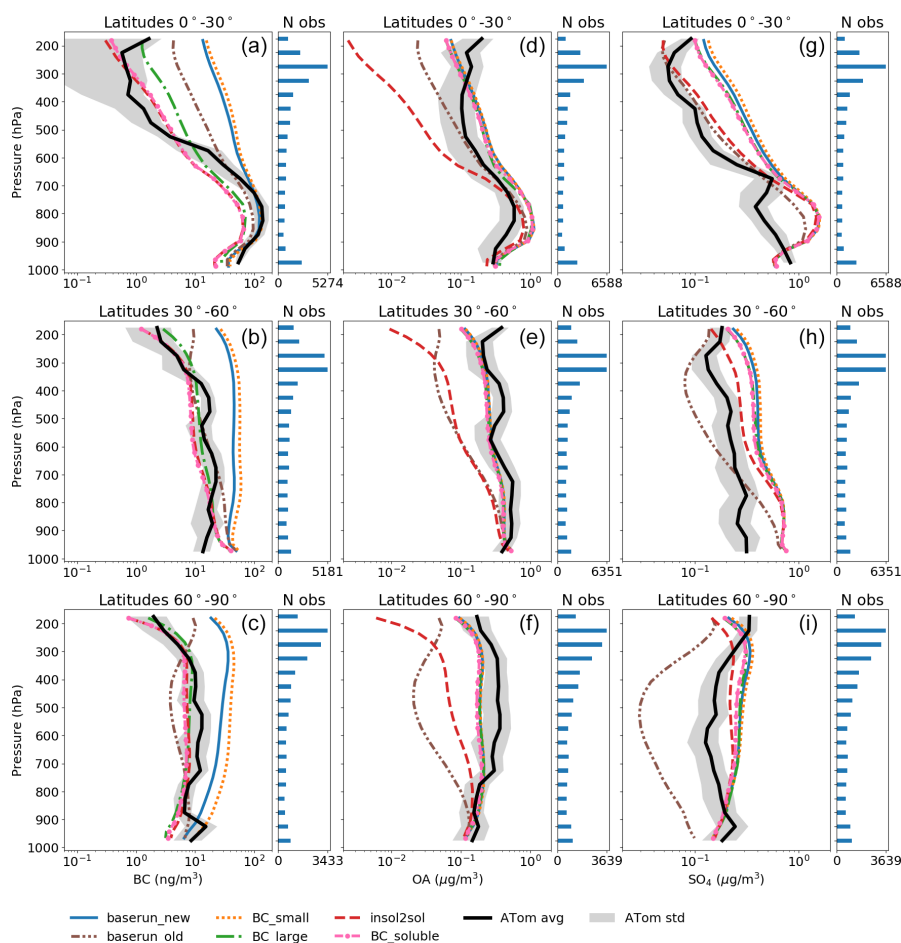


**Figure 5.** Mean vertical profiles of BC (a–c), OA (d–f), and  $\text{SO}_4$  (g–i), modeled with different studies, compared to the mean of ATom aircraft measurements at different latitude bands. To the right of every panel is the number of observations measured by the device, at each vertical level, from the ATom aircraft measurement campaigns. Note the different units for the different compounds.

better match with observed vertical profiles than the other simulations in every latitude band. These simulations fall between the standard deviation limits of the ATom aircraft simulations almost everywhere, with the exception of the tropics, where they underestimate the concentrations starting from  $\sim 600$  hPa downwards. In addition, in the tropics, BC\_soluble and insol2sol represent the BC concentrations slightly better than BC\_large and baserun\_old between 500 and 300 hPa. BC\_small and baserun\_new overestimate the BC concentrations at all latitudes, except in the tropics at lower altitudes starting from  $\sim 700$  hPa downwards, where they represent the BC concentrations slightly better than the other sensitivity simulations. As we saw in the previous chapter, the reduced efficiency in the wet deposition in-

creases BC concentrations at higher altitudes, which causes baserun\_new to overestimate the BC concentrations. This is because the default emission sizes of BC particles are not very susceptible to cloud activation. In addition, although BC\_small aimed at increasing BC wet removal by emitting BC to small particle sizes and thus enhancing their collection by coagulation to large particles, it is apparent that coagulation is not very efficient in doing so.

Compared to baserun\_new, most of the sensitivity studies show better agreement of the modeled BC profiles with the measurements. However, it needs to also be checked how they affect OA and  $\text{SO}_4$  concentrations. At all latitude regions OA concentrations in all of the simulations show similar results as the measurements. Exceptions exist for in-

sol2sol and baserun\_old simulations, which underestimate OA concentrations in the midlatitudes as well as at higher altitudes in the tropics and the Arctic. In the tropics the insol2sol simulation underestimates OA concentrations starting from approximately 700 hPa upwards and baserun\_old from approximately 400 hPa upwards. In addition, the old scheme underestimates the OA concentrations at higher altitudes in the midlatitudes and the Arctic. The shape of the curve of the old scheme is different compared to observations and the rest of the simulations, especially in the Arctic. The old scheme exhibits a concentration minimum between 400 and 500 hPa, while observations are near the maximum values at those altitudes. At most, insol2sol underestimates the measurements at the highest altitudes, in all of the latitude bands, where the concentrations are over 1 order of magnitude less than the measurements. As the aging of aerosol particles in insol2sol is simulated by moving all insoluble particles that can activate to cloud droplets at 0.5 % supersaturation, almost all OA that is originally emitted to insoluble size classes is moved to soluble size classes. Thus, this enhances the activation and consequently the wet deposition of OA. Faster wet removal reduces the amount of OA transported to higher altitudes and thus reduces the OA concentrations. OA concentrations from all other simulations fall between the standard deviation limits of the ATom aircraft measurements everywhere, with only a slight overestimation between approximately 900 and 800 hPa in the tropics.

For  $\text{SO}_4$ , all of the sensitivity simulations show similar trends as the measurements but overestimate concentrations almost everywhere. In the tropics, the shape of the vertical profile in baserun\_old is similar to the observations and the rest of the simulations. In the midlatitudes, the vertical profile in baserun\_old shows stronger variation than observations and the rest of the simulations, overestimating the values below 800 hPa and overestimating them above 600 hPa. Over the Arctic, baserun\_old underestimates concentrations throughout the whole column, the maximum difference to observed values being almost 1 order of magnitude. The effect that insol2sol has on OA concentrations is also visible in the  $\text{SO}_4$  profiles, but here the effect is much weaker. In the tropics, insol2sol and baserun\_old show better agreement with the measurements from 700 hPa upwards than the other simulations, with only a slight overestimation. Between approximately 900 and 700 hPa, all of the simulations overestimate the measurements. This may be due to simplified sulfate chemistry in the model as  $\text{SO}_4$  is mainly formed through chemical transformation (Feichter et al., 1996). In the midlatitudes, all simulations overestimate the  $\text{SO}_4$  concentrations, with the exception of insol2sol and baserun\_old. The insol2sol reproduces the  $\text{SO}_4$  profile slightly better than the other simulations from approximately 600 hPa upwards. However, near the surface, all simulations overestimate the  $\text{SO}_4$  concentrations by approximately half an order of magnitude. In the Arctic, all of the simulations have similar  $\text{SO}_4$  profiles with a slight overestimation between approximately

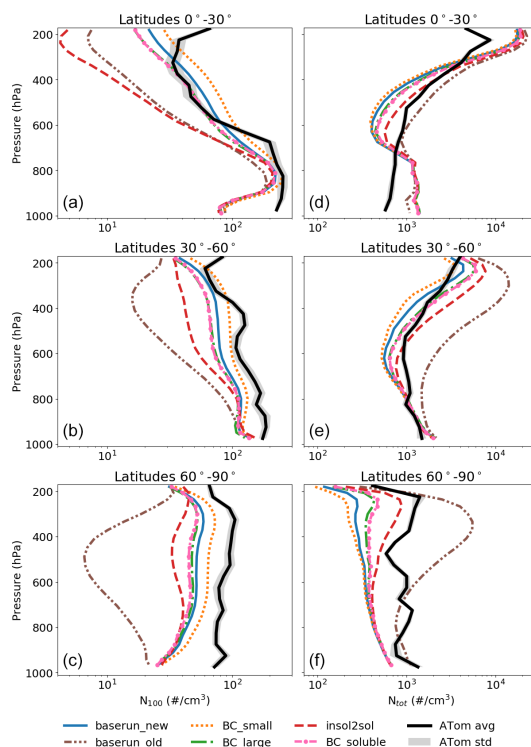


**Figure 6.** Mean vertical profiles of the  $N_{100}$  (a–c) and  $N_{\text{tot}}$  (d–f) concentrations, modeled with different studies, compared to the mean of ATom aircraft measurements in different latitude regions.

700 and 300 hPa altitude, with the exception of baserun\_old. In addition, at the highest altitudes all of the simulations underestimate the  $\text{SO}_4$  concentrations. The different sensitivity tests do not alter the  $\text{SO}_4$  concentrations much compared to baserun\_new because most of it condenses onto soluble particles. In addition, the new particles formed through nucleation are added to the soluble aerosol population. Thus, the  $\text{SO}_4$  vertical profiles are similar in all of the sensitivity simulations, with the exception of insol2sol where some of the  $\text{SO}_4$ , which repartitions from the insoluble to the soluble population, is activated more efficiently.

Figure 6 shows the vertical profiles of  $N_{100}$  and  $N_{\text{tot}}$ , simulated with different studies, together with ATom aircraft measurements. From the figure we can see that  $N_{100}$  profiles between different sensitivity simulations are similar in the midlatitudes and the Arctic. In these latitude bands, the sensitivity simulations slightly underestimate the  $N_{100}$  concentrations when compared to the measurements, but the trend is similar throughout the entire vertical column. However, insol2sol underestimates the  $N_{100}$  profiles slightly more in the midlatitudes and the Arctic. In addition, baserun\_old un-

derestimates  $N_{100}$  profiles even more than the other simulations, especially in the Arctic, where the maximum difference occurs at approximately 500 hPa altitude and is more than  $90 \text{ cm}^{-3}$  less than observed values. In the tropics, the simulations show a good correlation with the measurements as almost all of the profiles follow the shape of the profile of the ATom aircraft measurements, except for the surface concentrations, which are underestimated by a factor of approximately 2.5 compared to the measurements. In addition, in the tropics, insol2sol and baserun\_old underestimate  $N_{100}$  more than the other simulations from 800 hPa upwards. For insol2sol, this is also due to more efficient activation compared to baserun\_new for medium-sized particles which reduces the transport to higher altitudes.

The  $N_{\text{tot}}$  profiles are similar in shape in all sensitivity simulations, with only a modest difference ( $600 \text{ cm}^{-3}$  at maximum), mostly at higher altitudes. In the tropics the trend of the profiles varies between simulations and measurements. All of the simulations tend to overestimate the  $N_{\text{tot}}$  concentrations at the surface and at the highest altitudes by over 50 %. However, they underestimate the  $N_{\text{tot}}$  concentrations at approximately 400–700 hPa, with the exception of baserun\_old, which overestimates these concentrations. In the midlatitudes, all of the simulations represent  $N_{\text{tot}}$  concentrations fairly well (approximately  $500 \text{ cm}^{-3}$  underestimation and  $4000 \text{ cm}^{-3}$  overestimation at most) when compared to the measurements, with the exception of baserun\_old, which overestimates these concentrations at all altitudes with almost 1 order of magnitude at maximum. However, in the Arctic, all of the sensitivity simulations underestimate the  $N_{\text{tot}}$  profiles. At higher altitudes, starting from approximately 600 hPa upwards, insol2sol underestimates  $N_{\text{tot}}$  least, showing quite good agreement with the measurements with only around  $300 \text{ cm}^{-3}$  difference at most. The baserun\_old simulation, on the other hand, shows good agreement with the measurements at highest altitudes and below 600 hPa but overestimates the  $N_{\text{tot}}$  profile between 600 and 200 hPa by over  $5000 \text{ cm}^{-3}$  at most.

One of the reasons for the differences in the  $N_{\text{tot}}$  and  $N_{100}$  surface concentrations may be due to a misrepresentation of the emitted particle size distribution. In ECHAM-HAMMOZ the same aerosol emission size distribution per compound and emission sector is assumed throughout the whole world, which is not very realistic for every aerosol particle source (Paasonen et al., 2016). At higher altitudes, the aerosol microphysical processes correct the aerosol size distribution towards more realistic profiles.

To investigate the effects of the different sensitivity studies further, we computed the size and mass distribution of the wet deposition flux (Fig. 7). The mass fluxes in the soluble population do not change much between baserun\_new and the different sensitivity studies, except for the insol2sol simulation, which allows for sufficiently hygroscopic particles of the insoluble population to be repartitioned to the soluble population. This leads to an increase in DU mass in the

soluble population and a decrease in the insoluble population. In addition to more efficient wet removal of DU due to this process, this also increases dry deposition and sedimentation (not shown) of DU in insol2sol. For the mass fluxes in the insoluble population, BC\_large and BC\_soluble show an increase in the largest size class for DU. This effect is due to more efficient removal of BC-containing particles, which allows for more  $\text{SO}_4$  to condense on larger, DU-containing particles, which enhances the activation of these particles.

The number fluxes in the soluble population for the different sensitivity simulations show most change in the two smallest size classes, which increase by a factor of approx 1.3 in the insol2sol simulation and approximately 1.1 for BC\_large and BC\_soluble when compared to baserun\_new (shown in Fig. 4). These differences stem from changes in medium-sized and large particle concentrations, which act as a condensation sink for  $\text{SO}_4$  and thereby regulate the amount of  $\text{SO}_4$  available for new particle formation. In addition, there is a slight increase in OC in the insol2sol-simulated number distribution, which is being transferred from the insoluble population. Otherwise, there is no notable change in other compounds as the  $\text{SO}_4$  dominates the number distribution in the soluble population. The relative BC mass contribution to the wet deposition number flux of the insoluble aerosol population reflects the assumptions made in the different sensitivity studies very well. While for BC\_large and BC\_soluble the BC mass fraction in the medium-sized insoluble particles disappears, in BC\_small the BC fraction in the 50 to 100 nm insoluble particles is about 3 times larger than in baserun\_new (shown in Fig. 4). This shows that coagulation is not effective in moving BC from these small insoluble particles to large soluble particles. In insol2sol, most of the BC is transferred from the insoluble to the soluble aerosol population before removal, which can be seen in a strong decrease in removed insoluble aerosol number for that simulation.

In addition to the evaluation of the simulated vertical aerosol profiles, we used the modeled atmospheric lifetimes of all aerosol compounds as an indicator of the model skill in the different simulations. Here we estimated the atmospheric lifetime of a compound as the yearly and global mean mass burden of the compound divided by its total yearly mean emission. The compiled mean lifetimes for the different simulations and compounds as well as the mean and spread of lifetimes from several AEROCOM models (CAM5-ATRAS, EC-Earth, TM5, ECHAM-HAM, ECHAM-SALSA, ECMWF-IFS, EMEP, GEOS, GFDL-AM4, GISS-OMA, INCA, NorESM2, OsloCTM3, and SPRINTARS) are presented in Table 2 (Gliß et al., 2020). The spread is calculated as half the difference between the first and third quantiles (Gliß et al., 2020).

With the assumption that the AEROCOM mean atmospheric lifetimes are the current best guess, we can use Table 2 to select a simulation that best reproduces these mean lifetimes and therefore could be regarded as the best solution to address the overestimated BC lifetimes in baserun\_new.



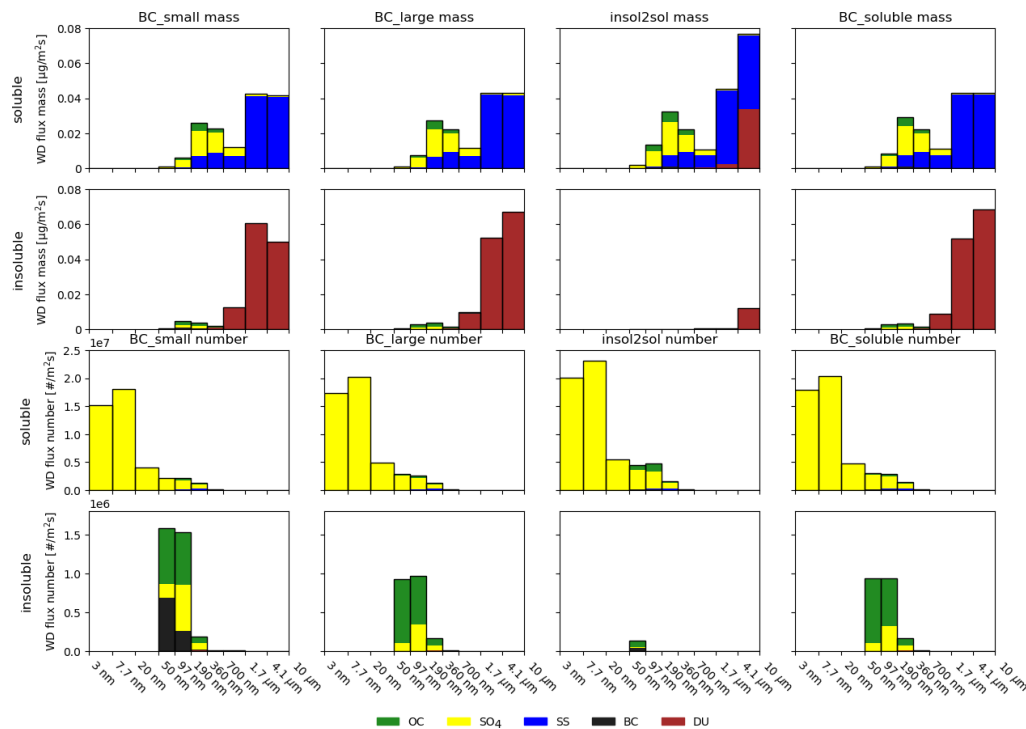


**Figure 7.** Wet deposition flux size distributions of different aerosol compounds simulated with different sensitivity simulations. Each column represents a different sensitivity study and each row the solubility type. The top two rows show the mass size distribution of the wet deposition flux and the bottom two rows the number size distribution.

**Table 2.** Lifetimes of compounds from different simulations as well as mean and spread from different AEROCOM models.

	baserun_old	baserun_new	BC_small	BC_large	insol2sol	BC_soluble	AEROCOM	$\sigma_{\text{AEROCOM}}$
$\tau_{\text{BC}}$ (d)	9.23	14.62	16.49	5.78	5.04	4.98	5.8	2.3
$\tau_{\text{DU}}$ (d)	4.07	5.36	5.69	5.00	1.06	4.86	4.5	1.9
$\tau_{\text{SO}_4}$ (d)	4.02	6.10	6.37	5.73	4.69	5.67	4.7	1.6
$\tau_{\text{OC}}$ (d)	6.38	9.44	9.52	9.03	4.90	8.90	6.1	2.0
$\tau_{\text{SS}}$ (d)	1.59	1.57	1.57	1.56	1.55	1.56	0.82	0.56

However, we must keep in mind that AEROCOM means are global-climate-model-based results, and thus it is not completely certain that these lifetimes of different compounds reflect the actual lifetimes in the real atmosphere. While baserun\_old, baserun\_new, and BC\_small overestimate the BC lifetime by factors of 1.6, 2.5, and 2.8, respectively, BC\_large, insol2sol, and BC\_soluble all produce BC lifetimes within 1 d of the AEROCOM mean. In addition, the BC lifetimes should be less than 5.5 d according to Lund et al. (2018). However, the different sensitivity studies also affect the atmospheric lifetimes of the other species, and some of them considerably. For instance, the lifetime of DU in insol2sol is almost 4.5 times shorter than the AERO-

COM mean, while both BC\_large and BC\_soluble overestimate this mean only slightly by half a day. On the other hand, the atmospheric lifetime of OC in insol2sol is closest to the AEROCOM mean compared to all other simulations using the current wet deposition scheme. However, in this setup of ECHAM-HAMMOZ all OC is emitted as primary particles, while in reality a large fraction of the organic aerosol is formed as secondary organic aerosol (SOA) in the atmosphere. Modeling the processes leading to SOA formation more realistically would most likely affect the modeled OC lifetimes quite substantially. The atmospheric lifetime of SO<sub>4</sub> in insol2sol is also closest to the AEROCOM mean, but BC\_large and BC\_soluble also model the SO<sub>4</sub> lifetime fairly



well. For SS, the atmospheric lifetime does not change when changing the wet removal algorithm or during any of the sensitivity tests as SS is only emitted to the soluble population. The lifetimes for all simulations are more than 0.7 d higher than the AEROCOM mean (about a factor of 2). This has already been discussed by Kokkola et al. (2018a) and Tegen et al. (2019).

#### 4 Conclusions

We developed an in-cloud nucleation wet deposition scheme for liquid and ice clouds. For liquid clouds, the scavenging coefficients are calculated using the size-segregated fraction of activated particles from a cloud activation scheme. For ice clouds, the scavenging coefficients are calculated based on the surface area concentration of each size class (see Tabazadeh et al., 2002).

We used the SALSA microphysics scheme coupled with the ECHAM-HAMMOZ global aerosol–chemistry–climate model to evaluate the differences between the old and current wet deposition schemes. In addition, we used ECHAM-HAMMOZ with SALSA to test the sensitivity of the simulated aerosol concentrations to model assumptions of emission sizes, mixing, and aging when the current in-cloud wet deposition scheme was used. In its original setup, SALSA used fixed scavenging coefficients for modeling wet deposition. Here, we used the Abdul-Razzak and Ghan (2002) cloud activation scheme for the calculations of size-dependent nucleation scavenging coefficients in liquid clouds. For ice clouds, we used the scheme of Lohmann (2002) for providing the ice nucleation rates for the nucleation scavenging scheme (see Tabazadeh et al., 2002). The in-cloud impaction scavenging for SALSA was adapted from the method for the modal scheme by Croft et al. (2010).

Compared to using fixed scavenging coefficients, the current scheme showed an increase in BC, OA, and SO<sub>4</sub> vertical profiles almost throughout the entire vertical domain for all latitude bands. In the Arctic region this increase was most pronounced, with a maximum increase of up to 800 %. The differences in vertical profiles had similar functional shapes in all latitude bands and for all three compounds. The increase was mainly due to a decrease in the nucleation scavenging of aerosol particles in the current scheme, which increased aerosol transport into the upper atmosphere and subsequently to the Arctic region. The current scheme also showed a significant increase of up to 600 % at maximum in the number concentration of particles larger than 100 nm, which was similar in shape to the change in aerosol compound mass. However, the number concentration of particles smaller than 100 nm decreased everywhere, with a maximum decrease of 90 % in the Arctic. This could imply that new particle formation was reduced in the current scheme due to the increased concentration of large particles, which increased the condensation sink for SO<sub>4</sub>. In addition, the changes in

impaction scavenging rates in the current scheme compared to the original setup can reduce the number concentration of particles smaller than 100 nm (Croft et al., 2010).

An evaluation of the current wet deposition scheme against ATom aircraft measurements showed that, using the default setup of the host model, the current scheme overestimated BC mass concentrations, especially at higher altitudes. Additional sensitivity simulations showed that the model skill of reproducing measured vertical BC mass concentration profiles could be improved a lot by directing the BC emissions to larger or to more soluble size classes or by transferring BC-containing particles to soluble size classes after aging. These sensitivity studies also produced BC atmospheric lifetimes which were closest to the AEROCOM model mean (Gliß et al., 2020). Emitting BC to smaller size classes, on the other hand, overestimated the aerosol mass concentrations and BC atmospheric lifetime even more. However, changing the distribution of BC in the sensitivity simulations also affected the mass concentrations of other aerosol compounds. For instance, transferring insoluble particles to soluble size classes after aging led to an underestimation of the observed OA concentrations at higher altitudes, while in the other simulations OA concentrations fell between the standard deviation limits of ATom measurements almost everywhere. The modeled atmospheric lifetime of OA, on the other hand, compared best to the AEROCOM mean when transferring aged insoluble particles to soluble size classes. However, as in this study secondary processes of OA formation were neglected, we did not use OA as an indicator for the skill of our wet deposition scheme. For SO<sub>4</sub>, the insoluble-to-soluble transfer reproduced the observed concentrations slightly better at higher altitudes in the tropics. Nevertheless, all simulations showed similar results for SO<sub>4</sub> concentrations, with only a slight overestimation when compared to the aircraft observations. In addition, SO<sub>4</sub> atmospheric lifetimes did not vary much across the different sensitivity studies. All of the sensitivity studies reproduced aerosol number concentration profiles fairly well. However, the insoluble-to-soluble transfer considerably underestimated the concentrations of activation-sized particles at the highest altitudes in the tropics, which was strongly tied to the underestimation of OC at these altitudes. Furthermore, the atmospheric lifetime of atmospheric mineral dust (DU) was strongly underestimated in the simulation using insoluble-to-soluble transfer of aged particles. The atmospheric lifetimes of SS did not change between the different sensitivity studies. All in all, while reasonable BC vertical profiles and atmospheric lifetimes could be achieved with the current wet deposition scheme in three of the sensitivity studies, namely emitting BC to more hygroscopic or to larger particles or transferring insoluble, BC-containing particles, to soluble size classes, only the first option is really suitable. Emitting BC to large particles is quite unrealistic because the emission size of BC-containing particles is fairly well established (Tissari et al., 2008; Krecl et al., 2017; Corbin et al., 2018; Zhang et al., 2019) and insoluble-

to-soluble transfer, on the other hand, leads to atmospheric lifetimes of DU that are too small.

To conclude, even though the current in-cloud wet deposition scheme is more physically sound than using fixed scavenging coefficients, it failed to reproduce global aerosol fields adequately in the default setup of the host model. This can be seen from the spuriously long lifetimes of all aerosol species. In particular, the BC atmospheric lifetime was almost 3 times as large as what observations indicate (Lund et al., 2018). Based on the results of our sensitivity simulations, the ECHAM-HAMMOZ global climate model with the SALSA aerosol module produces the best vertical profiles and aerosol lifetimes with the current scheme if BC is mixed with more soluble compounds at emission time. In the future, model development should include the study of the effects of the gas-to-particle partitioning of semivolatile compounds which could have a significant impact on the modeled aerosol vertical profiles. In addition, the issue of the level of mixing of BC with soluble compounds during emissions and in the subgrid-scale processing should be further investigated.

## Appendix A: Calculations for particles containing an insoluble core

The calculations for the particles containing an insoluble core are based on the technical report by Kokkola et al. (2008), where the critical supersaturation is obtained as

$$\frac{S_c}{A} = \frac{2\left(\frac{b}{3}\right)^2 + \left(\frac{b}{3}\right)\left[\left(\frac{\gamma_{\pm}}{2}\right)^{1/3} + \left(\frac{\gamma_{\mp}}{2}\right)^{1/3}\right] + \left[\left(\frac{\gamma_{\pm}}{2}\right)^{2/3} + \left(\frac{\gamma_{\mp}}{2}\right)^{2/3}\right]}{9\left(\frac{b}{3}\right)^3 + 6\left(\frac{b}{3}\right)^2\left[\left(\frac{\gamma_{\pm}}{2}\right)^{1/3} + \left(\frac{\gamma_{\mp}}{2}\right)^{1/3}\right] + 3\left(\frac{b}{3}\right)\left[\left(\frac{\gamma_{\pm}}{2}\right)^{2/3} + \left(\frac{\gamma_{\mp}}{2}\right)^{2/3}\right] + d}, \quad (\text{A1})$$

where

$$\gamma_{\pm} = \left[ 2\left(\frac{b}{3}\right)^3 + d \right] \pm \sqrt{4\left(\frac{b}{3}\right)^3 d + d^2}, \quad (\text{A2})$$

$$b = \sqrt{\frac{3B}{A}}, \quad (\text{A3})$$

and

$$d = D_{p,0}^3, \quad (\text{A4})$$

where  $D_{p,0}$  is the diameter of the insoluble core.

In Eq. (A3),  $A$  and  $B$  are obtained from Seinfeld and Pandis (2006).  $A$  describes the increase in water vapor pressure due to the curvature of the particle surface and is denoted as

$$A = \frac{4M_w\sigma_w}{R\rho_w T}, \quad (\text{A5})$$

where  $M_w$  is the molecular weight of water,  $\rho_w$  is the density of water,  $\sigma_w$  is the surface tension of the droplet,  $T$  is the temperature, and  $R$  is the universal gas constant.  $B$  is called the solute effect term and is denoted as

$$B = \frac{6n_s M_w}{\pi \rho_w}, \quad (\text{A6})$$

where  $n_s$  is the moles of solute in a droplet.

Using this new expression for the critical supersaturation, the effective critical supersaturation, maximum supersaturation, and the number fraction of activated particles for each size class can be calculated using Eqs. (8), (9), and (12)–(15) from Abdul-Razzak and Ghan (2002).

**Code availability.** The stand-alone zero-dimensional version of SALSA2.0 is distributed under the Apache-2.0 license and the code is available at <https://github.com/UCLALES-SALSA/SALSA-standalone/releases/tag/2.0> (last access: 23 May 2018; Kokkola et al., 2018b) with <https://doi.org/10.5281/zenodo.1251668>.

The ECHAM6-HAMMOZ model is made available to the scientific community under the HAMMOZ Software License Agreement, which defines the conditions under which the model can be used. The license can be downloaded from [https://redmine.hammoz.ethz.ch/attachments/291/License\\_ECHAM-HAMMOZ\\_June2012.pdf](https://redmine.hammoz.ethz.ch/attachments/291/License_ECHAM-HAMMOZ_June2012.pdf) (last access: 29 June 2012; HAMMOZ consortium, 2012).

The model data can be reproduced using the model revision r5511 from the repository [https://redmine.hammoz.ethz.ch/projects/hammoz/repository/changes/echam6-hammoz/branches/fmi/fmi\\_trunk](https://redmine.hammoz.ethz.ch/projects/hammoz/repository/changes/echam6-hammoz/branches/fmi/fmi_trunk) (last access: 8 March 2019; HAMMOZ consortium, 2019a, b). The settings for the simulations are given in the same folder (“gmd-2020-220”).

**Data availability.** The data for reproducing the figures and codes for the figures can be obtained directly from authors or from <https://etsin.fairdata.fi/dataset/f3cb5807-66fe-4a0d-a20a-ac208d3aab5a> (last access: 29 June 2020; Holopainen et al., 2020) with <https://doi.org/10.23729/301df277-8147-4700-8652-ca491f2b58a6>. All other input files are ECHAM-HAMMOZ standard and are available from the HAMMOZ repository (see <https://redmine.hammoz.ethz.ch/projects/hammoz>; HAMMOZ consortium, 2019a, b).

ATom aircraft data can be obtained through the Oak Ridge National Laboratory (ORNL) Distributed Active Archive Center (DAAC) [https://daac.ornl.gov/cgi-bin/dsviewer.pl?ds\\_id=1581](https://daac.ornl.gov/cgi-bin/dsviewer.pl?ds_id=1581) (last access: 25 November 2019; Wofsy et al., 2018) with <https://doi.org/10.3334/ORNLDAAC/1581>.

**Author contributions.** EH, TK, and HK designed the outline of the paper. EH wrote the majority of the paper. EH performed all the climate simulations. EH, TK, and HK developed the current wet deposition scheme. TK and HK provided the calculations for particles containing an insoluble core. EH and AL modified the emission distributions for the sensitivity simulations. EH, TK, HK, and AL performed the data analysis for the climate simulations, and EH produced the figures. All the authors contributed to the writing of the paper.

**Competing interests.** The authors declare that they have no conflict of interest.

**Acknowledgements.** ECHAM-HAMMOZ is developed by a consortium composed of ETH Zürich, Max Planck Institut für Meteorologie, Forschungszentrum Jülich, University of Oxford, the Finnish Meteorological Institute, and the Leibniz Institute for Tropospheric Research and managed by the Center for Climate Systems Modeling (C2SM) at ETH Zürich. We thank NASA/ORNL DAAC for Atmospheric Tomography Mission (ATom) aircraft data.

**Financial support.** This research has been supported by the Academy of Finland, Luonnontieteiden ja Tekniikan Tutkimuksen Toimikunta (grant nos. 317373, 308292), the European Research Council (CLIMASLOW, grant no. 678889), and the Tiina and Antti Herlin Foundation (grant no. 20190014).

**Review statement.** This paper was edited by Jason Williams and reviewed by two anonymous referees.

## References

- Abdul-Razzak, H. and Ghan, S.: A parameterization of aerosol activation. Part 3: Sectional representation, *J. Geophys. Res.*, 107, 1–6, <https://doi.org/10.1029/2001JD000483>, 2002.
- Albrecht, B. A.: Aerosols, Cloud Microphysics, and Fractional Cloudiness, *Science*, 245, 1227–1230, <https://doi.org/10.1126/science.245.4923.1227>, 1989.
- AMAP: AMAP assessment 2015: Black carbon and ozone as Arctic climate forcers, vol. 7, Arctic Monitoring and Assessment Programme (AMAP), Oslo, Norway, 2015.
- Andersson, C., Bergström, R., Bennet, C., Robertson, L., Thomas, M., Korhonen, H., Lehtinen, K. E. J., and Kokkola, H.: MATCH-SALSA – Multi-scale Atmospheric Transport and Chemistry model coupled to the SALSA aerosol microphysics model – Part 1: Model description and evaluation, *Geosci. Model Dev.*, 8, 171–189, <https://doi.org/10.5194/gmd-8-171-2015>, 2015.
- Andronache, C.: Estimated variability of below-cloud aerosol removal by rainfall for observed aerosol size distributions, *Atmos. Chem. Phys.*, 3, 131–143, <https://doi.org/10.5194/acp-3-131-2003>, 2003.
- Andronache, C., Grönholm, T., Laakso, L., Phillips, V., and Venäläinen, A.: Scavenging of ultrafine particles by rainfall at a boreal site: observations and model estimations, *Atmos. Chem. Phys.*, 6, 4739–4754, <https://doi.org/10.5194/acp-6-4739-2006>, 2006.
- Archuleta, C. M., DeMott, P. J., and Kreidenweis, S. M.: Ice nucleation by surrogates for atmospheric mineral dust and mineral dust/sulfate particles at cirrus temperatures, *Atmos. Chem. Phys.*, 5, 2617–2634, <https://doi.org/10.5194/acp-5-2617-2005>, 2005.
- Barahona, D. and Nenes, A.: Parameterization of cloud droplet formation in large-scale models: Including effects of entrainment, *J. Geophys. Res.-Atmos.*, 112, D16206, <https://doi.org/10.1029/2007JD008473>, 2007.
- Bergman, T., Kerminen, V.-M., Korhonen, H., Lehtinen, K. J., Makkonen, R., Arola, A., Mielonen, T., Romakkaniemi, S., Kulmala, M., and Kokkola, H.: Evaluation of the sectional aerosol microphysics module SALSA implementation in ECHAM5-HAM aerosol-climate model, *Geosci. Model Dev.*, 5, 845–868, <https://doi.org/10.5194/gmd-5-845-2012>, 2012.
- Berrisford, P., Dee, D., Poli, P., Brugge, R., Fielding, K., Fuentes, M., Kållberg, P., Kobayashi, S., Uppala, S., and Simmons, A.: The ERA-Interim archive Version 2.0, Shinfield Park, Reading, 2011.
- Bond, T. C., Doherty, S. J., Fahey, D. W., Forster, P. M., Berntsen, T., DeAngelo, B. J., Flanner, M. G., Ghan, S., Kärcher, B., Koch, D., Kinne, S., Kondo, Y., Quinn, P. K., Sarofim, M. C., Schultz, M. G., Schulz, M., Venkataraman, C., Zhang, H., Zhang, S., Bellouin, N., Guttikunda, S. K., Hopke, P. K., Jacobson,

- M. Z., Kaiser, J. W., Klimont, Z., Lohmann, U., Schwarz, J. P., Shindell, D., Storelvmo, T., Warren, S. G., and Zender, C. S.: Bounding the role of black carbon in the climate system: A scientific assessment, *J. Geophys. Res.-Atmos.*, 118, 5380–5552, <https://doi.org/10.1002/jgrd.50171>, 2013.
- Bourgeois, Q. and Bey, I.: Pollution transport efficiency toward the Arctic: Sensitivity to aerosol scavenging and source regions, *J. Geophys. Res.*, 116, D08213, <https://doi.org/10.1029/2010JD015096>, 2011.
- Brock, C. A., Williamson, C., Kupc, A., Froyd, K. D., Erdesz, F., Wagner, N., Richardson, M., Schwarz, J. P., Gao, R.-S., Katich, J. M., Campuzano-Jost, P., Nault, B. A., Schroder, J. C., Jimenez, J. L., Weinzierl, B., Dollner, M., Bui, T., and Murphy, D. M.: Aerosol size distributions during the Atmospheric Tomography Mission (ATom): methods, uncertainties, and data products, *Atmos. Meas. Tech.*, 12, 3081–3099, <https://doi.org/10.5194/amt-12-3081-2019>, 2019.
- Browse, J., Carslaw, K. S., Arnold, S. R., Pringle, K., and Boucher, O.: The scavenging processes controlling the seasonal cycle in Arctic sulphate and black carbon aerosol, *Atmos. Chem. Phys.*, 12, 6775–6798, <https://doi.org/10.5194/acp-12-6775-2012>, 2012.
- Chate, D., Rao, P., Naik, M., Momin, G., Safai, P., and Ali, K.: Scavenging of aerosols and their chemical species by rain, *Atmos. Environ.*, 37, 2477–2484, [https://doi.org/10.1016/S1352-2310\(03\)00162-6](https://doi.org/10.1016/S1352-2310(03)00162-6), 2003.
- Chate, D., Murugavel, P., Ali, K., Tiwari, S., and Beig, G.: Below-cloud rain scavenging of atmospheric aerosols for aerosol deposition models, *Atmospheric Research*, 99, 528–536, <https://doi.org/10.1016/j.atmosres.2010.12.010>, 2011.
- Chen, J.-P. and Lamb, D.: Simulation of Cloud Microphysical and Chemical Processes Using a Multicomponent Framework. Part I: Description of the Microphysical Model, *J. Atmos. Sci.*, 51, 2613–2630, [https://doi.org/10.1175/1520-0469\(1994\)051<2613:SOCMAC>2.0.CO;2](https://doi.org/10.1175/1520-0469(1994)051<2613:SOCMAC>2.0.CO;2), 1994.
- Corbin, J. C., Pieber, S. M., Czech, H., Zanatta, M., Jakobi, G., Massabò, D., Orasche, J., El Haddad, I., Mensah, A. A., Stengel, B., Drinovec, L., Mocnik, G., Zimmermann, R., Prévôt, A. S. H., and Gysel, M.: Brown and Black Carbon Emitted by a Marine Engine Operated on Heavy Fuel Oil and Distillate Fuels: Optical Properties, Size Distributions, and Emission Factors, *J. Geophys. Res.-Atmos.*, 123, 6175–6195, <https://doi.org/10.1029/2017JD027818>, 2018.
- roft, B., Lohmann, U., Martin, R. V., Stier, P., Wurzler, S., Feichter, J., Posselt, R., and Ferrachat, S.: Aerosol size-dependent below-cloud scavenging by rain and snow in the ECHAM5-HAM, *Atmos. Chem. Phys.*, 9, 4653–4675, <https://doi.org/10.5194/acp-9-4653-2009>, 2009.
- Croft, B., Lohmann, U., Martin, R. V., Stier, P., Wurzler, S., Feichter, J., Hoose, C., Heikkilä, U., van Donkelaar, A., and Ferrachat, S.: Influences of in-cloud aerosol scavenging parameterizations on aerosol concentrations and wet deposition in ECHAM5-HAM, *Atmos. Chem. Phys.*, 10, 1511–1543, <https://doi.org/10.5194/acp-10-1511-2010>, 2010.
- Croft, B., Martin, R. V., Leitch, W. R., Tunved, P., Breider, T. J., D'Andrea, S. D., and Pierce, J. R.: Processes controlling the annual cycle of Arctic aerosol number and size distributions, *Atmos. Chem. Phys.*, 16, 3665–3682, <https://doi.org/10.5194/acp-16-3665-2016>, 2016.
- de Bruine, M., Krol, M., van Noije, T., Le Sager, P., and Röckmann, T.: The impact of precipitation evaporation on the atmospheric aerosol distribution in EC-Earth v3.2.0, *Geosci. Model Dev.*, 11, 1443–1465, <https://doi.org/10.5194/gmd-11-1443-2018>, 2018.
- Dentener, F., Kinne, S., Bond, T., Boucher, O., Cofala, J., Geroso, S., Ginoux, P., Gong, S., Hoelzemann, J. J., Ito, A., Marelli, L., Penner, J. E., Putaud, J.-P., Textor, C., Schulz, M., van der Werf, G. R., and Wilson, J.: Emissions of primary aerosol and precursor gases in the years 2000 and 1750 prescribed data-sets for AeroCom, *Atmos. Chem. Phys.*, 6, 4321–4344, <https://doi.org/10.5194/acp-6-4321-2006>, 2006.
- Easter, R. C., Ghan, S. J., Zhang, Y., Saylor, R. D., Chapman, E. G., Laulainen, N. S., Abdul-Razzak, H., Leung, L. R., Bian, X., and Zaveri, R. A.: MIRAGE: Model description and evaluation of aerosols and trace gases, *J. Geophys. Res.-Atmos.*, 109, D20210, <https://doi.org/10.1029/2004JD004571>, 2004.
- Eckhardt, S., Quennehen, B., Olivé, D. J. L., Bernsten, T. K., Cherian, R., Christensen, J. H., Collins, W., Crepinsek, S., Daskalakis, N., Flanner, M., Herber, A., Heyes, C., Hodnebrog, Ø., Huang, L., Kanakidou, M., Klimont, Z., Langner, J., Law, K. S., Lund, M. T., Mahmood, R., Massling, A., Myriokefalitakis, S., Nielsen, I. E., Nøjgaard, J. K., Quaas, J., Quinn, P. K., Raut, J.-C., Rumbold, S. T., Schulz, M., Sharma, S., Skeie, R. B., Skov, H., Uttal, T., von Salzen, K., and Stohl, A.: Current model capabilities for simulating black carbon and sulfate concentrations in the Arctic atmosphere: a multi-model evaluation using a comprehensive measurement data set, *Atmos. Chem. Phys.*, 15, 9413–9433, <https://doi.org/10.5194/acp-15-9413-2015>, 2015.
- Feichter, J., Kjellström, E., Rodhe, H., Dentener, F., Lelieveld, J., and Roelofs, G.-J.: Simulation of the tropospheric sulfur cycle in a global climate model, *Atmos. Environ.*, 30, 1693–1707, [https://doi.org/10.1016/1352-2310\(95\)00394-0](https://doi.org/10.1016/1352-2310(95)00394-0), 1996.
- Flossmann, A. I. and Wobrock, W.: A review of our understanding of the aerosol–cloud interaction from the perspective of a bin resolved cloud scale modelling, *Atmos. Res.*, 97, 478–497, <https://doi.org/10.1016/j.atmosres.2010.05.008>, 2010.
- Garrett, T., Zhao, C., and Novelli, P.: Assessing the relative contributions of transport efficiency and scavenging to seasonal variability in Arctic aerosol, *Tellus B*, 62, 190–196, <https://doi.org/10.1111/j.1600-0889.2010.00453.x>, 2010.
- Gliß, J., Mortier, A., Schulz, M., Andrews, E., Balkanski, Y., Bauer, S. E., Benedictow, A. M. K., Bian, H., Checa-Garcia, R., Chin, M., Ginoux, P., Griesfeller, J. J., Heckel, A., Kipling, Z., Kirkevåg, A., Kokkola, H., Laj, P., Le Sager, P., Lund, M. T., Lund Myhre, C., Matsui, H., Myhre, G., Neubauer, D., van Noije, T., North, P., Olivé, D. J. L., Sogacheva, L., Takemura, T., Tsigaridis, K., and Tsyro, S. G.: Multi-model evaluation of aerosol optical properties in the AeroCom phase III Control experiment, using ground and space based columnar observations from AERONET, MODIS, AATSR and a merged satellite product as well as surface in-situ observations from GAW sites, *Atmos. Chem. Phys. Discuss.*, <https://doi.org/10.5194/acp-2019-1214>, in review, 2020.
- HAMMOZ consortium: HAMMOZ Software Licence Agreement, available at: [https://redmine.hammoz.ethz.ch/attachments/291/License\\_ECHAM-HAMMOZ\\_June2012.pdf](https://redmine.hammoz.ethz.ch/attachments/291/License_ECHAM-HAMMOZ_June2012.pdf), last access: 29 June 2012.
- HAMMOZ consortium: ECHAM-HAMMOZ model data, available at: <https://redmine.hammoz.ethz.ch/projects/hammoz/>

- repository/show/echam6-hammoz/branches/fmi/fmi\_trunk, last access: 8 March 2019.
- HAMMOZ consortium: ECHAM-HAMMOZ input data, available at: <https://redmine.hammoz.ethz.ch/projects/hammoz>, last access: 8 March 2019.
- Haywood, J. M. and Shine, K. P.: Multi-spectral calculations of the direct radiative forcing of tropospheric sulphate and soot aerosols using a column model, *Q. J. Roy. Meteor. Soc.*, 123, 1907–1930, <https://doi.org/10.1002/qj.49712354307>, 1997.
- Hobbs, P.: Aerosol-cloud-climate interactions, vol. 54, Academic Press, San Diego, 1993.
- Holopainen, E., Kokkola, H., Laakso, A., and Kühn, T.: In-cloud scavenging scheme for aerosol modules 2019–2020 data, Eemeli Holopainen <https://doi.org/10.23729/301df277-8147-4700-8652-ca491f2b58a6>, 2020.
- Horowitz, L. W., Walters, S., Mauzerall, D. L., Emmons, L. K., Rasch, P. J., Granier, C., Tie, X., Lamarque, J.-F., Schultz, M., and Brasseur, G. P.: A global simulation of tropospheric ozone and related tracers: Description and evaluation of MOZART, version 2, *J. Geophys. Res.-Atmos.*, 108, 4784, <https://doi.org/10.1029/2002JD002853>, 2003.
- IPCC: Climate Change 2013 – The Physical Science Basis: Working Group I Contribution to the Fifth Assessment Report of the Intergovernmental Panel on Climate Change, Cambridge University Press, 659–740, <https://doi.org/10.1017/CBO9781107415324.018>, 2014.
- Kipling, Z., Stier, P., Johnson, C. E., Mann, G. W., Bellouin, N., Bauer, S. E., Bergman, T., Chin, M., Diehl, T., Ghan, S. J., Iversen, T., Kirkevåg, A., Kokkola, H., Liu, X., Luo, G., van Noije, T., Pringle, K. J., von Salzen, K., Schulz, M., Seland, Ø., Skeie, R. B., Takemura, T., Tsigaridis, K., and Zhang, K.: What controls the vertical distribution of aerosol? Relationships between process sensitivity in HadGEM3–UKCA and inter-model variation from AeroCom Phase II, *Atmos. Chem. Phys.*, 16, 2221–2241, <https://doi.org/10.5194/acp-16-2221-2016>, 2016.
- Köhler, H.: The nucleus in and the growth of hygroscopic droplets, *Trans. Faraday Soc.*, 32, 1152–1161, <https://doi.org/10.1039/TF9363201152>, 1936.
- Kokkola, H., Vesterinen, M., Anttila, T., Laaksonen, A., and Lehtinen, K. E. J.: Technical note: Analytical formulae for the critical supersaturations and droplet diameters of CCN containing insoluble material, *Atmos. Chem. Phys.*, 8, 1985–1988, <https://doi.org/10.5194/acp-8-1985-2008>, 2008.
- Kokkola, H., Kühn, T., Laakso, A., Bergman, T., Lehtinen, K. E. J., Mielonen, T., Arola, A., Stadtler, S., Korhonen, H., Ferrachat, S., Lohmann, U., Neubauer, D., Tegen, I., Siegenthaler-Le Drian, C., Schultz, M. G., Bey, I., Stier, P., Daskalakis, N., Heald, C. L., and Romakkaniemi, S.: SALSA2.0: The sectional aerosol module of the aerosol–chemistry–climate model ECHAM6.3.0–HAM2.3–MOZ1.0, *Geosci. Model Dev.*, 11, 3833–3863, <https://doi.org/10.5194/gmd-11-3833-2018>, 2018a.
- Kokkola, H., Tonttila, J., Romakkaniemi, S., Bergman, T., Laakso, A., Kühn, T., Mielonen, T., Kudzsotsa, I., and Raatikainen, T.: SALSA-standalone 2.0, Zenodo, <https://doi.org/10.5281/zenodo.1251669>, 2018b.
- Korhonen, H., Carslaw, K. S., Spracklen, D. V., Ridley, D. A., and Ström, J.: A global model study of processes controlling aerosol size distributions in the Arctic spring and summer, *J. Geophys. Res.-Atmos.*, 113, D08211, <https://doi.org/10.1029/2007JD009114>, 2008.
- Korolev, A., Emery, E., Strapp, J., Cober, S., Isaac, G., Wasey, M., and Marcotte, D.: Small Ice Particles in Tropospheric Clouds: Fact or Artifact? Airborne Icing Instrumentation Evaluation Experiment, *B. Am. Meteorol. Soc.*, 92, 967–973, <https://doi.org/10.1175/2010BAMS3141.1>, 2011.
- Krecl, P., Johansson, C., Targino, A. C., Ström, J., and Burman, L.: Trends in black carbon and size-resolved particle number concentrations and vehicle emission factors under real-world conditions, *Atmos. Environ.*, 165, 155–168, <https://doi.org/10.1016/j.atmosenv.2017.06.036>, 2017.
- Kristiansen, N. I., Stohl, A., Olivé, D. J. L., Croft, B., Søvde, O. A., Klein, H., Christoudias, T., Kunkel, D., Leadbetter, S. J., Lee, Y. H., Zhang, K., Tsigaridis, K., Bergman, T., Evangelio, N., Wang, H., Ma, P.-L., Easter, R. C., Rasch, P. J., Liu, X., Pitari, G., Di Genova, G., Zhao, S. Y., Balkanski, Y., Bauer, S. E., Faluvegi, G. S., Kokkola, H., Martin, R. V., Pierce, J. R., Schulz, M., Shindell, D., Tost, H., and Zhang, H.: Evaluation of observed and modelled aerosol lifetimes using radioactive tracers of opportunity and an ensemble of 19 global models, *Atmos. Chem. Phys.*, 16, 3525–3561, <https://doi.org/10.5194/acp-16-3525-2016>, 2016.
- Kurppa, M., Hellsten, A., Roldin, P., Kokkola, H., Tonttila, J., Auvinen, M., Kent, C., Kumar, P., Maronga, B., and Järvi, L.: Implementation of the sectional aerosol module SALSA2.0 into the PALM model system 6.0: model development and first evaluation, *Geosci. Model Dev.*, 12, 1403–1422, <https://doi.org/10.5194/gmd-12-1403-2019>, 2019.
- Ladino, L., Stetzer, O., Hattendorf, B., Günther, D., Croft, B., and Lohmann, U.: Experimental Study of Collection Efficiencies between Submicron Aerosols and Cloud Droplets, *J. Atmos. Sci.*, 68, 1853–1864, <https://doi.org/10.1175/JAS-D-11-012.1>, 2011.
- Lamarque, J.-F., Bond, T. C., Eyring, V., Granier, C., Heil, A., Klimont, Z., Lee, D., Liousse, C., Mieville, A., Owen, B., Schultz, M. G., Shindell, D., Smith, S. J., Stehfest, E., Van Aardenne, J., Cooper, O. R., Kainuma, M., Mahowald, N., McConnell, J. R., Naik, V., Riahi, K., and van Vuuren, D. P.: Historical (1850–2000) gridded anthropogenic and biomass burning emissions of reactive gases and aerosols: methodology and application, *Atmos. Chem. Phys.*, 10, 7017–7039, <https://doi.org/10.5194/acp-10-7017-2010>, 2010.
- Lohmann, U.: Possible Aerosol Effects on Ice Clouds via Contact Nucleation, *J. Atmos. Sci.*, 59, 647–656, [https://doi.org/10.1175/1520-0469\(2001\)059<0647:PAEOIC>2.0.CO;2](https://doi.org/10.1175/1520-0469(2001)059<0647:PAEOIC>2.0.CO;2), 2002.
- Lohmann, U., Stier, P., Hoose, C., Ferrachat, S., Kloster, S., Roeckner, E., and Zhang, J.: Cloud microphysics and aerosol indirect effects in the global climate model ECHAM5–HAM, *Atmos. Chem. Phys.*, 7, 3425–3446, <https://doi.org/10.5194/acp-7-3425-2007>, 2007.
- Lund, M. T., Samset, B. H., Skeie, R. B., Watson-Parris, D., Katich, J. M., Schwarz, J. P., and Weinzierl, B.: Short Black Carbon lifetime inferred from a global set of aircraft observations, *Clim. Atmos. Sci.*, 1, 2397–3722, <https://doi.org/10.1038/s41612-018-0040-x>, 2018.
- Marcolli, C., Gedamke, S., Peter, T., and Zobrist, B.: Efficiency of immersion mode ice nucleation on surrogates of mineral dust,

- Atmos. Chem. Phys., 7, 5081–5091, <https://doi.org/10.5194/acp-7-5081-2007>, 2007.
- Paasonen, P., Kupiainen, K., Klimont, Z., Visschedijk, A., Denier van der Gon, H. A. C., and Amann, M.: Continental anthropogenic primary particle number emissions, Atmos. Chem. Phys., 16, 6823–6840, <https://doi.org/10.5194/acp-16-6823-2016>, 2016.
- Pruppacher, H. R. and Klett, J. D.: Microphysics of clouds and precipitation, Kluwer Academic Publishers, Dordrecht, Boston, London, 1997.
- Rasch, P. J., Feichter, J., Law, J., Mahowald, N., Penner, J., Benkovitz, C., Genthon, C., Giannakopoulos, C., Kasibhatla, P., Koch, D., Levy, H., Maki, T., Prather, M., Roberts, D. L., Roelofs, G.-J., Stevenson, D., Stockwell, Z., Taguchi, S., Kritz, M., Chipperfield, M., Baldocchi, D., McMurry, P., Barrie, L., Balkanski, Y., Chatfield, R., Kjellstrom, E., Lawrence, M., Lee, H. N., Lelieveld, J., Noone, K. J., Seinfeld, J., Stenchikov, G., Schwartz, S., Walcek, C., and Williamson, D.: A comparison of scavenging and deposition processes in global models: results from the WCRP Cambridge Workshop of 1995, Tellus B, 52, 1025–1056, <https://doi.org/10.1034/j.1600-0889.2000.00980.x>, 2000.
- Samset, B. H., Myhre, G., Schulz, M., Balkanski, Y., Bauer, S., Bernsten, T. K., Bian, H., Bellouin, N., Diehl, T., Easter, R. C., Ghan, S. J., Iversen, T., Kinne, S., Kirkevåg, A., Lamarque, J.-F., Lin, G., Liu, X., Penner, J. E., Seland, Ø., Skeie, R. B., Stier, P., Takemura, T., Tsigaridis, K., and Zhang, K.: Black carbon vertical profiles strongly affect its radiative forcing uncertainty, Atmos. Chem. Phys., 13, 2423–2434, <https://doi.org/10.5194/acp-13-2423-2013>, 2013.
- Schultz, M. G., Stadtler, S., Schröder, S., Taraborrelli, D., Franco, B., Krefting, J., Henrot, A., Ferrachat, S., Lohmann, U., Neubauer, D., Siegenthaler-Le Drian, C., Wahl, S., Kokkola, H., Kühn, T., Rast, S., Schmidt, H., Stier, P., Kinnison, D., Tyndall, G. S., Orlando, J. J., and Wespes, C.: The chemistry–climate model ECHAM6.3-HAM2.3-MOZ1.0, Geosci. Model Dev., 11, 1695–1723, <https://doi.org/10.5194/gmd-11-1695-2018>, 2018.
- Seinfeld, J. H. and Pandis, S. N.: Atmospheric Chemistry and Physics: From air pollution to climate change, 2nd edition, vol. 2, John Wiley & Sons, Hoboken, New Jersey, 2006.
- Seland, O., Iversen, T., Kirkevåg, A., and Storelvmo, T.: Aerosol–climate interactions in the CAM-Oslo atmospheric GCM and investigation of associated basic shortcomings, Tellus A, 60, 459–491, <https://doi.org/10.1111/j.1600-0870.2008.00318.x>, 2008.
- Sharma, S., Ishizawa, M., Chan, D., Lavoué, D., Andrews, E., Eleftheriadis, K., and Maksyutov, S.: 16-year simulation of Arctic black carbon: Transport, source contribution, and sensitivity analysis on deposition, J. Geophys. Res.-Atmos., 118, 943–964, <https://doi.org/10.1029/2012JD017774>, 2013.
- Simmons, A. J., Burridge, D. M., Jarraud, M., Girard, C., and Wergen, W.: The ECMWF medium-range prediction models development of the numerical formulations and the impact of increased resolution, Meteorol. Atmos. Phys., 40, 28–60, <https://doi.org/10.1007/BF01027467>, 1989.
- Slinn, W. G. N. and Hales, J. M.: A Reevaluation of the Role of Thermophoresis as a Mechanism of In- and Below-Cloud Scavenging, J. Atmos. Sci., 28, 1465–1471, [https://doi.org/10.1175/1520-0469\(1971\)028<1465:AROTRO>2.0.CO;2](https://doi.org/10.1175/1520-0469(1971)028<1465:AROTRO>2.0.CO;2), 1971.
- Stier, P., Feichter, J., Kinne, S., Kloster, S., Vignati, E., Wilson, J., Ganzeveld, L., Tegen, I., Werner, M., Balkanski, Y., Schulz, M., Boucher, O., Minikin, A., and Petzold, A.: The aerosol–climate model ECHAM5-HAM, Atmos. Chem. Phys., 5, 1125–1156, <https://doi.org/10.5194/acp-5-1125-2005>, 2005.
- Stone, R., Sharma, S., Herber, A., Eleftheriadis, K., and Nelson, D.: A characterization of Arctic aerosols on the basis of aerosol optical depth and black carbon measurements, Elementa, 2, 000027, <https://doi.org/10.12952/journal.elementa.000027>, 2014.
- Tabazadeh, A., Djikaev, Y. S., and Reiss, H.: Surface crystallization of supercooled water in clouds, P. Natl. Acad. Sci. USA, 99, 15873–15878, <https://doi.org/10.1073/pnas.252640699>, 2002.
- Tegen, I., Neubauer, D., Ferrachat, S., Siegenthaler-Le Drian, C., Bey, I., Schutgens, N., Stier, P., Watson-Parris, D., Stanelle, T., Schmidt, H., Rast, S., Kokkola, H., Schultz, M., Schroeder, S., Daskalakis, N., Barthel, S., Heinold, B., and Lohmann, U.: The global aerosol–climate model ECHAM6.3-HAM2.3 – Part 1: Aerosol evaluation, Geosci. Model Dev., 12, 1643–1677, <https://doi.org/10.5194/gmd-12-1643-2019>, 2019.
- Textor, C., Schulz, M., Guibert, S., Kinne, S., Balkanski, Y., Bauer, S., Bernsten, T., Berglen, T., Boucher, O., Chin, M., Dentener, F., Diehl, T., Easter, R., Feichter, H., Fillmore, D., Ghan, S., Ginoux, P., Gong, S., Grini, A., Hendricks, J., Horowitz, L., Huang, P., Isaksen, I., Iversen, I., Kloster, S., Koch, D., Kirkevåg, A., Kristjánsson, J. E., Krol, M., Lauer, A., Lamarque, J. F., Liu, X., Montanaro, V., Myhre, G., Penner, J., Pitari, G., Reddy, S., Seland, Ø., Stier, P., Takemura, T., and Tie, X.: Analysis and quantification of the diversities of aerosol life cycles within AeroCom, Atmos. Chem. Phys., 6, 1777–1813, <https://doi.org/10.5194/acp-6-1777-2006>, 2006.
- Tissari, J., Lyyräinen, J., Hytönen, K., Sippula, O., Tapper, U., Frey, A., Saarnio, K., Pennanen, A., Hillamo, R., Salonen, R., Hirvonen, M.-R., and Jokiniemi, J.: Fine particle and gaseous emissions from normal and smouldering wood combustion in a conventional masonry heater, Atmos. Environ., 42, 7862–7873, <https://doi.org/10.1016/j.atmosenv.2008.07.019>, 2008.
- Tonttila, J., Maalick, Z., Raatikainen, T., Kokkola, H., Kühn, T., and Romakkaniemi, S.: UCLALES-SALSA v1.0: a large-eddy model with interactive sectional microphysics for aerosol, clouds and precipitation, Geosci. Model Dev., 10, 169–188, <https://doi.org/10.5194/gmd-10-169-2017>, 2017.
- Twomey, S.: Aerosol, clouds, and radiation., vol. 25A, Atmospheric Environment, The University of Arizona, Tucson, AZ, USA, 1991.
- van Vuuren, D. P., Edmonds, J., Kainuma, M., Riahi, K., Thomson, A., Hibbard, K., Hurtt, G. C., Kram, T., Krey, V., Lamarque, J.-F., Masui, T., Meinshausen, M., Nakicenovic, N., Smith, S. J., and Rose, S. K.: The representative concentration pathways: an overview, Clim. Chang., 109, 5–31, <https://doi.org/10.1007/s10584-011-0148-z>, 2011.
- Wang, H., Easter, R. C., Rasch, P. J., Wang, M., Liu, X., Ghan, S. J., Qian, Y., Yoon, J.-H., Ma, P.-L., and Vinoj, V.: Sensitivity of remote aerosol distributions to representation of cloud–aerosol interactions in a global climate model, Geosci. Model Dev., 6, 765–782, <https://doi.org/10.5194/gmd-6-765-2013>, 2013.
- Wang, P., Grover, S., and Pruppacher, H.: On the Effect of Electric Charges on the Scavenging of Aerosol Particles by Clouds and Small Raindrops, J. Atmos.

- Sci., 35, 1735–1743, [https://doi.org/10.1175/1520-0469\(1978\)035<1735:OTEOEC>2.0.CO;2](https://doi.org/10.1175/1520-0469(1978)035<1735:OTEOEC>2.0.CO;2), 1978.
- Watson-Parris, D., Schutgens, N., Cook, N., Kipling, Z., Kershaw, P., Gryspeerdt, E., Lawrence, B., and Stier, P.: Community Intercomparison Suite (CIS) v1.4.0: a tool for intercomparing models and observations, *Geosci. Model Dev.*, 9, 3093–3110, <https://doi.org/10.5194/gmd-9-3093-2016>, 2016.
- Watson-Parris, D., Schutgens, N., Reddington, C., Pringle, K. J., Liu, D., Allan, J. D., Coe, H., Carslaw, K. S., and Stier, P.: In situ constraints on the vertical distribution of global aerosol, *Atmos. Chem. Phys.*, 19, 11765–11790, <https://doi.org/10.5194/acp-19-11765-2019>, 2019.
- Wofsy, S., Afshar, S., Allen, H., Apel, E., Asher, E., Barletta, B., Bent, J., Bian, H., Biggs, B., Blake, D., Blake, N., Bourgeois, I., Brock, C., Brune, W., Budney, J., Bui, T., Butler, A., Campuzano-Jost, P., Chang, C., Chin, M., Commane, R., Correa, G., Crounse, J., Cullis, P., Daube, B., Day, D., Dean-Day, J., Dibb, J., Digangi, J., Diskin, G., Dollner, M., Elkins, J., Erdesz, F., Fiore, A., Flynn, C., Froyd, K., Gesler, D., Hall, S., Hanisco, T., Hannun, R., Hills, A., Hints, E., Hoffman, A., Hornbrook, R., Huey, L., Hughes, S., Jimenez, J., Johnson, B., Katich, J., Keeling, R., Kim, M., Kupc, A., Lait, L., Lamarque, J.-F., Liu, J., McKain, K., McLaughling, R., Meinardi, S., Miller, D., Montzka, S., Moore, F., Morgan, E., Murphy, D., Murray, L., Nault, B., Neuman, J., Newman, P., Nicely, J., Pan, X., Paplawsky, W., Peischl, J., Prather, M., Price, D., Ray, E., Reeves, J., Richardson, M., Rollins, A., Rosenlof, K., Ryerson, T., Scheuer, E., Schill, G., Schroder, J., Schwarz, J., St.Clair, J., Steenrod, S., Stephens, B., Strode, S., Sweeney, C., Tanner, D., Teng, A., Thames, A., Thompson, C., Ullmann, K., Veres, P., Vizenor, N., Wagner, N., Watt, A., Weber, R., Weinzierl, B., Wennberg, P., Williamson, C., Wilson, J., Wolfe, G., Woods, C., and Zeng, L.: ATom: Merged Atmospheric Chemistry, Trace Gases, and Aerosols, ORNL DAAC, Oak Ridge, Tennessee, USA, <https://doi.org/10.3334/ORNLDAAAC/1581>, 2018.
- Zhang, X., Chen, X., and Wang, J.: A number-based inventory of size-resolved black carbon particle emissions by global civil aviation, *Nat. Commun.*, 10, 534, <https://doi.org/10.1038/s41467-019-08491-9>, 2019.
- Zikova, N. and Zdimal, V.: Precipitation scavenging of aerosol particles at a rural site in the Czech Republic, *Tellus B*, 68, 27343, <https://doi.org/10.3402/tellusb.v68.27343>, 2016.





## Paper III

E. Holopainen, H. Kokkola, C. Faiola, A. Laakso and T.  
Kühn

“Insect Herbivory Caused Plant Stress Emissions  
Increases the Negative Radiative Forcing of Aerosols”  
*Journal of Geophysical Research: Atmospheres* **127**,  
pp. e2022JD036733, 2022.

Reproduced under the Creative Commons Attribution 4.0 License  
(CC BY 4.0).



## Key Points:

- Increasing plant stress enhanced secondary organic aerosol (SOA) formation due to increase in volatile organic compound emissions
- Enhanced biotic stress increased the number of particles acting as cloud condensation nuclei and thus cloud droplet number concentration
- Increased SOA formation enhanced aerosol scattering which decreased all-sky and clear-sky radiative forcing

## Correspondence to:

E. Holopainen,  
eemeli.holopainen@fmi.fi

## Citation:

Holopainen, E., Kokkola, H., Faiola, C., Laakso, A., & Kühn, T. (2022). Insect herbivory caused plant stress emissions increases the negative radiative forcing of aerosols. *Journal of Geophysical Research: Atmospheres*, 127, e2022JD036733. <https://doi.org/10.1029/2022JD036733>

Received 4 MAR 2022

Accepted 22 JUN 2022





## Author Contributions:

**Conceptualization:** E. Holopainen, H. Kokkola, C. Faiola  
**Data curation:** E. Holopainen  
**Formal analysis:** E. Holopainen, H. Kokkola, C. Faiola, A. Laakso, T. Kühn  
**Investigation:** E. Holopainen  
**Methodology:** E. Holopainen  
**Supervision:** H. Kokkola, A. Laakso, T. Kühn  
**Validation:** E. Holopainen, H. Kokkola, C. Faiola  
**Visualization:** E. Holopainen  
**Writing – original draft:** E. Holopainen, H. Kokkola, C. Faiola

© 2022. The Authors.

This is an open access article under the terms of the [Creative Commons Attribution License](#), which permits use, distribution and reproduction in any medium, provided the original work is properly cited.

# Insect Herbivory Caused Plant Stress Emissions Increases the Negative Radiative Forcing of Aerosols

E. Holopainen<sup>1,2</sup> , H. Kokkola<sup>1</sup> , C. Faiola<sup>3,4</sup> , A. Laakso<sup>1</sup>, and T. Kühn<sup>1,2</sup> 

<sup>1</sup>Atmospheric Research Centre of Eastern Finland, Finnish Meteorological Institute, Kuopio, Finland, <sup>2</sup>Aerosol Physics Research Group, University of Eastern Finland, Kuopio, Finland, <sup>3</sup>Department of Ecology and Evolutionary Biology, University of California Irvine, Irvine, CA, USA, <sup>4</sup>Department of Chemistry, University of California Irvine, Irvine, CA, USA

**Abstract** Plant stress in a changing climate is predicted to increase plant volatile organic compound (VOC) emissions and thus can affect the formed secondary organic aerosol (SOA) concentrations, which in turn affect the radiative properties of clouds and aerosol. However, global aerosol-climate models do not usually consider plant stress induced VOCs in their emission schemes. In this study, we modified the monoterpene emission factors in biogenic emission model to simulate biotic stress caused by insect herbivory on needleleaf evergreen boreal and broadleaf deciduous boreal trees and studied the consequent effects on SOA formation, aerosol-cloud interactions as well as direct radiative effects of formed SOA. Simulations were done altering the fraction of stressed and healthy trees in the latest version of ECHAM-HAMMOZ (ECHAM6.3-HAM2.3-MOZ1.0) global aerosol-climate model. Our simulations showed that increasing the extent of stress to the aforementioned tree types, substantially increased the SOA burden especially over the areas where these trees are located. This indicates that increased VOC emissions due to increasing stress enhance the SOA formation via oxidation of VOCs to low VOCs. In addition, cloud droplet number concentration at the cloud top increased with increasing extent of biotic stress. This indicates that as SOA formation increases, it further enhances the number of particles acting as cloud condensation nuclei. The increase in SOA formation also decreased both all-sky and clear-sky radiative forcing. This was due to a shift in particle size distributions that enhanced aerosol reflecting and scattering of incoming solar radiation.

**Plain Language Summary** Recent studies have predicted that when trees and plants are attacked by insects they become stressed and start to emit more gaseous organic compounds. These compounds can then go through certain chemical processes to form atmospheric particles which affect the climate by scattering and reflecting incoming solar radiation, and affecting cloud formation. In order to understand the effects of plant stress caused by insects attacking trees, we modeled them using a climate model which can simulate how particles can affect the climate. We found out that the more trees were stressed, the more gases they emit, which in turn enhanced atmospheric particle formation. This increase in the amount of particles led to an increase in the amount of cloud droplets as there are more particles which can act as cloud seeds. The increase in particles also increased the amount of solar radiation reflected back to space.

## 1. Introduction

Atmospheric aerosols affect the climate by scattering and absorbing solar radiation directly (Seinfeld & Pandis, 2006). In addition, they have a possibility to go through aerosol-cloud-interactions impacting the life-time, formation, and the radiative properties of the clouds (Albrecht, 1989; Kerminen et al., 2005; Makkonen et al., 2009; Twomey, 1991). As the magnitude of the climate effects of atmospheric aerosol particles are uncertain, it causes a large uncertainty to the estimation of radiation budget of the Earth (IPCC, 2021).

One source of uncertainty in estimating the climate effects of anthropogenic aerosol is that the sensitivity of radiative forcing (RF) to perturbations by anthropogenic aerosol depends on the amount of natural background aerosol (Carslaw et al., 2013). One significant source of natural aerosol is vegetation as aerosol particles can be formed through oxidation of biosphere emitted volatile organic compounds (VOCs) (Donahue et al., 2013; Kulmala, Petäjä, et al., 2014; Schobesberger et al., 2013). VOCs are carbon-structured molecules which evaporate in ambient conditions (Faiola & Taipale, 2020). A majority of the emitted VOCs originate from terrestrial vegetation such as trees and plants (Guenther et al., 2012; Jimenez et al., 2009; Sporre et al., 2020). These biogenic

VOCs are highly reactive and play an important role in atmospheric chemistry processes (Carter, 1994; de Gouw et al., 2018; Griffith et al., 2016).

VOCs serve important ecological functions in plant defense and communication. Trees and plants emit VOCs to protect them from high temperature stress (Materić et al., 2015; Sharkey & Yeh, 2001) and to interact (such as attracting pollinators) with other organisms (Baldwin et al., 2002; Proffitt et al., 2020). It has also been suggested that trees communicate with each other through emitting VOCs (Runyon et al., 2006; Ueda et al., 2012; Zebelo et al., 2012). VOC emissions can be altered by abiotic (non-living) or biotic (living) plant stressors. Major abiotic plant stressors include extreme heat or drought (He et al., 2018). Major biotic plant stressors include insect herbivory or pathogens (J. K. Holopainen & Gershenzon, 2010; Zhao et al., 2017). Abiotic and biotic stress factors cause deviation from plants optimal living conditions and thus are known to alter the rate and spectrum of VOC emissions (Faiola & Taipale, 2020; J. K. Holopainen, 2004; J. K. Holopainen & Gershenzon, 2010; J. K. Holopainen et al., 2018; Niinemets, 2010). Especially the biotic stress factors can enhance the VOC emission rates of for example, monoterpene or sesquiterpene (Faiola & Taipale, 2020; Taipale et al., 2021).

Non-refractory particles less than 1 micron in diameter are composed of 20%–90% organic aerosol (OA) with a high level of spatial and temporal variation (Jimenez et al., 2009; Murphy et al., 2006; Zhang et al., 2007). From these OA particles around 60%–70% is secondary organic aerosol (SOA) in a global scale (Goldstein & Galbally, 2007; Hallquist et al., 2009; Zhang et al., 2007). SOA is formed through oxidation of volatile, and semivolatile, organic species and the subsequent gas-to-particle partitioning of the oxidation products (Faiola & Taipale, 2020; Hallquist et al., 2009; Jimenez et al., 2009; Zhang et al., 2007). Consequently, increased plant stress VOC emissions can lead to enhanced formation of SOA with subsequent impacts on cloud formation and radiative transfer (Kerminen & Kulmala, 2002; Taipale et al., 2021). The sources, sinks, and atmospheric processing of SOA are uncertain which causes also uncertainty to the estimation of RF of aerosols in global climate models (Sporre et al., 2020; Tsigaridis et al., 2014). In addition, the contribution of biotic stress to VOC emissions and further to SOA formation is not usually considered in global aerosol-climate models and thus more investigation is needed to more precisely evaluate the effects of SOA to atmosphere (Faiola & Taipale, 2020). However, there has been studies which state that biotic plant stress can massively influence the size and amount of formed SOA through enhancing of VOC emissions as well as affect the cloud condensation nuclei (CCN) concentrations in global model simulations. For example, Joutsensaari et al. (2015) found that increasing monoterpene emissions by 10-fold, and assuming that 10% of the boreal forest area is experiencing biotic stress, increases the total particulate mass by 480% and CCN concentrations by 45% locally. In addition, Taipale et al. (2021) showed that biotic stress in plants is capable to perturb the amount and size of aerosol particles as well as increase the amount of newly formed particles. Unfortunately, these studies are using assumptions of biotic stress factors or limited to process level only and does not take into account the actual feedbacks of biotic stress induced SOA to radiative effects.

Here, we used the ECHAM-HAMMOZ global aerosol-climate model (Schultz et al., 2018) with sectional aerosol representation, SALSA (Kokkola, Kuhn, et al., 2018), and MEGAN v2.1 emission model (Guenther et al., 2012) to simulate the effects of biotic stress, due to insect herbivore infestation, on needleleaf evergreen boreal and broadleaf deciduous boreal trees in terms of SOA formation, clouds and radiative effects. The structure of the study is as follows. In Section 2 we present details of the global aerosol-climate model, ECHAM-HAMMOZ with SALSA microphysics package, and MEGAN v2.1 emission model used in this study. In the same section, we also present the values used for monoterpene emission factors and the details of the simulations performed in this study. In addition, we present reasoning of the time period and areas of interest chosen for this study. In Section 3 we present comparisons of simulations ranging from 10% to 100% stressed tree emissions to a baseline scenario where all of the trees were healthy. The comparison is done in terms of SOA burden, CDNC at cloud top and top of the atmosphere (TOA) clear-sky and all-sky RF in 2D map figures from 40° latitude northward. Finally we present field mean values from land area SOA burden, CDNC at cloud top and TOA clear-sky and all-sky RF as a function of increasing stress percentage in the simulations.

## 2. Materials and Methods

In this section we will describe the ECHAM-HAMMOZ global aerosol-climate model and the MEGAN v2.1 emission module, which were used in this study to simulate the effects of increasing VOC emissions, due to biotic stress in needleleaf evergreen boreal and broadleaf deciduous boreal trees, on SOA formation, clouds and



**Figure 1.** Needleleaf evergreen boreal (a) and broadleaf deciduous boreal (b) tree plant functional types from MEGAN. The percentage is a representation from the total land cover of the Earth. The red dots represent the locations of the field measurements, which were used to determine the average of healthy and stressed emission factors of these trees.

radiative effects on a global scale. In addition, we will describe the different simulations, which were done using the ECHAM-HAMMOZ global model, by altering the stress percentage of the trees.

## 2.1. ECHAM-HAMMOZ

In this study we used the latest stable version of ECHAM-HAMMOZ (ECHAM6.3-HAM2.3-MOZ1.0) (Schultz et al., 2018), which is a 3-dimensional aerosol-chemistry-climate model. It consists of the host atmospheric model ECHAM (Stevens et al., 2013), aerosol model HAM (Kokkola, Kuhn, et al., 2018; Tegen et al., 2019), and chemistry model MOZ (Schultz et al., 2018). The general circulation model, ECHAM6.3, solves equations for surface pressure, vorticity, divergence and temperature (Stevens et al., 2013). ECHAM6.3 is further coupled with Hamburg Aerosol Model (HAM2.3), which is used to calculate all of the aerosol processes, including emissions, deposition, radiation and microphysics, within the global model (Tegen et al., 2019). HAM2.3 has also a comprehensive parameterization for both modal (M7, Tegen et al. (2019)) and sectional (SALSA, Kokkola, Kuhn, et al. (2018)) microphysics representations for the aerosol population and in this study the sectional approach was used.

## 2.2. MEGAN v2.1

In order to simulate how changes in biogenic VOCs affect aerosol-radiation and aerosol-cloud-interactions, Model of Emissions of Gases and Aerosols from Nature v2.1 (MEGAN) was used in ECHAM-HAMMOZ simulations. MEGAN was used as it provides the plant functional types (PFTs) and emission factors (EFs) of several different VOCs to ECHAM-HAMMOZ, which makes it easy to modify these PFTs and EFs for monoterpenes when simulating the plant damage effect on VOC emissions. MEGAN uses land cover, ambient meteorological properties, and atmospheric chemical composition as inputs estimating the net emissions of gases and aerosols from different types of terrestrial vegetation into the atmosphere (Guenther et al., 2012). In MEGAN there are 16 different PFTs which cover the whole land area of the Earth (Guenther et al., 2012; Wullschlegel et al., 2014). These PFTs have different EFs for different chemical compounds which are released to the atmosphere as VOCs. In this study, we focus on changes in VOC emissions due to plant damages to needleleaf evergreen boreal (NEB) and broadleaf deciduous boreal (BDB) trees. The percentage of needleleaf evergreen boreal and broadleaf deciduous boreal trees from the total land cover of the Earth are presented in Figure 1. In addition, we will analyze the changes in atmospheric aerosol load as well as the resulting changes in aerosol-cloud-interactions.

We will study changes in monoterpene emissions, due to insect herbivory, as the EFs for these trees and compound were readily available from several measurement studies (Achotegui-Castells et al., 2013; Blande et al., 2007, 2009, 2010; Brilli et al., 2009; Clavijo McCormick et al., 2014; Copolovici et al., 2011, 2017; Faiola & Taipale, 2020; Faiola et al., 2018; Ghimire et al., 2016; Ghirardo et al., 2012; Heijari et al., 2011; Joutsensaari et al., 2015; Kari et al., 2019; Kovalchuk et al., 2015; Litvak & Monson, 1998; Li et al., 2012; Maja et al., 2014; Mäntylä et al., 2008; Schaub et al., 2010; Yli-Pirilä et al., 2016), and since monoterpenes are a major contributor to biogenic SOA formation over the boreal area (Hakola et al., 2006; Rinne et al., 2009). In addition, as the model includes only one sesquiterpene, the modification and analysis for sesquiterpenes and green leaf volatiles are left for future studies. EFs for monoterpenes averaged from several different measurement studies as well as the original MEGAN values for insect herbivory stressed and healthy needleleaf evergreen boreal and broadleaf deciduous boreal tree are presented in Table 1 (Achotegui-Castells et al., 2013; Blande et al., 2007, 2009, 2010; Brilli et al., 2009; Clavijo McCormick et al., 2014; Copolovici et al., 2011, 2017; Faiola et al., 2018; Faiola & Taipale, 2020; Ghimire et al., 2016; Ghirardo et al., 2012; Heijari et al., 2011; Joutsensaari et al., 2015; Kari

**Table 1**  
*Emission Factors of Monoterpene for Healthy and Insect Herbivory Stressed Needleleaf Evergreen Boreal and Broadleaf Deciduous Boreal Trees Based on Measurements and the Original MEGAN Values*

PFT	Healthy ( $\frac{\mu\text{g}}{\text{m}^2\text{h}}$ )	Stressed ( $\frac{\mu\text{g}}{\text{m}^2\text{h}}$ )	MEGAN ( $\frac{\mu\text{g}}{\text{m}^2\text{h}}$ )
Needleleaf evergreen boreal	4,500	40,811	1270
Broadleaf deciduous boreal	7,700	21,000	840

et al., 2019; Kovalchuk et al., 2015; Li et al., 2012; Litvak & Monson, 1998; Maja et al., 2014; Mäntylä et al., 2008; Schaub et al., 2010; Yli-Pirilä et al., 2016). The averaged EFs were obtained from several field and laboratory experiments and the locations of the field measurements are marked as red dots in Figure 1.

As the measurement based EFs of monoterpene for healthy and stressed plants are much higher than the original MEGAN values, we scaled the values to be in line with the MEGAN values. The values for the measured healthy plants EFs were scaled to match those of the original EFs in MEGAN. The measurement based EFs for stressed plants were scaled with the same scaling

factor as the measurement based EFs for the healthy plants. Thus, the EFs of monoterpenes used in this study were  $1,270 \frac{\mu\text{g}}{\text{m}^2\text{h}}$  and  $11,518 \frac{\mu\text{g}}{\text{m}^2\text{h}}$  for the healthy and stressed needleleaf evergreen boreal trees and  $840 \frac{\mu\text{g}}{\text{m}^2\text{h}}$  and  $2,291 \frac{\mu\text{g}}{\text{m}^2\text{h}}$  for the healthy and stressed broadleaf deciduous boreal trees.

### 2.3. Simulations

In order to analyze the effects of insect herbivory caused plant stress VOC emissions on the atmosphere and radiative balance of the Earth, we conducted 6 different simulations using the ECHAM-HAMMOZ global aerosol-climate model. In the simulations, the fraction of stressed plants in the needleleaf evergreen boreal and broadleaf deciduous boreal trees were varied. The percentages were 0, 10, 25, 50, 75, and 100% stressed trees which represent different scenarios of biotic stress in plants caused by insect herbivory outbreaks. The simulation with 0% of plants stressed represents the base simulation using the default monoterpene EFs described in the model. The simulation with 10% of plants stressed (Stress10) represents the background aerosol (Kozlov & Zvereva, 2018). The simulation with 25% of plants stressed (Stress25) is a representation of the current day when the outbreaks of insect herbivore infestations are high (Michel et al., 2018). The simulation with 50% of plants stressed (Stress50) is a representation of a future scenario where current day infestation outbreaks are increased (Venäläinen et al., 2020). The simulation with 75% of plants stressed (Stress75) was done to verify if there is a linear correlation between plant stress and SOA burden, clouds and radiative effects. The simulation with 100% of plants stressed (Stress100) is a representation of the upper bound of stress percentages. Table 2 summarizes the simulations used in this study with simulation names, their details and descriptions. All of the simulations were for a 10-year period starting from January 2000 ending in December 2009. All simulations were preceded with a 1-year spin-up period. The data was simulated with 3-hourly output throughout the period. From the 3-hourly data, we calculated monthly means for the model values. The emissions were obtained from the CEDS (Community Emissions Data System) emission inventories and for all simulated years we used the monthly mean emissions from year 2010 (Hoesly et al., 2018). The sea surface temperature (SST) and sea ice cover (SIC) were prescribed and were obtained from monthly mean climatologies from AMIP (Atmospheric Model Intercomparison Project) (Taylor et al., 2012). In this study, we performed atmosphere-only simulations with fixed SST, but freely evolving atmosphere. This means that the model accounts for aerosol-radiation interactions (ARI), aerosol-cloud interactions (ACI) and rapid adjustments, but not for climate feedbacks. The aerosol-climate interactions are two-way in the sense that possible climate (cloud) modifications also affect aerosol processes, most prominently aerosol removal and aerosol transport. Because land surface temperature is not fixed, VOC

**Table 2**  
*Simulations Used in This Study*

Simulation name	Details	Description
Stress0	0% stressed and 100% healthy NEB and BDB trees	Base simulation
Stress10	10% stressed and 90% healthy NEB and BDB trees	Background simulation
Stress25	25% stressed and 75% healthy NEB and BDB trees	Current day high outbreak simulation
Stress50	50% stressed and 50% healthy NEB and BDB trees	Increased current day high outbreak simulation
Stress75	75% stressed and 25% healthy NEB and BDB trees	Linearity check simulation
Stress100	100% stressed and 0% healthy NEB and BDB trees	Upper bound simulation

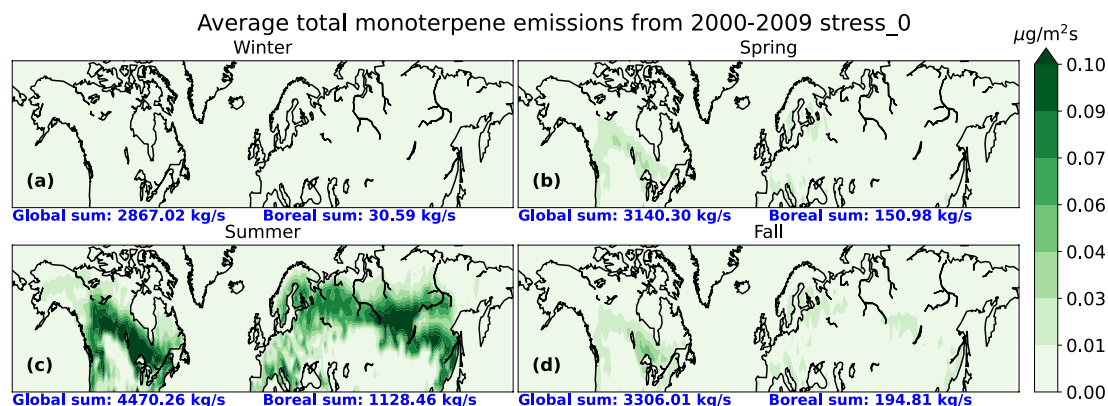


**Figure 2.** Seasonal average total monoterpene emission from years 2000 to 2009 simulated with the base simulation with the average global and boreal area sums for winter (December, January, and February) (a), spring (March, April, and May) (b), summer (June, July, and August) (c) and fall (September, October, and November) (d).

emissions may also change to some extent with changing aerosol loads. It should be noted that the simulations in this study are ideal and in reality the plant damages, due to herbivore infestation, are not assumed for the whole area simultaneously. However, the strongest effects are expected to be local and thus these simulations give indication where radiation and clouds are most susceptible to plant damage induced increase in SOA.

Figure 2 shows the seasonal averaged total monoterpene emissions from the base simulation as an average over 10-year period as well as the boreal area and global sum for winter (December, January, and February), spring (March, April, and May), summer (June, July, and August) and fall (September, October, and November). In Figure 2 the total monoterpene emissions for both the whole globe and the boreal area are highest in summer (Figure 2c). In addition, the monoterpene emissions from the needleleaf evergreen boreal and broadleaf deciduous boreal trees are highest during summer. Thus in this study, we focused only on the summer season, as during this period, emissions due to biotic stress will have the greatest effect on aerosol forcing.

First, we limited the study area to a region where SOA burdens from plant emitted VOCs are significantly perturbed in the simulation with 100% plant stress. This was done using the Wilcoxon signed-rank test which can be used to test if two related data sets come from a same distribution. The hypothesis of the test is that if the  $p$ -value is high (more than 0.05) the two data sets do not have statistically significant difference. In addition, if the  $p$ -value of the test is low (less than 0.05) there is a significant statistical difference between the two data sets (Wilcoxon, 1945). We used the Wilcoxon signed-rank test to see what areas of the Earth would be most sensible to analyze in terms of changes in SOA burden between the base simulation and the simulation where 100% of the plants are stressed. Wilcoxon signed-rank test of SOA burden from summer months from 10-year period between the upper bound and base simulation is presented in Figure 3. The large white areas are made to be unrepresentable Not-a-Number values as they represent the areas where the SOA burden in both of the simulations is fairly small (lower than  $2 \times 10^{-6} \text{ kg/m}^2$ ). In the Wilcoxon signed-rank test between the upper bound and base simulation the most statistically significant difference ( $p$ -value < 0.05) is achieved from  $40^\circ$  latitude northward. In addition, aerosol forcing is usually strongly dependent on the areas where aerosols are emitted and on the large ocean areas the dimethylsulfide and sea salt causes interference to the analysis. Thus, in our analysis we only focused on the Northern Hemisphere from  $40^\circ$  latitude northward and only on the land areas.

When studying cloud properties, it can be difficult to distinguish the actual signal from the noise caused by large temporal and spatial variability. In addition, as the length of the winter is long especially in the Northern Hemisphere the snow and ice covers can affect the surface albedo, even during summer months, causing a strong spatial and temporal fluctuation in aerosol radiative effects. Thus, in order to better separate the changes in cloud properties due to changes in VOC emissions, we conducted Gaussian filtering to smooth the 2D data in the results section following the approach of Miinalainen et al. (2021).



SOA burden 2000-2009 Wilcoxon signed-rank test summer stress 100 and 0

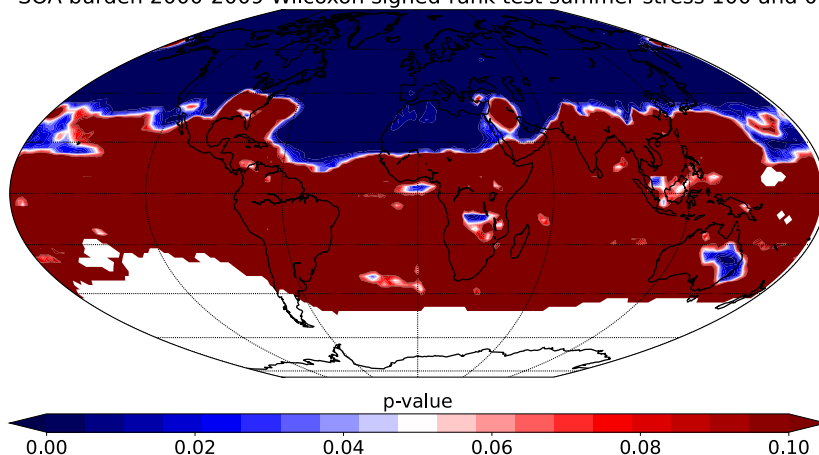


**Figure 3.** Wilcoxon signed-rank test of secondary organic aerosol (SOA) burden from summer from 10-year period between the upper bound and base simulations.

### 3. Results

We investigated the effect of elevated plant stress emissions on SOA formation, cloud properties, and radiative effects by analyzing simulation results for SOA burden, CDNC at cloud top, and clear-sky and all-sky shortwave RF at TOA. To evaluate regional variation of this effect, we plotted map figures from 40° latitude upward illustrating the absolute difference in SOA burden, CDNC at cloud top and shortwave RF between the base simulation and the plant stress simulations. In addition, to test the linearity of the increase or decrease in these variables, we generated a box plot from the field mean of the land area values for these variables.

First we investigated how increasing plant stress of the needleleaf evergreen boreal and broadleaf deciduous boreal trees affects the SOA formation, due to increasing VOC emissions. This was done by analyzing the difference in SOA burden between the base simulation and simulations where the monoterpene emissions of the trees were increased, over the inspected area.

Figure 4 shows the mean SOA burden in the base simulation and the absolute difference of the mean SOA burden, over land areas, between the stressed simulations and the base simulation for the summer period over 10 simulation years. There is an increase in the SOA burden when the stress imposed to needleleaf evergreen boreal and broadleaf deciduous boreal trees is increased. The increase is strongly dependent on the area where the majority of the aforementioned trees lay. The largest increase is in central Canada, Scandinavia, and throughout central Russia. There is no notable difference in the Stress10 simulation compared to the base simulation (Figure 4b), but already in Stress25 (Figure 4c) there is a significant increase in the SOA burden (approximately  $5 \times 10^{-6} \text{ kg/m}^2$  at maximum which is approximately 50% higher than in the base simulation). The Stress100 simulation shows an increase of approximately  $1.5 \times 10^{-5} \text{ kg/m}^2$  at maximum which is approximately 120% higher than in the base simulation (Figure 4f). In addition, the increase in SOA burden seems to be linear when going to larger stress values. This elevation in the SOA burden is due to higher monoterpene emissions from the trees of interest which in turn increases the SOA production via oxidation.

As explained above, enhanced SOA formation increases the number concentration of particles acting as CCN thus modifying cloud properties (Kuang et al., 2009; Kulmala, Nieminen, et al., 2014; Yli-Juuti et al., 2021). To see the effect of increase in SOA formation on cloud properties we studied the changes in CDNC at cloud top. Figure 5 presents the absolute difference in the mean cloud top CDNC, weighted with cloud time, over land areas between the stressed simulations and the base simulation for the summer period over 10 simulation years. There are only slight differences (approximately  $20 \text{ \#}/\text{cm}^3$  increase at maximum which is approximately 30% higher than in the base simulation) in cloud top CDNC between the Stress10 simulation and the base simulation

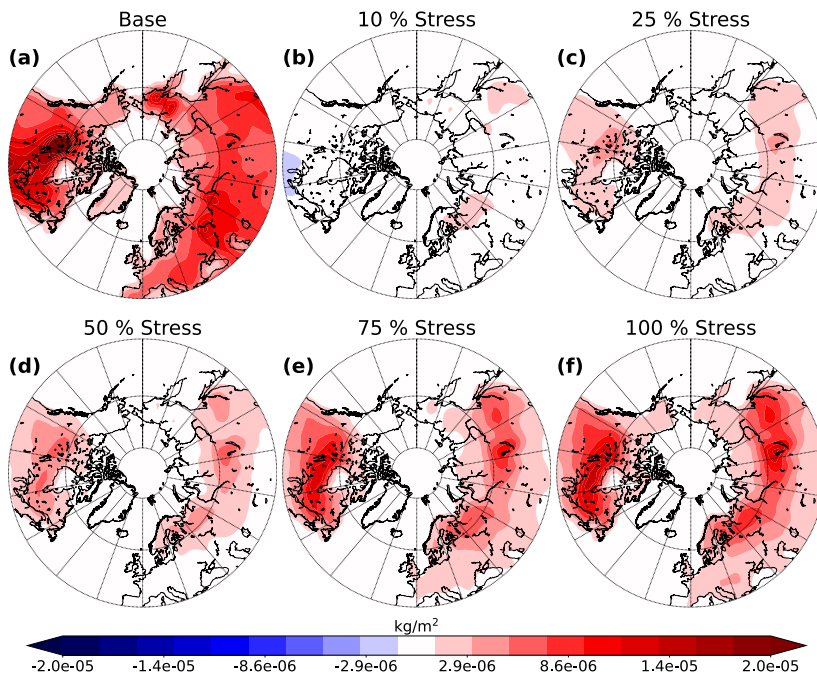


**Figure 4.** Absolute mean value of the base simulation (a) and absolute difference between the base simulation and the different stressed simulations (10% (b), 25% (c), 50% (d), 75% (e) and 100% (f)) of mean secondary organic aerosol (SOA) burden, over land areas, from summer over 10-year period.

(Figure 5a). However, when the percentage of stressed trees increases, the differences become more distinguishable. Between the base simulation and the Stress100 simulation (Figure 5e) the increase is approximately  $43 \text{ \#}/\text{cm}^3$  at maximum which corresponds to approximately 50% increase. Highest increase is seen in the western parts of Canada and Alaska as well as Scandinavia and central Russia. CDNC increases with increasing fraction of stressed trees and the increase in our simulations is quite linear. However, the change in CDNC does not change significantly when altering the stress percentage from 75 to 100 than from other stress percentages. This saturation in CDNC and the fact that the highest increases in CDNC do not correspond well with the places where we observed the highest increase in SOA, are due to CDNC susceptibility to CCN which decreases with increasing CCN concentrations (Carslaw et al., 2013).

Our simulations also show that change in SOA has an effect on the RF via increased scattering of solar radiation by aerosols. To investigate the magnitude of this effect, we studied the clear-sky and all-sky shortwave RF due to aerosol-radiation interactions. The mean clear-sky and all-sky shortwave RF due to increased VOC emissions over summer months for 10 simulation years are presented in Figures 6 and 7. The RF is calculated as  $RF = RF_{\text{ari, stress}} - RF_{\text{ari, base}}$ , where  $RF_{\text{ari, stress}}$  is the RF due to aerosol-radiation interactions at TOA from simulations where the plant stress was increased and  $RF_{\text{ari, base}}$  is the RF due to aerosol-radiation interactions at TOA from the base simulation. The  $RF_{\text{ari}}$  is calculated as  $RF_{\text{ari}} = F_{\text{aerosols}} - F_{\text{no-aerosols}}$ , where  $F_{\text{aerosols}}$  is the net radiative flux including aerosols and  $F_{\text{no-aerosols}}$  is the net radiative flux without aerosols (Ghan et al., 2012). These calculations do not include the aerosol-cloud interactions and in this study, we do not address the RF due to aerosol-cloud interactions as the actual signals were hard to detect from the variability caused by clouds even with the Gaussian filtering (Kühn et al., 2020).

The negative clear-sky RF (Figure 6) enhances with increasing stress percentage. This implies that there is more outgoing shortwave radiation in stressed simulations than there is in the base simulation. The effect is more obvious over areas where the majority of needleleaf evergreen boreal and broadleaf deciduous boreal forests are

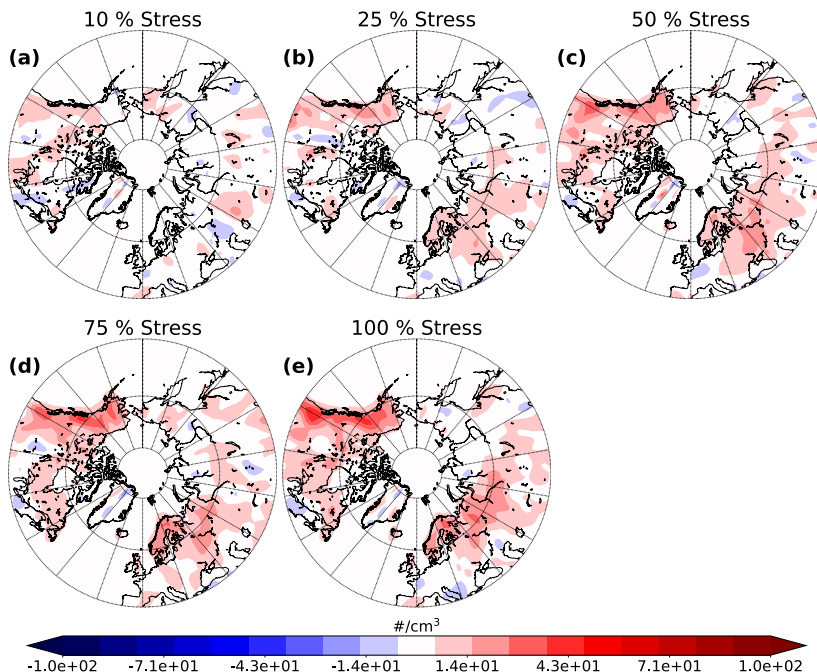


**Figure 5.** Absolute difference between the base simulation and the different stressed simulations (10% (a), 25% (b), 50% (c), 75% (d) and 100% (e)) of mean land area cloud top cloud droplet number concentration (CDNC) weighted with cloud time from summer over 10-year period.

located. Thus, areas most affected by the negative RF are Canada, northern parts of US, Scandinavia, and Russia with the strongest negative forcing (approximately  $-4.3 \text{ W/m}^2$ ) in the Stress100 simulation (Figure 6e). The decrease in RF seems to be quite linear when increasing the stress percentage. We can see similar linear decrease in all-sky RF (Figure 7) as in clear-sky RF (Figure 6), but the change in all-sky RF is less pronounced. This is due to calculation of all-sky values which take into account the values in the global model grid box where there are clouds, thus leaving less radiation for the aerosol particles to scatter. In addition, it causes more variation to the data. There are only slight differences (mainly due to noise) in the RF from 10, 25, and 50% stress simulations (Figures 7a–7c). However, the strongest negative all-sky forcing is over Canada and northern parts of US which is approximately  $-2 \text{ W/m}^2$  in Stress75 and Stress100 simulations (Figures 7d and 7e). In addition, there is a strong negative forcing (approximately  $-3 \text{ W/m}^2$ ) in the Stress100 simulation (Figure 7e) in eastern parts of Asia as well as slightly negative forcings over Scandinavia (approximately  $1 \text{ W/m}^2$ ). The linear dependence between the SOA burden, CDNC and the radiative effects can be more clearly seen from box plots of the 10-year period monthly mean values as a field mean from the land area from 40 to 90° latitude region which is presented in Figure 8.

There is a moderate correlation with the land area SOA burden and the extent of stress. The mean and median of SOA burden experience only a minor increase (mean increase of approximately  $0.1 \times 10^{-6} \text{ kg/m}^2$ ) when changing from 0 to 10% stress but all in all the increase is quite linear when going to higher stress percentages despite the fact that there is quite a strong deviation in the SOA burden which can be seen from the size of the boxes and black whiskers. Thus, increasing the plant stress enhances the VOC emissions and further the SOA production. The strongest increase in SOA burden (between base and Stress100 simulation) corresponds to approximately 95 % increase in field mean land area SOA mass concentration at surface which was approximately  $1.9 \mu\text{g/m}^3$  in the base simulation and approximately  $3.7 \mu\text{g/m}^3$  in the Stress100 simulation (not shown here). CDNC at cloud top increases with increasing stress percentage as well. However, the increase is not as linear as with SOA burden. There is only a weak correlation between plant stress and CDNC which can be mainly due to large variations in

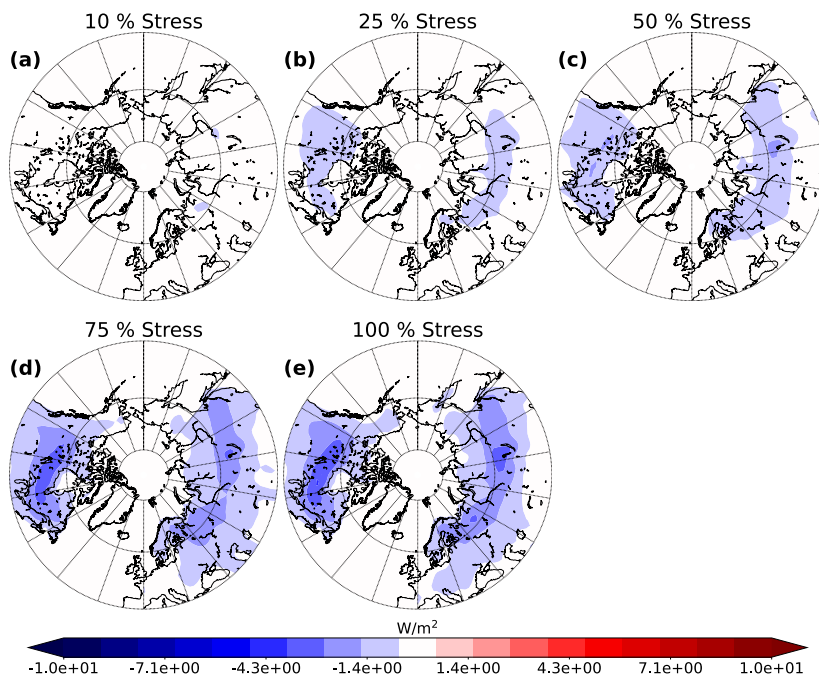


**Figure 6.** Mean land area clear-sky top of the atmosphere (TOA) shortwave radiative forcing (RF) (aerosols) between the base simulation and the different stressed simulations (10% (a), 25% (b), 50% (c), 75% (d) and 100% (e)) from June to August from 10-year period.

the data. However, there is an increase in mean values of CDNC especially at lower stress percentages (0%–50%). This is consistent with the increase in the SOA burden which increases the amount of particles acting as CCN. There is a moderate negative correlation between the extent of plant stress and TOA clear-sky shortwave RF over land areas. This is well in line with the SOA burden as the SOA increases in the atmosphere it causes stronger negative RF due to aerosol-radiation interactions. In addition, the TOA all-sky shortwave RF over land areas becomes more negative with increasing plant stress, but the correlation is weaker than for the clear-sky RF. This is because clouds mask part of aerosol forcing.

#### 4. Conclusions

We investigated the effects of biotic stress, due to herbivore infestation, on needleleaf evergreen boreal and broadleaf deciduous boreal trees in terms of changes in SOA burden, CDNC, and aerosol radiative effects. We only included insect herbivory stress, in this study, as there are enough studies on that subject to make some initial estimates of stressed EFs. Pathogens are also very important, but there is very little quantitative information on the impact of pathogens on biogenic VOC emission rates. We used the ECHAM-HAMMOZ global aerosol-climate model with SALSA microphysics scheme and MEGAN v2.1 biogenic emission model to evaluate how the percentage of plant damage changes the simulated SOA burden, CDNC at cloud top and radiative effects compared to a simulation where plants were assumed to be healthy.

We found out that increasing levels of biotic plant stress elevated the SOA burden. The most considerable increase was over the areas where there were most of the needleleaf evergreen boreal and broadleaf deciduous boreal trees are located. In addition, the largest increase in SOA burden (up to  $1.4 \times 10^{-5} \text{ kg/m}^2$ ) was between the base simulation and the simulation where 100% of the plants were stressed. The increase in SOA burden was due to larger emissions of monoterpenes of needleleaf evergreen boreal and broadleaf deciduous boreal trees which enhances the SOA formation. As the stress percentage increased there was also an increase in CDNC at cloud top. The

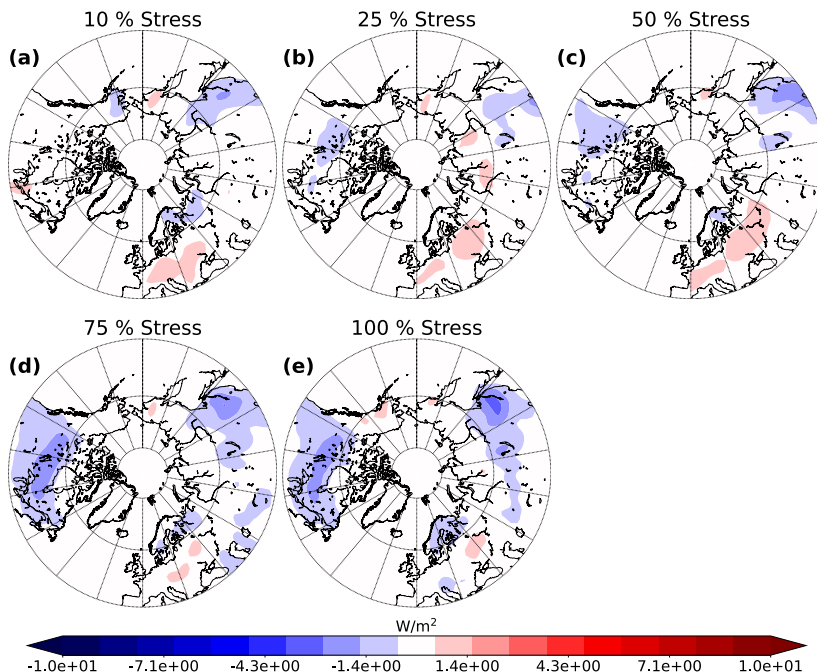


**Figure 7.** Mean land area all-sky top of the atmosphere (TOA) shortwave radiative forcing (RF) (aerosols) between the base simulation and the different stressed simulations (10% (a), 25% (b), 50% (c), 75% (d) and 100% (e)) from June to August from 10-year period.

main increase was at the areas where there was an elevation in SOA burden, but also at western parts of Canada and Alaska. The increase was at maximum (up to  $40 \text{ \#}/\text{cm}^3$ ) between the base simulation and the simulation where 100 % of the plants were stressed. As SOA formation increases, due to increasing plant stress, it causes increment in the particles which can act as CCN and thus an elevation in CDNC at cloud top. This increase in CDNC can have a potential to change the cloud albedo which can lead to enhanced cooling effect of the clouds (Twomey, 1974).

The clear-sky shortwave RF became strongly negative when the stress percentage was increased compared to the base simulation. In addition, the negative forcing is stronger over boreal forests. The simulation where 100% of the plants were stressed showed the strongest negative forcing (up to  $-4 \text{ W}/\text{m}^2$ ) for the clear-sky case. Negative all-sky shortwave RF was also enhanced when increasing the fraction stressed plants. However, the effect was weaker than in clear-sky case. The strongest negative forcing was in the simulation where 100% of the plants were stressed over eastern parts of China (up to  $-3 \text{ W}/\text{m}^2$ ). The increase in the negative shortwave RF was due to increase in SOA formation, with increasing stress percentage, which affects the aerosol-radiation interactions by reflecting more of the incoming solar radiation. These values are comparable to values given in the latest Assessment Report (AR6) of the Intergovernmental Panel on Climate Change (IPCC, 2021) where the multi-model mean net effective RF due to aerosol changes between 1850 and recent-past (1995–2014), in the boreal region, range between 0 and  $-6 \text{ W}/\text{m}^2$ . The strongest negative effect (between  $-4.5$  and  $-6 \text{ W}/\text{m}^2$ ) in the report is in central Russia which is mainly due to forest fires (IPCC, 2021).

Field mean SOA burden from  $40^\circ$  to  $90^\circ$  latitude over land areas showed a moderate correlation with increasing the fraction of stressed trees. Although there was a strong deviation in the SOA burden values, the mean and median values increase linearly with the stress percentage. This indicates that increasing monoterpene emissions of boreal trees increases SOA formation linearly. CDNC at cloud top, on the other hand, showed only a weak correlation with the stress percentage. The increase in mean CDNC at cloud top was linear when the stress

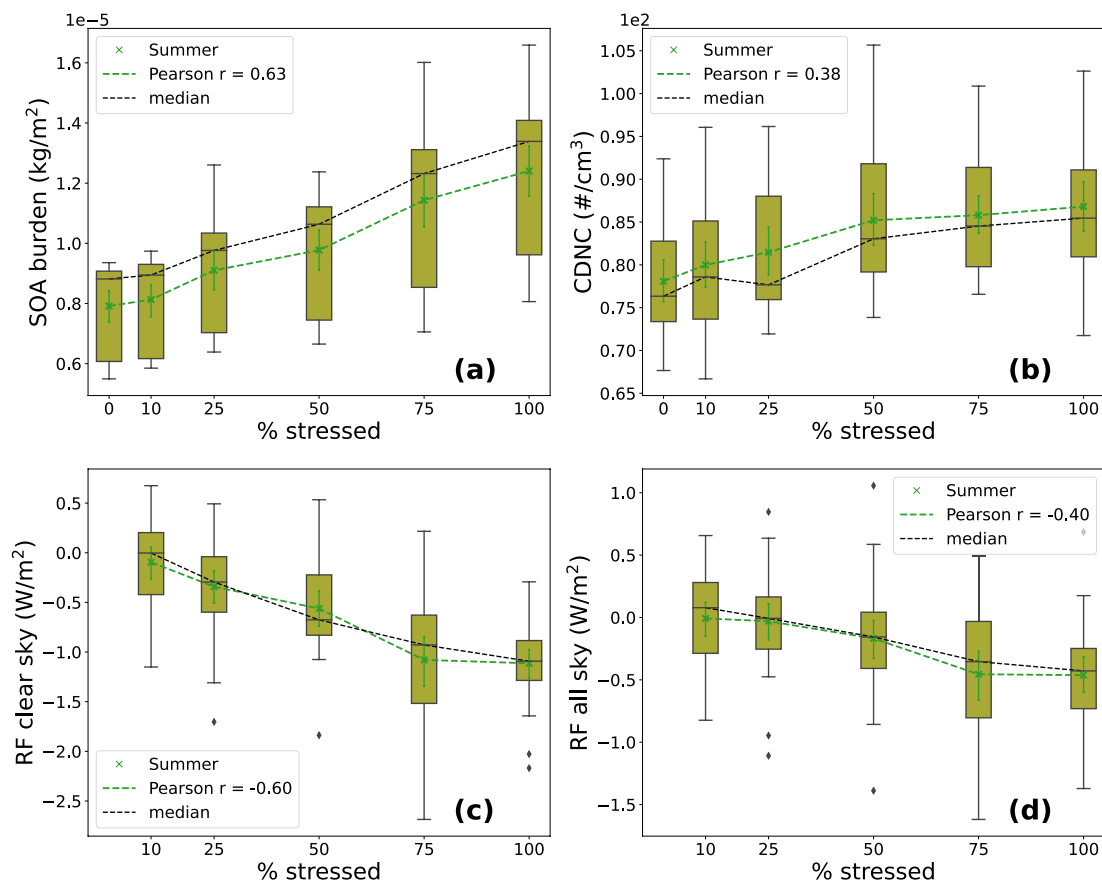


**Figure 8.** Box plots of field mean land area secondary organic aerosol (SOA) burden (a), cloud top cloud droplet number concentration (CDNC) weighted with cloud time (b) and clear-sky (c) and all-sky (d) top of the atmosphere (TOA) shortwave radiative forcing (RF) from 40° to 90° latitude region for summer from 10-year period for all of the simulations. The boxes represent the interquartile range (IQR) which shows the middle of 50% of the values (lower end of the box represents the 25th percentile and upper end 75th percentile). Black whiskers outside the boxes represent the values outside the middle 50% and the tips represent the minimum and maximum values (excluding outliers). Black vertical lines and dashed lines represent the median values. Green crosses and dashed lines represent the mean values and the green whiskers around the mean values represent the error in mean calculations. The black diamonds represent the outliers in the data.

percentages increased from 0 to 50 %, but after that the values saturated at approximately 85 #/cm<sup>3</sup> because CDNC becomes less susceptible with increasing CCN (Carslaw et al., 2013). The moderate negative correlation between clear-sky shortwave RF and increasing plant stress percentage is consistent with the increase in SOA burden. As the stress percentage increased, the SOA formation increased linearly which further induced stronger negative RF as there is a shift in aerosol particle size distribution which enhances the reflection and scattering of the incoming solar radiation. However, the all-sky shortwave RF had only weak negative correlation with increasing plant stress percentage. This is due to clouds which also reflect the incoming solar radiation masking the aerosol radiative effect.

As stated in Section 2, the simulations where 25% and 50% of the plants are stressed represent the current day high insect outbreak and future increased high insect outbreak scenarios, respectively (Michel et al., 2018; Venäläinen et al., 2020). On average the field mean SOA burden increases approximately 7.4% causing an increase of approximately 4.6% in CDNC between the current day and future high insect outbreak scenarios. In addition, on average the clear-sky RF shows approximately  $-0.22$  W/m<sup>2</sup> and all-sky RF  $-0.14$  W/m<sup>2</sup> stronger negative effect between



these scenarios. In SMEAR II station at Hyytiälä, Finland, the estimated growth in negative effect of RF due to aerosol-radiation interactions to be  $-1.15 \text{ W/m}^2$  for clear-sky and  $-0.33 \text{ W/m}^2$  for all-sky case for every degree of celsius increase over boreal forests (Yli-Juuti et al., 2021). Thus, in our simulations, the RF change from current day to future scenario corresponds to values of approximately  $0.2^\circ$  and approximately  $0.4^\circ$  increase in temperature for the clear-sky and all-sky cases, respectively. Using these stress percentages, the increase in SOA concentrations and their effect to CDNC and RF appears to be almost linear. It can be assumed that other factors increasing SOA through increasing VOC emissions (e.g., temperature driven increase VOC emissions), would be additive to these biotic stresses caused by herbivore infestation. This effect would also apply for other abiotic factors such as increased drought episodes or salinity. Although in this study, we focus on monoterpenes, biotic stresses affect the composition of the emitted VOC through changes in isoprene and sesquiterpene emissions which in turn modifies the hygroscopicity and CCN activity of the formed SOA (Zhao et al., 2017). However, isoprene emissions do not dominate as strongly as monoterpenes, in the boreal region, which was the area of focus in this study (Hantson et al., 2017). In addition, there are no existing sesquiterpene volatility basis set (VBS) parameters that adequately predict SOA formation from sesquiterpene oxidation (Barsanti et al., 2013). Nevertheless, including biotic stress effects on VOC composition and to isoprene and sesquiterpene emissions, would extend our understanding of the climate effects of plant stress induced aerosol and should be a topic for future studies.

To conclude, increasing monoterpene EFs for needleleaf evergreen boreal and broadleaf deciduous boreal trees (which simulates the plant stress caused by biotic stress factors) increases SOA formation through oxidation processes in ECHAM-HAMMOZ global aerosol-climate model. The increase in SOA burden is moderately dependent on increase in stress percentage of the plants. The increase in SOA burden affects the cloud formation by increasing the amount of particles acting as CCN and thus increasing CDNC at cloud top. In addition, the increase in SOA burden decreases the shortwave RF, which is due to increase in aerosol particles which reflect the incoming solar radiation. Even though our simulations are ideal and in reality the plant damages are not assumed for the whole area simultaneously, the global climate model development should include the effects of biotic plant stress in VOC emissions, to some extent, as this could have a significant effect on SOA formation, clouds and radiative effects.

## Data Availability Statement

The data and codes for reproducing the figures and the settings for the simulations are openly available (E. Holopainen et al., 2022). All other input files are ECHAM6-HAMMOZ standard and are available from the HAMMOZ repository (HAMMOZ consortium, 2020). The stand-alone zero-dimensional version of SALSA2.0 is distributed under the Apache-2.0 licence at <http://www.apache.org/licenses/LICENSE-2.0> and the code is openly available (Kokkola, Tonttila, et al., 2018). The model data can be reproduced using the model revision r6431 (HAMMOZ consortium, 2020). The ECHAM6-HAMMOZ model is made available to the scientific community under the HAMMOZ Software Licence Agreement, which defines the conditions under which the model can be used. The licence can be downloaded from [https://redmine.hammoz.ethz.ch/attachments/291/License\\_ECHAM-HAMMOZ\\_June2012.pdf](https://redmine.hammoz.ethz.ch/attachments/291/License_ECHAM-HAMMOZ_June2012.pdf).

## Acknowledgments

This research has been supported by the Academy of Finland, Luonnontieteiden ja Tekniikan Tutkimuksen Toimikunta (Grant Nos. 317390, 308292), University of Eastern Finland Doctoral Program in Environmental Physics, Health and Biology, the European Research Council (CLIMASLOW, Grant No. 678889), the Tiina and Antti Herlin Foundation (Grant No. 20190014) and the U.S. National Science Foundation Atmospheric and Geoscience (NSF-AGS) Division, Atmospheric Chemistry program (award no. 2035125). ECHAM-HAMMOZ is developed by a consortium composed of ETH Zürich, Max Planck Institut für Meteorologie, Forschungszentrum Jülich, University of Oxford, the Finnish Meteorological Institute and the Leibniz Institute for Tropospheric Research, and managed by the Center for Climate Systems Modeling (C2SM) at ETH Zürich.

## References

- Achotegui-Castells, A., Llusà, J., Hódar, J. A., & Peñuelas, J. (2013). Needle terpene concentrations and emissions of two coexisting subspecies of Scots pine attacked by the pine processionary moth (*thaumetopoea pityocampa*). *Acta Physiologiae Plantarum*, 35(10), 3047–3058. <https://doi.org/10.1007/s11738-013-1337-3>
- Albrecht, B. A. (1989). Aerosols, cloud microphysics, and fractional cloudiness. *Science*, 245(4923), 1227–1230. <https://doi.org/10.1126/science.245.4923.1227>
- Baldwin, I. T., Kessler, A., & Halitschke, R. (2002). Volatile signaling in plant–plant–herbivore interactions: What is real? *Current Opinion in Plant Biology*, 5(4), 351–354. [https://doi.org/10.1016/S1369-5266\(02\)00263-7](https://doi.org/10.1016/S1369-5266(02)00263-7)
- Barsanti, K. C., Carlton, A. G., & Chung, S. H. (2013). Analyzing experimental data and model parameters: Implications for predictions of SOA using chemical transport models. *Atmospheric Chemistry and Physics*, 13(23), 12073–12088. <https://doi.org/10.5194/acp-13-12073-2013>
- Blande, J. D., Korjus, M., & Holopainen, J. K. (2010). Foliar methyl salicylate emissions indicate prolonged aphid infestation on silver birch and black alder. *Tree Physiology*, 30(3), 404–416. <https://doi.org/10.1093/treephys/tpp124>
- Blande, J. D., Tiiva, P., Oksanen, E., & Holopainen, J. K. (2007). Emission of herbivore-induced volatile terpenoids from two hybrid aspen (*populus tremula* × *tremuloides*) clones under ambient and elevated ozone concentrations in the field. *Global Change Biology*, 13(12), 2538–2550. <https://doi.org/10.1111/j.1365-2486.2007.01453.x>
- Blande, J. D., Turunen, K., & Holopainen, J. K. (2009). Pine weevil feeding on Norway spruce bark has a stronger impact on needle VOC emissions than enhanced ultraviolet-B radiation. *Environmental Pollution*, 157(1), 174–180. <https://doi.org/10.1016/j.envpol.2008.07.007>

- Brilli, F., Ciccioli, P., Frattoni, M., Prestinini, M., Spanedda, A. F., & Loreto, F. (2009). Constitutive and herbivore-induced monoterpenes emitted by populus x euroamericana leaves are key volatiles that orient chrysomela populi beetles. *Plant, Cell and Environment*, 32(5), 542–552. <https://doi.org/10.1111/j.1365-3040.2009.01948.x>
- Carlsaw, K., Lee, L., Reddington, C., Pringle, K., Rap, A., Forster, P., et al. (2013). Large contribution of natural aerosols to uncertainty in indirect forcing. *Nature*, 503(7474), 67–71. <https://doi.org/10.1038/nature12674>
- Carter, W. P. (1994). Development of ozone reactivity scales for volatile organic compounds. *Air & Waste*, 44(7), 881–899. <https://doi.org/10.1080/1073161X.1994.10467290>
- Clavijo McCormick, A., Irmisch, S., Reinecke, A., Boeckler, G. A., Veit, D., Reichelt, M., et al. (2014). Herbivore-induced volatile emission in black poplar: Regulation and role in attracting herbivore enemies. *Plant, Cell and Environment*, 37(8), 1909–1923. <https://doi.org/10.1111/pce.12287>
- Copolovici, L., Kännaste, A., Rimmel, T., Vislap, V., & Niinemets, U. (2011). Volatile emissions from alnus glutinosa induced by herbivory are quantitatively related to the extent of damage. *Journal of Chemical Ecology*, 37(1), 18–28. <https://doi.org/10.1007/s10886-010-9897-9>
- Copolovici, L., Pag, A., Kännaste, A., Bodescu, A., Tomescu, D., Copolovici, D., et al. (2017). Disproportionate photosynthetic decline and inverse relationship between constitutive and induced volatile emissions upon feeding of quercus robur leaves by large larvae of gypsy moth (*lymantria dispar*). *Environmental and Experimental Botany*, 138, 184–192. <https://doi.org/10.1016/j.envexpbot.2017.03.014>
- de Gouw, J. A., Gilman, J. B., Kim, S.-W., Alvarez, S. L., Dusanter, S., Graus, M., et al. (2018). Chemistry of volatile organic compounds in the Los Angeles Basin: Formation of oxygenated compounds and determination of emission ratios. *Journal of Geophysical Research: Atmospheres*, 123(4), 2298–2319. <https://doi.org/10.1002/2017JD027976>
- Donahue, N. M., Ortega, I. K., Chuang, W., Riipinen, I., Riccobono, F., Schobesberger, S., et al. (2013). How do organic vapors contribute to new-particle formation? *Faraday Discussions*, 165, 91–104. Retrieved from <https://doi.org/10.1039/C3FD00046J>
- Faiola, C. L., Buchholz, A., Kari, E., Yli-Pirilä, P., Holopainen, J. K., Kivimäenpää, M., et al. (2018). Terpene composition complexity controls secondary organic aerosol yields from Scots pine volatile emissions. *Scientific Reports*, 8(1), 3053. <https://doi.org/10.1038/s41598-018-21045-1>
- Faiola, C. L., & Taipale, D. (2020). Impact of insect herbivory on plant stress volatile emissions from trees: A synthesis of quantitative measurements and recommendations for future research. *Atmospheric Environment: X*, 5, 100060. <https://doi.org/10.1016/j.aecoa.2019.100060>
- Ghan, S. J., Liu, X., Easter, R. C., Zaveri, R., Rasch, P. J., Yoon, J.-H., & Eaton, B. (2012). Toward a minimal representation of aerosols in climate models: Comparative decomposition of aerosol direct, semidirect, and indirect radiative forcing. *Journal of Climate*, 25(19), 6461–6476. <https://doi.org/10.1175/JCLI-D-11-00650.1>
- Ghimire, R. P., Kivimäenpää, M., Blomqvist, M., Holopainen, T., Lyytikäinen-Saarenmaa, P., & Holopainen, J. K. (2016). Effect of bark beetle (ips typographus l.) attack on bark VOC emissions of Norway spruce (picea abies karst.) trees. *Atmospheric Environment*, 126, 145–152. <https://doi.org/10.1016/j.atmosenv.2015.11.049>
- Ghirardo, A., Heller, W., Fladung, M., Schnitzler, J.-P., & Schroeder, H. (2012). Function of defensive volatiles in pedunculate oak (*quercus robur*) is tricked by the moth tortrix viridana. *Plant, Cell and Environment*, 35(12), 2192–2207. <https://doi.org/10.1111/j.1365-3040.2012.02545.x>
- Goldstein, A. H., & Galbally, I. E. (2007). Known and unexplored organic constituents in the Earth's atmosphere. *Environmental Science & Technology*, 41(5), 1514–1521. PMID: 17396635. Retrieved from <https://doi.org/10.1021/es072476p>
- Griffith, S. M., Hansen, R. F., Dusanter, S., Michoud, V., Gilman, J. B., Kuster, W. C., et al. (2016). Measurements of hydroxyl and hydroperoxy radicals during calnex-la: Model comparisons and radical budgets. *Journal of Geophysical Research: Atmospheres*, 121(8), 4211–4232. <https://doi.org/10.1002/2015JD024358>
- Guenther, A. B., Jiang, X., Heald, C. L., Sakulyanontvittaya, T., Duhl, T., Emmons, L. K., & Wang, X. (2012). The model of emissions of gases and aerosols from nature version 2.1 (megan2.1): An extended and updated framework for modeling biogenic emissions. *Geoscientific Model Development*, 5(6), 1471–1492. <https://doi.org/10.5194/gmd-5-1471-2012>
- Hakola, H., Tarvainen, V., Bäck, J., Ranta, H., Bonn, B., Rinne, J., & Kulmala, M. (2006). Seasonal variation of mono- and sesquiterpene emission rates of Scots pine. *Biogeosciences*, 3(1), 93–101. <https://doi.org/10.5194/bg-3-93-2006>
- Hallquist, M., Wenger, J. C., Baltensperger, U., Rudich, Y., Simpson, D., Claeys, M., et al. (2009). The formation, properties and impact of secondary organic aerosol: Current and emerging issues. *Atmospheric Chemistry and Physics*, 9(14), 5155–5236. <https://doi.org/10.5194/acp-9-5155-2009>
- HAMMOZ Consortium. (2020). ECHAM-HAMMOZ model data [Dataset]. Redmine (login required). Retrieved from [https://redmine.hammoz.ethz.ch/projects/hammoz/repository/show/echam6-hammoz/branches/fmi/fmi\\_trunk](https://redmine.hammoz.ethz.ch/projects/hammoz/repository/show/echam6-hammoz/branches/fmi/fmi_trunk)
- Hanson, S., Knorr, W., Schurgers, G., Pugh, T. A., & Arneth, A. (2017). Global isoprene and monoterpene emissions under changing climate, vegetation, CO<sub>2</sub> and land use. *Atmospheric Environment*, 155, 35–45. <https://doi.org/10.1016/j.atmosenv.2017.02.010>
- He, M., He, C.-Q., & Ding, N.-Z. (2018). Abiotic stresses: General defenses of land plants and chances for engineering multistress tolerance. *Frontiers of Plant Science*, 9, 1771. <https://doi.org/10.3389/fpls.2018.01771>
- Heijari, J., Blande, J. D., & Holopainen, J. K. (2011). Feeding of large pine weevil on Scots pine stem triggers localised bark and systemic shoot emission of volatile organic compounds. *Environmental and Experimental Botany*, 71(3), 390–398. <https://doi.org/10.1016/j.envexpbot.2011.02.008>
- Hoesly, R. M., Smith, S. J., Feng, L., Klimont, Z., Janssens-Maenhout, G., Pitkanen, T., et al. (2018). Historical (1750–2014) anthropogenic emissions of reactive gases and aerosols from the community emissions data system (CEDS). *Geoscientific Model Development*, 11(1), 369–408. <https://doi.org/10.5194/gmd-11-369-2018>
- Holopainen, E., Kokkola, H., Faiola, C., Laakso, A., & Kühn, T. (2022). Insect herbivory caused plant stress emissions increase the negative radiative forcing of aerosols 2021–2022 data [Dataset]. Fairdata. <https://doi.org/10.23729/276c1680-bce0-40d7-9254-f05038a3a6a9>
- Holopainen, J. K. (2004). Multiple functions of inducible plant volatiles. *Trends in Plant Science*, 9(11), 529–533. <https://doi.org/10.1016/j.tplants.2004.09.006>
- Holopainen, J. K., & Gershenzon, J. (2010). Multiple stress factors and the emission of plant VOCs. *Trends in Plant Science*, 15(3), 176–184. <https://doi.org/10.1016/j.tplants.2010.01.006>
- Holopainen, J. K., Virjamo, V., Ghimire, R. P., Blande, J. D., Julkunen-Tiitto, R., & Kivimäenpää, M. (2018). Climate change effects on secondary compounds of forest trees in the northern hemisphere. *Frontiers of Plant Science*, 9, 1445. <https://doi.org/10.3389/fpls.2018.01445>
- IPCC. (2021). *Climate change 2021: The physical science basis. contribution of working group i to the sixth assessment report of the inter-governmental panel on climate change*. In (p. 6-1-7-204). Cambridge University Press. Retrieved from <https://www.ipcc.ch/report/ar6/wg1/fullreport>
- Jimenez, J. L., Canagaratna, M. R., Donahue, N. M., Prevot, A. S. H., & Zhang, Q. (2009). Evolution of organic aerosols in the atmosphere. *Science*, 326(5959), 1525–1529. <https://doi.org/10.1126/science.1180353>
- Joutsensaari, J., Yli-Pirilä, P., Korhonen, H., Arola, A., Blande, J. D., Heijari, J., et al. (2015). Biotic stress accelerates formation of climate-relevant aerosols in boreal forests. *Atmospheric Chemistry and Physics*, 15(21), 12139–12157. <https://doi.org/10.5194/acp-15-12139-2015>



- Kari, E., Faiola, C., Isokääntä, S., Miettinen, P., Yli-Pirilä, P., Buchholz, A., et al. (2019). Time-resolved characterization of biotic stress emissions from Scots pines being fed upon by pine weevil by means of PTR-ToF-MS. *Boreal Environment Research*, 24, 25–49.
- Kerminen, V.-M., & Kulmala, M. (2002). Analytical formulae connecting the “real” and the “apparent” nucleation rate and the nuclei number concentration for atmospheric nucleation events. *Journal of Aerosol Science*, 33(4), 609–622. [https://doi.org/10.1016/S0021-8502\(01\)00194-X](https://doi.org/10.1016/S0021-8502(01)00194-X)
- Kerminen, V.-M., Lihavainen, H., Komppula, M., Viisanen, Y., & Kulmala, M. (2005). Direct observational evidence linking atmospheric aerosol formation and cloud droplet activation. *Geophysical Research Letters*, 32(14), L14803. <https://doi.org/10.1029/2005GL023130>
- Kokkola, H., Kuhn, T., Laakso, A., Bergman, T., Lehtinen, K. E. J., Mielonen, T., et al. (2018). SALSA2.0: The sectional aerosol module of the aerosol-chemistry-climate model ECHAM6.3.0-HAM2.3-MOZ1.0. *Geoscientific Model Development*, 11(9), 3833–3863. <https://doi.org/10.5194/gmd-11-3833-2018>
- Kokkola, H., Tonttila, J., Romakkaniemi, S., Bergman, T., Laakso, A., Kühn, T., et al. (2018). Salsa-standalone 2.0 [Software]. Zenodo. <https://doi.org/10.5281/zenodo.1251669>
- Kovalchuk, A., Raffaello, T., Jaber, E., Keriö, S., Ghimire, R., Lorenz, W. W., et al. (2015). Activation of defence pathways in Scots pine bark after feeding by pine weevil (*hylobius abietis*). *BMC Genomics*, 16(1), 1471–2164. <https://doi.org/10.1186/s12864-015-1546-9>
- Kozlov, M. V., & Zvereva, E. L. (2018). Background insect herbivory: Impacts, patterns and methodology. In F. M. Cánovas, U. Lüttge, & R. Matyssek (Eds.), *Progress in botany* (Vol. 79). Springer International Publishing. [https://doi.org/10.1007/124\\_2017\\_4](https://doi.org/10.1007/124_2017_4)
- Kuang, C., McMurry, P. H., & McCormick, A. V. (2009). Determination of cloud condensation nuclei production from measured new particle formation events. *Geophysical Research Letters*, 36(9), L09822. <https://doi.org/10.1029/2009GL037584>
- Kühn, T., Kupiainen, K., Miinalainen, T., Kokkola, H., Paunu, V.-V., Laakso, A., et al. (2020). Effects of black carbon mitigation on arctic climate. *Atmospheric Chemistry and Physics*, 20(9), 5527–5546. <https://doi.org/10.5194/acp-20-5527-2020>
- Kulmala, M., Nieminen, T., Nikandrova, A., Lehtipalo, K., Manninen, H. E., Kajos, M. K., et al. (2014). CO<sub>2</sub>-induced terrestrial climate feedback mechanism: From carbon sink to aerosol source and back. *Boreal Environment Research*, 19, 122–131. Retrieved from <http://hdl.handle.net/10138/228728>
- Kulmala, M., Petäjä, T., Ehn, M., Thornton, J., Sipilä, M., Worsnop, D., & Kerminen, V.-M. (2014). Chemistry of atmospheric nucleation: On the recent advances on precursor characterization and atmospheric cluster composition in connection with atmospheric new particle formation. *Annual Review of Physical Chemistry*, 65(1), 21–37. PMID: 24245904. <https://doi.org/10.1146/040412-110014>
- Li, T., Holopainen, J. K., Kokko, H., Tervahauta, A. I., & Blande, J. D. (2012). Herbivore-induced aspen volatiles temporally regulate two different indirect defences in neighbouring plants. *Functional Ecology*, 26(5), 1176–1185. <https://doi.org/10.1111/j.1365-2435.2012.01984.x>
- Litvak, M. E., & Monson, R. K. (1998). Patterns of induced and constitutive monoterpene production in conifer needles in relation to insect herbivory. *Oecologia*, 114(4), 531–540. <https://doi.org/10.1007/s004420050477>
- Maja, M. M., Kasurinen, A., Yli-Pirilä, P., Joutsensaari, J., Klemola, T., Holopainen, T., & Holopainen, J. K. (2014). Contrasting responses of silver birch VOC emissions to short- and long-term herbivory. *Tree Physiology*, 34(3), 241–252. <https://doi.org/10.1093/treephys/tpt127>
- Makkonen, R., Asmi, A., Korhonen, H., Kokkola, H., Järvenoja, S., Räisänen, P., et al. (2009). Sensitivity of aerosol concentrations and cloud properties to nucleation and secondary organic distribution in ECHAM5-HAM global circulation model. *Atmospheric Chemistry and Physics*, 9(5), 1747–1766. <https://doi.org/10.5194/acp-9-1747-2009>
- Mäntylä, E., Alessio, G. A., Blande, J. D., Heijari, J., Holopainen, J. K., Laaksonen, T., et al. (2008). From plants to birds: Higher avian predation rates in trees responding to insect herbivory. *PLoS One*, 3(7), 1–8. <https://doi.org/10.1371/journal.pone.0002832>
- Materić, D., Bruhn, D., Turner, C., Morgan, G., Mason, N., & Gauci, V. (2015). Methods in plant foliar volatile organic compounds research. *Applications in Plant Sciences*, 3(12), 1500044. <https://doi.org/10.3732/apps.1500044>
- Michel, A., Seidl, W., & Prescher, A.-K. e. (2018). Forest condition in Europe: 2018 technical report of ICP forests. Report under the UNECE convention on long-range transboundary air pollution (air convention). BFW-dokumentation, (Vol. 25, p. 92). Retrieved from <https://www.icp-forests.org/pdf/TR2018.pdf>
- Miinalainen, T., Kokkola, H., Lehtinen, K. E. J., & Kühn, T. (2021). Comparing the radiative forcings of the anthropogenic aerosol emissions from Chile and Mexico. *Journal of Geophysical Research: Atmospheres*, 126(10), e2020JD033364. <https://doi.org/10.1029/2020JD033364>
- Murphy, D. M., Cziczo, D. J., Froyd, K. D., Hudson, P. K., Matthew, B. M., Middlebrook, A. M., et al. (2006). Single-particle mass spectrometry of tropospheric aerosol particles. *Journal of Geophysical Research*, 111(D23), D23S32. <https://doi.org/10.1029/2006JD007340>
- Niinemets, U. (2010). Mild versus severe stress and BVOCs: Thresholds, priming and consequences. *Trends in Plant Science*, 15(3), 145–153. (Special Issue: Induced biogenic volatile organic compounds from plants). <https://doi.org/10.1016/j.tplants.2009.11.008>
- Proffit, M., Lapeyre, B., Buatois, B., Deng, X., Arnal, P., Gouzerh, F., et al. (2020). Chemical signal is in the blend: Bases of plant-pollinator encounter in a highly specialized interaction. *Scientific Reports*, 10(1), 10071. Retrieved from <https://doi.org/10.1038/s41598-020-66655-w>
- Rinne, J., Bäck, J., & Hakola, H. (2009). Biogenic volatile organic compound emissions from the Eurasian taiga: Current knowledge and future directions. *Boreal Environment Research*, 14, 807–826.
- Runyon, J. B., Mescher, M. C., & Moraes, C. M. D. (2006). Volatile chemical cues guide host location and host selection by parasitic plants. *Science*, 313(5795), 1964–1967. <https://doi.org/10.1126/science.1131371>
- Schaub, A., Blande, J. D., Graus, M., Oksanen, E., Holopainen, J. K., & Hansel, A. (2010). Real-time monitoring of herbivore induced volatile emissions in the field. *Physiologia Plantarum*, 138(2), 123–133. <https://doi.org/10.1111/j.1399-3054.2009.01322.x>
- Schobesberger, S., Junninen, H., Bianchi, F., Lönn, G., Ehn, M., Lehtipalo, K., et al. (2013). Molecular understanding of atmospheric particle formation from sulfuric acid and large oxidized organic molecules. *Proceedings of the National Academy of Sciences*, 110(43), 17223–17228. <https://doi.org/10.1073/pnas.1306973110>
- Schultz, M. G., Stadler, S., Schröder, S., Taraborrelli, D., Franco, B., Krefting, J., et al. (2018). The chemistry–climate model ECHAM6.3-HAM2.3-MOZ1.0. *Geoscientific Model Development*, 11(5), 1695–1723. <https://doi.org/10.5194/gmd-11-1695-2018>
- Seinfeld, J. H., & Pandis, S. N. (2006). *Atmospheric Chemistry and Physics: From air pollution to climate change*, 2. Edn. (Vol. 2). John Wiley & Sons.
- Sharkey, T. D., & Yeh, S. (2001). Isoprene emission from plants. *Annual Review of Plant Physiology and Plant Molecular Biology*, 52(1), 407–436. (PMID: 11337404). <https://doi.org/10.1146/annurev.arplant.52.1.407>
- Sporre, M. K., Blichner, S. M., Schrödner, R., Karset, I. H. H., Berntsen, T. K., van Noije, T., et al. (2020). Large difference in aerosol radiative effects from BVOC-SOA treatment in three Earth system models. *Atmospheric Chemistry and Physics*, 20(14), 8953–8973. <https://doi.org/10.5194/acp-20-8953-2020>
- Stevens, B., Giorgetta, M., Esch, M., Mauritsen, T., Crueger, T., Rast, S., et al. (2013). Atmospheric component of the MPI-M Earth system model: ECHAM6. *Journal of Advances in Modeling Earth Systems*, 5(2), 146–172. <https://doi.org/10.1002/jame.20015>
- Taipale, D., Kerminen, V.-M., Ehn, M., Kulmala, M., & Niinemets, U. (2021). Modelling the influence of biotic plant stress on atmospheric aerosol particle processes throughout a growing season. *Atmospheric Chemistry and Physics*, 21(23), 17389–17431. <https://doi.org/10.5194/acp-21-17389-2021>

- Taylor, K. E., Stouffer, R. J., & Meehl, G. A. (2012). An overview of CMIP5 and the experiment design. *Bulletin of the American Meteorological Society*, 93(4), 485–498. <https://doi.org/10.1175/BAMS-D-11-00094.1>
- Tegen, I., Neubauer, D., Ferrachat, S., Siegenthaler-Le Drian, C., Bey, I., Schutgens, N., et al. (2019). The global aerosol–climate model ECHAM6.3–HAM2.3—Part 1: Aerosol evaluation. *Geoscientific Model Development*, 12(4), 1643–1677. <https://doi.org/10.5194/gmd-12-1643-2019>
- Tsigaridis, K., Daskalakis, N., Kanakidou, M., Adams, P. J., Artaxo, P., Bahadur, R., et al. (2014). The AeroCom evaluation and intercomparison of organic aerosol in global models. *Atmospheric Chemistry and Physics*, 14(19), 10845–10895. <https://doi.org/10.5194/acp-14-10845-2014>
- Twomey, S. (1974). Pollution and the planetary albedo. *Atmospheric Environment*, 8(12), 1251–1256. [https://doi.org/10.1016/0004-6981\(74\)90004-3](https://doi.org/10.1016/0004-6981(74)90004-3)
- Twomey, S. (1991). *Aerosol, clouds, and radiation*. (Vol. 25A). The University of Arizona. Atmospheric Environment.
- Ueda, H., Kikuta, Y., & Matsuda, K. (2012). Plant communication. *Plant Signaling & Behavior*, 7(2), 222–226. PMID: 22353877. <https://doi.org/10.4161/psb.18765>
- Venäläinen, A., Lehtonen, I., Laapas, M., Ruosteenoja, K., Tikkanen, O.-P., Viiri, H., et al. (2020). Climate change induces multiple risks to boreal forests and forestry in Finland: A literature review. *Global Change Biology*, 26(8), 4178–4196. <https://doi.org/10.1111/gcb.15183>
- Wilcoxon, F. (1945). Individual comparisons by ranking methods. *International Biometric Society*, 1(6), 80. <https://doi.org/10.2307/3001968>
- Wullschlegel, S. D., Epstein, H. E., Box, E. O., Euskirchen, E. S., Goswami, S., Iversen, C. M., et al. (2014). Plant functional types in Earth system models: Past experiences and future directions for application of dynamic vegetation models in high-latitude ecosystems. *Annals of Botany*, 114, 1–16. <https://doi.org/10.1093/aob/mcu077>
- Yli-Juuti, T., Mielonen, T., Heikkinen, L., Arola, A., Ehn, M., Isokääntä, S., et al. (2021). Significance of the organic aerosol driven climate feedback in the boreal area. *Nature Communications*, 12(1), 5637. Retrieved from <https://doi.org/10.1038/s41467-021-25850-7>
- Yli-Pirilä, P., Copolovici, L., Kännaste, A., Noe, S., Blande, J. D., Mikkonen, S., et al. (2016). Herbivory by an outbreaking moth increases emissions of biogenic volatiles and leads to enhanced secondary organic aerosol formation capacity. *Environmental and Experimental Botany*, 50(21), 11501–11510. <https://doi.org/10.1021/acs.est.6b02800>
- Zebelo, S. A., Matsui, K., Ozawa, R., & Maffei, M. E. (2012). Plasma membrane potential depolarization and cytosolic calcium flux are early events involved in tomato (*solanum lycopersicon*) plant-to-plant communication. *Plant Science*, 196, 93–100. <https://doi.org/10.1016/j.plantsci.2012.08.006>
- Zhang, Q., Jimenez, J. L., Canagaratna, M. R., Allan, J. D., Coe, H., Ulbrich, I., et al. (2007). Ubiquity and dominance of oxygenated species in organic aerosols in anthropogenically-influenced northern hemisphere midlatitudes. *Geophysical Research Letters*, 34(13), L13801. <https://doi.org/10.1029/2007GL029979>
- Zhao, D., Buchholz, A., Tillmann, R., Kleist, E., Wu, C., Rubach, F., et al. (2017). Environmental conditions regulate the impact of plants on cloud formation. *Nature Communications*, 8(1), 14067. <https://doi.org/10.1038/ncomms14067>



ILMATIETEEN LAITOS  
METEOROLOGISKA INSTITUTET  
FINNISH METEOROLOGICAL INSTITUTE

## **FINNISH METEOROLOGICAL INSTITUTE**

Erik Palménin aukio 1  
P.O. Box 503  
FI-00560 HELSINKI  
tel. +358 29 539 1000  
**WWW.FMI.FI**

FINNISH METEOROLOGICAL INSTITUTE  
CONTRIBUTIONS No. 185

ISBN 978-952-336-168-3 (print)  
ISBN 978-952-336-169-0 (online)  
ISSN 0782-6117 (print)  
ISSN 2814-5658 (online)  
<https://doi.org/10.35614/isbn.9789523361690>

Helsinki 2023  
Edita Prima Oy

